N° D'ORDRE: D.U. 1952

UNIVERSITE BLAISE PASCAL
U.F.R. Sciences et Technologies
ECOLE DOCTORALE DES SCIENCES FONDAMENTALES (N°612)

THESE

presentèe pour obtenir le grade de DOCTEUR D'UNIVERSITE,
Specialité: Physique des Matériaux, par

Robert JOHNE
Master de Physique

Strong light matter coupling in semiconductor nanostructures - Nonlinear effects and applications

Soutenue publiquement le 18/09/2009, devant la comission d'examen:

TEJEDOR Carlos (président & rapporteur)
LOZOVIK Yurii E. (rapporteur)
WOUTERS Michiel (rapporteur)
BLOCH Jacqueline (examinateur)
MALPUECH Guillaume (directeur de thèse)
GIPPIUS Nikolay (directeur de thèse)
SOLNYSHKOV Dmitry (invité)

Contents

Acknowledgment

I have been working in Clermont for nearly three years. During this time I had the pleasure to collaborate and to meet a lot of bright scientists. Many of them influenced my work with fruitful discussions, helpful remarks, guidance, and of course criticism. These years in Clermont allowed me to expand my horizon not only from scientific point of view.

First, I would like to thank my two supervisors, Guillaume Malpuech and Nikolay Gippius. Both, each with slightly contrary ways to do research, have been the poles between which I worked on my thesis. Guillaume has been always dynamic, pushing us forward to new frontiers and topics, whereas Nikolay time to time slowed down to think and to discuss things more quietly and more critically. Both helped me a lot, on the one hand to be productive and to discover various – for me unknown – research topics and, on the other hand, to avoid mistakes and to get deeper understanding. I appreciate strongly that I had and have the possibility to work with Guillaume and Nikolay.

Beside the supervisors, I would like to thank the other members of our research group: Goran Pavlovic and Dmitry Solnyshkov. Beside the scientific questions, Dmitry's help in numerical calculations and, in general, on everything what is related to computers, saved me a long time of efforts. Also I acknowledge his help and his corrections to write the present thesis.

From our external collaborators it is Ivan Shelykh (presently a professor in Iceland), who played the most important role during these three years. His bright ideas and creativity have been always impressive and have stimulated a lot of works.

What I appreciate most, is the fruitful and very amicable working atmosphere, with all necessary freedom for a young scientist and student as well as the common interest in climbing (at least for three of us).

Last but not least, I would like to thank Christiane that she came to France and that she had to put up with me all the time. She and Mila showed me every day that there is a life outside Physics, which should not be forgotten.

Introduction

Exciton-polaritons, mixed light-matter quasiparticles, are on their way to break in the world of optoelectronic devices due to their unique properties. The exciton-polaritons result from the strong interaction of excitons and photons in microcavities. If this interaction is larger than all broadenings induced by different sources, the microcavity operates in the strong coupling regime which manifests itself in a mixed light-matter dispersion with separated nonparabolic polariton branches. The polaritons behave as interacting bosons in the low density limit and are the solid state counterpart of cold atoms. Thus, exciton-polaritons confined in 2D planar microcavities are in the focus of active research partly because of the possible device applications, partly because of the general interest in fundamental effects, such as quasi Bose-Einstein condensation in solid state systems. A second structure, for a long time less studied than the planar cavities, are 0D microcavities. This field is growing rapidly in recent years due to new developed applications for single- or two-photon sources in quantum communication and quantum information and the substantial progress of fabrication technologies.

The present theoretical thesis is focused on nonlinear effects and possible applications of exciton polaritons. The first chapter gives a general introduction to exciton-polariton physics including the main important mathematical tools, cavity realizations, as well as a small review on the main theoretical and experimental observations. Putting apart the general introduction on exciton-polaritons, the thesis can be divided into the three following parts discussed in chapters two, three and four.

The second chapter is devoted to the effects possible under resonant excitation, which means that the pumping laser is in quasi-resonance with the polariton dispersion. In some cases, the relaxation of polaritons toward the bottom of lower polariton branch can be described by rate equations - the so called semiclassical Boltzmann equations. Once a condensate in the ground state is formed, its behavior can be described by a nonlinear Schrdinger equation, the Gross-Pitaevskii equation. We present a new theoretical approach which builds a bridge between the semiclassical approach and the coherent picture using high order correlators. This theory is applied to the polariton parametric oscillator and a transition between the two regimes is shown.

The second topic of the second chapter is the bistability of the polariton system.

The polariton-polariton interaction results in a blue shift of the polariton dispersion with increasing external pump intensity. If the driving laser beam frequency exceeds that of the lower polariton branch by more than its linewidth, the density of polaritons can exhibit abrupt transitions between different stable values, demonstrating a hystersis cycle. Close to the stability edge, fluctuations become important for the transitions between the stable states. We compare different approaches to describe these fluctuation-induced transitions. In general, increasing the noise intensity leads to a narrowing of the hysteresis cycle.

Condensation phenomena and their applications are the subject of the third chapter of the thesis. Quasi Bose-Einstein condensation of exciton-polaritons makes possible a new device called polariton laser, which is strongly different from conventional lasers because it requires no population inversion. Wide bandgap semiconductors, such as GaN and ZnO, are probably the best candidates for a polariton laser working at room temperature. We simulate the relaxation of injected particles towards the bottom of the polariton dispersion for a ZnO microcavity and show the huge difference of kinetic and thermodynamic lasing thresholds. As a general result, larger Rabi splittings are advantageous for quasi-equilibrium polariton lasing, which shifts ZnO even more into the focus for the fabrication of such devices.

The unique spin structure of polaritons and polariton condensates creates another fascinating new field of applications: spin-optronics. We propose two novel devices. The first one is based on the Josephson effect of exciton-polaritons: the interplay of different nonlinear effects can result in a chaotic behavior, which can be used to transmit useful signals hidden in a chaotic background (chaotic communication) under the condition that two chaotic systems can be synchronized. We show that the synchronization of such systems and the high frequencies of the chaotic oscillations provide transmission rates for the useful signal up to 50 Gb/s. In addition, in the framework of spin-optronics, a polaritonic spin transistor is proposed, in analogy to the Datta and Das spin transistor for electrons. This spin-optronic device is based on the spin-Meissner effect of polariton condensates (suppression of the Zeeman splitting below critical magnetic field with a modification of the polarization of the condensate). The polarization of the injected particles is rotated and the transmission coefficient of such a device can be tuned by changing the density of the polariton condensate.

Beside the planar microcavities, the strong progress in the fabrication of cavity structures opens the field of cavity Quantum Electro-Dynamics in solid state systems. This will be the subject of the last chapter and the last part of the thesis. Therein, we develop the proposal for the generation of entangled photon pairs based on the biexciton decay in a quantum dot embedded in a photonic crystal. Several problems of the imperfect artificial atom picture of the quantum dots can be overcome by engineering the strong coupling of the exciton states with cavity modes. We believe that our proposal of a strongly coupled

dot-cavity system could be a worthy candidate for "on-chip" sources of entangled photon pairs.

Chapter 1

Microcavity exciton-polaritons - general aspects

The quasiparticle called "exciton-polariton", or simply polariton, possesses both excitonic and photonic properties. It can be formed in a microcavity, if the coupling between the free exciton and the photon field inside of the resonator is larger than the dephasing in the system. Due to the mixing of matter and light, polariton have unique properties, which allow to study application physics as well as fundamental effects in solid state materials. This means that on one hand polaritons are the best suited candidates for a lot of applications in optoelectronic devices and on the other hand exciton-polaritons open the possibility of quasi Bose-Einstein condensation in a solid state system, which has drawn a lot of attention to the field.

The following chapter gives an introduction to the strong coupling regime and to the physics of polaritons, discussion of the basic mathematical tools as well as the effects of different cavity designs. In addition, a small review of milestone experimental and theoretical works is included.

Contents

1.1 Two oscillator model of strong coupling

The exciton-polariton concept was initially introduced in bulk semiconductors by Hopfield (1958) [1]. It was independently proposed by Agranovic (1959) [2]. The most fruitful system, technologically and physically, from the beginning of the experimental observation of exciton-polaritons [3] were semiconductor heterostructures. Periodical structures containing quarter wave layers of different materials with different refractive indices - the Bragg mirrors - allow to trap the photons in the structure and quantum wells (QWs) as active layers allow to confine the excitons. The latter effect reduces the dimensionality and allows to place the exciton in the maximum of the electric field of cavity light. Thus, the coupling between light and matter in semiconductor heterostructures is strongly enhanced, which opens the possibility to observe the strong coupling regime.

The polariton can be considered as a new eigenstate, which arises from the coupling of two oscillators - in our case one exciton and one photon. In this simple model, the polariton can be seen as a chain process between the radiative relaxation of the exciton emitting a photon and the reabsorption of this photon creating an exciton. Finally the excitation, in form of a photon, finds its way out of the microcavity, which results in the annihilation of the polariton. The Hamiltonian for free excitons and cavity photons can be written as follows

$$H_0 = \sum_k E_X(k) b_k^\dagger b_k + \sum_k E_C(k) a_k^\dagger a_k. \tag{1.1}$$

The operators $b_k^\dagger, b_k, a_k^\dagger, a_k$ are creation and annihilation operators for excitons and photons, respectively. The in-plane dispersion relation of excitons is

$$E_X(k) = E_X(0) + \frac{\hbar^2 k^2}{2m_X} - \frac{i\hbar}{2}\Gamma_X(k), \tag{1.2}$$

where m_X is the free in-plane exciton mass and Γ_X is the phenomenological decay rate which governs the finite linewidth of the exciton resonance. The dispersion of the cavity mode reads

$$E_C(k) = \sqrt{E_C(0)^2 + \frac{\hbar^2 c^2 k^2}{n_C^2}} - \frac{i\hbar}{2}\Gamma_C(k), \tag{1.3}$$

with n_C as the cavity refractive index. The resonant energy of the cavity is denoted $E_C(0) = hc/\lambda_0$, where λ_0 is the resonant wavelength of the cavity. The decay rate $\Gamma_C(k)$ accounts for the escape of cavity photons through the cavity mirrors. Around $k = 0$ the cavity dispersion can be approximated by a parabola:

$$E_C(k) \approx E_C(0) + \frac{\hbar^2 k^2}{2m_C} - \frac{i\hbar}{2}\Gamma_C(k), \tag{1.4}$$

where

$$m_C = E_C(0)\frac{n_C^2}{c^2} = \frac{hn_C}{c\lambda}. \tag{1.5}$$

Introducing a linear coupling between exciton and photon, resulting from the interaction of the light field with the dipole moment of the electron-hole pair, one can write the coupling Hamiltonian in the following way

$$H_{XC} = \sum_k \hbar\Omega a_k^\dagger b_k + H.c., \tag{1.6}$$

$$\Omega = \frac{d}{2\pi a_b^{2D}}\sqrt{\frac{NE_X}{\hbar^2 n_c \lambda_0}}, \tag{1.7}$$

where d is the exciton dipole moment and N is the number of QWs within the cavity. The coupling strength Ω between an exciton and one photon is proportional to the exciton oscillator strength and to the number of QWs embedded in the cavity. Taking only one exciton resonance into account and neglecting the imaginary part of Eqs.(1.3) and (1.4), the description can be reduced to a two-level problem. The eigenstates of the system can be found by diagonalization of the matrix

$$M(k) = \begin{pmatrix} E_X(k) & \hbar\Omega \\ \hbar\Omega & E_C(k) \end{pmatrix}. \tag{1.8}$$

The eigenvalues of this matrix are given by:

$$det(M - \lambda I) = 0 \Leftrightarrow (E_X - \lambda)(E_C - \lambda) - \hbar^2\Omega^2 = 0. \tag{1.9}$$

Two solutions can be found for this equation, which read

$$E_{U(L)} = \frac{E_C(k) + E_X(k)}{2} \pm \frac{1}{2}\sqrt{(E_C(k) - E_X(k))^2 + 4\hbar^2\Omega^2}, \tag{1.10}$$

where E_U and E_L are the eigenenergies of the upper and lower polariton branch, respectively.

The corresponding eigenvectors are given by

$$M(k)\begin{pmatrix} X_U(k) \\ C_U(k) \end{pmatrix} = E_U(k)\begin{pmatrix} X_U(k) \\ C_U(k) \end{pmatrix}, \tag{1.11}$$

with the normalization condition $X_U(k)^2 + C_U(k)^2 = 1$ and they can be written as

$$C_U = \frac{E_U - E_X}{\sqrt{\hbar^2\Omega^2 + (E_U - E_X)^2}} \tag{1.12}$$

$$X_U = \frac{\hbar\Omega}{\sqrt{\hbar^2\Omega^2 + (E_U - E_X)^2}}. \tag{1.13}$$

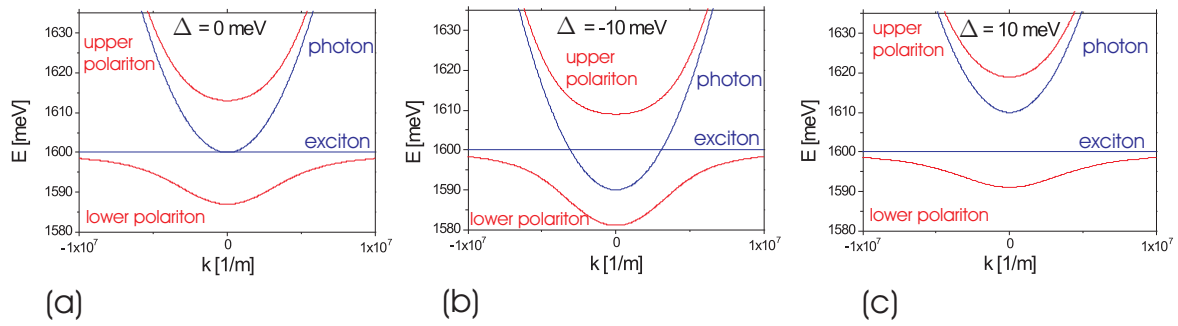

Figure 1.1 | Calculated polariton dispersions of a GaAs microcavity: The bare exciton and photon dispersions are plotted blue and the resulting polariton dispersions are plotted red. The used detunings are (a) $\Delta = 0$, (b) $\Delta = -10$ meV and (c) $\Delta = 10$ meV.

The eigenvectors corresponding to the second eigenvalue give similar results and the relation between them can be derived to:

$$X_L = C_U, C_L = -X_U, \tag{1.14}$$

where $X_{U(L)}$ and $C_{U(L)}$ are the Hopfield coefficients for the upper (lower) polariton branch.

The typical dispersion is shown in Fig(1.1)(a) calculated for a GaAs microcavity. This dispersion has a clear non-parabolic shape, which plays a crucial role for example for the parametric scattering.

It is possible to define upper and lower polariton annihilation and creation operators as combination of exciton and photon operators:

$$\begin{aligned} p_k &= X_L(k)b_k + C_L(k)a_k^\dagger \\ p_k^\dagger &= X_L(k)b_k^\dagger + C_L(k)a_k \\ pu_k &= X_U(k)b_k + C_U(k)a_k^\dagger \\ pu_k^\dagger &= X_U(k)b_k^\dagger + C_U(k)a_k. \end{aligned} \tag{1.15}$$

Using this transformation one can rewrite the Hamiltonian in the basis of polariton operators in which it becomes diagonal, with the eigenstates being the exciton-polaritons. The polariton Hamiltonian reads

$$H_p = \sum_k E_L(k)p_k^\dagger p_k + \sum_k E_U(k)pu_k^\dagger pu_k. \tag{1.16}$$

The exciton-polariton wavefunction is a linear superposition of photon and exciton wavefunctions. Of course, the photons themselves do not interact, so the interactions should be included only for the excitonic part. More detailed, the Coulomb interaction

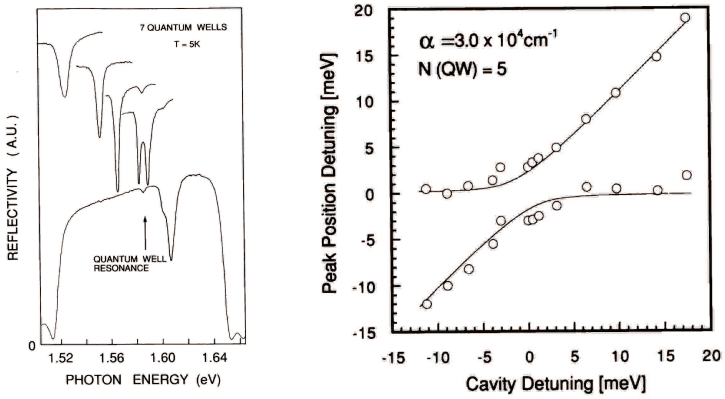

Figure 1.2 | Observation of the vacuum field Rabi splitting [3]: The left figure shows the reflectivity spectra in dependence on the photon energy for various detunings. The right figure presents the anticrossing behavior of the reflectivity dips in dependence on the detuning.

between the carriers is responsible for an effective exciton-exciton interaction. This description of exciton in terms of weakly interacting bosons has been recently criticized by Combescot et al. [4]. It is not our goal here to enter in this debate and to discuss the quality of such description which we will use as a starting point of more complex theoretical developments which are detailed all along this document. The Hamiltonian for excitons reads

$$H_{XX} = \frac{1}{2} \sum_{k,k',q} V_q b^\dagger_{k+q} b^\dagger_{k'-q} b_k b_{k'}. \tag{1.17}$$

The interaction of photon-like polaritons in the upper dispersion branch may be neglected if this branch is not expected to be strongly occupied, as in our case. Transformation of the interaction Hamiltonian in the polariton basis yields

$$H_{PP} = \frac{1}{2} \sum_{k,k',q} V^{PP}_{q,k,k'} p^\dagger_{k+q} p^\dagger_{k'-q} p_k p_{k'}, \tag{1.18}$$

with

$$V^{PP}_{q,k,k'} = V_q X_L(k+q) X_L(k'-q) X_L(k) X_L(k'). \tag{1.19}$$

Finally, the total Hamiltonian reads

$$H = H_P + H_{PP}. \tag{1.20}$$

This includes only the polariton-polariton interaction. Other interaction terms are discussed in the framework of the Boltzmann equations and in the appendix.

In principle, the excitonic mode $E_X(0)$ is not necessarily degenerate with the cavity mode $E_C(0)$. Introducing a small positive or negative detuning $\Delta = E_C - E_X$ allows to change the dispersion and to shift the properties to more exciton-like or photon-like,

respectively. This can be seen already from the distances of the polariton states to the initial exciton and photon dispersion in Fig(1.1)b and c. The excitonic component has a strong influence on the scattering rates, which is important for the relaxation process of polaritons in order to observe the quasi Bose-Einstein condensation, discussed in the first part of chapter 3.

As noted above, the energies of the excitonic and photonic modes can contain imaginary parts, which account for the dissipative processes in the system.

The seminal paper of Weisbuch et al. (1992) [3] was the starting point for the huge investigation of microcavity polaritons. The authors report the observed vacuum field Rabi splitting at 5K in GaAlAs with seven quantum wells. The left figure on Fig(1.2) shows the reflectivity in dependence on the photon energy for different detunings varied from the top to bottom. At the resonance of the cavity mode and the exciton confined in the quantum well (zero detuning) a splitting between two modes around the quantum well resonance is observed. Past the resonance (negative detuning) the strong coupling is lost again. The right hand side figure gives the splitting of the dips observed in the reflectivity measurements in dependence on the detuning. In contrast to the weak coupling regime, where the bare cavity mode and the bare exciton mode manifest themselves as straight lines, in the strong coupling regime a clear anticrossing at zero detuning takes place. This is the clear signature of the strong light matter interaction. As mentioned above, after this report the activities on microcavity polaritons increased enormously and the physics of exciton-polaritons has found its way into university courses and specialized textbooks [5, 6]. Room-temperature vacuum Rabi splitting has been observed for various semiconductor materials and systems and especially wide gap semiconductors have drawn a lot of attention. To the best of our knowledge the record vacuum Rabi splitting in conventional semiconductor materials is about 100 meV for ZnO microcavities, as reported recently [7].

1.2 Cavity design

A microcavity is an optical resonator with a typical thickness between $\lambda/2$ and $5\lambda/2$, λ being the wavelength of the studied optical mode. Micrometer- and submicrometer-sized resonators use two different schemes to confine light. The first one is based on a single interface reflection (e.g. on metallic surfaces) or on the total internal reflection at the boundary between two dielectrics. The second scheme is based on the microstructures periodically patterned on the scale of the resonant optical wavelength. As an example of this scheme one can give for instance the Bragg reflectors with high reflectivity or photonic crystals. In general, these structures can be combined to obtain a light confinement in all three spatial dimensions.

The resonant optical modes of each cavity realization have their own properties which govern their use. One of the main measures of the quality of microcavities is the *quality factor* Q. It is simply defined as the ratio of the resonant cavity frequency ω_c and its linewidth $\delta\omega_c$, the latter being nothing else than the full width at half maximum (FWHM) of the cavity mode:

$$Q = \frac{\omega_c}{\delta\omega_c}. \tag{1.21}$$

The Q-factor parametrizes the frequency width of the resonant enhancement. The second measure is the *finesse* F, which is defined as the ratio of the free spectral range (the frequency separation between neighboring longitudinal modes of the cavity) to the linewidth (FWHM) of the cavity mode:

$$F = \frac{\Delta\omega_c}{\delta\omega_c}. \tag{1.22}$$

The Q-factor is the rate at which the optical energy decays from within the cavity. Decay processes can be absorption, scattering, or leakage through imperfect cavity mirrors. Q^{-1} can be interpreted as the fraction of energy lost in a single round-trip around the cavity. It follows that the exponentially decaying number of photons has a lifetime given by $\tau = Q/\omega_c$. The quality factor plays an important role, because the strong coupling regime can only be achieved if the coupling between light and excitons is larger than all losses. Therefore, low quality microcavities are not suited for the investigation of the strong coupling regime. The quality factor and the lifetime of polaritons are also important for the polariton relaxation and their condensation. For example, room temperature polariton lasing from ZnO microcavities has not yet been observed due to the poor quality of the microcavity structure, even though the strong coupling has already been observed (which is in this case related to the problems to grow well adapted Bragg mirrors and the huge number of impurities in ZnO).

The separation of longitudinal modes $\Delta\omega_c$ in a microcavity is inversely proportional to the cavity length. Also transverse optical modes scale as the cavity length. It follows that microcavities have fewer modes than macroscopic cavities and the tuning of modes to a particular emission wavelength can become more important. The tuning is a big problem for planar microcavities. In case of photonic crystal structures very advanced techniques have been developed [8] which are discussed more in detail in chapter 4.

Finally the main important points, which should be kept in mind when considering microcavities, are:

- optical losses or finesse,
- coupling to incident light,

- optical mode volume,
- fabrication complexity and tolerance,
- incorporation of active emitters, and
- practicality of electronic contacting.

Optoelectronic devices based on optical microresonators that strongly confine photons and electrons form a basis for next-generation compact-size, low-power, and high-speed photonic circuits. By tailoring the resonator shape, size or material composition, the microresonator can be tuned to support a spectrum of optical modes with required polarization, frequency, and emission patterns. This offers the potential for developing new types of photonic devices such as light emitting diodes, low threshold lasers, polariton lasers etc. Furthermore, novel designs of microresonators open up very challenging fundamental-science applications beyond optoelectronic device technologies. The interaction of active or reactive material with the modal fields of optical microresonators provides key physical models for basic research such as cavity quantum electrodynamics (QED) experiments, spontaneous emission control, nonlinear optics, and quantum information processing.

However, high-Q microresonators of optical-wavelength size are difficult to fabricate, as the Q-factor decreases exponentially with the cavity size, and thus in general the demands for a high Q-factor and compactness are contradictory. A very wide range of microresonator shapes has been explored over the years for various applications. We will focus on planar microcavities with distributed Bragg reflectors as they are widely used for polariton lasing devices and photonic crystal cavities with their application to low dimensional active emitters like quantum dots. The latter will be a crucial prerequisite for the source of entangled photon pairs presented in chapter 4.

1.2.1 Planar microcavities with DBRs

Planar microcavities are widely used for optoelectronic devices. The development of microcavities is closely related to the development of solid state lasers. This started first in the last century when the first solid state lasing diodes were fabricated. They simply used the difference of the refractive index of active layer with the refractive index of the surrounding air to build a resonator structure, which is the simplest realization of a Fabry-Perot resonator. This works fine for lasing diodes, but the reflectivity of these, so called edge emitters, remains low. Especially to observation of the strong coupling between light and matter was far away to be realizable due to the broad cavity resonance. The next step was to use distributed Bragg mirrors to increase the reflectivity of the resonator structure. Vertical-Cavity Surface-Emitting Lasers (VCSEL) have been the next step in

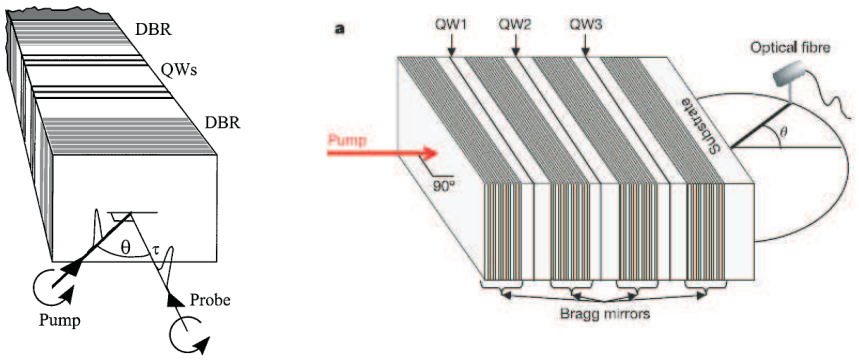

Figure 1.3 | Planar microcavity designs: (left) Planar microcavity structure designed for a pump probe experiment [9], and (right) Sketch of a triple-microcavity structure (sample A) with three λ-GaAs-cavities optically coupled via two intermediate AlAs/GaAs distributed Bragg reflectors (13 pairs each) [10]. Each cavity contains a single 80 Å$In_{0.05}Ga_{0.95}As$ quantum well. The substrate was polished to allow transmission.

laser fabrication with significantly decreased lasing threshold because of the long photon lifetimes.

Finally, the strong coupling regime was observed for a planar GaAlAs structure with seven quantum wells inside. The advantage of quantum wells is to place the exciton exactly at the maximum of the electric field distribution in the microcavity. This electrical field acts on the dipole moment of the excitons and provides the coupling between light and matter. In addition, embedding quantum wells inside of the Bragg mirrors reduce the mode volume of the cavities.

A schematic structure of a microcavity designed for a pump probe measurement is shown on the left in Fig(1.3). The two quantum well layers are at the position of the electric field maximum in this $3\lambda/2$ cavity. In addition, the pump and the probe beams are shown in this figure. Up to now, almost all experiments on microcavity polartions have been performed under optical excitation. Electrical injection of carriers for realistic operating laser devices are still under investigation and first simulations have been done only recently [11].

Of course, there are possibilities to extend these structures to double [12] or triple cavities [10] (right hand side Fig.(1.3)) with interesting configurations for e.g. intercavity optical parametric amplification.

A powerful method which allows to compute the optical properties of Bragg reflectors or microcavities as a whole (in the linear regime only) is the transfer matrix method. The idea is to represent the effect of each layer on the electromagnetic wave by a matrix, and the wave itself by a vector with components of the electric and magnetic field. The method is described in detail in [5] and we will not discuss it here.

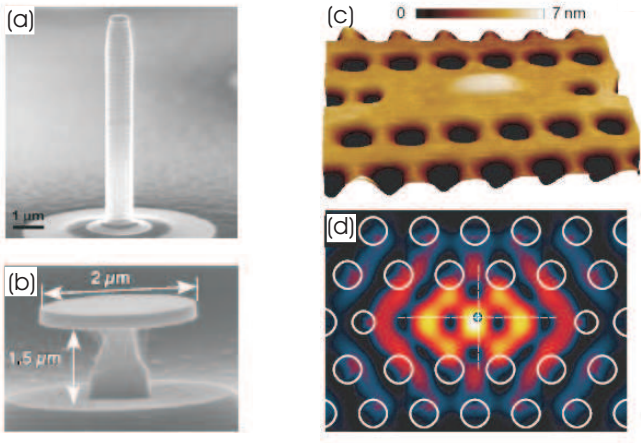

Figure 1.4 | Quantum dots in mcrocavities: (a) micropillar [13], (b) microdisk [14], and (c) photonic crystal [15]. (d) shows the corresponding electric field inside the photonic crystal cavity presented in (c) .

1.2.2 Quantum dots in cavities

Beside planar microcavities, there has been a huge interest in quantum dots embedded in microcavities for applications in quantum information and quantum communication proposes.

The easiest way to couple a quantum dot to a cavity mode is to grow a layer of quantum dots and to fabricate a top and bottom reflector (see for example Refs. [16] and [17] for entangled photon sources). Then a single dot can be addressed by μ-photoluminescence technique. This standard technique requires always a pre-selection of quantum dot and a precise measurement setup. One of the main problems is the challenging integration of the optoelectronic devices on a chip, which is limited by the array of dots and the pre-selection. These on-chip sources might be the future for the realization of quantum communication and quantum information schemes.

Therefore it is crucial to find an appropriate cavity, which allows to couple the cavity resonances exactly to one quantum dot and its resonances. Also the positioning of the dot is an important feature because the dot should be placed exactly at the maximum of the electric field to increase the coupling of light and matter. Different proposals have been published recently for strongly coupled dot-cavity systems. Reithmaier et al. [13] observed the strong coupling of a quantum dot embedded in a micropillar. Furthermore strong coupling of a quantum dot to a microdisk cavity has been reported recently [14]. The most interesting structure (from our point of view, see chapter 4 for details) is a quantum dot embedded in a photonic crystal. The strong coupling for such a system has been shown recently [15, 18]. The basic structures used to observe the strong coupling are shown in Fig.1.4.

Photonic crystals arise from multiple photon scattering within periodic dielectrics, and also exist in 3D and 2D versions. The ideal 3D photonic crystal microcavity would be a defect in a perfect 3D photonic lattice with high enough refractive index contrast, so

that there is a bandgap at particular wavelength in all directions. In principle, this would provide the highest optical intensity enhancement in any microcavity, however, currently no fabrication route to such system has been demonstrated.

In contrast, 2D photonic crystals etched in thin high refractive index membranes or films have shown the greatest promises, with the vertical confinement coming from the interfaces of the membrane. Quality factors exceeding 10^5 with extremely small mode volumes can be fabricated, which are advantageous for many applications. The introduction of small defects in such planar microcavities and embedding a quantum dot therein has been demonstrated [15, 19]. This allows to couple perfectly the cavity resonances to the matter resonances and the strong coupling regime has been observed [18, 15].

Also photonic crystal slabs are under investigation to create resonator structures for planar active layers like quantum wells [20, 21]. The quality factor of such resonators will exceed strongly the one of dielectric Bragg mirrors and the tunable bandgap of such structures inspires hope for the applications, for example in ZnO structures, where perfectly adapted Bragg mirrors are still not available.

1.3 Bose condensation and dynamics of polaritons

In the rest of the chapter 1, we will concentrate on planar cavities and two-dimensional polaritons, which is, by far, a more developed research area with respect to the field of 0D polaritons evocate in the previous section. The 2D polaritons are a mixture of cavity photons and QW excitons. QW excitons are expected to behave as weakly interacting bosons in the low density limit, which is, therefore, also the case for polaritons.

Therefore, one expects them to exhibit a bosonic phase transition known as Bose-Einstein condensation (BEC). This possibility, when implemented, has become the first example of Bose condensation in a solid-state system [22]. Imamoglu and Ram (1996) were the first to point out the application of such a polaritonic condensate that would emit coherent light. This coherent light emitter is called *polariton laser*. The buildup of a coherent ground state population from an incoherent exciton reservoir can be seen as a phase transition towards a Bose condensed state, or as polariton lasing effect resulting from bosonic stimulated scattering. At this point the polariton relaxation kinetic come into play due to the finite lifetime: the relaxation process should be fast enough to populate the ground state of the system.

The configuration studied in this section is characterized by off-resonant excitation. The carriers (electrons and holes) are injected electrically or optically, and then form excitons. The excitons self-thermalize at their own temperature mainly through exciton-exciton interactions. The reduction of the kinetic energy of the excitons and exciton-

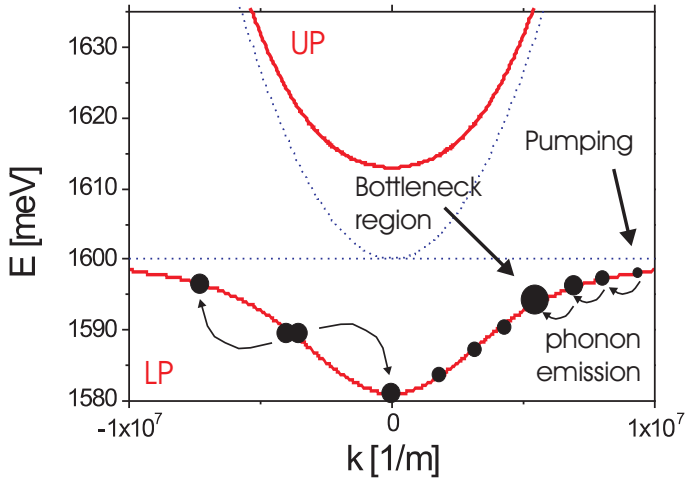

Figure 1.5 | Relaxation of cavity polaritons: Schematic dispersion curves of the QW exciton and cavity photon (blue, dotted), and the resulting LP and UP branch (red). The two relaxation mechanisms, acoustic and optical phonon emission, which can be blocked by the bottleneck effect (right hand side), and LP-LP scattering (left hand side), which will be discussed later, are depicted.

polaritons (in the region of strong coupling) takes place by interaction with phonons. The particles relax towards the bottom of the lower branch of the polariton dispersion as illustrated in Fig. 1.5 by phonon emission. The mentioned bottleneck effect, where phonon scattering is no more efficient, will be discussed a bit later in this section. The polaritons scatter finally to the bottom of the lower dispersion branch, where they accumulate. Once again, the coherence of the condensate builds up from an incoherent equilibrium reservoir, and the phase transition can be interpreted as a Bose-Einstein condensation.

The condensate emits spontaneously coherent light so that there is no population inversion condition. In addition, in the special case of zero temperature and infinitely long polariton lifetime, there is no threshold for the coherent condensate emission as it is the case for conventional laser.

Moreover, because of the small polariton mass, critical temperatures larger than 300 K can be achieved. All these characteristics allow to suppose that polariton-lasers are ideal candidates for the next generation of laser-light emitting devices.

1.3.1 Einstein's proposal

The tendency of Bosons to accumulate in unlimited quantity in a single state is a very fascinating property, which has drawn a lot of attention since the first proposal by Einstein (1925) [23]. This property led him to the prediction of a new phase transition for an ideal Bose gas. Let us consider N noninteracting bosons at temperature T in a volume R^d, where R is the system size and d is the dimensionality. The distribution is given by function

$$f_B(k,T,\mu) = \frac{1}{e^{\frac{E(k)-\mu}{k_B T}} - 1}, \tag{1.23}$$

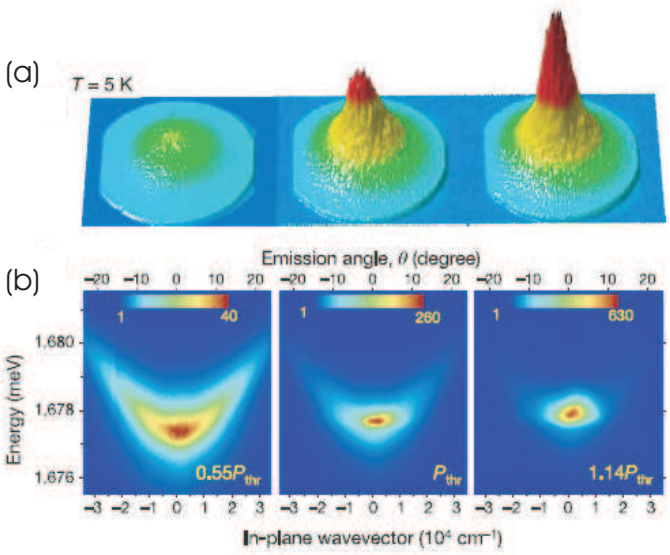

Figure 1.6 | Quasi-Bose-Einstein condensation of microcavity polaritons [22]: (a) Far field emission pattern for three different excitation powers at 5K increasing form the left to the right. (b) Energy resolved spectra of (a). A clear BEC behavior is observable: Increase and narrowing of the real space luminescence intensity accompanied by the clear concentration of the emission in the ground state of the polariton dispersion.

where k is the particle d-dimensional wavevector, $E(k)$ is the dispersion function of the bosons, k_B is the Boltzmann constant and μ is the chemical potential, which is a negative number if the lowest value of E is zero.

To add an particle to the system the energy $-\mu$ is needed. Its value is given by the normalization condition for the fixed total number of particles N,

$$N(T,\mu) = \sum_k f_B(k,T,\mu). \tag{1.24}$$

The thermodynamic limit means here an infinite system size and infinite number of particles, with a finite density. The total number of particles with separated ground state population term in the thermodynamic limit reads

$$N(T,\mu) = \frac{1}{e^{\frac{-\mu}{k_B T}} - 1} + \sum_{k,k\neq 0} f_B(k,T,\mu). \tag{1.25}$$

The total boson density (in the thermodynamic limit) is given by replacing the sum by an integral over the reciprocal space:

$$n(T,\mu) = \lim_{R\to\infty} \frac{N(T,\mu)}{R^d} = n_0 + \frac{1}{(2\pi)^d} \int_0^\infty f_B(k,T,\mu) d^d k, \tag{1.26}$$

where

$$n_0(T,\mu) = \lim_{R\to\infty} \frac{1}{R^d} \frac{1}{e^{\frac{-\mu}{k_B T}} - 1}. \tag{1.27}$$

If μ is nonzero, the ground state density vanishes. On the other hand, the integral on the right hand side is an increasing function of μ. So, if one increases the particle density n in

the system, the chemical potential also increases. The maximum particle density which can be accommodated following the Bose-Einstein distribution is therefore:

$$n_c(T) = \lim_{\mu \to 0} \frac{1}{(2\pi)^d} \int_0^\infty f_B(k, T, \mu) d^d k. \tag{1.28}$$

This function can be calculated analytically in the case of a parabolic dispersion relation. It converges for $d > 2$ and it diverges for $d \leq 2$. This means an infinite number of bosons can always be accommodated in the system following a Bose-Einstein distribution, the chemical potential is never zero and there is no phase transition in 2 or less dimensions. In higher dimensions, n_c is a critical density above which it would seem no more particles can be added. Einstein proposed that at such high densities the extra particles collapse into the ground-state, whose density is therefore given by

$$n_0(T) = n(T) - n_c(T). \tag{1.29}$$

This is a phase transition characterized by the accumulation of a macroscopic number of particles in a single quantum state. The key parameter in physics of Bose-Einstein condensates is the chemical potential, which becomes zero at the transition.

For the 2D case we consider, the Bose-Einstein condensation is strictly speaking forbidden. However, transitions to a superfluid state called Kosterlitz-Thouless transition can take place. In a finite 2D system a quasi-condensation of bosons is also possible, because in this case the integral in Eq.(1.28) takes finite value, since the integration is done on the reciprocal space excluding the diverging region around the ground state.

Beside atomic systems, quasi Bose-Einstein condensation has been observed in 2006 by Kasprzak et al. [22] at 5K in a CdTe/CdMgTe microcavity with 16 quantum wells. Later other reports about the observation of quasi-Bose condensation appeared in the literature [24, 25, 26]. Fig(1.6) shows the results of this experimental paper. Fig(1.6) displays pseudo-3D images of the angular distribution of the spectrally integrated emission. Below threshold (left), the emission exhibits a smooth distribution centered around an emission angle of zero degrees, that is, around $k = 0$. When the excitation intensity is increased, the emission from the zero momentum state becomes predominant at threshold (center) and a sharp peak forms at $k = 0$ above threshold (right). (b) shows the energy and angle-resolved emission intensities. The width of the momentum distribution shrinks with increasing excitation intensity, and above threshold, the emission mainly comes from the lowest energy state at $k = 0$.

All specific ingredients of a true BEC have been observed: above some critical density, condensation takes place in the ground state, out of a degenerate Bose gas fully thermalized at 19 K. The phase-transition character of the phenomenon is clearly seen. It has been later shown that, despite the finite polariton lifetime, the polariton gas can be in

a thermal equilibrium with the phonon bath [27]. Spontaneous symmetry breaking has also been demonstrated by measuring random (from pulse to pulse) polarization of the condensate and studying its statistics in bulk GaN sample [26], where the polarization of the condensate is not pinned.

1.3.2 Semiclassical Boltzmann equation

As mentioned before, in case of the polariton laser the microcavity is excited non-resonantly and the injected carriers have to relax to the ground state to form a condensate. To describe this relaxation process and the relaxation dynamics one uses the rate equations, also called Boltzmann equations. The classical Boltzmann equations describe the dynamics of classical particles.

It was first proposed by Uhlenbeck and Gropper [28] to include into the Boltzmann equation the quantum nature of the particles involved, taking into account their fermionic or bosonic character. In this section we describe the derivation of the spinless kinetic Boltzmann equation for bosons interacting with phonons. Finally, the main scattering mechanisms in a semiconductor microcavity are presented briefly.

The starting point is the Liouville-von Neumann equation for a quantum system:

$$i\hbar\frac{d\rho}{dt} = \left[\hat{H}(t), \rho\right], \tag{1.30}$$

where ρ is the density operator of the system in the interaction representation and $\hat{H}(t)$ is the time dependent Hamiltonian describing the interaction of bosons and phonons. In the following we will use polaritons instead of bosons, but of course, the procedure is valid for all bosonic particles. The time dependent Hamiltonian reads

$$\hat{H}(t) = \sum_{k,k'} V_{k,k'} e^{i(\Omega_{k'} - \Omega_k - \omega_{k'-k})t} b_{k'-k} a_k a_k^\dagger + h.c. \tag{1.31}$$

In Eq.(1.31) a ($a^\dagger$) are the annihilation (creation) operators for polaritons and b ($b^\dagger$) are the annihilation (creation) operators for phonons with respect to the wavevector k, Ω_k is the energy of noninteracting polaritons and ω_k is the energy of the phonon. Both are given by dispersion relations. Finally, $V_{k,k'}$ is the transition matrix element.

The Liouville equation can be transformed by time integration of Eq(1.30) and resubstitution in Eq(1.30):

$$\frac{d\rho}{dt} = -\frac{1}{\hbar^2}\int_{-\infty}^{t}\left[\hat{H}(t), \left[\hat{H}(\tau), \rho(\tau)\right]\right] d\tau \tag{1.32}$$

After the application of the Markov approximation, which means physically, that the system has no phase memory, Eq(1.32) can be integrated and this yields

$$\frac{d\rho}{dt} = \frac{1}{2}\sum_{k}\sum_{k\neq k'} W_{k'\to k}(2a_k^\dagger a_{k'}\rho a_{k'}^\dagger a_k - a_k a_k^\dagger a_{k'}^\dagger a_{k'}\rho - \rho a_k a_k^\dagger a_{k'}^\dagger a_{k'}) \tag{1.33}$$
$$+\frac{1}{2}\sum_{k}\sum_{k\neq k'} W_{k\to k'}(2a_{k'}^\dagger a_k \rho a_{k'} a_k^\dagger - a_{k'} a_{k'}^\dagger a_k^\dagger a_k \rho - \rho a_{k'} a_{k'}^\dagger a_k^\dagger a_k),$$

where

$$W_{k\to k'} = \frac{2\pi}{\hbar}\sum_{k-k'} |V_{k,k'}|^2 (0, 1+n_{k-k'})\delta\left(E(k') - E(k) \mp \hbar\omega_{k-k'}\right). \tag{1.34}$$

The use of the Markov approximation makes impossible any description of coherent processes.

The density matrix can be factorized into the product of phonon density matrix and boson density matrix corresponding to the different states in the reciprocal space by using the Born approximation

$$\rho = \rho_{ph} \otimes \prod_k \rho_k. \tag{1.35}$$

The populations of polariton states with wavevector k are given by the diagonal elements of the density matrix ρ_k: $n_k = Tr(a_k^\dagger a_k \rho_k)$. The same can applied to the phonon density matrix. Both populations are assumed to be given by an equilibrium distribution. One obtains

$$\frac{dn_k}{dt} = -n_k \sum_{k'} W_{k\to k'}(1+n_{k'}) + (1+n_k)\sum_{k'} W_{k'\to k} n_{k'}. \tag{1.36}$$

To include pump, decay, and the polariton-polariton interactions, one can rewrite Eq.(1.36)

$$\frac{dn_k}{dt} = P_k - \Gamma_k n_k - n_k \sum_{k'} W_{k\to k'}(1+n_{k'}) + (1+n_k)\sum_{k'} W_{k'\to k} n_{k'}, \tag{1.37}$$

where P_k is the pump generation term, Γ_k is the particle decay rate and $W_{k\to k'}$ is the total scattering rate between states k and k'. This total scattering rate can be any physical process i.e. interaction of phonons and polaritons.

It was first proposed by Uhlenbeck and Gropper [28] to include the quantum character of the particles, by taking into account their fermionic or bosonic nature. The Boltzmann equation for bosons is given in Eq.(1.37) and the corresponding equation for fermions reads:

$$\frac{dn_k}{dt} = P_k - \Gamma_k n_k - n_k \sum_{k'} W_{k\to k'}(1-n_{k'}) + (1-n_k)\sum_{k'} W_{k'\to k} n_{k'}. \tag{1.38}$$

Equations (1.37) and (1.38) are called the *semiclassical Boltzmann equations*. A similar procedure, mathematically slightly more heavy, can be used to describe the polariton-polariton scattering process, which has been performed by Porras et al. (2002) [29].

The main task to be performed in order to describe the relaxation kinetics of particles in this framework is to compute the scattering rates. One should first identify the physical processes that provoke the scattering of particles. Then, the scattering rates can be calculated using the Fermi Golden rule. This procedure is correct only if the scattering processes are weak and can be treated in a perturbative way. Interactions should provoke scattering of particles within their dispersion relation and should not provoke the energy renormalization. In general, this can be not assumed for a strongly coupled microcavity. One should first treat non-perturbatively the exciton-photon coupling giving rise to a polariton basis. Then, the polaritons indeed can be said to weakly interact with their environment, which provokes the scattering of polaritons within their dispersion relation and the Boltzmann equations can be used. The scattering rates can then be calculated in a perturbative way, because they are induced by weak interactions. Nevertheless, the blueshift of the polariton dispersion can not be described within the Boltzmann equations and further theoretical treatments are necessary [30, 31].

In a semiconductor microcavity the main scattering mechanisms identified are:

- Polariton decay (mainly radiative),
- Polariton-phonon interaction,
- Polariton-free-carrier interaction,
- Polariton-polariton interaction, and
- Polariton-structural-disorder interaction.

A detailed discussion and the calculations of the rates of these different scattering mechanisms are presented in the appendix following the textbook [5]. These scattering rates are closely connected with the names Malpuech [32], Tassone[33, 34], and Porras [29, 35], who developed in their works the state of the art for the simulation of the polariton relaxation dynamics.

Many phenomena linked with polaritons derive from their dynamical properties, even their nature as a coherent superposition of the exciton and the photon is intrinsically dynamic. The energy is exchanged between these two fields at a rate $\Omega/\hbar$, which lies in the sub-picoseconds range. Another aspect of the dynamics is linked with their finite lifetime, due to the escaping of the photons through the mirrors of the cavity.

One of the restrictions blocking the way toward a polariton laser is the speed of the relaxation of the injected carriers, which is somehow limited by the shape of the polariton

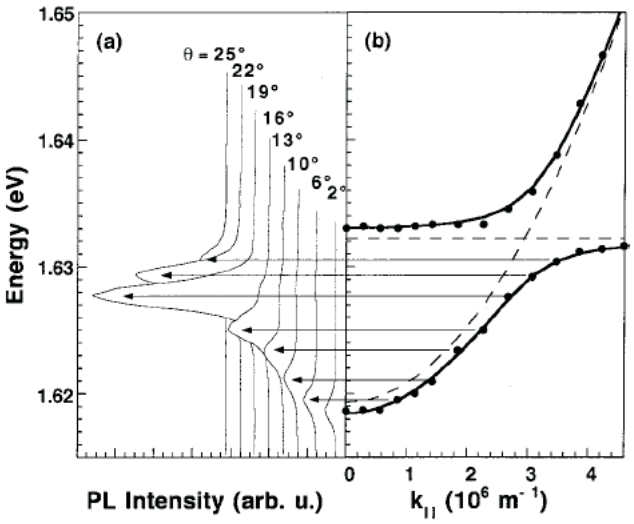

Figure 1.7 | Bottleneck effect in a CdTe based microcavity [37]: (a) shows the photoluminescence spectra at 9K and negative detunings and (b) shows the corresponding theoretical polariton dispersion to indicate the position of the polaritons. The relaxation process to the dispersion minimum is visibly blocked and the polaritons are accumulated around $k \approx 2.7\ 10^6\ m^{-1}$.

dispersion. One of the problems arising has been called the bottleneck effect, introduced by Tassone et al. (1997) [33] and observed experimentally by Tartakovskii et al. (2000) [36] and by Müller et al. (2000) [37]. The bottleneck appears because of the particularity of the interaction with acoustic phonons. In the excitonic part of the dispersion the exciton-polaritons relax towards the ground state via scattering with phonons. This relaxation is faster than the particle decay, which is almost the excitonic one. Once the edge of the strongly coupled part of the dispersion is reached, the polaritons still need to dissipate some small amount of energy (in the meV range) to reach the ground state of the trap. Depending on the steepness of the dispersion (that is, on the detuning), this process, if assisted only by acoustic optical phonons, may be take a long time, longer than the polariton lifetime in this region. Therefore polaritons can not strongly populate the states of the dispersion minimum and they accumulate at the edge of the polariton trap. Fig(1.7) shows the observation of the bottleneck effect taken from the experimental paper of Müller et al. [37]. This effect manifests itself clearly in a strong maximum of the photoluminescence intensity at the edge of the polariton dispersion minimum.

This bottleneck can be overcome using higher excitation powers, but this increases of course the threshold of future polariton lasing devices. In fact there are other ways to decrease the bottleneck effect. The increase of the number of quantum wells increases the number of polaritons and scattering processes are improved. The "magic" numbers of quantum wells are 12 for GaAs, 16 for CdTe and 67 for GaN microcavities. At the same time, more quantum wells means larger Rabi splitting, which is also favorable for the relaxation process (see chapter 3.1). Malpuech et al. propose the scattering with free carriers [38], and of course higher Q factors increase the polariton lifetime, which

also helps to overcome the bottleneck effect. Finally, wide gap semiconductors, such as GaN and ZnO, are predicted to be the good candidates for polarition lasers at room temperature with an almost invisible bottleneck effect due to the higher Rabi splitting, which makes the dispersion less steep and at the same time improves the efficiency of LO phonons.

1.3.3 Gross-Pitaevskii equation

Once a polariton condensate is formed, the Boltzmann equations are no longer suitable to describe the properties of the system. Since we deal with the properties of a condensate, the coherence should not be lost in the description and therefore a new mathematical treatment is necessary - the Gross-Piatevskii equation. This equation is based on the Bogoliubov theory [39], which treats uniform Bose gases. This theory has been extended to non-uniform and dilute Bose gas (a more general case) by Gross and Pitaevskii. We will follow in this section the treatment of Ref. [40]. Similarly to the case described in the previous chapter, the starting point is to consider the Hamitonian of weakly interacting bosons without phonons.

In a Bose condensate (macroscopically occupied state) the field operator $\hat{\Psi}(r)$ can be written in a basis of single particle wavefunctions ϕ_i. This results from the long range correlations between the elements of the one-body density matrix and works also in the nonuniform and dilute systems. The field operator has the following form

$$\hat{\Psi}(r) = \sum_i \phi_i a_i, \tag{1.39}$$

where $a_i(a_i^\dagger)$ are the annihilation (creation) operators of an particle in the state ϕ_i, which obey the commutation relations

$$\left[a_i, a_j^\dagger\right] = \delta_{ij}, [a_i, a_j] = 0. \tag{1.40}$$

The wave function relative to the macroscopic eigenvalue N_0, which is the population of the ground state and, therefore, the number of particles in the condensate, plays a crucial role in BEC and characterizes the so called condensate wavefunction. It is useful to separate in the field operator the condensate term $i = 0$ from the other components:

$$\hat{\Psi}(r) = \phi_0(r)a_0 + \sum_{i\neq 0} \phi_i a_i. \tag{1.41}$$

This is the natural starting point of the Bogoliubov approximation [39], which consists of replacing the operators a_0 and $a_0^\dagger$ with the c-number $\sqrt{N_0}$. This is equivalent to ignoring the non-commutativity of the operators a_0 and $a_0^\dagger$ and is a good approximation for

describing the macroscopic phenomena associated with BEC, where $N_0 = \left\langle a_0^\dagger a_0 \right\rangle >> 1$. In fact, the commutator between the operators a_0 and $a_0^\dagger$ is equal to one, while the operators themselves are of the order of $\sqrt{N_0}$. The Bogoliubov approximation is equivalent to treating the macroscopic component of $\phi_0 a_0$ of the field operator (Eq.(1.41) as a classical field, so that Eq.(1.41) can be written as

$$\hat{\Psi}(r) = \Psi_0(r) + \delta\hat{\Psi}(r), \tag{1.42}$$

where we have defined $\Psi_0(r) = \sqrt{N_0}\phi_0$ and $\delta\hat{\Psi}(r) = \sum_{i\neq 0} \phi_i a_i$. If one can neglect the non-condensate component $\delta\hat{\Psi}(r)$, as happens, e.g. in dilute Bose gases at very low temperatures, then the field operator coincides exactly with the classical field Ψ_0 and the system behaves like a classical object. The validity of the Bogoliugov approximation is guaranteed by the occurrence of a macroscopic occupation of a single particle state $N_0 >> 1$.

The function Ψ_0 is called condensate wavefunction and plays a role of an order parameter, which is a complex quantity, characterized by a modulus and a phase $S(r)$:

$$\hat{\Psi}_0(r) = |\hat{\Psi}_0(r)|e^{iS(r)}. \tag{1.43}$$

The order parameter characterizes the Bose-Einstein condensate phase and vanishes above the critical temperature.

In order to study the interacting nonuniform Bose gases one must generalize the Bogoliubov theory. We will use the Bogoliubov field operator in its general form (Eq.(1.41)). This implies that one can simply replace the operator $\hat{\Psi}(r,t)$ with a classical field $\Psi_0(r,t)$ (the order parameter). This procedure has indeed a deep physical meaning: I the present case the noncommutativity of the field operators is not important and one can describe the electromagnetic field by classical function, i.e the Maxwell equations for electric and magnetic fields. Here, the presence of a large number of particles in a single state permits the introduction of the classical functions.

The starting point is the many-body Hamiltonian:

$$\hat{H} = \int dr \hat{\Psi}^\dagger(r) \left[-\frac{\hbar}{2m}\Delta + V(r) + \frac{1}{2}\int dr' \hat{\Psi}^\dagger(r') V(r-r') \hat{\Psi}(r') \right] \hat{\Psi}(r). \tag{1.44}$$

In fact, the interaction term of this Hamiltonian is the same as in the staring Hamiltonian to derive the semiclassical Boltzmann equations but here boson-phonon interactions are neglected.

The next task is to obtain an equation, which governs the field $\Psi_0(r,t)$. For this purpose we remember that the field operator $\hat{\Psi}(r,t)$, in the Heisenberg representation, fulfills the exact equation

$$
\begin{aligned}
i\hbar\frac{\partial}{\partial t}\hat{\Psi}(r,t) = & \quad \left[\hat{\Psi}(r,t),\hat{H}\right] = \\
= & \quad \left[-\frac{\hbar^2\nabla^2}{2m} + V_{ext}(r,t) + \int \hat{\Psi}^\dagger(r',t)V(r'-r)\hat{\Psi}(r',t)dr'\right]\hat{\Psi}(r,t).
\end{aligned} \tag{1.45}
$$

It would be wrong to replace $\hat{\Psi}(r,t)$ with $\Psi_0(r,t)$ for a realistic potential. The replacement is however accurate if one uses an effective soft potential $V_{eff} = \alpha\delta(r'-r)$, where the Born approximation is applicable. The soft potential should reproduce the same low energy scattering properties as the bare potential V. By assuming that the function $\Psi_0(r,t)$ varies slowly on the distances of the order of the range of the inter-bosonic force, one can substitute r' for r in the arguments of Ψ_0 to finally obtain the equation

$$
i\hbar\frac{\partial}{\partial t}\Psi(r,t) = \left(-\frac{\hbar^2\nabla^2}{2m} + V_{ext}(r,t) + \alpha|\Psi_0(r,t)|^2\right)\Psi_0(r,t). \tag{1.46}
$$

For the case of 2D exciton-polaritons the interaction constant has been determined numerically [34, 41] to

$$
\alpha = \frac{6E_b|X_L|^2a_B^2}{S}, \tag{1.47}
$$

where E_b is the exciton binding energy, a_B is the 2D exciton Bohr-radius, X_L is the exciton fraction of the lower polariton and S is the surface of the microcavity.

One important approximation is the negligence of dephasing processes in the Gross-Pitaevskii equation. This means that the system is by definition coherent, which is the opposite of the Born-Markov approximation used for the derivation of the Boltzmann equations.

The validity of Eqs.(1.46) and (1.47) is not restricted to soft potentials, but holds, in general, for arbitrary forces, the s-wave scattering amplitude providing the relevant interaction parameter. Eq.(1.46) was derived independently by Gross (1961) [42] and Pitaevskii (1961) [43] and is the main theoretical tool for investigating nonuniform dilute Bose gases at low temperatures. It is also often called nonlinear Schrdinger equation.

To find the dispersion of the weak excitations of the classical field Ψ we follow the description of [40]. One shall consider small deviations from the constant average value $\sqrt{N}$:

$$
\Xi(r,t) = \sqrt{n} + Ae^{i(kx-\omega t)} + B^*e^{-i(kx-\omega t)}, \tag{1.48}
$$

where A and B are the small complex amplitudes. Substitution of this expression into the Gross-Pitaevskii equation 1.46, linearization, and separation of terms with different

exponential factors yields a system of linear equations with $p = \hbar k$:

$$\hbar\omega A = \frac{p^2}{2m}A + \alpha n(A + B), \tag{1.49}$$

$$-\hbar\omega B = \frac{p^2}{2m}B + \alpha n(A + B). \tag{1.50}$$

The solution of this system of equations is the famous Bogoliubov dispersion law, which is linear for small k and tends to the dispersion of a free particle in case of large k:

$$(\hbar\omega)^2 = \left(\frac{p^2}{2m}\right)^2 + \frac{p^2}{m}\alpha n. \tag{1.51}$$

The change between the two regimes takes place when the energy becomes equal to αn. Below this energy, the speed of excitations or the speed of sound in a dilute Bose gas with interactions can be derived to

$$c = \sqrt{\frac{\alpha n}{m}}. \tag{1.52}$$

One very interesting and fascinating property of condensates described by the Gross-Pitaevskii equation is superfluidity. The superfluidity follows directly from the Landau criterion: if the spectrum of elementary excitations satisfies this criterion, the motion of the fluid cannot give rise to dissipation. These dissipationless fluid flows have been studied in detail for atomic systems in the first half of the last century [44, 45].

Also excitons might be interesting depending on their density and on temperature. They behave either as weakly interacting Bose gas, a metallic liquid, or an electron hole plasma. A number of theoretical works have been published dealing with Bose condensation of excitons [46, 47, 48, 49]. The key point of these formalisms is that they assume infinite lifetimes of the semiconductor excitations. This means that the excitations should have a lifetime much longer than the relaxation time. So dark excitons as for example indirect excitons are good candidates for condensation phenomena. Recent works claimed the experimental observation of exciton condensation and superfluidity [50, 51, 52, 53] but the results have not been confirmed by theoretical works [54, 55] and a clear evidence of ecxitonic BEC has not yet been achieved.

Let us now introduce the Landau criterion of superfluidity. We consider a uniform fluid at zero temperature flowing along a capillary with a constant velocity v. Dissipation may come only from the scattering with walls from the capillary. The basic idea of the derivation is to calculate energy and momentum in the reference frame moving with the fluid and in the static one. The link between the two frames is given by the Galilean transformation. If a single excitation with momentum $\hbar k$ appears, the total energy in the moving frame is $E = E_0 + \epsilon(k)$, where E_0 is the energy of the ground state and $\epsilon(k)$

is the dispersion of the fluid excitations. In the static frame however, the energy E' and momentum P' of the fluid read:

$$E' = E_0 + \varepsilon(k) + \hbar k v + \frac{1}{2} M v^2 \tag{1.53}$$

$$P' = p - Mv, \tag{1.54}$$

where M is the total mass of the fluid. The energy of the elementary excitations in the static case is $\epsilon(k) + \hbar k v$. Dissipation is possible only if the creation of elementary excitations is profitable energetically, which means mathematically:

$$\varepsilon(k) + \hbar k v < 0. \tag{1.55}$$

Therefore, the dissipation can take place only if $v > \frac{\varepsilon(k)}{\hbar k}$. In other words, the flow stays superfluid if the velocity is smaller than the critical velocity v_c. This is the Landau criterion:

$$v_c = \min\left(\frac{\varepsilon(k)}{\hbar k}\right). \tag{1.56}$$

In the case of the parabolic dispersion v_c is zero and there is no superfluidity, but in case of the Bogoliubov dispersion, v_c is the speed of sound and the fluid is superfluid for all velocities smaller than v_c.

Bose-Einstein condensation and superfluidity are also connected. If $\Psi(r,t)$ is a solution of the equation for the field operator in Heisenberg representation then

$$\Psi'(r,t) = \Psi(r - vt, t) e^{\frac{i}{\hbar}\left(mvr - \frac{1}{2}mv^2 t\right)}, \tag{1.57}$$

where v is a constant vector, is also a solution of the same equation. This follows directly from the Galilean transformation of the field operator. In the moving coordinate system the condensate wavefunction of a uniform fluid is given by $\Psi_0 = \sqrt{n_0} e^{-i\mu t/\hbar}$, where n_0 is a constant. In the other case (the coordinate systems do not move), the order parameter takes the form $\Psi = \sqrt{n_0} e^{iS}$, where

$$S = \frac{1}{\hbar}\left(mvr - \left(\frac{1}{2}mv^2 + \mu\right)t\right) \tag{1.58}$$

is the new phase, while the amplitude n_0 has not changed. It follows that the velocity is proportional to the gradient of the phase:

$$v_s = \frac{\hbar}{m}\nabla S. \tag{1.59}$$

This velocity is often called superfluid velocity. This equation establishes the irrotationality of the superfluid motion. The phase of the order parameter is playing the role of a velocity potential.

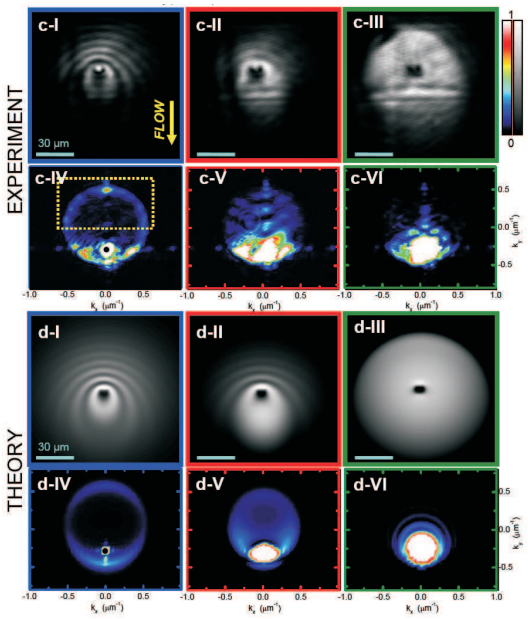

Figure 1.8 | Superfluid motion of a polariton droplet and collision with a structural defect [56]: (c-I)–(c-III) shows the near field image for increasing excitation. (c-IV)–(c-VI) are the momentum space images. At high powers, the emission patterns are show the onset of a superfluid regime characterized by an undisturbed flow around the defect (c-III). In momentum space, the approach and eventual onset of a superfluid regime is evidenced by the shrinkage (c-V) and then collapse (c-VI) of the scattering ring while for low powers the elastic scattering ring is observed. Panels (d) show the corresponding calculated images. The black solid dot in (c-IV) and (d-IV) indicates the momentum coordinates of the excitation beam.

In contrast to the basic theory and the superfluid velocity, the first observation of quasi Bose-Einstein condensation of polaritons [22] did not support the superfluid picture. Strong spatial patterns and a flat dispersion around $k = 0$ provoked a controversial discussion of possible explanations. Various works tried to describe this effect using different models [57, 58, 59] e.g. disorder effects and glassy phases [57].

Recently different groups claimed the observation of superfluidity of cavity polaritons [60, 56, 61]. Fig(1.8) shows a series of images of a polariton droplet colliding with a structural defect for different excitation powers (C-I–C-III) in real space and (C-IV–C-VI) in reciprocal space [56]. The figures indicated from d-I to d-IV are the corresponding theoretical simulations. The authors claim superfluid motion, as the polariton droplet passes the defect characterized by an undisturbed flow around the defect (c-III and d-III). For small excitation one see the typical parabolic wavefronts resulting from the scattering with the defect (c-I and d-I).

Also under resonant excitation, Utsunomiya et al. [61] report the first observation of interaction effects on the exciton-polariton condensate and the excitation spectra, which are in quantitative agreement with the Bogoliubov theory [39]. The sound velocity deduced from their experiments is in the order of $10^8\ cms^{-1}$. This value is eight orders of magnitude larger than that of atomic BECs, which results from the fact that the polariton mass is eight orders of magnitude smaller than the atomic mass and the polariton interaction energy is seven orders of magnitude larger than the atomic interaction energy. According to the Landau criterion (Eq. 1.56), the observation of this linear dispersion in the low-momentum regime is an indication of superfluidity in the exciton-polariton system. However, the polariton system is a dynamical system with a finite lifetime, so

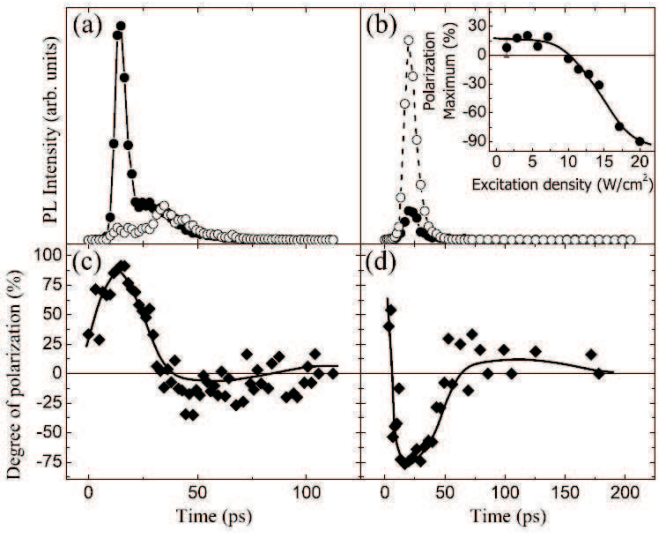

Figure 1.9 | Temporal evolution of the photoluminescence of an CdTe-based microcavity [63]: The pump is circularly polarized and (a) at the positive detuning, upper polariton branch and (b) negative detuning, lower polariton branch. The filled circles (open circles) denote the $\sigma_+(\sigma_-)$ emission. The deduced time evolution of the circular polarization degree for positive and negative detunings is shown in (c) and (d), respectively. The inset shows the maximum value of polarization degree at 20 ps in the negative detuning case.

the Landau criterion might be modified on a quantitative level.

Nevertheless, the superfluidy of cavity polaritons call for future theoretical and experimental works to understand this exotic bosonic behavior for the specific system of cavity polaritons.

Especially the coherent propagation, which is associated with superfluidity [62] under non-resonant pumping is one of the greatest experimental challenges in our days.

1.4 Spin and polarization of polaritons

When created optically, polaritons inherit their spin and dipole moment from the exciting light. Their polarization properties can be fully characterized by a Stokes-vector or - using the language of quantum physics - a pseudospin accounting for both spin and dipole moment orientation of a polariton. Polaritons start to change their pseudospin from the first moment of their creation in a semiconductor microcavity. Various effects are in the origin of this pseudospin rotation, such as effective magnetic fields of various natures and scattering effects with acoustic phonons, defects, and other polaritons. This richness of possible pseudospin rotation sources make the dynamics of the polariton pseudospin very unique and complex which manifests itself in nontrivial changes of the polarization of the emitted light in dependence on the pump energy, time etc. as shown by Fig. 1.9.

The spin of excitons governs the polarization of the due to the recombination emitted light. The conservation of spin allows the spin-orientation of excitons by polarized light beams. This results in the polarization of the photoluminescence light. Excitation lasers which are σ_+ or σ_- polarized excite $J = 1$ and $J = -1$ excitons, respectively. Linear polarized light excites a linear combination of $+1$ and -1 exciton states, so that the total exciton spin projection on the structure growth axis is zero in this case.

The exciton itself is formed by an electron and hole, i.e. by two fermions having projections of the angular momenta on a given axis equal to $J_z^e = S_z^e = \pm 1/2$ for an electron in the conduction band with S-symmetry and $J_z^h = S_z^h + M_z^h = \pm 1/2, \pm 3/2$ for a hole in the valence band with P-symmetry. The holes with $\pm 1/2$ spin component are called light holes, the others are called heavy holes. In bulk semiconductors both types are degenerate, while in quantum wells the confinement lifts the degeneracy and the heavy hole states are closer to the bottom of the well. Thus the ground-state exciton is formed by an electron and a heavy hole. The total angular momentum has the projections ± 1 and ± 2 on the structure axis. Bearing in mind that the photon spin is 0 or ± 1 and that the spin is conserved in the process of photoabsorption, excitons with spin projection ± 2 can not be optically excited, so they are called dark excitons. This induces directly, that the excitons with projection ± 1 are bright states. The dark states can be neglected in the following consideration, but nevertheless, they can still come into play.

The polarization of exciting light cannot be retained infinitely long by excitons. Sooner or later they loose their spin due to spin and dipole relaxation. The main important mechanisms are: the Elliot-Yaffet mechanism, the D'yakonov and Perel mechanism, the Bir-Aronov-Pikus mechanism, and the spin flip scattering between carriers and magnetic ions.

In a key paper Maialle et al. [64] have shown that the third mechanism is the main dominant for the quantum confined excitons in non-magnetic semiconductors. The long-range electron-hole interaction leads to the longitudinal-traverse splitting of exciton states. This splitting is responsible for rapid spin relaxation of excitons in quantum wells. This has an important consequence for the description of exciton-polaritons in quantum wells: the dark states can be neglected, which allows us to consider the exciton-polariton as a two level system and use the well-developed pseudospin formalism for its description.

The unique spin structure of polaritons lead to various interesting effects with or without the presence of magnetic fields: the optical spin Hall effect, an analog of the Aharonov-Bohm interferometer [65], and the so called spin-Meissner effect [66]. The latter one is described more in detail in chapter three in the framework of the Datta-Das spin transistor of polaritons. For the other effects the interested reader should address the references and the text books on microcavity polaritons [5, 6] for a more detailed discussion.

1.5 Resonant effects

This section is focused on the effects observable under resonant or quasi-resonant excitation. We will discuss in detail the parametric amplification and the bistability or multistability because of intra-condensate interaction.

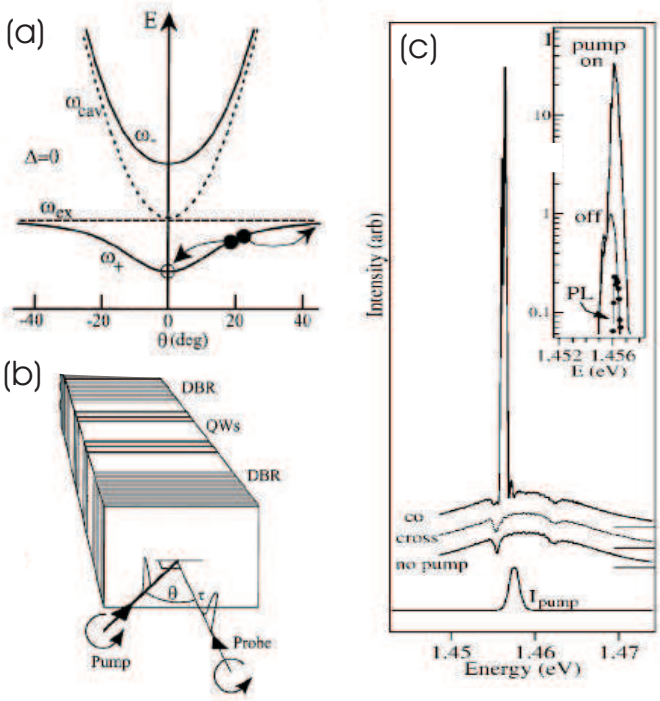

Figure 1.10 | Parametric scattering of polaritons – Savvidis experiment [9]: (a) Schematic parametric scattering, (b) sketched experimental setup and (c) reflected probe spectra at $\tau = 0$ ps for pump off, co-, and cross-circularly polarized to the probe. Pump spectrum on lower trace. Inset: Reflected narrow band probe spectra at $\tau = 0$ ps, with pump pulse on/off, together with pump PL without probe pulse.

1.5.1 Optical parametric oscillator

One of the most influential work demonstrating the bosonic character of polaritons is that reported by Savvidis et al. (2000) [9]. The authors announce the observation of low temperature (4K) stimulated scattering of polaritons in a pump-probe experiment. They varied the angle of the resonant excitation to change the k-vector of the injected polaritons. A sketch of the experimental setup is shown on Fig(1.10)(b). The cavity has a various thicknesses around the average value of $3\lambda/2$ which allows to access different detunings. In the zero detuning case, the lower polariton branch was excited by varying the angle of the pump beam. A weak probe excites with delay τ the $k = 0$ state. In case of no pumping the reflected spectra shows the two polariton peaks separated by the Rabi splitting, which is about 7 meV in the present case. When the pump is switched on and for small delays τ an enhancement of the emission of the lower polariton branch was observed. For a specific angle of $\Theta = 16.5 \pm 2$, the so called magic angle, the emission rises up to a gain of 70. The measured intensity is shown on Fig(1.10)(c).

The nature of this process is the scattering of two pump polaritons (k_p) into a signal polariton at $k = 0$ and an idler polariton at $2k_p$. This takes place at the magic angle with energy and momentum conservation. The whole process is sketched on Fig(1.10)(a). This experiment supported strongly the polariton picture and brought three new features to the polariton field:

First, polaritons can scatter strongly on each other, provided that both energy conservation and momentum conservation can be simultaneously satisfied in the two-particle

collision. This effect requires a non-parabolic dispersion, which supports the polariton picture.

Second, polariton scattering can be enhanced by the occupation of the final state. In other words, polariton scattering can be stimulated, as expected for bosons.

Third, polaritons can be present in relatively large numbers at the bottom of the polariton trap in spite of their short lifetime governed by photon decay.

There are different ways to describe the parametric scattering effect. We will briefly present the *semiclassical* description and the three level model developed by Ciuti et al. (2000) [67].

1.5.1.1 Semiclassical Description

The parametric scattering can be described using rate equations. These rate equations for occupation numbers are closely linked to the Boltzmann equations (see Eq.1.36). The advantage of the description is that it allows easily to account for all interaction processes affecting the polariton relaxation. The important disadvantage is that the dressing of the polariton dispersion can not be easily included in this model. In the resonant configuration one can single out the states, where the energy-momentum transfer is very efficient and dominates the system. This leads in the simplest case to a three level model containing the ground or *signal* state, the *pump* state and the *idler* state. The names of these states arise from similar physics in nonlinear optics. The losses, such as the dominant radiative losses and the scattering processes driven by disorder, can be taken into account by phenomenological decay rates. The disorder effects are neglected in this model, but scattering with phonons can be taken into account. The broadening can be written as

$$\frac{1}{\Gamma_k} = \frac{|X_L|^2}{\Delta + \Gamma_{phonons}} + \frac{|C_L|^2}{\gamma_c}, \tag{1.60}$$

where X_L and C_L are the exciton and photon Hopfield coefficients, respectively, Δ is the exciton inhomogeneous broadening, Γ_{phonon} is the phonon-induced broadening and γ_c is the cavity-photon broadening. At low temperatures $\Gamma_{phonon} << \Delta$ and in most of the cavity samples $\Delta \approx \gamma_c$. We will use Γ as the decay constant.

Using these rate equations, the system can be written as a set of three equations

$$\begin{aligned} \dot{n}_0 = &\quad P_0 - \Gamma n_0 - \alpha n_0 n_i (n_p+1)^2 + \alpha (n_0+1)(n_i+1) n_p^2, \\ \dot{n}_p = &\quad P_0 - \Gamma n_p + 2\alpha n_0 n_i (n_p+1)^2 - 2\alpha (n_0+1)(n_i+1) n_p^2, \\ \dot{n}_i = &\quad P_0 - \Gamma n_i - \alpha n_0 n_i (n_p+1)^2 + \alpha (n_0+1)(n_i+1) n_p^2, \end{aligned} \tag{1.61}$$

where

$$\alpha = \frac{2\pi}{\hbar^2} \frac{|M|^2}{\pi\Gamma/2}. \tag{1.62}$$

M is the polariton-polariton matrix element of interaction, which is here approximately equal to one fourth of the exciton-exciton matrix element of interaction. This system can be easily solved numerically. In the *cw* excitation case $P_0 = P_i = 0$, this gives $n_0 = n_i$ and the system can be reduced to two equations.

Using the evolution equation for the ground state population

$$\dot{n}_0 = n_0(W_{in} - W_{out}) + W_{in}, \tag{1.63}$$

where W_{in} and W_{out} include all channels for incoming and outgoing polaritons, respectively. The threshold of parametric scattering is given by the condition $W_{in} - W_{out} = 0$. This implies

$$n_0 = \frac{\alpha n_p^2 - \Gamma}{\alpha(2n_p + 1)}. \tag{1.64}$$

The population n_0 should be positive or zero. This is given by $n_p = \sqrt{\Gamma/\alpha}$ and using $n_p \approx P/\Gamma$ yields

$$P_{thres} = \Gamma\sqrt{\frac{\Gamma}{\alpha}} = \gamma\frac{\hbar\Gamma}{2|M|} \tag{1.65}$$

for the threshold of parametric scattering.

1.5.1.2 Quantum model

The quantum model has been developed by Ciuti et. al (2000) [67] and is similar to the Gross-Pitaevskii approach discussed previously, but considering three modes. The starting point is the Hamiltonian, where interactions with phonons and free carriers are neglected. To obtain the equation of motion for polariton operators a_k and $a_k^\dagger$ we write the Heisenberg equation:

$$\begin{aligned} i\hbar\frac{da_k}{dt} &= [a_k, H] = E_{LP}(k)a_k + \sum_{k,k''} E^{int}_{k,k',k''}a^\dagger_{k'+k''-k}a_{k'}a_{k''} + P(k), \\ i\hbar\frac{da_k^\dagger}{dt} &= [a_k^\dagger, H] = E^*_{LP}(k)a_k^\dagger - \sum_{k,k''} E^{int}_{k,k',k''}a_{k''}a_{k'}a^\dagger_{k'+k''-k} + P(k), \end{aligned} \tag{1.66}$$

where E_{LP} is the lower polariton branch dispersion relation

$$E^{int}_{k,k',k''} = \frac{1}{2}(V_{k',k'',k-k'} + V_{k',k'',k''-k}), \tag{1.67}$$

and $P(k)$ the polarization amplitude induced by an external pumping field.

Once again, only the signal, pump, and idler states are considered, and it is assumed that all states are macroscopically and coherently occupied. In other words, the states are assumed to behave as classical coherent fields and one can replace them by there

c-numbers as it has been done first by Bogoliubov. Ciuti used the same approximations but assuming three macroscopically occupied states. Keeping the signal and idler state operators and replacing the pump state by a complex number, one can describe the system by three equations:

$$\begin{aligned} -i\hbar\dot{a}_0 = &\quad \tilde{E}_{LP}(0)a_0 + E_{int}a^\dagger_{2k_p}P^2_{k_p} + P_{probe}(t), \\ -i\hbar\dot{P}_{k_p} = &\quad \tilde{E}_{LP}(k_p)P_{k_p} + E_{int}P^*_{k_p}a_0a_{2k_p} + P_{pump}(t), \\ i\hbar\dot{a}^\dagger_{2k_p} = &\quad \tilde{E}_{LP}(2k_p)a^\dagger_{2k_p} + E^*_{int}a_0P^{*2}_{k_p}, \end{aligned} \tag{1.68}$$

where

$$\begin{aligned} \tilde{E}_{LP}(0) = &\quad E_{LP}(0) + 2V_{0,k_p,0}|P_{k_p}|^2, \\ \tilde{E}_{LP}(k_p) = &\quad E_{LP}(k_p) + 2V_{k_p,k_p,k_p}|P_{k_p}|^2, \\ \tilde{E}_{LP}(2k_p) = &\quad E_{LP}(2k_p) + 2V_{2k_p,k_p,0}|P_{k_p}|^2, \end{aligned} \tag{1.69}$$

and

$$\tilde{E}_{int} = \frac{1}{2}(V_{k_p,k_p,k_p} + V_{k_p,k_p,-k_p}). \tag{1.70}$$

The advantage of this formalism with respect to the one presented in the previous section is that it allows one to account for the energy renormalization processes driven by the inter-particle interaction. Here, a blueshift of the three states considered is induced by the pump intensity. The blueshift itself can result in another nonlinear effect, which will be discussed in the next section. On the other hand, spontaneous scattering processes and the phonon scattering cannot be described.

This system of equations can be easily solved numerically by replacing all operators by complex numbers. Finally, further treatments given in detail in e.g. [6, 5] result in a similar equation for the parametric scattering threshold. This illustrates the equivalence of the semi-classical and quantum models in this aspect.

1.5.2 Bistability and Multistability

1.5.2.1 Bistability

An important feature of the resonant excitation scheme is the renormalization of the polariton energies. This renormalization is observed in the polariton emission, but it plays also a key role in the absorption of the pump light. Two situations can be distinguished. If the laser is below the bare polariton energy, the absorption is simply reduced by the pump-induced blue shift, which drives the mode out of the resonance. If the laser is above the bare polariton energy, the polariton energy gets closer to the pump energy because of

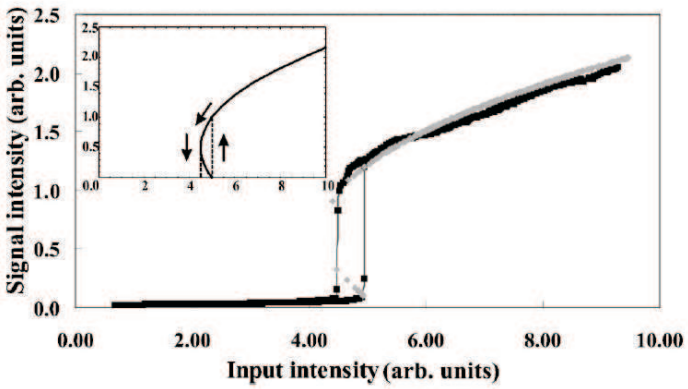

Figure 1.11 | Experimental observation of the polariton bistability [68]: Variations of the signal output power (in transmission) as a function of the pump power for a pump detuning $\Delta = -0.42$ meV. The gray curve is the result of a theoretical fit. The inset shows more clearly the unstable branch and the series of intermediate states that are obtained when varying the input intensity in both directions.

the blueshift, which in turn increases the blueshift, that enhances the absorption and so on. Two different regimes can be distinguished in this case. First, at low pump intensities the polariton energy remains below the pump energy. At higher pump intensities the polariton energy passes the pump energy and stabilizes above. This results in a dramatic increase of the population of the pump state, as the absorption reaches a maximum by passing the pump laser energy. The threshold is called bistable threshold, as there are two possible polariton populations for the same pump intensity. The same effect can be also due to the saturation of the exciton oscillator strength[69]. The bistability was first observed experimentally in 2004 by Baas et al. [68]. Also the interplay of the two nonlinear effects (parametric amplification and bistability) opened a interesting field of research [70, 71]. To analyze the bistability theoretically the dynamics of the pump state can be written as follows

$$\dot{\bar{P}}_{k_p} = i(\omega_{k_p} - \omega_p + i\Gamma_{k_p})\bar{P}_{k_p} + i\frac{2}{\hbar}V_{k_p,k_p,k_p}\left|\bar{P}_{k_p}\right|^2\bar{P}_{k_p} + P_{pump}(t). \tag{1.71}$$

This last quantity should be zero in the stationary regime. Then multiplying Eq.(1.71) by its complex conjugate and replacing $\bar{P}_{k_p}$ by the population of the pump state and $|\bar{P}_{k_p}|^2$ by the pump intensity I_p, one gets:

$$\left[\left((\omega_{k_p} - \omega_p) + \frac{2}{\hbar}V_{k_p,k_p,k_p}N_p\right)^2 + \Gamma_{k_p}^2\right]N_p = I_p. \tag{1.72}$$

The experimental observation of the bistability of cavity polaritons [68] is shown in Fig.(1.11). It is the so called s-shape. Increasing the pump intensity results in a clear jump of the population at the turning point 1. Starting now from the upper branch and decreasing the pump intensity, the populations drops down at turning point 2. This exhibits clearly a hysteresis cycle, when the pump intensity is stepwise increased and decreased. The part of the curve, which connect the two turning points is instable, which can be analyzed by stability calculations using the famous Ljapunov exponents and adding

a small perturbation. The turning points can be found by the condition $dI_p/dN_p = 0$, which yields:

$$3(\frac{2}{\hbar}V_{k_p,k_p,k_p})^2 N_p^2 + 4(\omega_{k_p} - \omega_p)^2 + \Gamma_{k_p}^2 = 0. \tag{1.73}$$

The bistability region is given if there are two positive different solutions for this quadratic equation and thus one has the condition

$$\omega_p > \omega_{k_p} + \sqrt{3}\Gamma_{k_p}. \tag{1.74}$$

It follows directly from this condition, that it is necessary to pump at least one linewidth above the bare polariton state to observe the bistability. So, finally the solution for the turning points reads

$$N_p = \frac{2(\omega_p - \omega_{k_p}) \pm \sqrt{(\omega_p - \omega_{k_p})^2 - 3\Gamma_{k_p}^2}}{\frac{6}{\hbar}V_{k_p,k_p,k_p}}. \tag{1.75}$$

The solution with the minus sign corresponds to the turning point with the higher pumping. Plugging Eq.(1.75)into Eq.(1.72) leads to the pumping threshold intensity.

1.5.2.2 Multistability

It was first reported by Gippius et al. [72] that the polariton bistability can be expanded to polarization multistability. It is shown that the interplay between the nonlinearity caused by the polariton-polariton interactions and the polarization dependence of these interactions results in a remarkable multistability of a driven polariton system, contrary to the ordinary optical bistability in the spinless nonlinear case.

The polarization-dependent system can be described by the spinor Gross-Pitaevskii equation

$$\left[\omega_0 - \omega - \frac{i}{\tau} + \alpha_1|\Psi_\sigma|^2 + \alpha_2|\Psi_{-\sigma}|^2\right]\Psi_\sigma + \frac{P_\sigma}{4\tau} = 0, \tag{1.76}$$

where the number of the particles in the system with spin σ is $N_\sigma = |\Psi_\sigma|^2$, τ is the polariton lifetime, and $\alpha_{1(2)}$ is the matrix element of polariton-polariton interaction in the triplet (singlet) configuration, respectively. A solution of this equation gives an interesting hysteresis cycle of the polarization degree inside the microcavity. For a given polarization of the pump and depending on the history of the pumping process, the polariton polarization can, in general, take three different values. For instance, a linearly polarized laser can create a strongly right circularly, strongly left circularly, or a linearly polarized polariton state. This is illustrated in Fig(1.12) (a) in dependence on the intensity

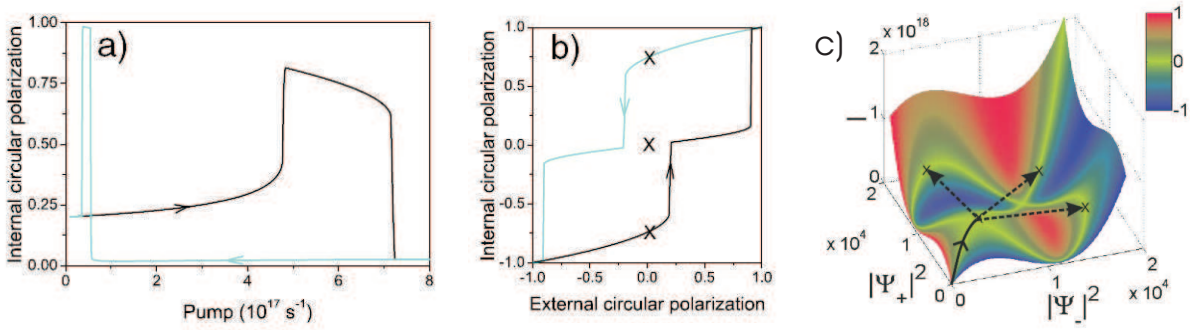

Figure 1.12 | Multistability of cavity polaritons [72]: (a) Circular polarization degree of the driven mode versus external pumping intensity for slightly elliptical pump, (b) Circular polarization degree of the driven mode versus circular polarization degree of the pump, and (c) The pump intensity I and polarization (color) versus the circular polarized components of the driven mode . Color shows the polarization of the pump (bright green corresponds to linear polarization). The crosses mark the four stable points for the driven mode corresponding to the same linearly polarized pump intensity. Arrows show the three possible jumps in case if the pump intensity is slightly increased.

of the elliptical pump intensity and (b) in dependence of the polarization of the pump. In both cases complicated hysteresis structures arise.

Figure (c) shows the functional dependence between σ_+ and σ_- components of the polariton population and the intensity and polarization of pump calculated accounting for the coupling between polaritons with opposite spins described by $\alpha_1 = -0.1\alpha_2$. This value of α_2 corresponds to recent estimations of Ref. [73]. The circular polarization degree of the pump laser is represented by the color of the surface of solution and the intensity of the pump is on the vertical z axis. The linear part of the polarization of the laser is kept aligned along x direction. The green areas correspond to nearly linearly polarized pumping. If the intensity of the pump increases, while its polarization is kept linear, the system follows the black solid line and then the black arrows shown in the Fig.(1.12) (c). One can see that from the critical point at the end of the solid black line the system can jump into three possible stable points (shown by crosses). One of them corresponds to the linearly polarized state and two others to nearly right- and left-circularly polarized states. The choice of the final state by the system is random and is triggered by fluctuations.

Chapter 2

Resonant excitation

In this chapter, we discuss effects under resonant or quasi-resonant excitation of polaritons such as the polariton parametric scattering and the bistability. For the former one we present a new theoretical approach which builds a bridge between the semi-classical approach of the Boltzmann equations and the coherent picture using high order correlators. Both regimes, the quantum nature and the transition to the classical Boltzmann equation are shown. The second part of this chapter is focused on bistable transitions of the nonlinear polariton oscillator and the influence of fluctuations near the stability edge. This fluctuations result in a narrowing of the hysteresis cycle and have thus a strong impact on experimental outcomes.

Contents

2.1 Quantum kinetic equations for interacting bosons

2.1.1 Introduction

The systems of interacting bosons are the focus of experimental and theoretical research at present. The interest in these systems is stimulated by recent experimental demonstration of Bose Einstein condensation (BEC) of cold atoms [74, 75, 76] and exciton-polaritons in microcavities [77, 22, 24, 25, 26]. BEC of cold alkali atoms is characterized by extremely low critical temperatures (in nanokelvin region), while exciton-polaritons can be condensed up to room temperature. On the other hand, strictly speaking, BEC is forbidden in two-dimensional systems like planar microcavities, so the observed phenomena [77, 22, 78, 24, 25] should be rather called a quasi-condensation of the polaritons in a finite size system. In an ideal infinite planar microcavity there is no BEC, but a superfluid phase transition may take place [62, 60, 61], which requires polariton-polariton interactions.

The dynamics of condensation of interacting bosons is an extremely complex process which is successfully treated theoretically only in particular cases and using strong approximations. Here, we present a dynamical quantum model allowing the description of various systems of interacting bosons and apply it to the microcavity parametric oscillators. Our model goes beyond existing theories as it relaxes the Born-Markov approximation. It allows describing the transition between the quantum and classical limits for the microcavity polariton parametric oscillators (PPOs).

To be specific, we shall consider a system of n_D interacting excitons and assume that the following condition is satisfied:

$$n_D a_B^D << 1, \tag{2.1}$$

where D is the dimensionality of the system (D=1,2,3) and a_B is the exciton Bohr radius. We shall further assume that this excitonic system is strongly coupled with light in a semiconductor microcavity. The presence of the photonic component results in the extremely small effective mass of cavity polaritons ($10^{-4}10^{-5}$ of the electron mass [5]), while the excitonic component makes possible effective polariton-phonon and polariton-polariton interactions. These factors are crucial for polariton BEC, whose critical temperature was predicted to be relatively high (tens of kelvins for GaAs and CdTe microcavities, up to room temperatures for GaN and ZnO cavities [5, 79, 80]).

Similar to the exciton condensate as studied theoretically by Keldysh and Kopaev more than 40 years ago [81], polariton condensate emits coherent light and, thus can be used for the creation of a new generation optoelectronic device known as "polariton laser" [82].

Investigation of the mechanisms of polariton redistribution (and bosons, in general)

in the reciprocal space is crucial for the comprehension of the formation of BECs. For the cavity polaritons, two mechanisms are of major importance: the polariton-phonon and polariton-polariton interactions. The former is dominant at small densities, while the latter becomes dominant in the nonlinear regime and especially at the bottleneck region, where polariton relaxation with acoustic phonons is no more efficient [33]. Polariton-polariton scattering is even more important in the case of resonant optical pumping that creates coherent macroscopic population of polaritons at their lower dispersion branch. In this case, two main nonlinear mechanisms have been identified, which are polariton parametric scattering [83, 67, 10] and the blueshift of the polariton dispersion [78]. These two mechanisms often occur simultaneously, leading to the number of intriguing nonlinear phenomena such as bistability of the polariton system [68, 70, 84, 71].

As explained in the first chapter, the existing models of the PPO either consider all three states involved in the parametric process as classical fields coupled by a four-wave mixing process [71] or consider the case of cw pumping, neglecting the pump depletion [83, 67].

The exception is the recent work of Glazov and Kavokin [85], where the hyperspin formalism was applied for the analysis of the parametric amplifier. The hyperspin formalism allows describing up to a certain point the quantum correlations in a three-level system, while its extension to more complex systems would require extremely heavy analytics. Other works [70, 84] are based on Gross-Pitaevskii equations. This allows taking into account all states of reciprocal space, but the decoherence or relaxation associated with phonons are completely neglected as well as processes of spontaneous polariton-polariton scattering.

In the following sections, we derive quantum kinetic equations for the system of interacting bosons. They describe the dynamics of the occupation numbers and of nonclassical offdiagonal four-particle correlators. We argue that decoherence process leading to the decay of the nonclassical correlators leads to the transition between the quantum oscillatory regime and semiclassical relaxation regime. We show that in the limit of very fast dephasing, the system of quantum equations becomes similar to the semiclassical system of Boltzmann equations. These quantum kinetic equations are then applied to describe the three state model corresponding to the PPO.

2.1.2 Quantum kinetic equations for a system of interacting bosons

Here and further, we consider a system of spinless interacting bosons, e.g., cavity polaritons. We address the readers interested in the spin dynamics of exciton-polaritons to the recent review paper [86]. Here, we consider a model quantum system described by the

Hamiltonian

$$H = \sum_{\mathbf{k}} \varepsilon_{\mathbf{k}} a^{\dagger}_{\mathbf{k}} a_{\mathbf{k}} + \sum_{\mathbf{k},\mathbf{q}} U_{\mathbf{k},\mathbf{q}} a^{\dagger}_{\mathbf{k}} a_{\mathbf{k}-\mathbf{q}} \left(b_{\mathbf{q}} + b^{\dagger}_{-\mathbf{q}} \right) + \frac{1}{2} \sum_{\mathbf{k},\mathbf{k}',\mathbf{q}} V_{\mathbf{k},\mathbf{k}',\mathbf{q}} a^{\dagger}_{\mathbf{k}} a^{\dagger}_{\mathbf{k}'} a_{\mathbf{k}-\mathbf{q}} a_{\mathbf{k}'+\mathbf{q}} + H.c., \quad (2.2)$$

where the operators a_k are the boson annihilation operators for polaritons and b_q – the acoustic phonon annihilation operators. The first term corresponds to the free particle motion, the second term describes exciton-acoustic phonon scattering, and the third term describes polariton-polariton scattering. The latter arises from the Coulomb interaction between the excitonic fractions of two colliding polaritons and plays a major role in polariton relaxation. The matrix element of this scattering is determined by the exciton binding energy E_B, exciton Bohr radius a_B, and the area occupied by the condensate S. Roughly, it can be estimated as

$$V_{\mathbf{k},\mathbf{k}';\mathbf{k}'',\mathbf{k}'''} = \langle \mathbf{k}, \mathbf{k}' | \, V_{\text{int}} \, | \mathbf{k}'', \mathbf{k}''' \rangle \sim \frac{E_B a_B^2}{S} X^*_{\mathbf{k}} X^*_{\mathbf{k}'} X_{\mathbf{k}''} X_{\mathbf{k}'''} \delta_{\mathbf{k}+\mathbf{k}'-\mathbf{k}''-\mathbf{k}'''}, \quad (2.3)$$

where X_k is a Hopfield coefficient giving the percentage of the excitonic fraction in the state k, and the delta function ensures the momentum conservation during the scattering act. An estimation of this quantity within the mean-field approximation [41] has given a prefactor of 6 in the left hand side of Eq.(2.3) . We neglected in Eq. (2.3) the saturation terms [29], assuming that condition (2.1) is satisfied.

When considering the dynamics of the polariton system described by Eq.(2.2), the phonon field can be treated classically. The usual way to deal with it is to use the Born-Markov approximation for the Liouville von Neumann equation for the density matrix of the system. The resulting system of kinetic equations is of the Boltzmann type. This procedure is well described in literature (see, e.g., Ref. [87]) and we will not further consider the interaction with acoustic phonons in the rest of the chapter. We note, however, that a strong advantage of the approach we use, with respect to the models assuming the full coherence as the Gross-Pitaevskii equations, is that it allows taking simultaneously into account the coherent and noncoherent aspects of the polariton dynamics.

Let us now consider the term describing particle-particle interactions [last term in Eq. (2.3)] . Formally, the Born- Markov approximation can be applied also in this case [88]. The justification of this approximation is, however, less straightforward since there is no classical reservoir in the system. To consider the dynamics of the system, we start from the Liouvillevon Neumann equation which reads

$$\begin{aligned} i\hbar \frac{d\rho}{dt} &= [H; \rho] \quad (2.4) \\ &= \sum_{\mathbf{k}} \varepsilon_{\mathbf{k}} \left[a^{\dagger}_{\mathbf{k}} a_{\mathbf{k}} \rho - \rho a^{\dagger}_{\mathbf{k}} a_{\mathbf{k}} \right] + \frac{1}{2} \sum_{\mathbf{k},\mathbf{q}} V_{\mathbf{k},\mathbf{k}',\mathbf{q}} \left[a^{\dagger}_{\mathbf{k}} a^{\dagger}_{\mathbf{k}'} a_{\mathbf{k}-\mathbf{q}} a_{\mathbf{k}'+\mathbf{q}} \rho - \rho a^{\dagger}_{\mathbf{k}} a^{\dagger}_{\mathbf{k}'} a_{\mathbf{k}-\mathbf{q}} a_{\mathbf{k}'+\mathbf{q}} \right]. \end{aligned}$$

It yields the following dynamics of the occupation numbers $N_k = Tr(a_k^\dagger a_k \rho)$:

$$\begin{aligned}\frac{dN_{\mathbf{k}}}{dt} &= Tr\left(a_{\mathbf{k}}^\dagger a_{\mathbf{k}} \frac{d\rho}{dt}\right) \\ &= -\frac{1}{\hbar}\sum_{k',q} \mathrm{Im}\left[V_{\mathbf{k},\mathbf{k'},\mathbf{q}} \left\langle a_{\mathbf{k}-\mathbf{q}}^\dagger a_{\mathbf{k'}+\mathbf{q}}^\dagger a_{\mathbf{k}} a_{\mathbf{k'}}\right\rangle\right] = -\frac{1}{\hbar}\sum_{k',q} \mathrm{Im}\left[V_{\mathbf{k},\mathbf{k'},\mathbf{q}} A_{\mathbf{k},\mathbf{k'},\mathbf{q}}\right].\end{aligned} \tag{2.5}$$

The right part of Eq. (2.5) contains the fourth-order correlators

$$A_{\mathbf{k},\mathbf{k'},\mathbf{q}} = \left\langle a_{\mathbf{k}-\mathbf{q}}^\dagger a_{\mathbf{k'}+\mathbf{q}}^\dagger a_{\mathbf{k}} a_{\mathbf{k'}}\right\rangle = Tr\left[\rho a_{\mathbf{k}-\mathbf{q}}^\dagger a_{\mathbf{k'}+\mathbf{q}}^\dagger a_{\mathbf{k}} a_{\mathbf{k'}}\right]. \tag{2.6}$$

It follows from Eq.(2.5) that the total number of particles in the system is conserved, $d/dt \sum_k N_k = 0$, as it should be in the absence of damping. Note that Eq. (2.5) is obtained from Eq. (2.4) without any simplifying assumptions. In order to take into account the finite lifetime of exciton-polaritons, an additional term $-N_k/\tau_k$ should be introduced into Eq.(2.5).

To complete the set of kinetic equations, we derive an expression for the temporal derivative of $A_{k,k',q}$ which reads

$$\begin{aligned}&\frac{dA_{\mathbf{k},\mathbf{k'},\mathbf{q}}}{dt} = Tr\left(\frac{d\rho}{dt} a_{\mathbf{k}} a_{\mathbf{k'}} a_{\mathbf{k}-\mathbf{q}}^\dagger a_{\mathbf{k'}+\mathbf{q}}^\dagger\right) = \frac{i}{\hbar} Tr\left([\rho; H]\, a_{\mathbf{k}-\mathbf{q}}^\dagger a_{\mathbf{k'}+\mathbf{q}}^\dagger a_{\mathbf{k}} a_{\mathbf{k'}}\right) \\ &= \frac{i}{\hbar}\left(\varepsilon_{\mathbf{k'}+\mathbf{q}} + \varepsilon_{\mathbf{k}-\mathbf{q}} - \varepsilon_{\mathbf{k}} - \varepsilon_{\mathbf{k'}}\right) A_{\mathbf{k},\mathbf{k'},\mathbf{q}} + \frac{i}{\hbar}\sum_{\mathbf{k''},\mathbf{q'}}\Big[V_{\mathbf{k},\mathbf{k''},\mathbf{q'}}\left\langle a_{\mathbf{k''}} a_{\mathbf{k}-\mathbf{q'}}^\dagger a_{\mathbf{k''}+\mathbf{q'}}^\dagger a_{\mathbf{k'}}^\dagger a_{\mathbf{k}-\mathbf{q}} a_{\mathbf{k'}+\mathbf{q}}\right\rangle \\ &+ V_{\mathbf{k'},\mathbf{k''},\mathbf{q'}}\left\langle a_{\mathbf{k}}^\dagger a_{\mathbf{k''}} a_{\mathbf{k'}-\mathbf{q'}}^\dagger a_{\mathbf{k''}+\mathbf{q'}}^\dagger a_{\mathbf{k}-\mathbf{q}} a_{\mathbf{k'}+\mathbf{q}}\right\rangle - V_{\mathbf{k}-\mathbf{q},\mathbf{k''},\mathbf{q'}}\left\langle a_{\mathbf{k}}^\dagger a_{\mathbf{k'}}^\dagger a_{\mathbf{k''}}^\dagger a_{\mathbf{k}-\mathbf{q}-\mathbf{q'}} a_{\mathbf{k''}+\mathbf{q'}} a_{\mathbf{k'}+\mathbf{q}}\right\rangle \\ &- V_{\mathbf{k'}+\mathbf{q},\mathbf{k''},\mathbf{q'}}\left\langle a_{\mathbf{k}}^\dagger a_{\mathbf{k'}}^\dagger a_{\mathbf{k}-\mathbf{q}} a_{\mathbf{k''}}^\dagger a_{\mathbf{k'}+\mathbf{q}-\mathbf{q'}} a_{\mathbf{k''}+\mathbf{q'}}\right\rangle\Big] = \\ &= \frac{i}{\hbar}\left(\varepsilon_{\mathbf{k'}+\mathbf{q}} + \varepsilon_{\mathbf{k}-\mathbf{q}} - \varepsilon_{\mathbf{k}} - \varepsilon_{\mathbf{k'}}\right) A_{\mathbf{k},\mathbf{k'},\mathbf{q}} + F_1 + F_2 + F_3 + F_4\end{aligned} \tag{2.7}$$

In Eq. (2.7), we have expanded the sum of the sixth-order correlators into four parts, $F1+F2+F3+F4$. At this stage, we are going to break the hierarchy decoupling the sixth-order correlators. Our goal is to write a closed system of equations for the occupation numbers and the fourth-order correlators $A_{k,k',q}$.

Depending on the wave vectors, all the terms in Eq. (2.7) can be collected into four distinct groups:

(1) The term F_1 corresponds to the correlators with $q' = 0$. It describes forward scattering and reads

$$\begin{aligned}F_1 = &\quad \frac{i}{\hbar}\sum_{k''}(V_{k-q,k'',0} + V_{k'+q,k'',0} - V_{k,k'',0} - V_{k',k'',0}) \times \left\langle a_{k'+q}^\dagger a_{k-q}^\dagger a_k a_{k'} a_{k''}^\dagger a_{k''}\right\rangle \\ = &\quad \frac{i}{\hbar} A_{k,k',q}\sum_{k''}(V_{k-q,k'',0} + V_{k'+q,k'',0} - V_{k,k'',0} - V_{k',k'',0}) N_{k''},\end{aligned} \tag{2.8}$$

where in the passage from the first to the second line we have used the mean-field approximation, i.e., we neglected the correlations between the states inside and outside the correlator. The term F_1 is responsible for the energy renormalization of the states coupled by polariton-polariton interactions.

(2) The second term F_2 contains the correlators, in which the momenta of the three incoming creation operators coincide with momenta of the three annihilation operators. It accounts for the scattering of the states forming the correlator. As we shall argue below, it is the most important correlator for the polariton-polariton interactions in the limit of strong dephasing. We have

$$\begin{aligned} F_2 = \quad & \frac{i}{\hbar}V_{k,k',q}[\left\langle a_k^\dagger a_k a_{k'}^\dagger a_{k'} a_{k'+q} a_{k'+q}^\dagger \right\rangle + \left\langle a_k^\dagger a_k a_{k'}^\dagger a_{k'} a_{k-q}^\dagger a_{k-q} \right\rangle \\ & - \left\langle a_{k'}^\dagger a_{k'} a_{k-q}^\dagger a_{k-q} a_{k'+q}^\dagger a_{k'+q} \right\rangle - \left\langle a_k a_k^\dagger a_{k-q}^\dagger a_{k-q} a_{k'+q}^\dagger a_{k'+q} \right\rangle] \\ \approx \quad & \frac{i}{\hbar}V_{k,k',q}[N_k N_{k'}(N_{k-q} + N_{k'+q} + 1) - N_{k-q}N_{k'+q}(N_k + N_{k'} + 1)], \end{aligned} \tag{2.9}$$

where we used the symmetry of the matrix element $V_{k,k',q} = V_{k',k,-q} = V_{k-q,k'+q,-q} = V_{k'+q,k-q,q}$ for the systems with time inversion and again used the mean-field approximation to pass from the first to the second line.

Equation 2.9 has a clear physical sense. The term in its right hand side is the collision term of the classical Boltzmann equation (note, however, that the Boltzmann equation does not contain fourth-order correlators). We see that within this assumption the dynamics of the fourth-order correlator is governed by the dynamics of the occupation numbers. The term F_2 provides the spontaneous buildup of correlators, which initially were absent in the system, and also takes into account the effects of the final state bosonic stimulation.

(3) The term F_3 contains the correlators, in which the momentum of one creation operator coincides with the momentum of one annihilation operator. These correlators are decoupled following the usual procedure used to decouple the Bogoliubov chains,

$$\begin{aligned} F_3 \approx \quad & \frac{i}{\hbar}\sum_{q'} V_{k,k',q'}[(N_{k-q} + N_{k'+q} + 1)A_{k,k',q-q'} - (N_k + N_{k'} + 1)A_{k-q',k'+q',q-q'}] \\ & + \frac{i}{\hbar}[\sum_{k''\neq k'+q} V_{k'',k-q,q} N_k A_{k'',k',q} + \sum_{k''\neq k-q} V_{k'+q,k'',q} N_{k'} A_{k,k'',q} \\ & - \sum_{k''\neq k'} V_{k,k'',q} N_{k-q} A_{k''+q,k',q} - \sum_{k''\neq k} V_{k'',k',q} N_{k'+q} A_{k,k''+q,q}]. \end{aligned} \tag{2.10}$$

It should be noted once more that the procedure of the decoupling used in Eqs. (2.8)(2.10) is not exact. This way a number of the nonclassical correlators of the new types will appear that do not conserve kinetic momentum, such as $\left\langle a_k^\dagger a_{k'} \right\rangle$, $\langle a_k a_{k'} \rangle$, $\left\langle a_k a_{k'} a_{k''} a_{k'''}^\dagger \right\rangle$,

etc. These correlators, however, cannot appear spontaneously as a result of the particle-particle scattering. Their appearance is possible either due to the strong Rayleigh scattering in the system or to the presence of the coherent excitation by two or more laser beams. Both these processes are not considered here.

(4) Finally, the term F_4 involves six creation or annihilation operators corresponding to six different quantum states:

$$
\begin{aligned}
F_4 \quad = \frac{i}{\hbar} \sum_{\substack{k'',q' \\ k'',k-q,k'+q \\ \neq k',k-q',k''+q'}} V_{k,k'',q'} \left\langle a_{k''} a^\dagger_{k-q'} a^\dagger_{k''+q'} a^\dagger_{k'} a_{k-q} a_{k'+q} \right\rangle + \qquad (2.11)
\\
+\frac{i}{\hbar} \sum_{\substack{k'',q' \\ k'',k-q,k'+q \\ \neq k,k'-q',k''+q'}} V_{k',k'',q'} \left\langle a^\dagger_{k} a_{k''} a^\dagger_{k'-q'} a^\dagger_{k''+q'} a_{k-q} a_{k'+q} \right\rangle -
\\
-\frac{i}{\hbar} \sum_{\substack{k'',q' \\ k-q-q',k''+q',k'+q \\ \neq k,k',k''}} V_{k-q,k'',q'} \left\langle a^\dagger_{k} a^\dagger_{k'} a^\dagger_{k''} a_{k-q-q'} a_{k''+q'} a_{k'+q} \right\rangle -
\\
-\frac{i}{\hbar} \sum_{\substack{k'',q' \\ k-q,k'+q-q',k''+q' \\ \neq k,k',k''}} V_{k'+q,k'',q'} \left\langle a^\dagger_{k} a^\dagger_{k'} a_{k-q} a^\dagger_{k''} a_{k'+q-q'} a_{k''+q'} \right\rangle .
\end{aligned}
$$

We assume that their contribution is negligible ($F_4 = 0$). Neglecting the terms F_4 means that the phase coherence between six distinct states is negligible because of some finite amount of decoherence in the system. In the case of six-wave mixing experiments, for instance, this approximation will fail. Also, for the polaritons in a random external potential, there are strong high-order correlations between the states with different k, resulting in the inhomogeneous polariton density. This means that the suggested approach cannot describe spatially inhomogeneous systems with induced or spontaneous pattern formation.

The set of Eqs. (2.5) - (2.11) describes the dynamics of bosonic systems accounting for particle-particle interactions beyond the Born-Markov approximation. Equations (2.5)(2.11) allow for non-energy-conserving processes and may predict a qualitatively different dynamics of the system with respect to the Boltzmann equations. We remind

that the Boltzmann equations only contain the occupation numbers, while in the system (2.5)(2.11), the correlations between different states in the reciprocal space are described by means of the fourthorder nonclassical correlators.

2.1.3 Decoherence and classical limit

The formalism derived in the previous section assumes that decoherence is weak enough in order to allow for the conservation of the fourth-order correlator. In this section, we consider the regime of strong decoherence. The decoherence processes are mainly governed by forward scattering of polaritons with acoustic phonons which do not affect directly the occupation numbers. Also, the polariton-polariton forward scattering treated beyond the Born approximation[89] can contribute to the temporal decay of fourth-order correlators. To treat the above mentioned process phenomenologically, one can introduce a decoherence time τ_{dec} in Eq. (2.7). This approach allows one to describe a smooth transition between the coherent regime described in the previous section and the Boltzmann limit. It allows the equation for $A_{k,k',q}$ to be rewritten in the following form:

$$\frac{dA_{k,k',q}}{dt} = \left[\frac{i}{\hbar}(\epsilon_{k-q} + \epsilon_{k'+q} - \epsilon_k - \epsilon_{k'}) - \frac{1}{\tau_{dec}}\right] A_{k,k',q} + F_1 + F_2 + F_3. \tag{2.12}$$

Though this is not always the case in the experimental situation, let us suppose that the decoherence time is short enough, so that $VN_{tot} << 1/\tau_{dec}$, where N_{tot} is the total number of polaritons in the system and V is the mean value of the matrix element. In this case, one can neglect in Eq.(2.12) the terms corresponding to the energy renormalization F_1 together with the terms F_3. The latter terms can also be neglected because they contain a sum of the fourth-order correlators corresponding to different states in the reciprocal space whose phases are more or less random so that together they yield a zero contribution (random phase approximation). Then, one can assume that due to the strong decoherence the values $A_{k,k',q}$ reach their equilibrium much faster than the occupation numbers, i.e., we divide the variables in our system into the slow ones (occupation numbers) and the fast ones (correlators). Such an approach is frequently applied in chemical kinetics, where all the intermediate products of chemical reactions are considered to be in quasiequilibrium (and in our case, the fourth-order correlator is indeed an intermediate product). Thus, one can write

$$\frac{dA_{k,k',k-q,k'+q}}{dt} = \left[\frac{i}{\hbar}(\epsilon_{k-q} + \epsilon_{k'+q} - \epsilon_k - \epsilon_{k'}) - \frac{1}{\tau_{dec}}\right] A_{k,k',k-q,k'+q} + F_2 = 0, \tag{2.13}$$

$$A_{k,k',k-q,k'+q} = \frac{F_2}{\frac{1}{\tau_{dec}} - \frac{i}{\hbar}(\epsilon_{k-q} + \epsilon_{k'+q} - \epsilon_k - \epsilon_{k'})} \tag{2.14}$$
$$= \frac{iV_{k,k',q}}{(\epsilon_{k-q} + \epsilon_{k'+q} - \epsilon_k - \epsilon_{k'}) + i\frac{\hbar}{\tau_{dec}}} \times$$
$$\times [N_k N_{k'}(N_{k-q} + N_{k'+q} + 1) - N_{k-q}N_{k'+q}(N_k + N_{k'} + 1)].$$

Substituting this expression for $A_{k,k',q}$ into the equation for the occupation numbers Eq.(2.7) , one obtains a set of semiclassical Boltzmann equations:

$$\frac{dN_k}{dt} = \sum_{k',q} W_{k,k',q}[N_{k-q}N_{k'+q}(N_k + N_{k'} + 1) - N_k N_{k'}(N_{k-q} + N_{k'+q} + 1)], \tag{2.15}$$

where the scattering rates are given by the following formula:

$$W_{k,k',q} = \frac{|V_{k,k',q}|^2}{\hbar} \frac{1/\tau_{dec}}{(\epsilon_{k-q} + \epsilon_{k'+q} - \epsilon_k - \epsilon_{k'})^2/\hbar^2 + 1/\tau_{dec}^2}. \tag{2.16}$$

One can see from Eq.(2.16) that the scattering rate is the fastest for the energy-conserving processes, where it is simply given by the Fermi golden rule:

$$W_{k,k',q} = |V_{k,k',q}|^2 \tau_{dec}/\hbar. \tag{2.17}$$

For the non-energy-conserving processes, the probability of scattering is reduced by a standard Lorentzian factor.

2.1.4 Polariton parametric oscillator

2.1.4.1 Formalism and parameters

The complete set of kinetic Eqs.(2.5)-(2.11) is extremely complicated and, for the general case of nonresonant pumping, requires hard numerical modeling. In the present section, we consider the simple example of polariton parametric amplifier (PPO) involving only three quantum states. Due to the strong nonparabolicity of the lower polariton branch, a pair of exciton-polaritons created by the pump pulse at the so called magic angle scatters into nondegenerate signal and idler states with both energy and momentum conserved, as shown in Fig. (2.1) Our goal is to describe the transition from the Boltzmann limit to the coherent regime. We do not consider here in detail the selection of the signal-idler states among the continuum of polariton states. The selection problem, however, is far from being trivial because of strong renormalization of the polariton branches with the increase of the pump intensity. At high polariton density, the conservation of energy and momentum

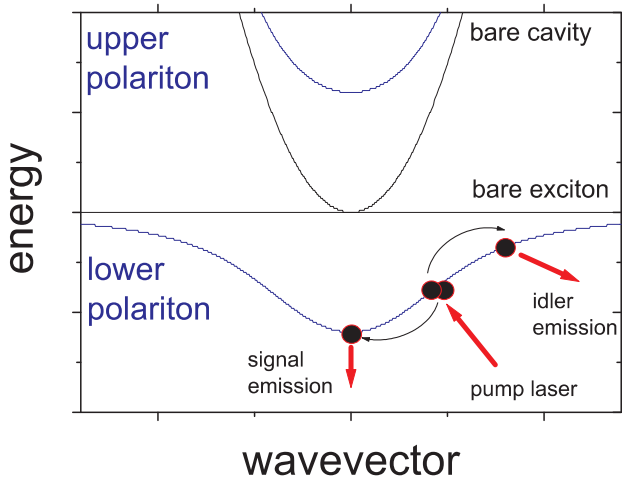

Figure 2.1 | Parametric scattering: Polariton dispersion (blue) and schematic parametric scattering of two pump polaritons into signal and idler polaritons at the magic angle. The bare cavity and exciton energies are shown dashed.

takes place for the states essentially different from those in the low density limit [70, 84]. Bearing this in mind, we consider here the simplest model based on the assumption that the PPO may be described by only three quantum states, namely, the pump, signal, and idler states. An advantage of our formalism with respect to the precedent ones derived in the same spirit [67, 71] is that it allows to take into account simultaneously signal-idler correlation and pump depletion. The Hamiltonian of this system can be written in the following form:

$$\begin{aligned} H = \quad & (\epsilon_s a_s^\dagger a_s + \epsilon_i a_i^\dagger a_i + \epsilon_p a_p^\dagger a_p) + U(|X_s|^2 a_s^\dagger a_s + \\ & + |X_p|^2 a_p^\dagger a_p + |X_i|^2 a_i^\dagger a_i)(|X_s|^2 a_s^\dagger a_s + |X_p|^2 a_p^\dagger a_p + |X_i|^2 a_i^\dagger a_i) + \\ & + (V a_p^\dagger a_p^\dagger a_s a_i + V^* a_p a_p a_s^\dagger a_i^\dagger), \end{aligned} \tag{2.18}$$

where the indices p, s, and i correspond to the pump, signal, and idler, respectively. The first term describes free particles, the second one describes energy blueshifts (X is the Hopfield coefficient corresponding to the percentage of the exciton fraction in each of the states), and the third term corresponds to the parametric process. Equations (2.7)-(2.11) reduce in this case to

$$\frac{dN_s}{dt} = -\frac{N_s}{\tau_s} - \frac{2}{\hbar} Im\left\{V\left\langle a_s^\dagger a_i^\dagger a_p a_p\right\rangle\right\} = -\frac{N_s}{\tau_s} + \frac{2}{\hbar} Im\left\{VA\right\}, \tag{2.19}$$

$$\frac{dN_i}{dt} = -\frac{N_i}{\tau_i} + \frac{2}{\hbar} Im\left\{VA\right\}, \tag{2.20}$$

$$\frac{dN_p}{dt} = -\frac{N_p}{\tau_p} - \frac{4}{\hbar} Im\left\{VA\right\} + P\frac{\hbar^2\tau_p^{-2}}{\delta_p^2 + \hbar^2\tau_p^{-2}}, \tag{2.21}$$

$$\frac{dA}{dt} = -(\frac{1}{2\tau_s} + \frac{1}{2\tau_i} + \frac{1}{\tau_p} + \frac{1}{\tau_{dec}})A + \frac{i}{\hbar}\delta_{PPO}A + \tag{2.22}$$

$$+\frac{iV}{\hbar}[N_p^2(N_s + N_i + 1) - 4N_sN_i(N_p + 1)],$$

where we have introduced the polariton lifetimes and external pumping term P; E_0 is the energy of the pump laser and τ_{dec} is the decoherence time. If pump depletion and decoherence are neglected, we recover the results obtained earlier by Ciuti et al. [67].

One can see that there are two energy detunings that play a crucial role. The first one, in Eq. (2.19), is the energy difference between the laser and the renormalized pumped polariton state. It is responsible for the bistable behavior of the PPO and will be referred to as the pump detuning in our further consideration,

$$\delta_p(N_p) = E_0 - \epsilon_p - U|X_p|^2(|X_p|^2N_p + |X_s|^2N_s + |X_i|^2N_i). \tag{2.23}$$

The second detuning, in Eq. (2.19), represents the dynamical energy mismatch between renormalized signal, pump, and idler states of the PPO:

$$\delta_{PPO}(N_p, N_s, N_i) = (\epsilon_s+\epsilon_i-2\epsilon_p)+U(|X_i|^2+|X_s|^2-2|X_p|^2)\times(|X_p|^2N_p+|X_s|^2N_s+|X_i|^2N_i). \tag{2.24}$$

In our numerical simulations, we consider a realistic case of a GaAs microcavity similar to that in Ref. [9]. The Rabi splitting is 6 meV and the cavity photon lifetime is $\tau_{ph} = 2$ ps. The signal, pump, and idler lifetimes are respectively given by

$$\tau_{s,p,i} = \frac{\tau_{ph}}{1 - |X_{s,p,i}|^2}. \tag{2.25}$$

The exciton-exciton matrix element of interaction is taken as [85] $U = 6E_b(a_b^2/S)$, where $E_b = 10$ meV is the exciton binding energy, $a_b = 100$ Åthe two-dimensional (2D) exciton Bohr radius, and S the surface of the laser spot for which we take a lateral size of 5 μ m.

2.1.4.2 Single mode dynamics under the cw laser pumping

In order to separate the contributions of the two main nonlinearities in the system, we first consider the case of a single mode system with $\delta_p(0) > 0$. Figure (2.2)(a)shows the

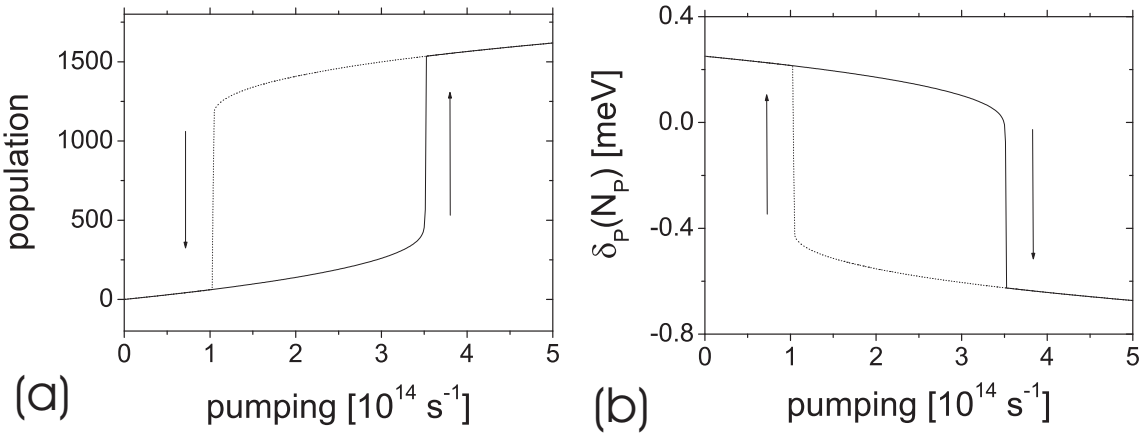

Figure 2.2 | Single mode model for a positive detuning $\delta_p(0) = 0.25$ meV: (a) Pump population versus pump intensity which is adiabatically increased (solid line) or decreased (dashed line). (b) Detuning $\delta_p(Np)$ versus the pump intensity adiabatically increased (solid line) and decreased (dashed line).

steady state polariton population versus cw pumping whose energy lies above the bare energy of the pumped state. *cw* pumping is adiabatically turned on (solid line) and turned off (dashed line). Figure (2.2)(b) shows $\delta_p(Np)$ for the same pumping conditions. One can see the typical hysteresis cycle of a bistable system. At low pumping, N_p depends superlinearly on P. The absorption of light by the mode decreases the value of $|\delta_p(N_p)|$, which, in turn, results in the increase of the absorption. This process finds its paroxysm at the turning point of the curve where $\delta_p(N_p)$ changes sign. In the model case which we consider here, the pump population jumps by a factor of 5 at this point. Above this point, N_p depends sublinearly on P since further increase of pumping provokes an increase of $|\delta_p(N_p)|$, which limits the increase of absorption. If P is decreasing, similar processes take place except that the turning point is situated at lower P than in the case of increasing pumping. All these processes result in the typical hysteresis cycle shown in Fig. (2.2). The hysteresis strongly affects the dynamics of the PPO as has been first outlined in Refs. [70] and [84], and as we shall see in the next subsections.

2.1.4.3 Dynamics of three modes under steplike onset at t=0

We first focus on the establishment of the steady state regime under cw pumping switching at $t = 0$. Figure (2.3)(a) shows the signal and the pump state populations versus the pump laser intensity. The pump laser energy is now taken to be resonant with the bare polariton energy so that no bistability is expected. We also take $\delta_{PPO}(0, 0, 0) = 0$. The parametric process starts to be efficient for rather low pump intensities and small polariton populations, so that the corresponding value of δ_p remains smaller than the linewidth [Fig.

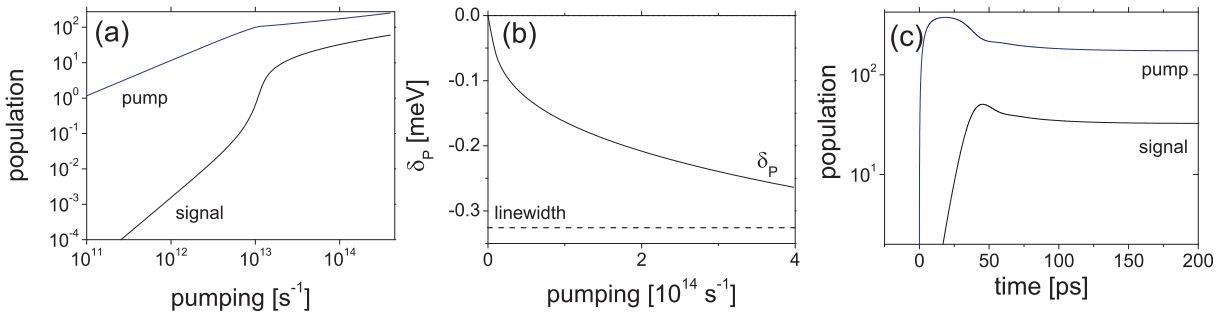

Figure 2.3 | Three modes model with resonant excitation of the pump state $\delta_p(0) = 0$: (a) Steady state signal (black) and pump populations (blue) versus the cw pump intensity which is adiabatically enhanced. (b) Detuning $\delta_p(Np)$ versus the pump intensity adiabatically enhanced. (c) Time dependence of the signal (black) and pump populations (blue) for a pumping intensity of 10^{14} particles/s. The corresponding particle density in the steady state is $2.3x10^9 cm^{-2}$.

(2.3)(b)] . Figure (2.3)(c) shows the temporal dynamics of the signal and pump states under cw excitation far above threshold. The buildup time of the signal is about 50 ps and it is longer than that of the pump state. However, the signal dynamics is quite smooth and shows no oscillations. In this regime, we do not expect that the Boltzmann approach would give qualitatively different results, except for the weak maxima at about 25 ps for the pump and at 50 ps for the signal. One can observe in Fig. (2.3)(a) that N_p continues to grow even above the nonlinear threshold. This contrasts with the results of the previous models, which neglect the pump dynamics and fix the pump population above threshold. The same quantities as in Fig. (2.3) are shown in Figs. (2.4)(a)(d) for the pump detunings $\delta_p(0) = 1$ and 0.25 meV. In Fig. (2.3)(a), the pump and signal populations show a nonlinear dependence on the laser intensity. Two very different regimes can be achieved depending on the value of the pump detuning. If the detuning is large, the PPO threshold is reached before the bistability threshold (solid lines). In this case, there are two jumps in the signal intensity as a function of pumping intensity, as is shown by the black curve. On the contrary, for smaller values of $\delta_p(0)$, the bistable threshold takes place before the PPO threshold (dashed lines). In that case, only one intensity jump is observed for both pump and signal intensities. However, this result and the next one can be altered if we would consider a realistic 2D microcavity [71].

The time domain results are shown in Fig. (2.3)(c) for $\delta_p(0) = 1$ meV and in Fig. (2.3)(d) for $\delta_p(0) = 0.25$ meV. The signal and pump intensities show abrupt jumps once the threshold is reached for both detunings. The populations show oscillations after reaching the threshold, demonstrating the important role played by the correlations between signal, pump, and idler states in this regime. These oscillations are damped because of the continuous filling of the pump state by the external laser beam. For moderate pumping and at large detuning, two successive thresholds can be seen in Fig. (2.3)(c) (solid lines)

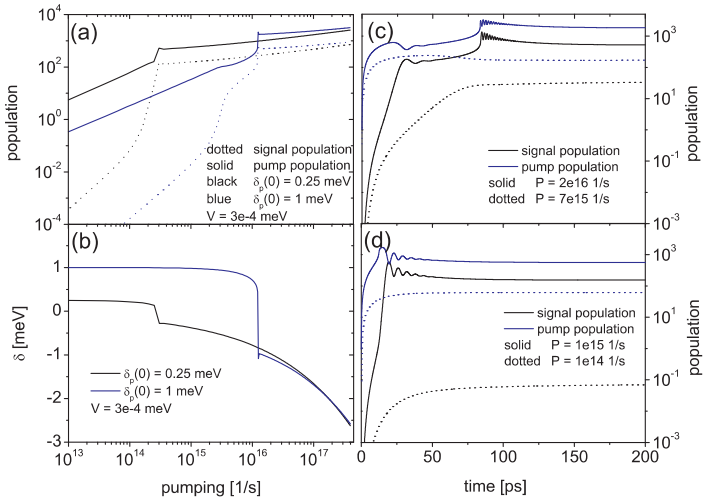

Figure 2.4 | Three modes model for the positive pump detuning $\delta_p(0)$: (a) Steady state signal (black) and pump populations (blue) for $\delta_p(0) = 0.25$ meV (dashed) and $\delta_p(0) = 1$ meV (solid). The cw pump intensity shown on the y axis is adiabatically increased. (b) Detuning $\delta_p(Np)$ versus the pump intensity for $\delta_p(0) = 0.25$ meV (black) and $\delta_p(0) = 1$ meV (blue). (c) $\delta_p(0) = 1$ meV. Time dependence of the signal (black) and pump populations (blue) for a pumping intensity of $2x10^{16}$ particles/s (dashed) and $7x10^{16}$ particles/s (solid). (d) $\delta_p(0) = 0.25$ meV. Time dependence of the signal (black) and pump populations (blue) for a pumping intensity of 10^{14} particles/s (dashed) and 10^{15} particles/s (solid).

for the signal and pump populations. The dotted lines show the population numbers for pumping below threshold. In the case of high laser intensities, these two thresholds take place simultaneously. In Fig. (2.3)(d), the PPO starts after passing the bistable threshold and leads to a jump of the signal intensity. For pumping below the threshold, the signal state is filled only by spontaneous scattering and remains weak for the two detunings.

2.1.4.4 Kick effect

In this section, we consider the effect of a short kick pulse resonant with the pump mode which comes after the establishment of the steady state. We consider the case $\delta_p(0) = 1$ meV. The intensity of the cw pumping laser is chosen in order to maintain the system just below the bistable threshold. The intensity emitted by the signal is, therefore, rather weak. Then a 1 ps long kick pulse is sent to the pump state. It induces the increase of the pump intensity sufficient to pass the bistable threshold, as Fig. (2.5) shows. Consequently, after the arrival of the kick, the signal intensity increases by almost 1 order of magnitude. Remarkably, the system does not go back to its initial state after the kick pulse has passed, but it stabilizes to a new equilibrium state characterized by an intense signal emission. This effect can be used for the realization of low threshold optical switches.

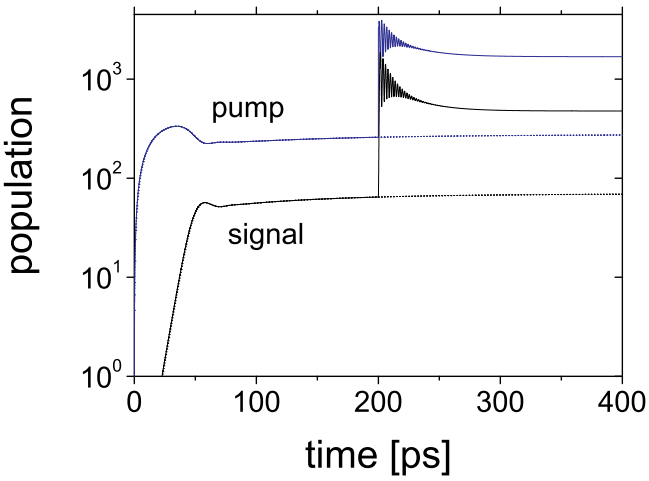

Figure 2.5 | Kick effect for the three modes model: Time dependence of signal (black) and pump state populations (blue). The pumping is composed of a cw laser $\delta_p(0) = 1$ meV, 1×10^{16} particles/s and a short kick pulse at $t = 100$ ps 2.5×10^{17} particles/s. The dashed lines correspond to the populations without kick.

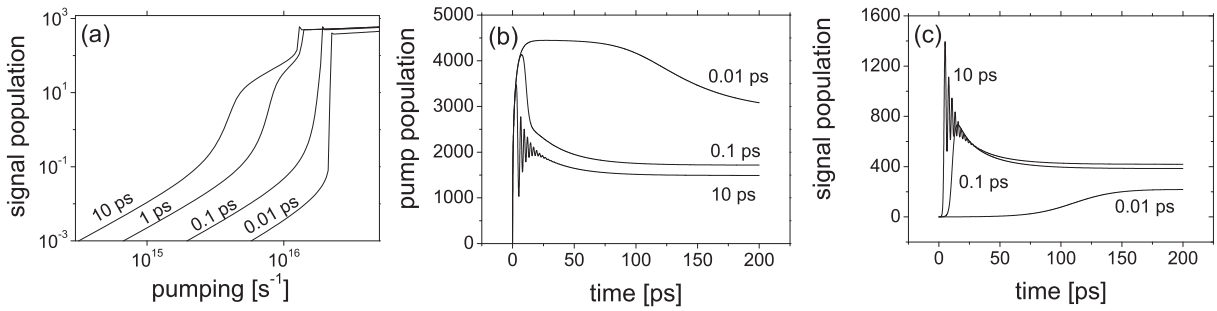

Figure 2.6 | From quantum to classical limit: Signal and pump populations versus the pump intensity for different decoherence times $\delta_p(0) = 1$ meV. The condition VN_{tot}/τ_{dec} is satisfied for decoherence times shorter than 0.1 ps. (a) Steady state population of the signal state. (b) Time dependence of the signal population 2.5×10^{16} particles/s. (c) Time dependence of the pump population 2.5×10^{16} particles/s.

2.1.4.5 From quantum to classical limit

Figure (2.6) shows the impact of the decoherence on the dynamics of the PPO. It can be clearly seen that the decrease of the decoherence time leads to the increase of both bistable and PPO thresholds. In the time domain, it leads to the washing out of the oscillations in pump and signal intensities due to the suppression of the nonclassical correlations between them. It is also seen that the decoherence makes longer the time needed for the pump and signal states to reach stationary values under cw excitation. It is clearly seen from Fig. (2.6)(c) that in the limit of the small decoherence times, the system recovers the Boltzmann-limit dynamics.

2.1.5 Conclusion

In conclusion, we have derived a closed set of kinetic equations describing a system of interacting bosons beyond the Markovian approximation. The dynamics of the occupation numbers is shown to be strongly altered by the buildup of the nonclassical four-particle correlators. The decoherence process leading to the fast suppression of these correlators is shown to provoke the transition from the quantum to the classical limit. This system of kinetic equations is applied to the dynamics of a three state polariton parametric oscillator. The general equation set which is obtained by us is quite heavy, and its solution requires great numerical effort. However, this formalism has an important advantage of taking into account the incoherent phonon dynamics and the coherent nature of the polariton-polariton scattering process in the presence of macroscopically occupied polariton modes. It represents a bridge between the fully coherent picture (Gross-Pitaevskii equations) and the fully incoherent picture (Boltzmann approach).

2.2 Fluctuation induced bistability transitions

2.2.1 Introduction

The blueshift and the bistability of exciton-polaritons have been introduced in the first chapter. We will remind them at this point briefly because they will be the major effects discussed and investigated in the following section. The blueshift comes from the polariton-polariton interaction, which has been under deep investigation in recent years [90, 91, 92].

These correlations and the resulting polariton-polariton interaction manifests itself in a blue shift of the polariton resonance with the increase of external pumping. In case the driving laser beam frequency exceeds that of the lower polariton (LP) branch by more than LP-linewidth, the polariton field amplitude can exhibit abrupt transitions between different stable states [68]. The theoretical treatment of these nonlinear oscillators gives a typical S-shape of the polariton amplitude depending on external excitation [68, 70, 71] (Fig.2.7(b)), with finite range of pump intensities where the polariton system can be bistable.

The second important nonlinear effect, studied in detail in the previous section, is the parametric polariton scattering within the polariton dispersion branch with energy and momentum conservation [83, 84, 71, 93].

Both nonlinear effects - parametric scattering and bistability - can often occur simultaneously [84, 93].

In fact, accounting for the polarization of light expands the bistability to multistability and polarization hysteresis of the coherently driven polariton mode [72]. These effects arise from polarization-dependent polariton-polariton interactions and can be measured in polarization resolved transmission and photoluminescence experiments.

Fluctuations and noise are always present in physical systems and they can strongly influence the dynamics of the physical phenomena. The origin of the noise lies in a large number of physical processes e.g. spontaneous emission (internal fluctuations); amplitude fluctuations of the external driving laser field and/or phase noise of the laser (external fluctuations) in the case of optical pumping. The noise can become very important if the driven system exhibits some critical behavior due to a nonlinear feedback mechanism.

The strong dependence of transition probabilities from the lower amplitude state of a bistable nonlinear oscillator on the driving parameters and noise near the stability edge sets a challenging problem of controlling these processes.

There are different ways to describe the nonlinear oscillator disturbed by noise. One of them is the use of the generalized diffusion equation - the Fokker-Planck-equation (FPE). It can be used to study peculiarities of the dynamics in case of bistable potentials.[94, 95, 96, 97, 98] Nonlinear systems disturbed by white [94] and colored additive noise [95] or

multiplicative noise [96] have been considered.

In the following part we describe the dynamics of the driven nonlinear oscillator with an additive external white noise under presence of damping. More specifically, we investigate the time the system needs to jump from the low-energy stable state to the high-energy stable state depending on the external noise intensity. This noise intensity is not coupled to the damping, as it is given by the fluctuation-dissipation theorem. We investigate an open system, where the damping is given by the leak mode of the cavity - the losses through the cavity mirrors. We use three different methods to calculate the escape times from the quasi-stable low intensity state and compare the results obtained for different system parameters. We start with the direct numerical solution of the dynamic equation. After that, we compare it with a two dimensional (2D) Fokker-Planck-Equation in order to build a bridge to a one dimensional (1D) Fokker-Planck-Equation derived in Ref. [99]. These one dimensional analytical approach can give easily estimations of the jump times. A special advantage is, that it could simplify the treatment including the polarization degree of freedom by reducing the dimensionality of the system. We check the validity of the reduction to the one dimensional quasi-energy picture and study the influence of damping and noise on the mean escape time of the driven polariton mode from the lower-density quasi-stable state, i.e. the expectation time of the internal field jump in the microcavity.

2.2.2 Analytical models

2.2.2.1 Equation of motion

The dynamics of the driven nonlinear oscillator can be described in the quasi-energy state representation. The effective Hamiltonian in rotating wave approximation with slow varying polariton amplitude operators a and a^+ reads

$$H = -\Delta a^\dagger a + \frac{\alpha}{4}(a^\dagger a)^2 - f(a^\dagger + a). \tag{2.26}$$

The first term is the energy detuning with $\Delta = \hbar(\omega - \omega_{LP})$, where ω is the frequency of the laser field and ω_{LP} is the frequency of the lower polariton branch. The second term describes the nonlinearity of polariton system, where α is the nonlinearity constant and the last term is the driving force with amplitude f. In the classical approach, the eigenvalues of H correspond to the quasi-energy E and the operators a and $a^\dagger$ are the classical canonical slow variables. One can easily obtain the following equation of motion for slow varying amplitude

$$i\hbar\frac{da}{dt} = -\Delta a + \alpha a|a|^2 - f. \tag{2.27}$$

Transformation to dimensionless variables $a\,\Delta/f \rightarrow a$ yields

$$i\frac{da}{d\tau} = -a + \beta a|a|^2 - 1, \quad \tau = t\frac{\Delta}{\hbar}, \tag{2.28}$$

and the corresponding Hamiltonian takes the form

$$H = -a^+a + \frac{\beta}{4}(a^+a)^2 - (a + a^+), \quad \beta = \frac{\alpha f^2}{\Delta^3}. \tag{2.29}$$

The transformation of Eq.(2.26,2.27) to dimensionless variables simplifies the investigation of the system because only the parameter β is left. It defines the shape of the phase trajectories and the probabilities to find the system in different quasi-energy states. Fig.3.4(a) shows a typical phase diagram ($u = Re(a)$, $v = Im(a)$) of the driven nonlinear oscillator. The contour lines stand for different trajectories corresponding to different quasi-energies E and periods of particle motions along the trajectories T(E). The critical points are indicated with '1' (small oscillation amplitude (u_1, v_1)) and '2' (large oscillation amplitude (u_2, v_2)) separated by an unstable state called separatrice. Fig.3.4(b) shows these states schematically in the typical S-shape diagram. The middle branch including the state 'S' is unstable. The parameter β shifts the dashed line with the three points along the abscissa axis. This dimensionless parameter allows one to determine the distance between the external field and its critical value, where the bistability jump will take place without external fluctuations at $\beta_c = 4/27$.

After introducing phenomenologically the polariton damping and noise terms, the dynamic equation, which reads as follows

$$i\frac{da}{dt} = -i\vartheta a - a + \beta a|a|^2 - 1 + \xi(t), \tag{2.30}$$

where ϑ is the damping parameter and $\xi(t)$ is the external Gaussian white noise with the following correlation functions:

$$\langle \xi^*(0)\xi(t)\rangle = Q\delta(\tau), \quad \langle \xi(0)\xi(t)\rangle = 0. \tag{2.31}$$

This equation is a stochastic equation also called Langevin equation, as it describes a dynamic process with an additional white noise.

The damping is caused by e.g. losses through the cavity mirrors. We assume here, that noise and damping are not coupled through the famous Fluctuation-Dissipation Theorem. This theorem has been formulated by Nyquist (1928) [100] and first proved by Callen et al. (1951) [101] and couples fluctuations and dissipation of a system. This theorem is valid for linear equilibrium systems, which interact only with a thermal bath. But in contrast, the present system is a non-equilibrium, nonlinear, and open system. In addition, we assume that the damping given by the leakage through the cavity mirrors is much larger

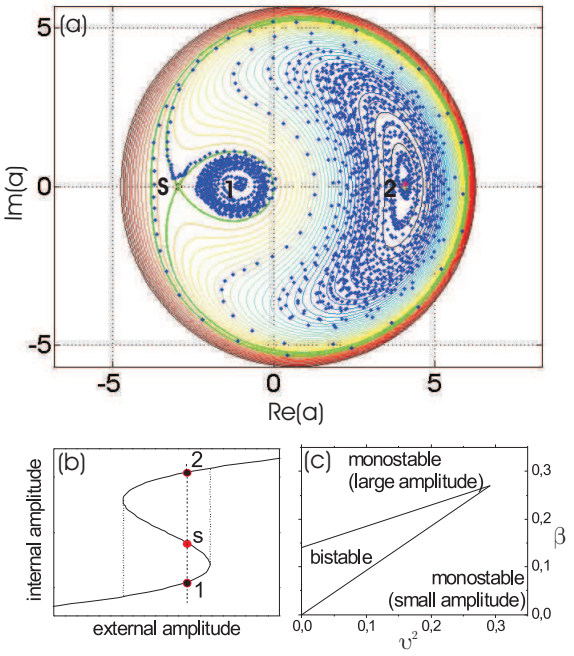

Figure 2.7 | Numerical experiment: (a) Phase portrait of the numerical experiment. The lines are the contour plot of the Hamiltonian and the blue points are the results of the numerical experiment starting from stable point '1'. The parameters are $\vartheta = 0.01$, $\beta = 0.075$ and $Q = 0.09$. (b) shows schematically the bistable region of nonlinear oscillator with two stable points '1' and '2' and one unstable point 'S'. The dotted lines show the hysteresis cycle and the dashed line shows the point of the calculation. (c) is the phase diagram of our system depending on the nonlinearity constant β and the damping ϑ. The solid line borders the bistable area.

than the damping induced by the coupling with the exciton bath. However, once again, we treat both parameters independently.

In Fig.2.7(a) a typical solution of the numerical experiment using Eq.(2.30) is shown. Each blue point corresponds to the solution of Eq.(2.30) separated by fixed time step. The averaged escape time (jump time) has been calculated over 100 numerical solutions for each set of parameters Q, ϑ and β. The larger is the damping ϑ the stronger is its influence on the dynamics of nonlinear oscillator and the deviation from the pure Hamiltonian case for zero damping. In order to determine the position of the critical states in phase space, one should find the zeros of the right part of Eq.(2.30) neglecting the noise term. With the increase of the damping, the shape of the trajectories changes, the stable points of the system shift away from the Re(a)-axis and disappear completely for large damping coefficients [102]. In Fig.2.7(c) the phase diagram of our system in the plane of dimensionless parameters β and ϑ^2 is depicted. The solid lines border the parameter settings where the bistable behavior can be observed in case one neglects the effects of noise. Large dephasing as well as large nonlinearity constant lead to the disappearance of the bistability, the critical values are $\vartheta = 0.53$ and $\beta = 0.27$.

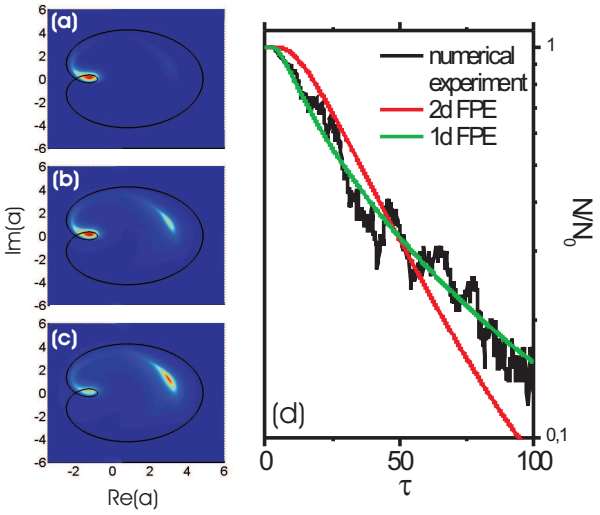

Figure 2.8 | 2D Fokker-Plack equation and comparison of the models: Distribution function calculated with the 2D-FPE after 20 (a), 30 (b), and 100 (c) timesteps in the phase space. The dynamic colorbar shows the value of the distribution function from small (blue) to high (red). (d) presents the calculated decay of particles in the closed separatrice around the small amplitude stable point for numerical experiment (black), 2D FPE(red), and 1D FPE (green). The calculation parameters are $Q = 0.09$, $\vartheta = 0.01$ and $\beta = 0.125$.

2.2.2.2 2D Fokker-Planck Equation

The distribution of the probability to find the oscillator in a given point of the phase space can also be obtained from the Fokker-Planck-Equation:

$$\frac{\partial n(t)}{\partial t} = -(\frac{\partial}{\partial a}A(a,a^*) + \frac{\partial}{\partial a^*}A^*(a,a^*))n(t) + B(a,a^*)\frac{\partial^2}{\partial a \partial a^*}n(t), \tag{2.32}$$

where A is the so called drift term and B the diffusion coefficient. The derivation of the Fokker-Planck equation starting from the Langevin equation is given in the appendix.

In the case treated here, the two terms were described as follows (see appendix and Refs. [103, 104]):

$$A(a,a^*) = -i(-i\vartheta a - a - \beta a|a|^2 - 1) \tag{2.33}$$

and

$$B(a,a^*) = Q \equiv \frac{\sigma^2}{f^2}\frac{\Delta}{\hbar}. \tag{2.34}$$

The diffusion coefficient is the external noise intensity and the drift term is governed by the right hand side of Eq.(2.30) without noise.

We can estimate the ratio between the escape times t_1 and t_2 from stable states 1 and 2 of the nonlinear driven oscillator from the stationary solution of the 2D-FPE. The arbitrary drift vector $\vec{A} = (A_u, A_v)$ can be decomposed into potential and rotary parts: $\vec{A} = \vec{A}_{pot} + \vec{A}_{rot}$, with $\vec{A}_{pot} = (\partial_u W, \partial_v W)$ and $\vec{A}_{rot} = (\partial_v H, -\partial_u H)$, where $W = W(u,v)$ and $H = H(u,v)$ are arbitrary functions of (u,v) variables.

The analytic solution of 2D FPE can be found if $\vec{A}_{pot}$ and $\vec{A}_{rot}$ are orthogonal, i.e. the following condition is fulfilled:

$$\partial_u W \partial_v H - \partial_v W \partial_u H = 0. \tag{2.35}$$

In this case $n(u,v) = \exp\left(W(u,v)/Q\right)$, and the ratio between escape times t_1 and t_2 can be estimated as

$$\frac{t_2}{t_1} = \frac{n_2}{n_1} = \exp[(W(u_2,v_2) - W(u_1,v_1))/Q)]. \tag{2.36}$$

Unfortunately in the case of driven nonlinear oscillator the condition (2.35) is not fulfilled, and to study fluctuation-induced transitions in this system one should develop some approximate analytical methods for solving 2D FPE and compare the obtained solution with numerical results.

The 2-dimensional FPE should in principle provide the same results as the numerical experiment since in the derivation no assumptions were made. To illustrate the dynamics, Fig.2.8 presents the distribution function n at 3 different times. Starting from the small amplitude state, the distribution function spreads due to diffusion and rotates around the first stable point (Fig.2.8(a)). Then the particles cross the separatrice and reach the large amplitude state. One intermediate picture is mapped in Fig.2.8(b). Fig.2.8(c) shows the distribution probability after a long time. Almost all particles arrived in the surroundings of the high energy stable state. In the phase space, it is not exactly at $y = 0$, as it is the result of the shift of the stable points in presence of damping [102].

2.2.2.3 1D Fokker-Planck Equation

The third way to treat the problem is to solve the one dimensional FPE [99]. Using the Keldysh diagram technique, the two dimensional problem can be transformed to a one dimensional problem averaging over the trajectories with the same energy E:

$$\frac{\partial n_i(E)}{\partial E} = \frac{\partial}{\partial E}\left((\vartheta K) n_i(E) + QD\frac{\partial n_i(E)}{\partial E}\right), \tag{2.37}$$

where $i = 1,2$ for low and high intensity stable points, respectively. The parameters ϑ and Q are dimensionless damping and random force intensity. The terms $K(E)$ and $D(E)$ are determined by integrals along the phase trajectories with particular quasi-energy E-closed curve $C(E)$ in dimensionless variables:

$$\begin{aligned} K(E) &= \frac{1}{2iT(E)}\oint_{C(E)} ada^* - a^*da \\ D(E) &= \frac{1}{2iT(E)}\oint_{C(E)} \frac{\partial H}{\partial a}da - \frac{\partial H}{\partial a^*}da^*. \end{aligned} \tag{2.38}$$

Once again, because the damping of polariton system is caused not only by the interaction with the exciton reservoir but also due the losses in mirrors we handle Q (noise) and ϑ (damping) as independent parameters. We assume that the fluctuations of the illumination do not affect the losses of cavity mirrors and vice versa. The derivation of Eq.(2.37) is described in detail in Ref. [99].

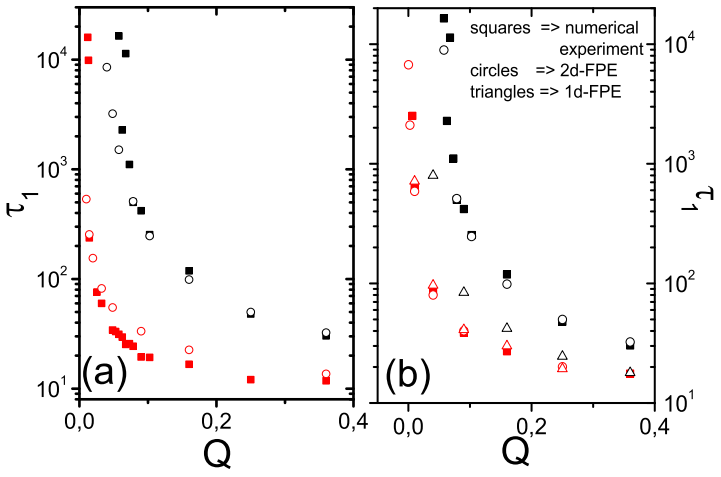

Figure 2.9 | Escape time and fluctuations: (a) Escape time depending on external noise intensity for constant dissipation $\vartheta = 0.1$ and $\beta = 0.125$ (red), $\beta = 0.075$ (black). In (b) the calculations for $\beta = 0.075$ for two different damping coefficients are depicted. The red (black) points correspond to a $\vartheta = 0.01/$ $(\vartheta = 0.1)$. Squares/circles/triangles correspond to NE/ 2D-FPE/ 1D-FPE, respectively.

The relations connecting the dimensionless parameter of the numerical calculations ϑ, Q, β with the physical parameters: noise spectral density σ^2, pump amplitude f, pump detuning Δ, oscillator dephasing γ and nonlinearity constant α are listed below:

$$\beta = \frac{\alpha f^2}{\Delta^3}, \quad \vartheta = \frac{\gamma}{\Delta}, \quad Q = \frac{\sigma^2}{f^2}\frac{\Delta}{\hbar}, \quad t_1 = \tau_1 \frac{\hbar}{\Delta}. \tag{2.39}$$

2.2.3 Numerical Results

In the following, we will discuss the influence of the fluctuations on the escape time from the low energy point. It is defined as the time when the particle first leaves the region bordered by the separatrice around the first stable point in phase space. We integrate over the closed separatrice circle surrounding the low amplitude stable state (compare Fig.2.7(a)) to obtain the number of particles in this area. The time dependence of this value shows an exponential decay with the time constant τ_1 (first escape time). One example of the corresponding decay curves for the NE (black), FP2D (red) and FP1D (green) is shown in Fig.2.8(d). We see a more or less good agreement between all three methods. The decays are calculated for $Q = 0.09$, $\vartheta = 0.01$ and $\beta = 0.125$.

Fig.2.9(a) presents the results of the numerical experiment and the 2D-FPE for a constant dissipation parameter $\vartheta = 0.1$ and two different values of β, depending on the external noise intensity. The damping is large and the ratio between damping and detuning reproduces the experimental situation. As expected, the numerical experiment and the 2D-FPE coincide. The escape time for small noise amplitude is large, because it is hard to push the system over the bistability. For large noise intensities the sum of pump amplitude and noise intensity strongly exceeds the bistability threshold – the jump takes

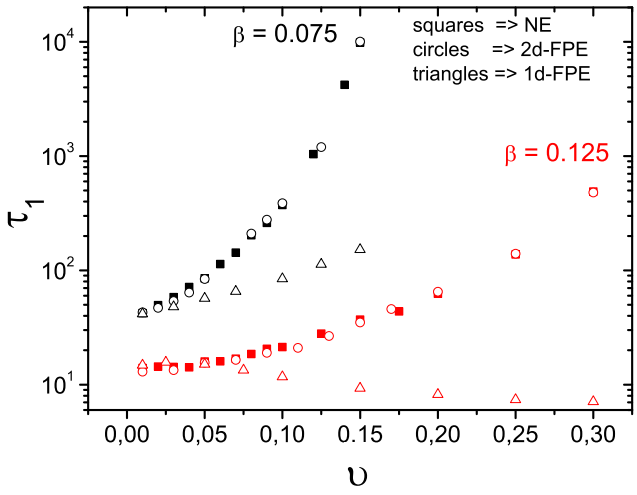

Figure 2.10 | Escape time and dissipation: Escape time in dependence of the dissipation parameter for a constant noise Q=0.09 and two different nonlinearity constants $\beta = 0.125$ (red) and $\beta = 0.075$ (black). The squares/circles/triangles correspond to the solution method using numerical experiment/ 2D-FPE/ 1D-FPE, respectively.

place almost immediately and shows a rather weak dependence on stronger fluctuations. The same happens for larger nonlinearity constants. For $\beta = 0.125$, the system settings are closer to the bistability jump and smaller noise intensities are sufficient to push the system to the upper state.

In Fig.2.9(b) the dependency of the jump time on the noise intensity is shown for two different damping parameter. The numerical experiment (squares) and the 2D-FPE (circles) are in good agreement, while the 1D-FPE solution (triangles) fails for large damping parameters (black). The origin lays in the averaging over the trajectories, which is done within low dissipation approximation. Under the presence of strong damping, the system is considerably disturbed and the form of the trajectories changes completely (not shown), so the approximation is no longer valid. In addition, the numerically obtained decay times of the 1D-formalism show a mismatch with the other two methods for large noise intensities. This originates from the larger sensitivity of the 1D approximation to the edge of stability of the trajectories.

To show clearly the range of damping where the 1D-FPE is valid, we have calculated the dependency of τ_1 on the damping ϑ for fixed noise intensity Q=0.09. The corresponding results for all three methods for two different nonlinearity constants are depicted in Fig.2.10. The 1D-FPE is in good agreement with the other descriptions up to ϑ=0.04. After that, the discrepancy between it and the NE grows with increasing dissipation, due to the increased modification of the phase portrait. Furthermore, the decay times calculated with the 1D-FPE for $\beta = 0.125$ appear even to decrease with increased damping due to relatively stronger modification of the phase portrait for the β close to the critical value $\beta_c = 4/27$. Additional damping shifts the critical point '1' closer to the separatrice and the diffusion induced decay will dominate the system.

The critical resonance width γ in Fig.4, which limits the valid parameter settings for the one dimensional FPE, is determined to be 0.04 meV in case of a detuning Δ of 1 meV.

To transform the obtained dimensionless escape times into real units and to show their influence on experimental results we use the relations (14). Below we assume the following set of parameters: CW pump detuning from the polariton resonance Δ=1 meV and a resonance width γ= 0.1 meV. The dimensionless noise spectral density reads as $Q = (\delta f/f)^2 \tau_c \Delta/\hbar$, where τ_c is the noise correlation time. We take now as an example two points for $\beta = 0.125$ from Fig.2.9 at Q=0.01 and Q=0.02. The corresponding dimensionless escape times τ_1 are 10^4 and 100. For these values one obtains escape times t_1 of 40 ns and 0.4 ns, which appear to be long enough for experiments with pulses shorter than 1 ns. With decreasing noise intensities, the escape times increase exponentially. These large fluctuation-induced transition times are in agreement with bistable jumps observed in experiments.[68, 84, 105]

2.2.4 Narrowing of the Hysteresis cycle

The question is, how the fluctuations can affect the outcome of experimental results. To elucidate their impact, we show a fluctuation-affected hysteresis cycle in Fig.2.11. The escape time t_1 in dependence on the external amplitude f for the two directions is shown in (a): (1) left hand side from upper to lower branch (decreasing pump intensity) and (2) right hand side from lower to upper branch of the s-shape diagram (increasing pump intensity). The times are calculated using the 2D-FPE. The escape times show a strong dependence on the external amplitude close to the stability edges. Fig.5 (b) shows the hysteresis cycle without fluctuations (red/gray) and with fluctuations (blue/dark gray) for a given measurement time τ_{exp} indicated with the dashed line in Fig.5(a). As one can see, the experimental observed hysteresis cycles are more narrow in comparison to the undisturbed case. Due to the strong exponential dependence of the escape time on the excitation power, the hysteresis cycle will not change strongly for longer measurement periods. The noise intensity is chosen to be 0.01 and the damping γ is 0.1 meV. The influence of the noise is quite strong and the closed hysteresis cycle with fluctuations seems to be very small. In the experiments the noise is definitively smaller than what we have studied here. We used a large noise intensity to show clearly the impact of these fluctuations and to keep the numerical effort in a reasonable limit. However, it is not easy to estimate the realistic noise intensity.

In case of additional illumination of the cavity by e.g. non-resonant excitation, the fluctuations can be significantly increased and they can stimulate a transition to the high-energy stable state. In contrast, the amplitude fluctuations of the driving lasers fields are frequency-dependent and the resulting colored noise is much less efficient to stimulate the transitions, than white noise.[106]

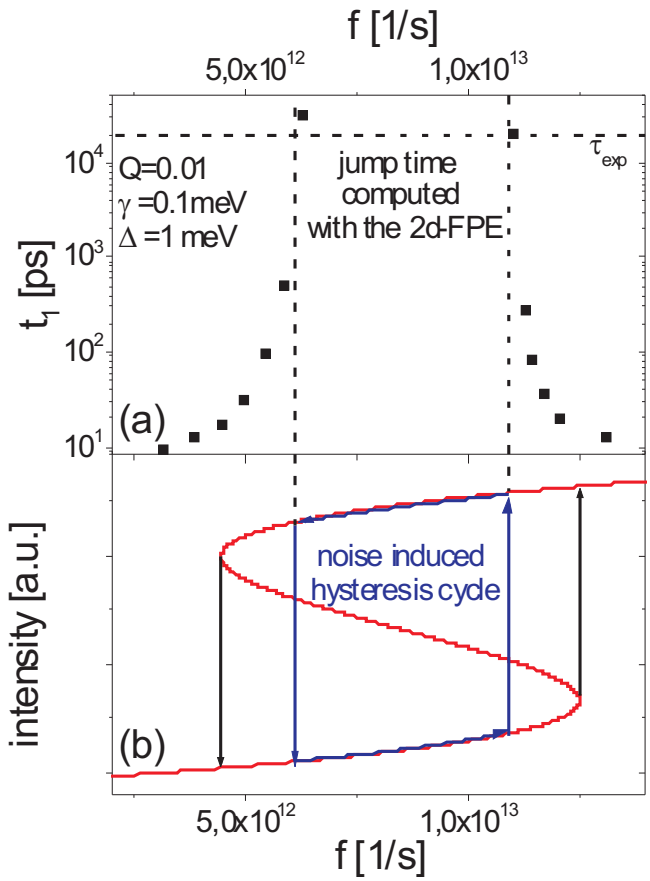

Figure 2.11 | Narrowing of the hyeresis cycle: (a) Dependence of the escape time t_1 on the driving field amplitude f calculated for a GaAlAs cavity. (b) s-shape (red line) for the undisturbed case. The black arrows show the jumps of the internal amplitude without noise. The blue line corresponds to the noise induced hysteresis cycle for a defined time τ_{exp} of the measurement indicated by the dotted lines. The calculation parameters are $Q = 0.01$ and $\gamma = 0.1$.

But, nevertheless, we obtain an exponential decay of t_1 for large white noise intensities, which can change experimental results drastically.

The effect might be more important for the multistability, which has not yet been observed. Therein, at the critical point one has the possibility to jump to three different states. The probability of these transitions will also be governed by intensity or polarization fluctuations in the system. Bearing this in mind, a nice polarization pattern in a disordered system might be possible to observe.

2.2.5 Conclusion

Summarizing, we have considered the problem of a driven nonlinear polariton system in three different ways and compared the obtained solutions. As expected, the numerical experiment and the 2D-FPE show a good agreement and are valid for all regarded parameter settings. In contrast, the 1D-FPE in quasi-energy space becomes invalid for large damping and strong fluctuations, because the averaging over the trajectories is not possible anymore. The 1D-approximation is shown to be valid for the polariton line widths less

than 0.04 meV for a detuning of 1 meV between the driving field frequency and polariton resonance. Finally, the fluctuations can narrow significantly experimental results as we have shown for the hysteresis cycle of a polariton system.

Chapter 3

Condensation Phenomena

In the following chapter we will study in detail the condensation phenomena. From the practical point of view, speaking of condensation means that the excitation is not coherent (the pump laser is not in resonance with the polariton dispersion), and the coherence appears in the system only thanks to the condensation process. The external pumping creates electron hole pairs, which form a cloud of excitons. These excitons will interact and relax towards the bottom of the polariton dispersion. The principal mathematical description is given in Chapter 1, which is based on the Boltzmann equations for the relaxation process. Once the condensate is formed, it can be treated within the Gross-Pitaevskii equation. In the first part of this chapter we study the relaxation dynamics of a ZnO based microcavity intend to operate as a polariton laser. ZnO has some huge advantages in comparison with other semiconductors (even in comparison with other wide gap semiconductors), such as the huge oscillator strength and Rabi splitting. As one will see, the kinetics of the relaxation has an important impact on the lasing threshold and the use of the infinite lifetime picture does not hold anymore to describe the relaxation process. Polariton condensates are now observed experimentally for various systems and one can start to think about possible applications beside the polariton laser. Interestingly, the spin structure of polaritons can lead to some interesting analogies between electronic and polaritonic systems. One of them is the Josephson effect (or Josephson junctions) with its recent developed polaritonic analogue. The second part will be devoted to a polaritonic analog of the electronic Datta Das transistor. We develop a new all optical spin transistor based on the spin Meissner effect allowing fast switching of the transmission and relfection of this device by changing the condensate density. Basing on the nonlinearities in the dynamics of polaritonic Josephson junctions, the emission of such structures can show chaotic behavior. This can be used for a scheme of chaotic communication, which is the subject of the last part. Synchronization of chaotic systems and chaotic communication are discussed in detail in this part. All together, one may say the second and third part is devoted a new research field: spin-optronics. Many interesting features and devices, in-

vestigated intensive in spintronics (electrons with spin), can be modified for spin-optronic devices using polaritons and their unique spinstructure.

Contents

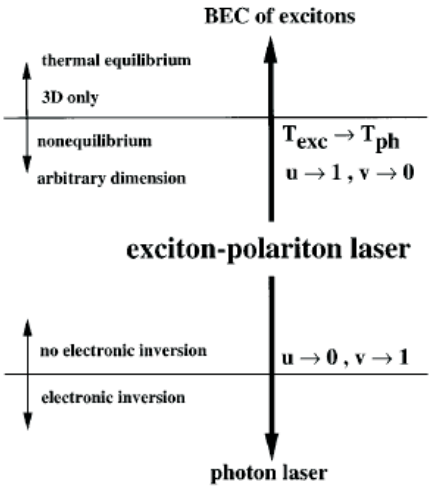

Figure 3.1 | Comparison of polariton and photon laser [107]: Diagram comparing the exciton-polariton laser to the more familiar concepts of Bose-Einstein condensate of excitons and photon lasers. u and v determine the exciton and photon character of the polariton, respectively.

3.1 Theory of exciton-polariton lasing in ZnO microcavities

3.1.1 Polariton laser

The concept of an exciton-polariton laser was first proposed by Imamoglu et al. 1996 [107] as a device that generates coherent optical waves using stimulated scattering of polaritons in their ground state. In previous works it was called *exciton boser*[82]. In contrast to conventional lasers, which are based on population inversion, this device of a new type is based on the natural properties of bosons to form a condensate, called Bose-Einstein condensate, and on the natural property of the condensate, namely, its coherence. Polaritons are, due to their bosonic character at low densities, a well-suited system to undergo such a phase transition and to form a condensate, which emits coherent light once the stimulated diffusion rate exceeds the spontaneous one. Beside the pure device-oriented interest, polaritons also raise the opportunity to study the fundamental properties of condensation phenomena. Exciton polariton lasing is a phenomenon which occurs between the full thermodynamic equilibrium, as it is the case for BEC of massive bosonic particles, such as Rb^{87} atoms, and the photon laser, which emits coherent light while being completely out of thermodynamic equilibrium. Fig. 3.1 illustrates this point of view. For a thermal equilibrium reservoir and a vanishing photon character of the exciton polaritons, one obtains a BEC of excitons. In the opposite limit of a nonequilibrium (inverted) reservoir and a vanishing exciton character, the polariton laser is indistinguishable from a photon laser.

To realize such a device the microcavity should be in the strong coupling regime – the coupling constant of light and excitons should be larger than all broadenings induced by

different effects. Especially, the temperature dependence of this broadenings limits the possible materials to those with huge exciton oscillator strength, if one is interested in high-temperature operation. Two of these materials, GaN and ZnO, have been in the focus of research for the fabrication of a polariton laser at room temperature as pointed out by Malpuech et al. and Zamfirescu et al. [80, 79].

Since the proposal and the works on huge oscillator strength materials, the interest of the physical community grows strongly: on one hand, optoelectronic devices, such as LED and semiconductor lasers, find a lot of applications nowadays. Polariton lasers or diodes could create a revolution in this field due to the reduced threshold and the economization of energy in the sense of low heating which could facilitate the on chip integration together with electronic devices and reduced consumption of power in portable devices. On the other hand, as mentioned above, the interesting fundamental physics can be easily studied within the polariton picture.

One of the main problems on the way towards polariton lasing is the bottleneck effect (see previous chapter). The relaxation of polaritons slows down in the steep part of the polariton dispersion. This effect can be suppressed working at high temperature which speed up the relaxation kinetic of polaritons. The second way is to go to positive detuning of the bare photon mode with respect to the bare exciton. The particles become more exciton like, which results in a increased lifetime and more efficient scattering processes due to a shallower dispersion. Thus the system is close to an quasi-equilibrium situation. In contrast, photonic-like polaritons accumulate in the steepest part of the dispersion and a bottleneck behavior is usually observed, which results in an out of equilibrium situation.

3.1.2 Strong coupling in ZnO

ZnO is an II-VI semiconductor with a direct dipole allowed band gap around 3.4 eV and a relatively large exciton binding energy of 60 meV. After a period of great interest in ZnO as a wide band gap semiconductor in the middle of the 20th century, the interest faded away partly due to huge problems to dope ZnO both n-type and p-type, partly because the interest moved to structures of reduced dimensionality, which were at that time almost exclusively based on the III-V systems. After a period of silence ZnO came again into the focus of research due to the possibility to grow i.e. epitaxial layers, quantum wells and nanorods, and due to a renewed hope to tap the full potential of its physical properties as a radiation hard material for blue/UV emitting lasers and other electronic and optoelectronic devices. A review on this topic is given by Klingshirn et. al [108]. Even the biggest problem to dope ZnO p-type has been overcome (for more information see Ref.[109, 110] and references therein).

Alongside, there has been a huge interest into coupled exciton-photon modes since their first observation in 1992 by Weisbuch et al. [3]. After the proposal of a polariton

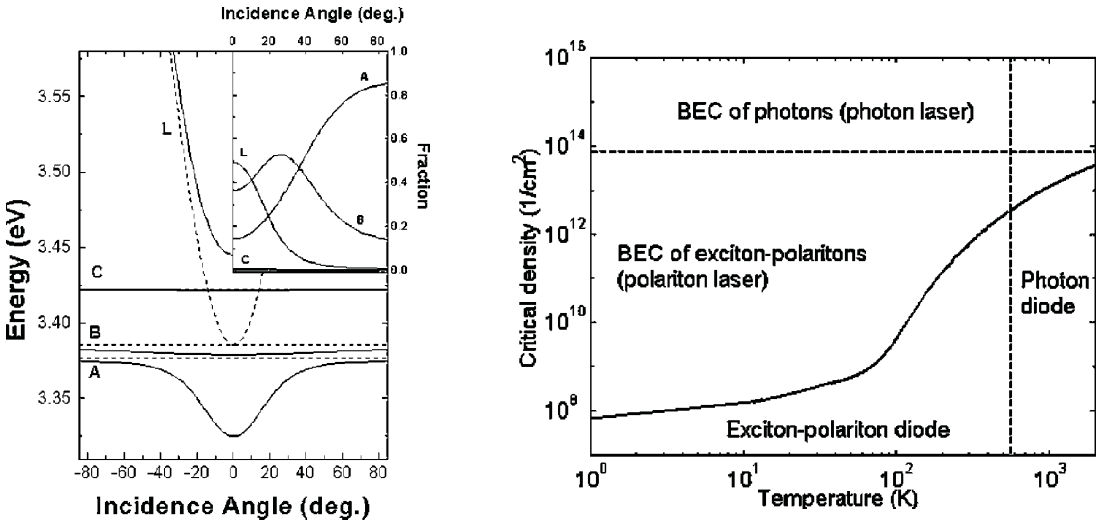

Figure 3.2 | Theoretical predictions for a ZnO polariton laser [79]: (left) Eigenenergies of the ZnO cavity modes versus the incidence angle. Dotted lines indicate the positions of the unperturbed modes: L indicates the light mode, and A,B,C indicate the A,B,C exciton resonances in ZnO, respectively. The inset shows the percentage of the excitonic components and the photonic component in the eigenmode of the lowest cavity-polariton state versus the inplane wave vector, (right) Exciton-polariton phase diagram in the ZnO microcavity . The solid line shows the polariton critical density versus lattice temperature. The vertical dashed line shows the exciton thermal dissociation limit. The horizontal dashed line shows the Mott transition for excitons.

laser [82] and experimental report about quasi-Bose-Einstein condensation in CdTe at low temperatures [22] the number of publications dealing with exciton-polaritons has significantly increased and the subject became a textbook topic [5, 6].

ZnO has been predicted to be one of the best candidates to observe polariton lasing at room temperature due to its huge exciton binding energy and its incredible oscillator strength [79] (the other possible candidate being GaN, studied theoretically in [111, 38]). Therein, the authors stress the giant Rabi splitting of more than 100 meV, which is two times larger than the Rabi splitting of GaN based microcavities. Fig. 3.2 shows the dispersion and the calculated phase diagram of a ZnO microcavity [79]. The three excitons in ZnO, labeled A, B, C, when coupled to a photonic mode, give rise to a complex dispersion with various polariton branches possessing different coupling properties as shown by the inset on the left hand side. The huge oscillator strength and the huge exciton binding energy could make exciton-polariton lasing possible up to more than 500 K, limited by the dissociation energy of the exciton with a binding energy about 60 meV.

While strong exciton-photon coupling and polariton emission have been observed experimentally for GaN [112, 113, 114] and finally the polariton lasing regime has been achieved [115, 26, 116], the strong coupling regime in ZnO is far away from being easy to

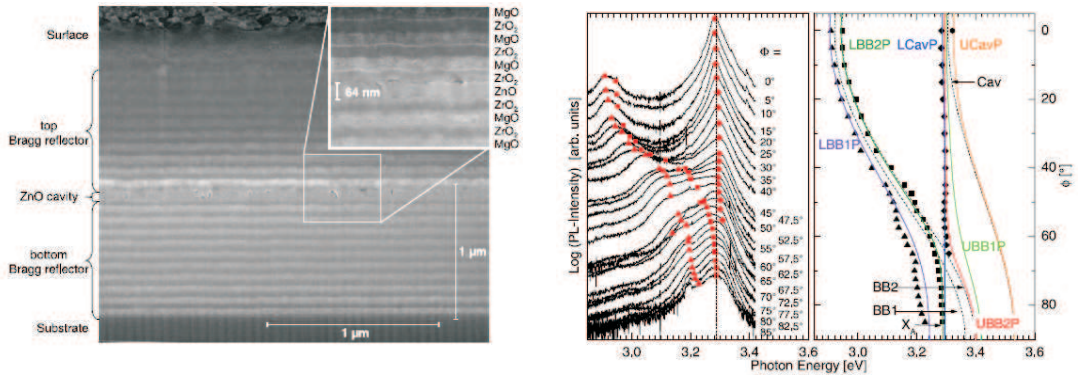

Figure 3.3 | Observation of strong exciton-photon coupling in ZnO microcavity [7]: (left) Sample structure containing a ZnO quantum well sandwiched by MgO/ZrO Bragg resonators. (right) Observed photoluminescence spectra for various excitation angles with the extracted and calculated dispersions for the different modes.

realize. Recently the first observations of strong exciton-photon coupling in ZnO based microcavities have been reported [117, 118, 7], which have confirmed that Ω close of 100 meV could indeed be achieved. Fig.3.3 shows the results of Ref.[7]. The authors use a Bragg resonator of the basis of MgO/ZrO which contains a $3\lambda/2$ ZnO active region. These are the first results using distributed all oxide Bragg reflectors, which are far from being optimal, but which should provide in principle much better reflectivity as for example AlO mirrors [119].

The observed photoluminescence spectra are shown on the left hand side of Fig.3.3. The three excitonic resonances result in a complicated dispersion with various branches with different coupling properties. The authors claim the observation of vacuum Rabi splittings up to 94 meV in these samples, which is the highest reported value except the organic structures [120, 121, 122].

However, the existing ZnO cavities are far from being optimal: they show broad lines due to inhomogeneous linewidth broadening and low quality factors of the confined optical mode. Additionally, due to the huge self absorption in ZnO, the upper polariton branch is almost invisible in the observed spectra. Nevertheless, first signatures of the mentioned advantages of ZnO microcavity strong coupling have been observed.

Also some alternative systems to planar microcavities based on ZnO technology, such as micropillars or microdisks, have allowed the observation of the strong coupling regime at RT [123].

The only theoretical work published so far on ZnO polariton laser [79] reports only the

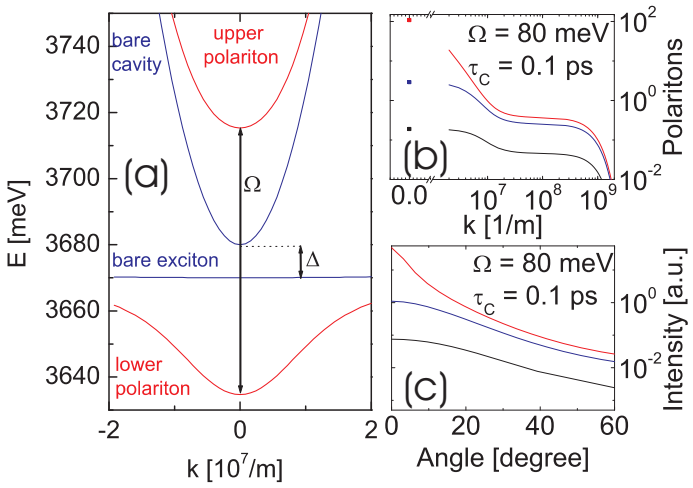

Figure 3.4 | Strong coupling in a bulk ZnO microcavity:(a) Polariton dispersion (red lines) of a ZnO microcavity with only one exciton mode. The blue lines correspond to the bare cavity and exciton mode. The Rabi splitting Ω and the detuning $\Delta = E_c(k = 0) - E_x(k = 0)$ (black arrows) are indicated. (b) Polariton distribution below (black) close above (blue) and far above threshold (red). (c) Emission intensity versus angle below (black) close above (blue) and far above threshold (red). Ω=80 meV and the cavity lifetime is 0.1 ps.

calculation of a phase diagram in the thermodynamic limit (see Fig. 3.2) which means that the finite polariton life time is neglected. Within this limit the larger value of Ω provides a lower threshold which in principle makes advantageous the use of ZnO, with respect to GaN. On the contrary taking into account finite particle lifetime and the relaxation process, a larger Ω means more energy to dissipate for a particle to reach the ground state from the excitonic reservoir. If this relaxation time becomes comparable or larger than the polariton life time, the polariton gas is not anymore at thermal equilibrium, which increases the threshold value which in this case is governed by kinetic limitations [27]. A good balance of the cavity parameters should therefore be found in order to optimize the compromise between these two limiting factors. The aim of this section is to analyze in detail these aspects giving the answers to the following questions: can we expect RT polariton lasing in ZnO based microcavities regarding the quality of the existing samples? Is there an advantage to use microcavities with a very large Ω?

3.1.3 Model and Simulation

In order to reply these questions we have simulated the polariton relaxation in a bulk ZnO microcavity using semi-classical Boltzmann equations. We calculate kinetic phase diagrams of the microcavity, showing the threshold dependence on crucial parameters, such as Ω, the quality factor of the cavity, and the detuning between the bare cavity and exciton mode. A special emphasis is put on the role and advantages of a large Ω.

We consider in our simulations a bulk ZnO cavity similar to the one of [7] but a $3\lambda/2$ ZnO layer. To simplify the picture we keep only the lower polariton branch (with a 2D density of states) and the five other calculated branches are modeled as an effective exciton reservoir (with a 3D density of states). Ω is treated as a external parameter. We

consider continuous off-resonant pumping with a laser spot of 6 μm radius. A typical polariton dispersion is shown in Fig.3.4(a), where also the meanings of the detuning Δ and of Ω are defined.

The polariton relaxation is described by solving a set of semi-classical Boltzmann equations. The general procedure for polaritons has been described in Ref.[5], and the specifics of bulk polariton lasers have been first accounted for in Ref.[11]. The equations read

$$\frac{dn_{\mathbf{k}}}{dt} = P_{\mathbf{k}} - \Gamma_{\mathbf{k}} n_{\mathbf{k}} - n_{\mathbf{k}} \sum_{\mathbf{k}'} W_{\mathbf{k}\to\mathbf{k}'}(n_{\mathbf{k}'}+1) + \tag{3.1}$$
$$+(n_{\mathbf{k}}+1)\sum_{\mathbf{k}'} W_{\mathbf{k}'\to\mathbf{k}} n'_{\mathbf{k}}.$$

Here n_k is the polariton distribution function and P_k is the pumping term. We consider a non-uniform grid in the reciprocal space. We assume that the off-resonantly pumped excitons are completely thermalized when they reach the reservoir. $W_{\mathbf{k}\to\mathbf{k}'}$ are the scattering rates between the states with corresponding wavevectors k and k'. $W_{\mathbf{k}\to\mathbf{k}'}$ includes exciton-phonon scattering rates $W^{ph}_{\mathbf{k}\to\mathbf{k}'}$, and exciton-exciton contribution which depends on the polariton distribution function: $\sum_{\mathbf{q}} W^{xx}_{\mathbf{k}\to\mathbf{k}',\mathbf{q}} n_{\mathbf{q}} (1 + n_{\mathbf{q}+\mathbf{k}'-\mathbf{k}})$, where $W^{xx}_{\mathbf{k}\to\mathbf{k}',\mathbf{q}}$ is the constant of exciton-exciton interaction for corresponding wavevectors. These rates are calculated using the Fermi golden rule taking the 3D matrix elements. We assume cylindrical symmetry of the reciprocal space, but the scattering processes with different directions of wavevectors are properly taken into account. The parameters used in the simulation are: exciton energy $E_x = 3.377$ eV, LO-phonon energy $E_{LO} = 72$ meV, exciton Bohr radius $a_b = 18$Å, effective electron mass $m_e = 0.24m$ and effective hole mass $m_h = 0.98m$,[124] where m is the free electron mass, deformation potential $D = 15$ eV [110], exciton lifetime $\tau_{ex} = 300$ ps [125], inhomogeneous broadening of 50 meV. The matrix element of the exciton-acoustic phonon interaction for any wavevectors is directly proportional to the deformation potential D. The dependences on Ω and on the detuning are less straightforward. Qualitatively, steeper dispersion is less favorable for scattering with acoustic phonons; for optical phonons it is the energy difference between the ground state and the exciton reservoir which plays the major role. For exciton-exciton scattering the strongest dependence is on the occupation numbers of the states.

The exciton density at threshold at room temperature is about $5 * 10^{16} cm^{-3}$, which is 4 times smaller than the Mott density for excitons. This confirms that the polariton lasing effect should indeed take place within the strong coupling regime.

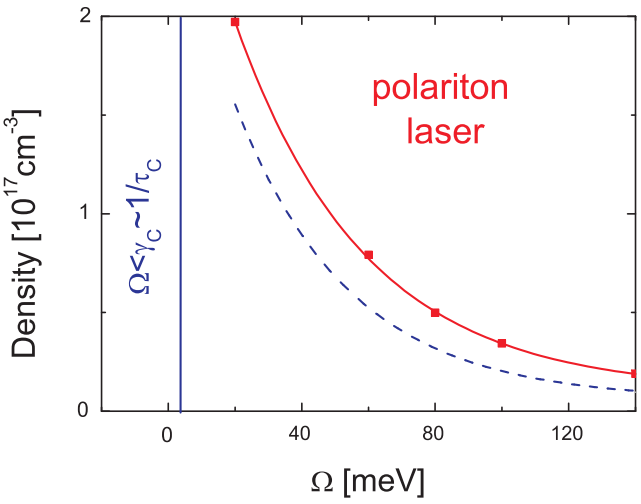

Figure 3.5 | Polariton relaxation and Rabi splitting: Kinetic lasing threshold density versus RAbi splitting Ω (red line, squares). The solid blue lines indicate the critical lifetime, where the strong coupling is lost, and the dashed blue line corresponds to the thermodynamic threshold (infinite lifetime approximation). The cavity lifetime is 0.1 ps.

3.1.4 Numerical results

Fig.3.4 (b) and (c) illustrate the dynamics of the relaxation process: (b) shows the polariton distribution versus wavevector k and (c) shows the angular emission of the cavity. There is no bottleneck effect [33] and the kinetic distribution function above threshold has a shape of a thermalized Bose-Einstein distribution . In the angular distribution (c) the emission intensity is broad below the threshold and becomes peaked around $k = 0$ above threshold.

In the following we want to focus on the crucial role of Ω and its influence on the threshold dynamics for polariton lasing. The results of the simulations are depicted in Fig.3.5. It shows the threshold polariton density versus Ω for a cavity lifetime of $\tau_c = 0.1$ ps ($Q \approx 500$) [7], and a detuning between the cavity mode and the exciton energy $\Delta = 0$. The vertical solid blue line delimits the range where the strong coupling is holding which is guaranteed by the condition $\Omega < \gamma_c = \hbar/\tau_c$. The dashed blue line shows the threshold density calculated in the thermodynamic limit (infinite particle lifetime approximation). The gap between the kinetic and the thermodynamic threshold is increasing versus Ω because the relaxation kinetics becomes slower. However this kinetic effect remains weak and for all the range of Rabi energies the system is operating close to thermal equilibrium. As a result the kinetic threshold value reduces 10 times between $\Omega = 20$ meV and $\Omega = 140$ meV.

The second crucial issue is the quality factor of the cavity, especially for ZnO based structures, for which perfect lattice-matched Bragg mirrors and high quality structures are still not available. Fig.3.6 shows the density of polaritons as a function of the cavity lifetime and the corresponding quality factor. We take Ω=80 meV and $\Delta = 0$ for all the calculations. The solid blue line again delimits the range of persistence of the strong coupling. The dashed blue line indicates the thermodynamic threshold density of polariton

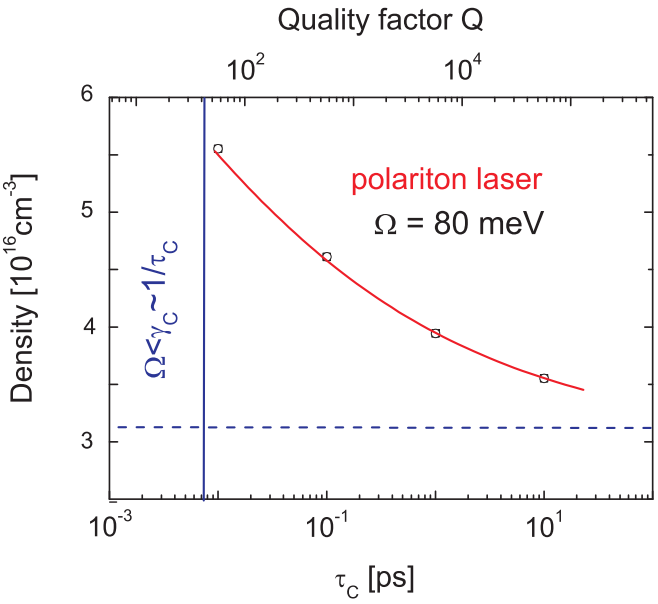

Figure 3.6 | Polariton relaxation and cavity lifetime: Kinetic lasing threshold density (red line, squares) versus cavity lifetime τ_C and the corresponding quality factor $Q = \omega_C/\Gamma$. The dashed blue line is the thermodynamic threshold density (infinite lifetime approximation).

lasing. The red line shows the kinetic threshold density which decreases versus Q up to the thermodynamic value for large quality factors. Actually, the decrease of the lasing threshold density is smaller than what one may expect. Of course, the increase of the quality would provide the polaritons a longer time to relax into the ground state because of the increased lifetime. But the excitonic reservoir does not change its properties and the relaxation to the bottleneck region is not affected. The relaxation towards the bottom of the dispersion in ZnO turns out to be good enough to thermalize the polaritons even at relatively short lifetimes. All this together makes the influence of the cavity quality factor on the lasing threshold density for ZnO smaller than one could expect.

To underline the advantage of large Ω we calculate the threshold density versus Ω and detuning, keeping the value $(\Omega - \Delta)$ constant. Indeed one may think that a deep polariton trap could be obtained with a small Ω but working at negative detuning. The results of the kinetic simulations are shown in Fig.3.7(a) together with the infinite life time limit. The kinetic threshold is found to decay three times between the small and the large Ω limit.

In the small Ω case, the difference between the kinetic and thermodynamic threshold is almost one order of magnitude which means that the system is not in thermal equilibrium with the lattice. For such a geometry, the polariton is mostly photon-like having a small effective mass, which reduces the scattering rates toward the ground state. The polariton life time is shorter for the same reason. The combination of slow scattering and of a short life time is responsible for a relaxation bottleneck effect, which increases the threshold density.

For large Ω values and positive detunings, the situation is reversed. The polariton

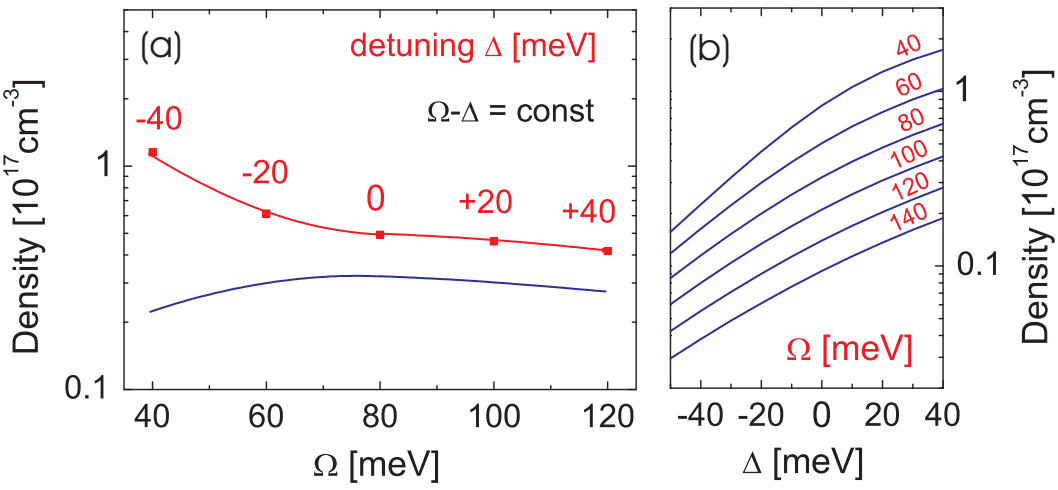

Figure 3.7 | Polariton relaxation and detuning: (a) Lasing threshold density (squares) versus Ω for various detunings Δ (red numbers). The thermodynamic threshold density is plotted as blue line. The cavity lifetime is 0.1 ps and the value $(\Omega - \Delta)$ is kept constant. (b) Thermodynamic threshold density versus detuning for various Ω (red numbers).

is mostly excitonic with a larger effective mass and longer life time than for negative detuning and small Ω, which allows the achievement of a quasi-equilibrium situation where the kinetic and thermodynamic thresholds become very close to each other. To complete the picture, Fig.3.7(b) illustrates the dependence of the thermodynamic threshold on the detuning for different Ω. In this limit one can reduce the threshold by going to negative detunings, which contrasts with the kinetic simulations results.

The results can also be translated to the general case independent of the cavity material: large Rabi splittings and positive detuning improve the lasing threshold of polariton device due to the improved relaxation process. In contrast, negative detunings make the polaritons more photonic, which decreases the scattering rates, and thus the operation close to a quasi-equilibrium is not possible. All this make the use of large Rabi splitting materials much more attractive for lasing devices.

3.1.5 Conclusions

To conclude, we have determined the polariton lasing threshold of bulk ZnO microcavities using the semiclassical Boltzmann equations. We have shown that the cavity quality factor values experimentally measured in these systems are good enough to observe room temperature polariton lasing. We have also analyzed the impact of the extremely large exciton oscillator strength of ZnO giving rise to Ω up to 100 meV. We have shown that such

large values allow to decrease the polariton lasing threshold and facilitates the formation of a quasi-thermal equilibrium for the polariton gas, that is, the achievement of polariton Bose Einstein condensation at room temperature - a phenomenon of strong scientific interest.

Our results for the discussed ZnO microcavity can be extended to the general case: the relaxation simulations show clearly, that huge Rabi-splittings are much more advantageous for the relaxation process because situations close to thermodynamic equilibrium can be realized. Small splittings and, in addition, negative detunings lead to an increased lasing threshold, due to the diminution of the excitonic component of the lower polariton branch. This excitonic component governs the scattering processes and increases the lifetime, so that scattering events are more probable and the polaritons can relax easier to lower energies.

3.2 Polaritonic analog of the Datta and Das spin transistor

As mentioned before, the condensates and the spin structure of polaritons lead to various analogies with electronic systems. In the following we will develop the idea of a polaritonic Spin transistor, which works very close to the scheme of the electronic exemplar invented by Datta and Das (1990) [126], which will be presented in the next section. In this framework, another effect, which came basically from superconductor physics and was transformed to polariton condensates, called spin-Meissner effect [66], will be used.

3.2.1 Electronic Datta and Das spin transistor

Spintronics is one of the trends in modern mesoscopic physics [127]. It was born in 1990, when S. Datta and B. Das in their pioneer work proposed a theoretical scheme of the first spintronic device [126], which afterwards was named Datta and Das spin transistor. It consists of two ferromagnetic 1D or 2D electrodes, usually with collinear magnetizations, separated by a non-magnetic semiconductor region in which a Spin-Orbit Interaction (SOI) of the Rashba type is induced by a top gate electrode,

$$\widehat{H}_{SOI} = \alpha \left[\widehat{\mathbf{k}} \times \sigma\right] \cdot \mathbf{e}_z, \tag{3.2}$$

where $\mathbf{e}_z$ is a unity vector in the direction of the structure growth axis z, σ denote a set of Pauli matrices, $\widehat{\mathbf{k}} = -i\nabla$. α is a characteristic Rashba parameter, which depends on the degree of asymmetry of a quantum well (QW) in the z-direction. It can be efficiently tuned by varying the top gate voltage V_g [128, 129, 130]. The Hamiltonian can be interpreted in terms of an effective magnetic field lying in the plane of a QW and being perpendicular

to the carrier's kinetic momentum. This effective field provokes the rotation of the spin of the carriers in the semiconductor region and results in the oscillations of the transmitted current I_{tr} as a function of Rashba coupling controlled by the gate voltage V_g [131]:

$$I_{tr} \sim \cos^2\left(2m_{\text{eff}}\alpha L/\hbar^2\right), \tag{3.3}$$

where m_{eff} is the carrier effective mass in the semiconductor. The above formula has a very clear physical meaning: only the spin component parallel to the magnetization can propagate in the outgoing ferromagnetic lead. The outgoing current should be proportional to the rotation angle accumulated over a distance L between the two leads, $\Delta\phi = 2m_{\text{eff}}\alpha L/\hbar^2$.

Although the scheme of the Datta and Das spin transistor seems very simple from a theoretical point of view, due to the problems of spin injection and decoherence its practical implementation appears to be extremely complicated. More than 15 years of intensive experimental work in this direction did not result in any breakthrough, and the Datta and Das device still remains a theoretical concept.

On the other hand, it was recently proposed that in the domain of mesoscopic optics the controllable manipulation of the (pseudo)spin of excitons and exciton-polaritons can provide a basis for the construction of optoelectronic devices of the new generation, called spin-optronic devices [132], that would be the optical analogs of spintronic devices. The first element of this type, namely polarization-controlled optical gate, was recently realized experimentally [133], and the principal schemes of other devices (Berry phase interferometer [65], polariton neuron [134] etc.) were theoretically proposed.

Exciton polaritons (or cavity polaritons) are the elementary excitations of semiconductor microcavities in the strong coupling regime. An important peculiarity of the polariton system is its spin structure: being formed by bright heavy-hole excitons, the lowest energy polariton state has two allowed spin projections on the structure growth axis (± 1), corresponding to the right and left circular polarizations of the counterpart photons. The states having other spin projections are split-off in energy and normally can be neglected while considering polariton dynamics. Thus, from the formal point of view, the spin structure of cavity polaritons is analogical to the spin structure of electrons (both are two-level systems), and their theoretical description can be carried out along similar lines. The possibility to control the spin of cavity polaritons opens a way to control the polarization of the light emitted by a cavity, which can be of importance in various technological implementations including optical information transfer.

It should be noted, however, that the fundamental nature of elementary excitations is different in two kind of systems: electrons and holes (i.e. fermions) in the case of spintronics, exciton polaritons (i.e. bosons) in the case of spin-optronics. Also, it appears that the account of many-body interactions is of far greater importance for spinoptronic devices

with respect to the spintronic ones. The polariton-polariton interactions in microcavities are strongly spin-anisotropic: the interaction of polaritons in the triplet configuration (parallel spin projections on the structure growth axis) is much stronger than that of polaritons in the singlet configuration (antiparallel spin projections)[4]. This leads to a mixing of linearly polarized polariton states which manifests itself in remarkable nonlinear effects in polariton spin relaxation, such as self-induced Larmor precession and inversion of linear polarization upon parametric scattering [135], polarization multistability [136], and others, which are of great importance for the functioning of spinoptronic devices in nonlinear regime.

3.2.2 Spin Meissner effect

Polariton have some peculiarities in the presence of a magnetic field. Additionally to the TE-TM splitting (not discussed in the present thesis), which has an effect of an effective magnetic field, polariton condensates show the so called spin Meissner effect, which will be discussed in the following section and which will be the most important effect for the polariton analog of a Datta-Das Transistor. The properties of a polariton condensate are substantially different from a spinless Bose condensate. Moreover, an applied magnetic field B changes drastically the excitation spectrum of the system and can completely suppress the superfluidity. The effect is described briefly and the interested reader should address the original paper of Rubo et al. [66]. Exciton-polariton condensate in a semiconductor microcavity are strongly sensitive to the external magnetic field normal to the cavity plane. In particular, the superfluidity is suppressed at a critical magnetic field B_c proportional to the polariton concentration n:

$$B_c = \frac{n(\alpha_1 - \alpha_2)}{\mu_B g}, \tag{3.4}$$

where μ_B is the Bohr magneton and g is the electron g-factor. The parameters α_1 and α_2 are the interaction constants of polaritons with the same or perpendicular polarization.

One can now distinguish two different regimes, depending on the magnetic field:

1. $B < B_c$: In this range, the Zeemann splitting is fully compensated by the polariton-polariton interactions in the elliptically polarized condensate. After some algebra (see. Ref. [40]) one obtains for two Bogoliubov dispersion branches (see appendix for the detailed calculation):

$$\omega_{\pm}^2 = \omega_0^2 + \omega_0 n \left[\alpha_1 \pm \sqrt{\alpha_2^2 + (\alpha_1^2 - \alpha_2^2)\frac{B^2}{B_c^2}} \right], \omega_0 = \frac{k^2}{2m}. \tag{3.5}$$

The energy of the excitations is now given by $E_{\pm} = \mu + \omega_{\pm}^2$. One can see that both branches start at the same point at $k = 0$, which corresponds to the bottom of the

lowest polariton band blue-shifted by the chemical potential, so that the Zeeman splitting turns out to be fully suppressed in this regime. Note also that two branches of quasiparticles are elliptically polarized (see appendix and the following section).

2. $B > B_c$: The spectrum of excitations is qualitatively different from the small magnetic field domain. The condensate is now circularly polarized. In this case, there remains only one Bogoliubov-like branch with an independent of magnetic field dispersion

$$\omega_+^2 = \omega_0^2 + 2\omega_0 n\alpha_1. \tag{3.6}$$

The quasiparticles belonging to this branch have the same circular polarization as the condensate. The quasiparticles with the opposite circular polarization form a parabolic branch blueshifted with respect to the condensate by a value proportional to $(B - B_c)$,

$$\omega_- = \mu_b g(B - B_c) + \omega_0. \tag{3.7}$$

Once again the energies of the excitations are $E_\pm = \mu + \omega_\pm^2$. The two branches are split by an effective Zeemann splitting.

The two branches of excitation spectrum can be characterized by the long-wavelength sound velocity

$$v_\pm = \left.\frac{d\omega_\pm}{dk}\right|_{k=0}. \tag{3.8}$$

In the weak field regime one has now two sound velocity branches. In the strong field regime one of the sound velocities is zero.

This is shown in Fig.(3.8) for the energies at $k = 0$. The suppression of the Zeeman splitting, illustrated in the inset, is clearly seen for magnetic fields smaller than the critical one. Weak magnetic fields make the polariton condensate elliptically polarized and slow down the speed of sound for one of two excitation branches in the system. The exact expression of the polarization vector is given in the following section and is derived in the appendix. The speed of sound vanishes and the polariton superfluidity is suppressed at the critical magnetic field B_c proportional to the population of the condensate. At the critical field the polarization of the condensate becomes fully circular. The polariton condensates exhibit an anomalous Zeeman splitting, which is equal to zero below the critical field and linearly depends on the field at $B > B_c$. The magnetic susceptibility of the system is discontinuous at the critical field at zero temperature.

3.2.3 Polaritonic Datta and Das Spin transistor

As shown in [65], the analog of Rashba SOI in microcavities can be provided by the longitudinal-transverse splitting (TE-TM splitting) of the polariton mode. However, the

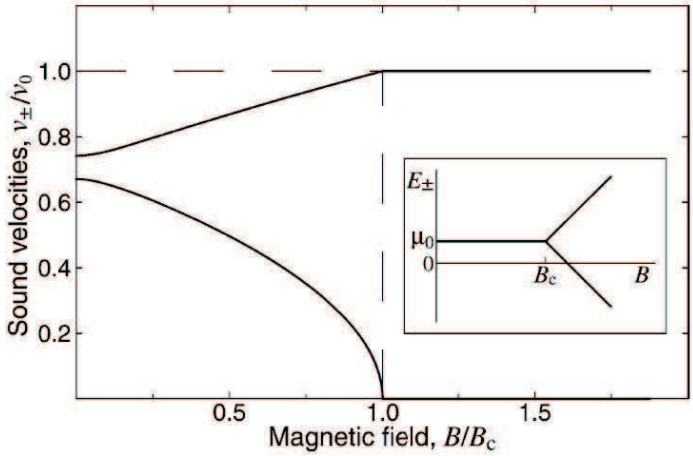

Figure 3.8 | Spin Meissner Effect [66]: The dependence of the long-wavelength sound velocities of excitations of polariton condensate on the applied magnetic field. The Zeeman splitting at k = 0 is shown in the inset.

TE-TM splitting cannot be easily tuned by the simple application of a voltage, unlike the Rashba SOI. The control of the polariton Berry phase therefore requires to modulate an external magnetic field, which is expected to be relatively slow.

In principle, the analog of Rashba SOI in microcavities is provided by the longitudinal-transverse splitting (TE-TM splitting) of the polariton mode. It is well known that due to the long-range exchange interaction between the electron and the hole, for excitons having non-zero in-plane wavevectors the states with dipole moment oriented along and perpendicular to the wavevector are slightly different in energy [64]. In microcavities, the splitting of longitudinal and transverse polariton states is amplified due to the exciton coupling with the cavity mode and can reach values of about 1 meV [137].

We propose to use as analogous of the Rashba field, not the TE-TM splitting, but the change of the polarization eigenstates induced by the formation of polariton Bose Einstein condensate in the presence of magnetic field. In that case the modulation of the signal will be driven, not by the modulation of the magnetic field, but by the modulation of the condensate density, which can be achieved either by the modulation of a pumping laser intensity, or by the modulation of a voltage in case of electrically driven condensate [138, 139, 140, 11].

The device is constituted by a planar microcavity showing a confining potential having the shape of a stripe of width L as shown on the upper panel of the Fig.(3.9)),

$$U = \begin{cases} -U_0 & , 0 < x < L \\ 0 & , x < 0, x > L \end{cases} \tag{3.9}$$

We divide the system into three regions: (1) $x < 0$, (2) $0 < x < L$ and (3) $x > L$. We assume that critical conditions for the formation of a quasi-equilibrium BEC of polaritons are fulfilled [22]. We also assume that the chemical potential μ stands below the edge of the barriers, so that the condensate is confined in the central region and absent in the flanking regions.

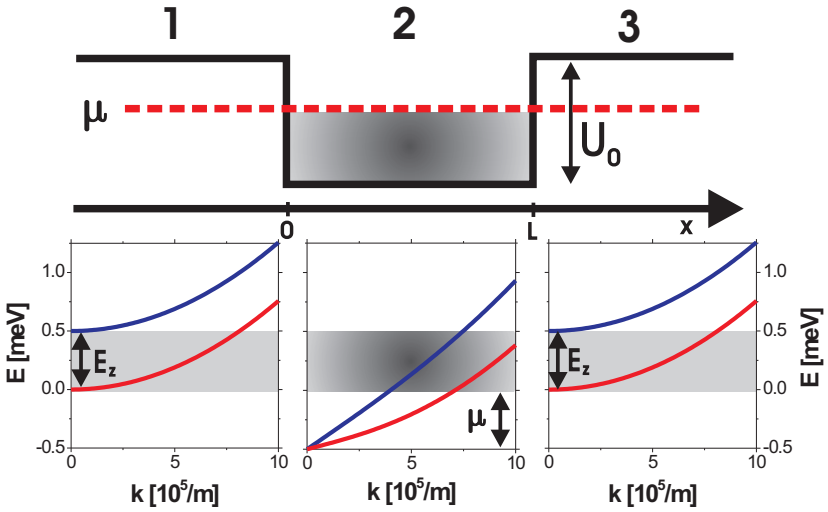

Figure 3.9 | Polaritonic analogue of Datta and Das spin transistor: Schematic illustration of a polariton spin transistor (upper panel) with the corresponding renormalized polariton dispersions (lower panel). The regions are indicated with 1 ($x < 0$), 2 ($0 < x < L$) and 3 ($x > L$). Dark gray (blue) corresponds to σ_- and light gray (red) for σ_+ polarization. In region 2 the mixing of both circular polarizations results in an elliptical polarized condensate, while in flanking regions only the σ_+ component can propagate.

We consider the effect of an external magnetic field B applied perpendicularly to the structure interface. In the lateral regions 1 and 3, the normal Zeeman splitting E_z between the polariton modes occurs as shown in the lower panel of the fig 1. This opens an energy gap $E < E_z = \mu_b g B$ where only one of the two circularly polarized component can propagate. We assume here, and in the following that the Zeeman splitting is much larger than the TE-TM splitting which can therefore be neglected. In the central region however, the presence of the condensate leads to the so-called spin Meissner effect [66]. For a given field B, the critical density n_c in the polariton condensate can be defined as

$$n_c = \mu_b g B/(\alpha_1 + \alpha_2), \tag{3.10}$$

where $\alpha_{1(2)}$ are the interaction constants for particles with the same (perpendicular) spin projection, g is the exciton g-factor and μ_b is the Bohr magneton. Above this critical density n_c, the spin anisotropy of the polariton-polariton interactions leads to a full paramagnetic screening of the Zeeman splitting E_Z resulting in a quenching of the Zeeman gap, as shown in the lower part of the Fig.3.9. This effect is what is called the spin Meissner effect. The polariton condensate is elliptically polarized, which is also the case for the propagative modes in the central region. The polarization degree of these modes depends on the condensate density. Therefore a circularly polarized σ_+ pulse with an energy located within the Zeeman gap of the lateral regions can enter into the central region.

During its propagation in this region its polarization vector will be rotated by an effective magnetic field whose direction is associated with the polarization of the eigenstates in this region. This effective "spin-Meissner field" has some in-plane component and plays the role of the Rashba SOI effective field. The intensity of the outgoing current depends on the angle $\Delta\phi$ between the pseudospin vector of a polariton reaching the outgoing lead. If the precession is so that the pulse becomes fully σ_- polarized on the interface between 2 and 3, the pulse will be fully reflected. If the pulse is fully σ_+ polarized, it will be fully transmitted. Working in this energy range means that for polaritons we create a situation analogical to ferromagnetic-nonmagnetic- ferromagnetic interface, which one needs for a creation of the Datta and Das device.

Such a configuration has a number of possible advantages with respect to classical spintronics: the dramatic impact of carrier spin relaxation or decoherence, which has severely limited the achievement or the functionality of any semiconductor-based spintronic devices, is strongly reduced [141]. Besides, the solution of spin injection problem is now trivial: it is performed simply by choosing an appropriate polarization of the exciting laser.

3.2.4 Model

Quantitatively the outgoing amplitude can be calculated by solving a system of linear equations. The wavefunctions of a propagating mode in the three regions can be written in the following way:

$$\Psi_1 = (e^{ikx} + re^{ikx}) \begin{pmatrix} 1 \\ 0 \end{pmatrix} + Ae^{\gamma x} \begin{pmatrix} 0 \\ 1 \end{pmatrix}, \tag{3.11}$$

$$\begin{aligned} \Psi_2 = &(C_1^+ e^{ik_1 x} + C_1^- e^{-ik_1 x}) \begin{pmatrix} cos\beta_+ \\ sin\beta_+ \end{pmatrix} + \\ &+(C_2^+ e^{ik_2 x} + C_2^- e^{-ik_2 x}) \begin{pmatrix} cos\beta_- \\ sin\beta_- \end{pmatrix}, \end{aligned} \tag{3.12}$$

and

$$\Psi_3 = (te^{ikx}) \begin{pmatrix} 1 \\ 0 \end{pmatrix} + De^{\gamma x} \begin{pmatrix} 0 \\ 1 \end{pmatrix}, \tag{3.13}$$

where r is the amplitude of reflectivity, t is is transmission amplitude, $C_{1,2}^{+(-)}$ are the complex amplitudes of forward (backward) running waves in the trap with different polarization and wavevector k_1 and k_2. The wavevectors are determined by the dispersion relations for each region Ref.[66], which read:

$$k = \sqrt{\frac{2m}{\hbar^2}(E)} \tag{3.14}$$

$$\gamma = \sqrt{\frac{2m}{\hbar^2}(E_z - E)} \tag{3.15}$$

$$k_1 = \sqrt{\frac{m}{\hbar^2}(-n_2 U_+ + \sqrt{4E_{eff}^2 + n_2^2 U_-^2})} \tag{3.16}$$

$$k_2 = \sqrt{\frac{m}{\hbar^2}(-n_2 U_- + \sqrt{4E_{eff}^2 + n_2^2 U_+^2})} \tag{3.17}$$

with $E_{eff} = E - \mu$ and

$$U_\pm = \alpha_1 \pm \sqrt{\alpha_2^2 + (\alpha_1^2 - \alpha_2^2)\left(\frac{B}{B_C}\right)^2}. \tag{3.18}$$

The polarization of the excitations in region 1 and 3 is σ_+ and σ_-. The polarization of the elementary excitations of the condensate in the Spin-Meissner phase (region 2) have never been calculated. They can be found by the standard method of linearization with respect to the amplitude of the elementary excitations of the condensate and can be written as follows:

$$\begin{pmatrix} cos\beta_\pm \\ sin\beta_\pm \end{pmatrix}, tan\beta_\pm = \frac{-\alpha_1 cos2\Theta \pm \sqrt{\alpha_1^2 cos^2 2\Theta + \alpha_2^2 sin^2 2\Theta}}{\alpha_2 sin2\Theta}, \tag{3.19}$$

where $\Theta = 1/2 arcsin\sqrt{1-(B/B_C)^2}$.

Interestingly, the polarization of the excitations, associated with the angle Θ are different from the one of the condensate associated with the angle β. The Spin-Meissner effective field is directed along $(cos\beta_-, sin\beta_-)$, with an amplitude

$$\Omega_t = \frac{E}{2\hbar}\frac{k_1^2 - k_2^2}{k_1 k_2}. \tag{3.20}$$

To find the amplitude of the outgoing beam one has different possibilities. Using an analytical approach close to the transfer matrix method, one obtains for the reflected amplitudes r and transmitted amplitude t

$$t = e^{ik_1 L}\cos^2\beta_+ + e^{ik_2 L}\sin^2\beta_+ + \tag{3.21}$$

$$+\frac{\left[\cos\beta_+ \sin\beta_+ \left(e^{ik_1 L} - e^{ik_2 L}\right)\right]^2 \left[\sin^2\beta_+ e^{ik_1 L} + \cos^2\beta_+ e^{ik_2 L}\right]}{1 - \left[\sin^2\beta_+ e^{ik_1 L} + \cos^2\beta_+ e^{ik_2 L}\right]^2} \tag{3.22}$$

$$r = \frac{\left(\left[e^{ik_1 L} - e^{ik_2 L}\right]\cos\beta_+ \sin\beta_+\right)^2}{1 - \left[\sin^2\beta_+ e^{ik_1 L} + \cos^2\beta_+ e^{ik_2 L}\right]^2}. \tag{3.23}$$

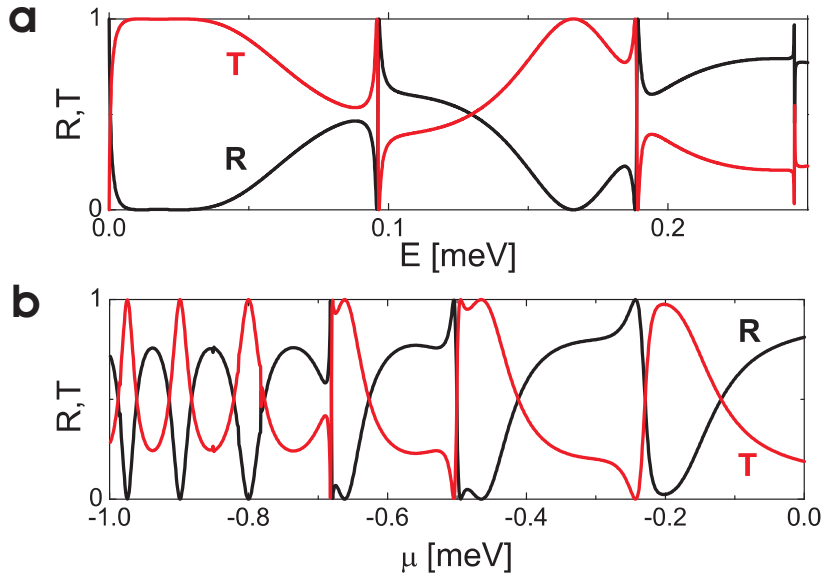

Figure 3.10 | Reflection and transmission coefficient versus energy of the probe pulse and chemical potential: (a) Dependence of T (red) and reflection coefficient R (black) on the excitation energy E ($\mu = -0.7$ meV) and (b) T and R versus chemical potential μ ($E = 0.2$ meV). The used parameters are: $B = 5$ T, $E_Z = 0.25$ meV, $L = 20\mu$ m, and $U_0 = -1$ meV.

In this analytical approach σ_- polarized part is fully reflected and can not escape and decay from the central region. Thus the results (not shown) from this analytical approach reflect not the real life.

A more exact approach is to use the wave-functions (Eqs. (3.11)-(3.13)) and boundary conditions, which ensure the continuity of the wave-function and current conservation at the interfaces. The system of equations, which has to be solved reads as follows:

$$\begin{aligned} \Psi_1(0) &= \Psi_2(0) \\ \Psi_3(L) &= \Psi_2(L) \\ \hat{v}_1\Psi_1(0) &= \hat{v}_2\Psi_2(0) \\ \hat{v}_3\Psi_3(L) &= \hat{v}_2\Psi_2(L), \end{aligned} \tag{3.24}$$

where the operators $\hat{v}_i$ can be found from Heisenberg's equation of motion assuming simply linear dispersions in the central region:

$$\hat{v}_{1,3} = \frac{i\hbar}{m}\frac{d}{dx}, \hat{v}_2 = V_{k_1,k_2}. \tag{3.25}$$

The system of equations is solved numerically and the transmission and reflection coefficients defined as $T = |t|^2, R = |r|^2$.

Fig.3.10 shows the dependence of the transmission coefficient $T = |t|^2$ and reflection coefficient $R = |r|^2$ on the excitation energy E (a) and on the chemical potential of the condensate μ (b). The polarization of the particles is rotated during the propagation in region 2 with elliptically polarized excited states. The calculation is performed taking into account realistic parameters of a GaAs microcavity. Varying the energy of the injected particles, which can be done by change the excitation -angle of the resonant laser,

increases or decreases the value of the Spin-Meissner effective field affecting the particle propagation in the central region. Another way to modulate the outgoing beam keeping the particle energy constant (close to the resonances on Fig.3.10(a)), is to change the particle concentration (and thus the chemical potential μ) in region 2. This can be simply realized by the modulation of the optical or electrical pumping of the condensate. The impact of the particle concentration is shown in Fig.3.10(b). Close to the resonances, the outgoing beam drops from full transmission to zero transmission for a very weak change of μ. This gives a possibility to tune rapidly the outgoing current of the proposed device simply by changing one external parameter.

Of course the outgoing intensity can also be modulated by the magnetic field, but the change of the magnetic field intensity is rather slow in comparison to intensity modulation of a pumping laser or to modulation of the applied voltage (in case of electrical pumping). From the point of view of experimental realization, increasing the magnetic field enlarges the Zeemann splitting and the energy range where only one polarization component can propagate outside the condensate. Thus, on one hand it should be preferable to apply a huge magnetic field in order to increase the operating energy range. On the other hand, high magnetic fields complicate the practical applications.

3.2.5 Gross-Pitaevskii based simulations

We have also performed a realistic numerical simulation of the device operation. We have first calculated the wavefunction of the condensate in the trap region by minimizing the free energy (equation 3.26) of the system on a grid, as in Ref. [142], taking into account the two polarization components and the interactions between them. All the parameters are taken the same as in the previous formulas.

$$F = \int dr \left(\frac{\hbar^2}{2m} \left(\Psi_+^* \Delta \Psi_+ + \Psi_-^* \Delta \Psi_- \right) + U \left(|\Psi_+|^2 + |\Psi_-|^2 \right) \right. \\ \left. + \frac{\alpha_1}{2} \left(|\Psi_+|^4 + |\Psi_-|^4 \right) + \frac{E_Z}{2} \left(- |\Psi_+|^2 + |\Psi_-|^2 \right) \right) \tag{3.26}$$

We have then simulated the propagation of a circularly polarized pulse through the system with the spinor Gross-Pitaevskii equation for polaritons using the wavefunction of the condensate found previously. The main difference with the analytical model presented above is the spatial profile of the wavefunction of the condensate; this difference becomes negligible at larger densities, when the interaction energy is much higher than the kinetic one. Another difference is that we consider pulse propagation, more important from the practical point of view, instead of solving a steady-state problem.

Figure 3.11 shows the snapshots of the pulse propagation through the device. Only the wavefunction of the pulse is shown, without the condensate, which is located in the

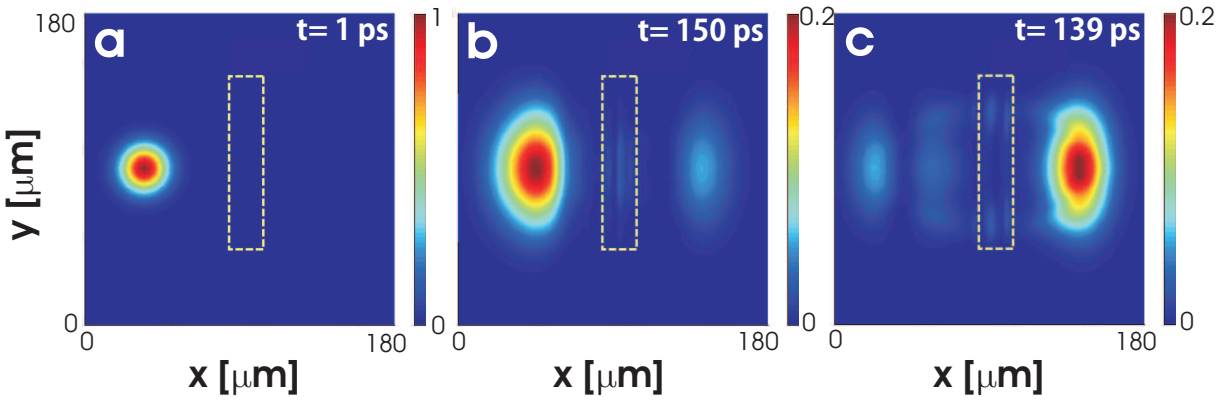

Figure 3.11 | Propagation of a wavepacket through the spin transistor: (a) wavepacket created by a laser pulse; (b) wavepacket reflected by the condensate; (c) wavepacket transmitted almost without reflection.

trap shown by the rectangle. Panel (a) shows the initial state: a Gaussian wavepacket is created by a short laser pulse to the left of the trap with the condensate. Panels (b,c) show the system after the wavepacket has interacted with the condensate: in (b) the packet is mostly reflected, whereas in (c) a larger part passes through. The two latter panels correspond to two different regimes of the transistor operation depending on the condensate density: closed (b) and open (c). The broadening of the wavepacket is due to the interaction with the condensate; however this relatively small broadening should not be detrimental for the device.

3.2.6 Conclusions

In conclusion, we proposed a scheme of a polaritonic analog of Datta and Das spin transistor. The proposed geometry allows to solve the problems of decoherence and inefficient spin injection which were blocking the experimental realization of Datta and Das spin transistor for electrons.

3.3 Chaotic Josephson oscillations of polaritons

3.3.1 Josephson effect of excitons and polaritons

Polaritons are two dimensional objects. Thats why, strictly speaking Bose-Einstein condensation is forbidden in such systems. The 2D objects need to be confined in a potential trap to undergo phase transitions such as BEC. The latter can appear due to the intrinsic lateral photonic disorder in a cavity [22] or can be created in a controllable way by external laser beams, by application of stress [24], or by using photolithographic techniques. The

possibility of engineering the confinement of the condensates allows to study the Josephson effects for excitons and polaritons, related to the tunneling between two condensates possessing macroscopic phase coherence. The Josephson effect was first predicted [143] and experimentally observed [144, 145] for two superconductors separated by a thin insulator layer. Also realizations with superfluid helium [146] and cold atomic condensates [147] have been reported in recent years.

The crucial property of the condensates of cold atoms and the condensates of excitons and polaritons, as compared to the superconductors, is the interaction between the tunneling particles. This leads to the striking nonlinear effects in Josephson dynamics, such as anharmonicity of the Josephson oscillations [148] and macroscopic quantum self-trapping (MQST) in the case when the initial imbalance between the two condensates exceeds some critical value [149, 150].

In the following we will present briefly the predictions of Shelykh at al. [151] for the Josephson effect of exciton-polaritons, which will be the basic effect used to observe the chaotic oscillations. The interested reader should address the original paper for a more detailed description.

The model Hamiltonian for interacting bosons with pseudospin confined in two traps (R and L), which is the starting point of the description, reads as follows:

$$\begin{aligned} H \quad &= E \sum_{i=R,L;\sigma=\uparrow,\downarrow} c^{\dagger}_{i\sigma} c_{i\sigma} + J \sum_{\sigma=\uparrow,\downarrow} \left(c^{\dagger}_{L\sigma} c_{R\sigma} + c^{\dagger}_{R\sigma} c_{L\sigma} \right) + \\ &+ \Omega \sum_{i=L,R} \left(c^{\dagger}_{i\uparrow} c_{i\downarrow} + c^{\dagger}_{i\downarrow} c_{i\uparrow} \right) + \frac{\alpha_1}{2} \sum_{i=L,R;\sigma=\uparrow,\downarrow} c^{\dagger}_{i\sigma} c^{\dagger}_{i\sigma} c_{i\sigma} c_{i\sigma}. \end{aligned} \tag{3.27}$$

The first term corresponds to free particles, the second term describes the spin-conservative tunneling of particles between the two traps, and the third term describes the possibly existing anisotropy of the QW (in the direction of the structure growth-axis), which is equivalent to the application of an effective in-plane magnetic field able to provoke spin-flip processes. The last term of the Hamiltonian corresponds to the interactions between particles. The interactions between particles situated in different traps and particles having opposite circular polarizations are neglected. The system with all coupling constants is schematically shown in Fig.3.12.

The coupling constant J can be written

$$J \approx 4V e^{-\hbar^{-1}\sqrt{2mV}D}, \tag{3.28}$$

where V is the well deepness, and D is the interwell distance. The interaction constant $U \approx E_B a_B^2/S$ and Ω has been determined experimentally in the range of $50 - 100\mu$ eV.

The dynamic equations can be obtained by means of Heisenberg's equation of motion,

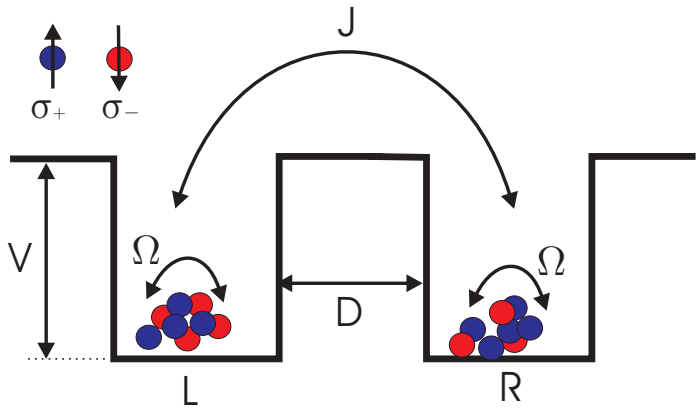

Figure 3.12 | Model system for the Josephson effect of exciton polaritons: Ω is the coupling of particles in one well with different polarization, J is the coupling of particles with the same polarization but in different wells, D is the interwell distance and V the potential depth. L and R are the indices for the two wells.

neglecting here all dephasing effects. The resulting coupled 4 equations for the order parameter read as follows:

$$\begin{aligned} i\hbar\frac{d\psi_{L\sigma}}{dt} &= (E+\alpha_1\left|\psi_{L\sigma}\right|^2)\psi_{L\sigma}+J\psi_{R\sigma}+\Omega\psi_{L,-\sigma} \\ i\hbar\frac{d\psi_{R\sigma}}{dt} &= (E+\alpha_1\left|\psi_{R\sigma}\right|^2)\psi_{R\sigma}+J\psi_{L\sigma}+\Omega\psi_{R,-\sigma}. \end{aligned} \tag{3.29}$$

One can distinguish now two different cases, when either J or Ω is equal to zero:

- *extrinsic Josephson effect*: In the case of the absence of the effective in-plane magnetic field $\Omega = 0$, one has independent coherent tunneling of the condensates with opposite circular polarizations between two traps, completely analogical to the conventional Josephson effect for atomic condensates.

- *intrinsic Josephson effect*: If different traps are uncoupled $J = 0$ but $\Omega \neq 0$ in each of the traps, we have coherent exchange of particles between the condensates with different polarizations.

The nonlinear term plays a crucial role in Josephson dynamics. Once nonlinearity is neglected, Eqs.(3.29) give a well-known expression for the Josephson current for both extrinsic and intrinsic Josephson effects: $I_{i,e} = I_{i,e}^{(0)} sin\phi$, where ϕ is the difference between the phases of the two condensates; $I_e^{(0)} = N_T J\hbar^{-1}$,$I_i^{(0)} = N_T\Omega\hbar^{-1}$ with N_T being the total number of particles. In this regime the occupancies of the coupled condensates exhibit harmonic oscillations with periods given by J and Ω for extrinsic and intrinsic Josephson effects, respectively.

If both wells have the same number of particles and only the tunneling term is present, one has a situation similar to the *dc* Josephson effect in superconductors: a small tunneling current is flowing without any applied field. This current is proportional to the sine of the phase difference across the barrier.

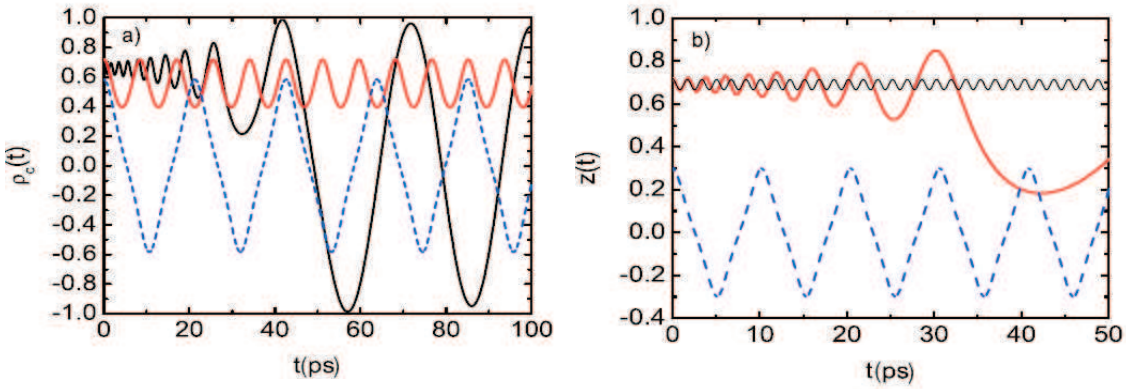

Figure 3.13 | Extrinsic and intrinsic Josephson effect [151]: (a) ρ_c for the intrinsic Josephson effect illustrating nonlinear oscillations (blue), MQST (blue) and finite lifetime effects (red). (b) Population imbalance for the extrinsic Josephson effect illustrating once again nonlinear oscillations (blue), MQST (black), and finite lifetime effects (red/gray).

The situation changes drastically if the nonlinear terms are taken into account such as the blueshift of the polaritons dispersion. The oscillations of the occupation numbers become anharmonic and their period depends on N_T [148, 149]. Besides, if the initial imbalance between the occupation numbers of the two coupled condensates exceeds some critical value N_c, the effect of the MQST occurs. In this regime the tunneling between the condensates is suppressed and the particles remain in the state where they have been created. The imbalance of the occupation numbers results in a different blueshift in each well. This potential difference between the two wells is similar to the *ac* Josephson effect in superconductors: A flow of a small ac current when there is a potential difference between the two superconductors. The initial populations are almost unperturbed.

Figure 3.13(a) illustrates the intrinsic Josephson effect ($J = 0$). It shows the time oscillations of the circular polarization degree $\rho_c(t)$ for two different initial values $\rho_c(0) = 0.58$ and $\rho_c(t) = 0.71$, respectively, the critical value for the MQST effect being 0.63. In that case the MQST leads to the suppression of beats of ρ_c which can be also expressed as the onset of the self-induced Larmor precession, which is an oscillation of the linear part of the polarization about the effective magnetic field created by the circular polarization degree [86, 152]. The black curve is calculated considering a pulsed resonant excitation and taking into account the decay of polaritons. At short times, the polarization oscillations are suppressed. However, the decay of the number of particles leads to the increase in the critical value ρ_c and after 40 ps the oscillatory regime is recovered. Fig. 3.13 (b) shows the extrinsic Josephson effect. For different population imbalances $z(t)$ of the particles one can obtain different regimes: simple linear Josephson oscillations, microscopic quantum self trapping as well as the transition from one to another induced by finite lifetime effects.

Using elliptically polarized condensates, the oscillations become more complex. The Josephson effects in the nonlinear regime lead to nontrivial polarization dynamics and produce a spontaneous separation of the condensates with opposite polarizations in the real space. We will not go into details of the description. Once again, the interested reader is referred to Ref.[151] for a more detailed discussion.

In conclusion with a special focus on the following sections, the system of four coupled equations 3.29 contains already enough complexity to show nontrivial oscillations, which can be pushed towards chaotic oscillations.

3.3.2 Chaotic Josephson oscillations

Chaotic behavior of perfectly deterministic systems has been fascinating scientists since its discovery by H. Poincaré [153] and its popularization by E. Lorenz [154] and B. Mandelbrot [155]. Chaotic behavior has been observed in nature as well as in laboratory in a variety of systems including mechanical, chemical, electrical, and optical ones. A necessary condition for a system to be chaotic is nonlinearity. Moreover, the complexity of the system should be sufficient in order to allow the existence of the chaotic attractor in the phase space.

In this section we will consider two spatially separated macroscopically occupied modes of cavity exciton-polaritons (polaritons) with a Josephson coupling between them, taking into account their polarization.

It is the exciton-exciton interaction which brings the nonlinearity necessary for the chaotic behavior into the polaritonic system. This interaction is spin-anisotropic: strongly repulsive for excitons with the same spin projection on the growth axis and weakly attractive for excitons with opposite projections [73, 41]. A single macrooccupied polariton mode can be considered as a nonlinear oscillator demonstrating bistable behavior under quasi-resonant pumping as already discussed in the previous chapters. The Josephson coupling can arise between two weakly overlapping spatially separated modes with the same spin (extrinsic Josephson effect). It can also arise between the two polariton spin components without spatial separation. It was called intrinsic in the previous section. The coupling between the two polarizations is provided by the natural splitting of the ground state due to the anisotropy of the cavities.

The inherent property of polaritons is their relatively short lifetime (of the order of several picoseconds). Therefore, the decay and the pumping should be included in the description of such system. The Josephson oscillations in a driven polariton system have been first considered by D. Sarchi et al [156], who demonstrated the validity of a simplified single-mode approximation. The model of D. Sarchi did not include spin degree of liberty and was not capable of demonstrating chaotic behavior. Like the cold atomic condensates [149], the coupled macrooccupied polariton modes have been predicted [151]

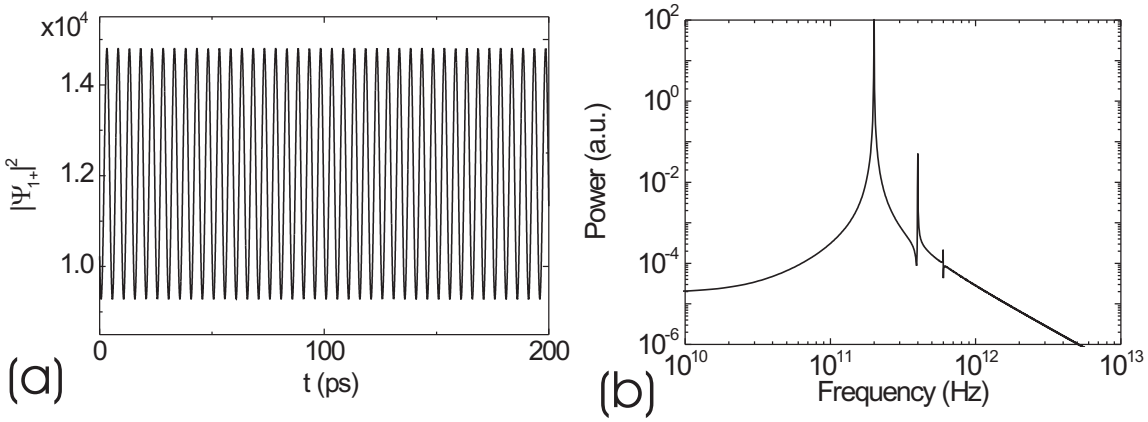

Figure 3.14 | Periodic oscillations of the Jospehson coupled system: (a) shown the oscillations of $|\Psi_{1+}|^2$ on the time domain, and (b) shows the Fourier-spectrum of the spin-up component for periodic oscillations.

to exhibit nonlinearities and macroscopic quantum self-trapping due to the interparticle interactions. Chaotic Josephson oscillations and their synchronization have been studied before in arrays of superconductors with Josephson junctions, with a different non-linear term in the equation [157, 158], but not in optical systems.

We consider in the following two traps with two polarization components in each trap with both extrinsic and intrinsic coupling mechanisms present. This coupling brings in the complexity sufficient to observe chaotic behavior.

We consider two confined polariton states separated by a potential barrier. Such a potential profile can be realized by applying stress on the microcavity surface [159], or by patterning two micro-pillars close to each other [160]. In such case the equation describing the dynamics of the coupled confined polariton states can be written as

$$
\begin{aligned}
i\hbar\frac{\partial\psi_{1+}}{\partial t} &= -i\frac{\hbar\psi_{1+}}{\tau} + \alpha_1\left|\psi_{1+}\right|^2\psi_{1+} + \alpha_2\left|\psi_{1-}\right|^2\psi_{1+} - J\psi_{2+} - \Omega\psi_{1-} + P_0 e^{-i\omega t} \quad (3.30)\\
i\hbar\frac{\partial\psi_{1-}}{\partial t} &= -i\frac{\hbar\psi_{1-}}{\tau} + \alpha_1\left|\psi_{1-}\right|^2\psi_{1-} + \alpha_2\left|\psi_{1+}\right|^2\psi_{1-} - J\psi_{2-} - \Omega\psi_{1+}\\
i\hbar\frac{\partial\psi_{2+}}{\partial t} &= -i\frac{\hbar\psi_{2+}}{\tau} + \alpha_1\left|\psi_{2+}\right|^2\psi_{2+} + \alpha_2\left|\psi_{2-}\right|^2\psi_{2+} - J\psi_{1+} - \Omega\psi_{2-}\\
i\hbar\frac{\partial\psi_{2-}}{\partial t} &= -i\frac{\hbar\psi_{2-}}{\tau} + \alpha_1\left|\psi_{2-}\right|^2\psi_{2-} + \alpha_2\left|\psi_{2+}\right|^2\psi_{2-} - J\psi_{1-} - \Omega\psi_{2+}.
\end{aligned}
$$

This are, except the additional pump term in the first equation and the decay terms, exactly the equations discussed in the previous subsection. P_0 is the pump intensity, while $\hbar\omega$ is the pump detuning or the energy difference between the pumping energy of the laser and the energy of the bare polariton mode. In the calculations we use the parameters of

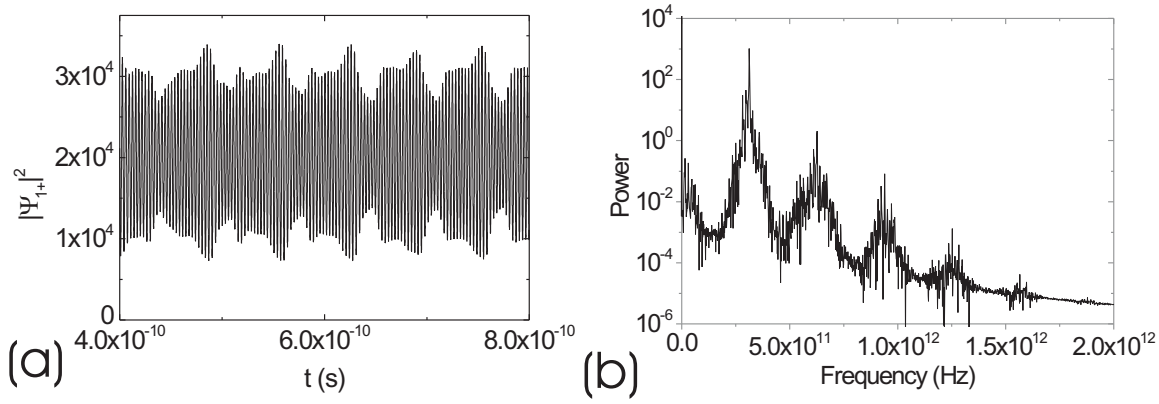

Figure 3.15 | Chaotic oscillations of the Jospehson coupled system: (a) shown the oscillations of $|\Psi_{1+}|^2$ on the time domain, and (b) shows the Fourier-spectrum of the spin-up component.

a typical cavity with GaAs quantum wells, since such cavities presently show the longest lifetimes (we take $\tau = 20ps$). We take $\Omega = 150\mu eV$, in the range of values measured experimentally, and $J = 93\mu eV$. Both should be comparable with each other and with the inverse lifetime $\Gamma = \hbar/\tau$, in order to observe chaotic behavior.

Fig. 3.14 shows the oscillations of the spin-up component of the first pillar $|\Psi_{1+}|^2$ in the time domain (a) together with the corresponding Fourier-spectra. It is clear, that for periodic oscillations one obtains a clear Fourier spectrum with some well defined frequencies. In contrast, changing the parameter set, the oscillations become chaotic and then one observes a continuous Fourier spectrum with a random peak structure. This is shown in Fig. 3.15 (a) and (b).

Another typical visualization of chaotic behavior is the Poincaré section. The general principle is shown in Fig. 3.16 together with the Poincaré section obtained for the chaotic oscillations shown in the previous figure. The Poincaré-section (Fig. 3.16) cuts the multidimensional phase space by an arbitrary chosen plane S. The Poincaré map P(x) maps now all intersections of a trajectory in the phase space with the arbitrary plane. In case of a periodic, this means closed, trajectory, the Poincaré map consists of a finite number of points. In the chaotic case, the Poincaré section shows a fractal structure, which is illustrated in Fig. 3.16 (b) for the chaotic oscillations of the previous picture.

Furthermore, a nonlinear system can be efficiently analyzed using the conditional Lyapunov exponent λ, that is, the logarithms of the eigenvalues of a function of the Jacobian matrix of the system

$$\lim_{t\to\infty} \left(J^*(t) \cdot J(t)\right)^{\frac{1}{2t}} \tag{3.31}$$

calculated along its trajectory. Stable system contains negative Lyapunov exponents,

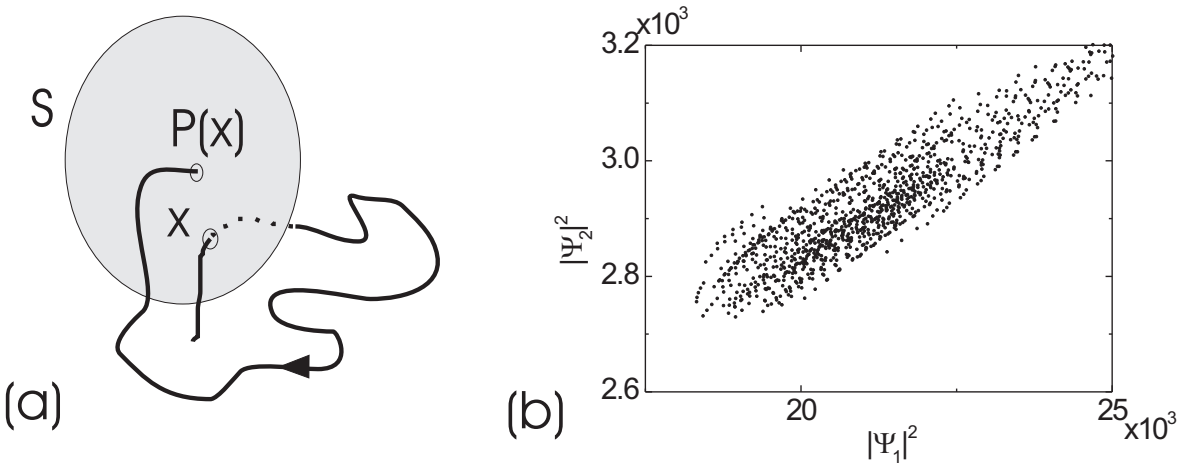

Figure 3.16 | Poincaré section of a trajectory in phase space: (a) schematical description of the Poincaré section: In Poincaré section S, the Poincaré map P projects point x onto point P(x); and (b) Poincaré section of the chaotic oscillations of the previous picture.

which means, that the system falls back to the initial trajectory even if a small perturbation is applied. One can use the simple model system of a ball in a potential minimum: applying a small impulse on the ball, the final state will always be the potential minimum. The system is stable. Chaotic regime is characterized by the presence of positive Lyapunov exponents, which indicate the divergence of the tranjectory in the presence of any small perturbation. Coming back to the simple model, the ball is now placed on a potential maximum. Applying once again a small perturbation, the ball will leave the initial point and will never come back. Qualitatively, the chaotic regime is obtained when the bistability transition of the mode pumped directly (ψ_{1+} in our case) is constantly invoked by the changes of its population due to the Josephson oscillations of both types. To carry out quantitative analysis, we have performed simulations at different pumpings and detunings (which are the most easily variable parameters in experiments, since they are determined only by the external laser). Figure 3.17 summarizes the results of these simulations showing the phase diagram of the system in the detuning-pumping intensity coordinates, the other parameters of the system being kept constant. The boundaries of the chaotic regions are shown by black solid lines. One can see that almost for any detuning under certain pumping the system should exhibit chaotic oscillations. Outside the chaotic regions, the oscillations are periodic or absent, as already predicted for a simpler system [156].

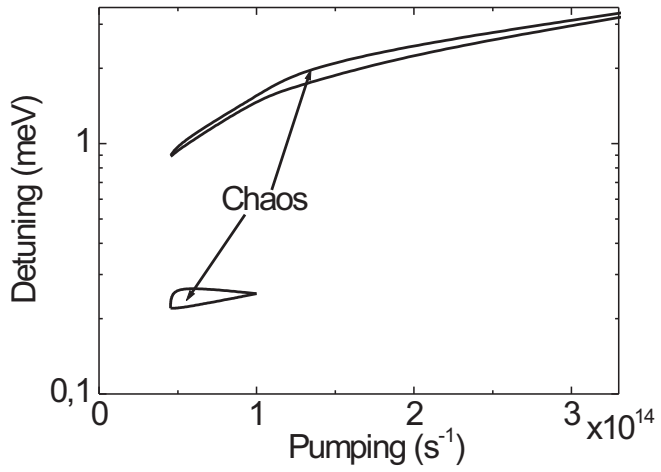

Figure 3.17 | Phase diagram for chaotic behavior: Phase diagram of the double-trap system with 2 polarizations. Solid lines mark the boundaries of the regions with chaotic behavior in dependence on the detuning and the pump intensity. Outside the marked regions the oscillations are periodic or absent.

3.3.3 Chaos synchronization

The developed chaotic cryptography is based on the synchronization of two chaotic systems. The synchronization means that two chaotic systems are chaotic, but follow the same trajectory in phase space. This has been first proposed by Pecora and Carroll (1990) [161] and was later called Pecora-Carroll method. A recent review paper is given in Ref. [162]. The principle of the synchronization together with the possible communication scheme is shown in Fig. 3.18. It is taken from Ref. [163], where the experimental realization of chaos synchronization and communication using electric circuits is reported. One couples now a chaotic system (positive Lyapunov exponents) containing three subsystems u, v, w via the output of the first subsystem $u(t)$ with a second system of the same structure (v_r, w_r) but stable against chaos (negative Lyapunov exponents). Putting apart for a while the signal $n(t)$ (Fig. 3.18) the output $u(t)$ drives v_r and w_r. Due to the positive Lyapunov exponents the subsystems v_r and w_r will drive the u_r in the same way as the first system. The result is, that $u(t)$ and $u_r(t)$ are equal in the perfect case and the two systems are synchronized. This can be used to mask a useful signal $n(t)$, which can be added to the chaotic driving output $u(t)$ of the first system. Due to the negative Lyapunov exponents of the second system, this small deviation does not destroy the synchronization and $u_r(t)$ will follow the same trajectory as $u(t)$. Comparing now $s(t)$ with $u_r(t)$ opens the possibility to recover the useful signal, which has been masked in the chaotic output of the first system $u(t)$.

We use a similar way for our system: We divide our system into two subsystems, one of them being intrinsically chaotic, and the other - intrinsically stable against chaos. These two conditions are checked calculating the conditional Lyapunov exponents along the trajectory in the chaotic regime. This calculation shows that for the chosen parameters (pumping $1 \times 10^14\ s^-1$, detuning -1.5 meV, appearing to be optimal values) the system

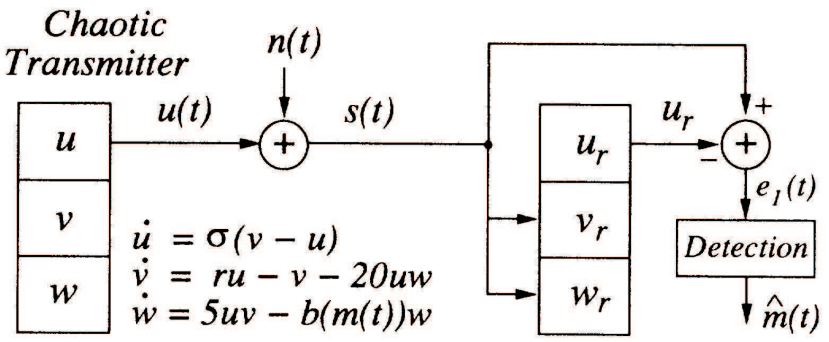

Figure 3.18 | Chaos synchronization and communication system [163]: A useful signal $n(t)$ can be transmitted hidden in a chaotic transport signal $u(t)$ by synchronization of two systems. The extracted signal $\hat{m}(t)$ is in case of perfectly synchronized systems equal to $n(t)$.

can be divided into two subsystems, one of them associated with the first trap, and the other with the second trap. The Lyapunov exponents are positive for the wavefunctions of the first subsystem and negative for the wavefunctions of the second subsystem.

Therefore the synchronization between two systems should be performed by connecting the output of the first trap of the master system (both polarization components) with the only trap of the slave system (with parameters corresponding to the second trap of the master system), as shown by the blue arrows in Fig.3.19(a). We describe this numerically by adding a term proportional to the wavefunction of the driving system $\Psi_{1\pm}$ to the equations describing the slave system $\Psi'_{2\pm}$:

$$
\begin{aligned}
i\hbar\frac{\partial\psi'_{2+}}{\partial t} &= -i\frac{\hbar\psi'_{2+}}{\tau} + \alpha_1\left|\psi'_{2+}\right|^2\psi'_{2+} + \alpha_2\left|\psi'_{2-}\right|^2\psi'_{2+} - V\psi_{1+} - \Omega\psi'_{2-} \\
i\hbar\frac{\partial\psi'_{2-}}{\partial t} &= -i\frac{\hbar\psi'_{2-}}{\tau} + \alpha_1\left|\psi'_{2-}\right|^2\psi'_{2-} + \alpha_2\left|\psi'_{2+}\right|^2\psi'_{2-} - V\psi_{1-} - \Omega\psi'_{2+}.
\end{aligned}
\tag{3.32}
$$

This coupling represents the only source of pumping for the slave system. A certain time delay proportional to the transmission time between the two systems is present between the master and the slave systems, which should be taken into account when decoding a useful signal.

To transmit information masked in the chaotic oscillations we introduce a communication channel to the system shown by the red lines in Fig. 3.19 (a). A useful digital signal with a repetition rate of 50 GHz is added to the output of the second polarization component of the master system in point 1 and transmitted to the receiver 2, where the useful signal is reconstructed by the comparison with the output of the synchronized slave system. The corresponding Fourier spectrum of the chaotic output with the added useful signal is shown in Fig.3.19 (b), where the arrow indicates the frequency position of the masked useful signal. Obviously, the oscillations invisible in the Fourier spectrum are completely masked in the time domain as well (not shown). The signal $s(t)$ itself is shown in (d). The subtraction of the chaotic output of the synchronized slave system from

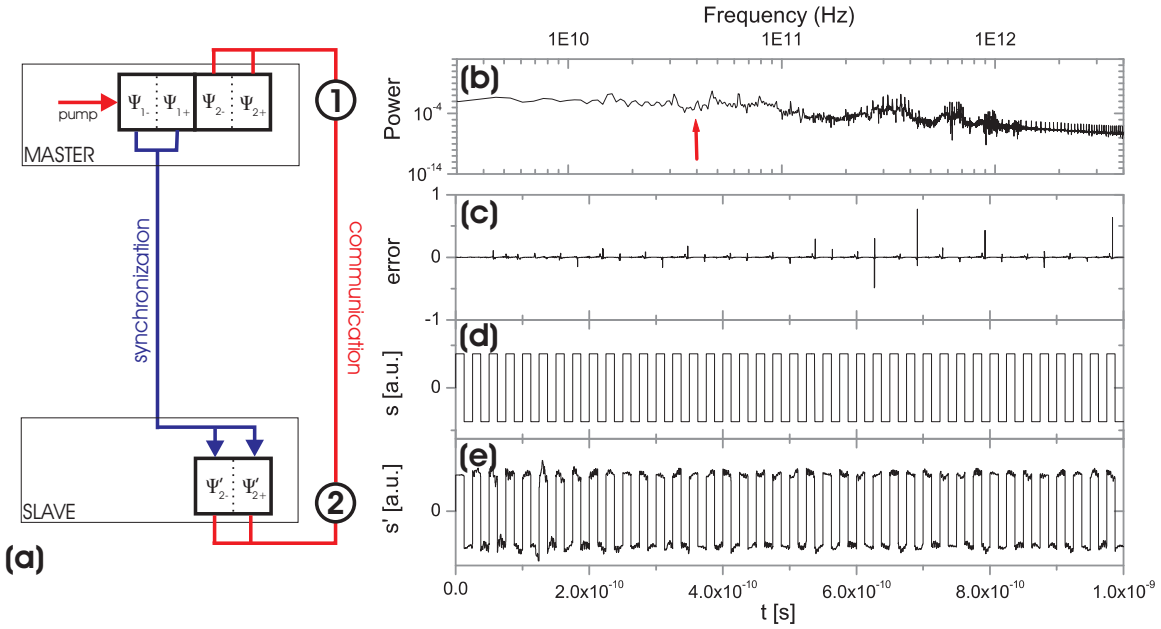

Figure 3.19 | Synchronization of the chaotic systems and chaotic communication: (a) schematic system with a separated synchronization channel (blue) and a communication channel (red); (b) Fourier spectrum of the chaotic behaviour of the second polarization component of the master system modulated with a signal (red arrows); (c) synchronization error without signal versus time; (d) transmitted signal s versus time, and (e) recovered signal s'.

the received signal from the master system allows recovering of the transmitted signal (Fig.3.19 (e)).

Figure 3.19 (c) shows the relative synchronization error between two corresponding wavefunction components $\left(|\psi'_{2+}|^2 - |\psi_{2+}|^2\right) / \left(|\psi'_{2+}|^2 + |\psi_{2+}|^2\right)$ from the driving and the slave systems with a mismatch of 0.5% of the coupling between polarizations within the same well Ω. Although there are several peaks rising up, the synchronization is always recovered on the long term, allowing a continuous signal transmission for communication.

The chaotic oscillations for the given parameters allow signal frequencies up to some THz for extremely well synchronized systems. But the recovering of the transmitted signals is restricted by the frequency spectrum of the synchronization error caused by the parameter mismatch of the coupling constants and by the noise, which are always present in experimental setups. One of the most important aspects of a cryptographic system is its security. A set of criteria for estimation of the security of chaotic cryptographic systems has been proposed recently [8]. These criteria include, for example, resistance to message signal extraction attacks: the useful signal should not be visible in the Fourier spectra. Another criterion is the robustness against noise in the communication channels. We have checked that such criteria are well verified for our system.

The experimental implementation of this polarization dependent communication scheme

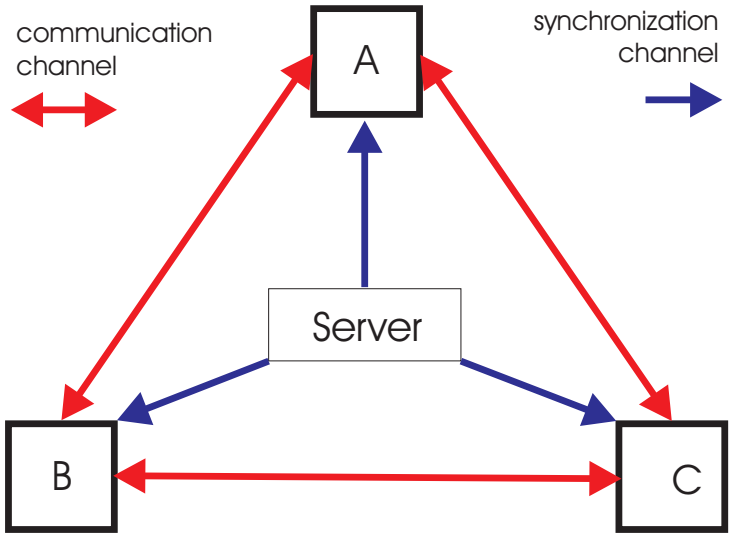

Figure 3.20 | Chaotic communication networks: A possible chaotic communication network containing one server and three participants. The Server is a master system which drives the slave system A, B and C. Communication is possible between A, B, and C if all lengths (and "flight times") of the communication channels are known.

might seem challenging due to technical restrictions, such as that the polarization is not maintained during the transmission through an optical fiber. Therefore, we have tested a similar system without the polarization degree of freedom. However, to have sufficient complexity, it is necessary to have at least three traps, with two Josephson couplings between them. This can be obtained by arranging the traps in a line and pumping the central one. In this configuration one can observe chaotic oscillations and their synchronization, with the slave system consisting of a single trap. However, since the coupling between the two circular polarizations within a trap is always present because of the quantum well anisotropy, this model, although working, is not an adequate representation of the real system. We therefore recommend the first scheme (two traps, two polarizations) for realizing the chaotic communication systems.

3.3.4 Chaos communication network

Using separate synchronization and communication channels opens the possibility of bidirectional communication, while the synchronization is provided by a unidirectional coupling of the master and slave system. Within such a scheme one can even implement chaotic communication networks.

A scheme of a chaotic communication network is shown in Fig 3.20. This network contains a server, which is nothing else than the master system. This server drives the three slave systems A, B and C. Once all three slave systems are synchronized with the master, one can send and receive messages from one slave system to another. The knowledge of all "flight" times of the signal between the slave systems is a necessary requirement to reconstruct the information.

3.3.5 Conclusions

We have studied chaotic Josephson oscillations between two macrooccupied polariton modes under quasi-resonant pumping taking into account the polarization degree of freedom. Chaos synchronization is possible for such systems, allowing the transmission of useful signals with chaotic masking at rates up to $50Gb/s$, which is an important advantage with respect to other optical chaotic communication systems. Polaritons have unique properties extremely useful for chaotic communication system. With respect to electronic system, there advantage is to deal with the efficient transmission of data by light beams. With respect to purely photonic systems, they show much stronger nonlinearities which are absolutely required for the achievement of the chaotic regime. These two advantages combined results in the very high communication rate we have demonstrated.

Chapter 4

Strongly coupled dot-cavity system

Strongly coupled dot-cavity systems are under deep investigation in recent years and they give hopes for new sources of single and entangled photon pairs. This section discusses in detail one proposal to use a strongly coupled dot-cavity system as a new "on-chip" source of entangled photon pairs, possessing several advantages with respect to previous proposals. The main point is the overcome of the impact of deviations of the dot or its environment from the artificial atom picture. In case of entangled photon sources, the main problem is the splitting of the exciton levels due to the anisotropic electron-hole interaction, which can be overcome by our approach for almost all quantum dots.

Contents

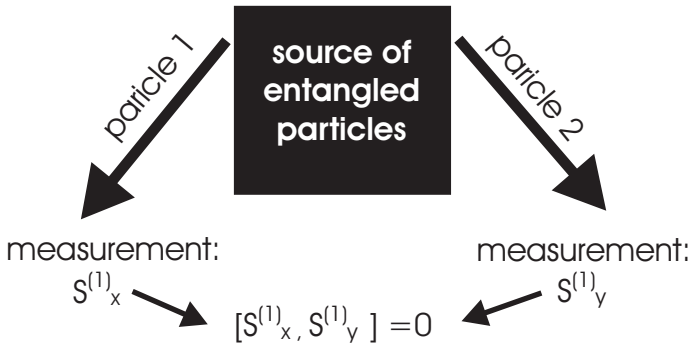

Figure 4.1 | Illustration of the EPR-paradox: Two measurements made at the same time give a full set of spin components of the two entangled particles, which contradicts the basics of quantum mechanics, where the spin components do not commute.

4.1 Introduction

It was first pointed out by Einstein, Podolsky, and Rosen [164] that, according to the usual interpretation of quantum mechanics, there exist two-particle states with the fascinating property that a measurement of one chosen variable of particle 1 determines completely the outcome of the measurement of the same variable of particle 2. At the measurement the particles may be so far away, that no effect of one measurement can propagate to the other particle in the available time. Such situations can arise if both particles are emitted from a common source in some entangled (non-factorisable) quantum state

$$|\Psi\rangle = \frac{1}{\sqrt{2}}[|\Phi\rangle_1 |\chi\rangle_2 - |\chi\rangle_1 |\Phi\rangle_2]. \tag{4.1}$$

According to Einstein, Podolsky, and Rosen, when the outcome of one measurement of some particle variable (for the second particle) can be predicted with certainty, without disturbing the particle, then "...there exists an element of physical reality corresponding to this physical quantity...". In other words, the particle two really has this value of the variable, irrespective if it is measured or not. This must be contrasted with the quantum point of view, according to which the measurement creates the reality, in a sense. On the other hand, one may consider a different variable, say, one that is canonically conjugate to the previous one measured for the 1st particle. Then the entanglement predetermines the value of the conjugate variable of the 2nd particle, and, by the foregoing arguments, particle two has really this value of the variable. But if the two variables are canonical conjugates, then they do not commute and they can not both have definite values at the same time.

Now the decision whether to measure one or the other variable of particle 1 can be made when the two particles are far apart and cannot "communicate" in the available time, yet it influences the state of particle two. This contradiction led Einstein, Podolsky, and Rosen to conclude that quantum mechanics is "incomplete". Such counter-intuitive non-local correlations have, however, been observed experimentally.

The implication itself of quantum entanglement has been widely discussed in the last century [165, 166, 167, 168, 169, 170, 171, 172, 173, 174, 175].

To illustrate the so called EPR-paradox more explicitly, let us imagine a simple example, which is illustrated in Fig.4.1. We consider a black box, which emits two entangled spin $\frac{1}{2}$ particles in opposite directions with total spin angular momentum zero. If we were to measure the spin $S_x^{(1)}$ of the first particle in the x-direction for example and obtain the value $\hbar/2$, we would know that the second particle is in a eigenstate of its spin $S_x^{(2)}$ with eigenvalue $-\hbar/2$. On the other hand, if we were to measure the $S_y^{(2)}$ of the second particle and obtain the value $-\hbar/2$, we would determine the value of the y-component of the spin of the first particle to $\hbar/2$. Performing these measurement for both particles we would obtain a definite set of the spin eigenvalues of the two particles. But $S_x^{(1)}$ and $S_y^{(1)}$ do not commute and, according to quantum mechanics, they cannot both have definite values. The paradox arises, because we tend intuitively to think in classical terms, i.e. to associate an objective physical reality with each particle and its variable, whereas in quantum mechanics a dynamical variable does not have actually a value until it is measured. In a sense, the measurement creates the physical reality. Various proposals have been made to account for the correlations of the two particles in terms of hidden variables, or unmeasurable parameters [166]. But it was later shown by Bell and others [167, 168, 176, 169, 171, 172] that such nonlocal effects are fundamentally quantum mechanical, and that no realistic local theory can account for the correlations quantitatively.

Real applications of the entanglement have been developed within modern quantum computing and communication schemes [177]. For the communication purposes, the word *teleportation* is often used to describe these processes. Actually it comes from science fiction and means to make disappear a person or an object at one place, while an exact replica appears somewhere else. (In real life only coherent states, which can be described by a wavefunction, can be transported and this limits strongly the teleportation of a macroscopic object.) We will not discuss in detail the *teleportation* of an quantum state, but we refer to Ref. [178] for the interested reader. Of course there are various different communication protocols based on entangled photon pairs e.g [179] but we will describe the modified BB84 protocol [180] which transforms the initial proposal based on polarized single photons [177] to entangled photon pairs. The practical implementation has been carried out by Jennewein et al. in 2000 [181].

In general, Quantum cryptography, or quantum key distribution (QKD), uses quantum mechanics to guarantee secure communication. It enables two parties to produce a shared random bit string known only to them, which can be used as a key to encrypt and decrypt messages, which are transmitted over a standard (classical) communication channel. We will only scratch the surface of the QKD, which grew enormously in recent years and became a separate research field. More detailed informations are given, e.g. in a recent

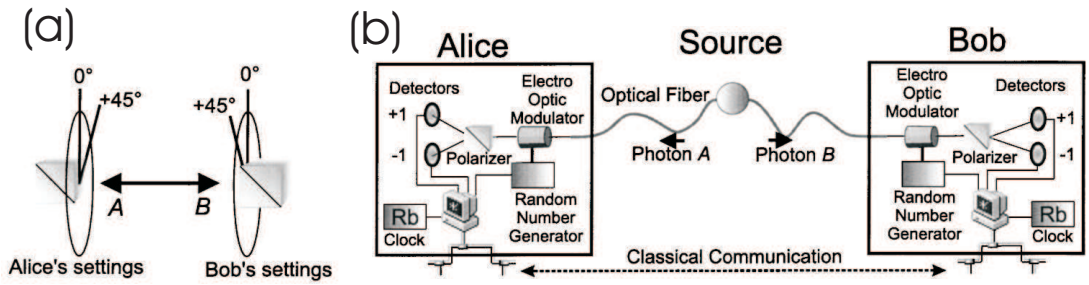

Figure 4.2 | Realization of the modified BB84 protocol [181]: (a) Settings for Alices and Bobs analyzers for realizing quantum key distribution based on the BB84 protocol and (b) schematically experimental realization.

review paper [182].

An important and unique property of quantum cryptography is the ability of the two communicating users to detect the presence of any third party trying to gain knowledge of the key. This results from a fundamental aspect of quantum mechanics: the process of measuring a quantum system in general disturbs the system. A third party trying to eavesdrop on the key must in some way measure it, thus introducing detectable anomalies. By using quantum superpositions or quantum entanglement and transmitting information in quantum states, a communication system can be implemented which detects eavesdropping. If the level of eavesdropping is below a certain threshold a key can be produced that is guaranteed to be secure (i.e. the eavesdropper has no information about), otherwise no secure key is possible and communication is aborted.

The quantum states of two (or more) separate objects can become linked together in such a way that they must be described by a combined quantum state, not as individual objects. This is known as entanglement and means that, for example, performing a measurement on one object will affect the other. If an entangled pair of objects is shared between two parties, anyone intercepting either object will alter the overall system, allowing the presence of the third party (and the amount of information they have gained) to be determined.

Let us go a bit more into the details of the modified BB84 protocol [180]. The system is constructed as follows: A entangled photon source is placed in between Alice and Bob. Alice and Bob receive now one of the entangled photons and they randomly vary their analysis directions between 0° and 45° which is shown in Fig 4.2(a). Alice and Bob observe perfect anticorrelations of their measurements whenever they happen to have parallel oriented polarizers, leading to bitwise complementary keys. Alice and Bob obtain identical keys if one of them inverts all bits of the key. Whenever Alice makes a measurement on photon A, photon B is projected into the orthogonal state which is then analyzed by Bob, or vice versa. After collecting the keys, Alice and Bob authenticate

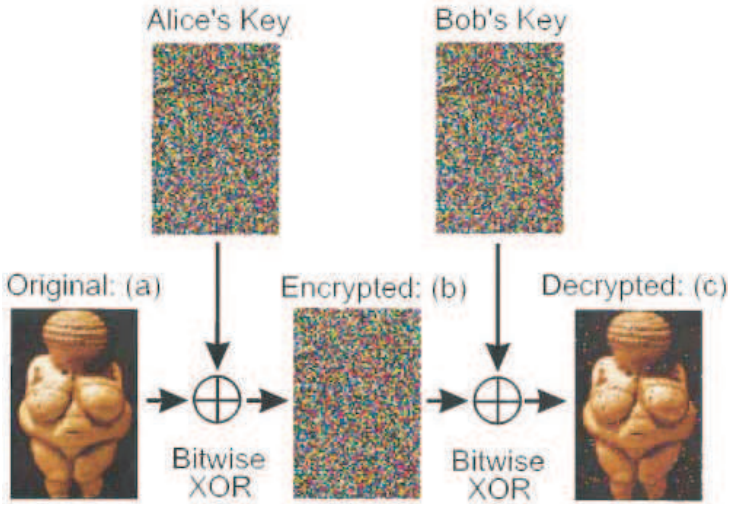

Figure 4.3 | Transmission of an encrypted image [181]: The 49984 bit large keys generated by the BB84 scheme are used to securely transmit an image (a) of the Venus von Willendorf effigy. Alice encrypts the image with her key and transmits the encrypted image (b) to Bob via the computer network. Bob decrypts the image with his key, resulting in (c) which shows only a few errors due to the remaining bit errors in the keys.

their keys by openly comparing a small subset of their keys and evaluating the bit error rate.

The schematic experimental realization of the quantum key distribution system following [181] is sketched in Fig. 4.2(b).

We will not go into detail in the experimental realization of the modified BB84 protocol. We only show in Fig. 4.3 the result from [181] to transmit an image of the Venus von Willendorf effigy. This is the first full implementation of entangled state quantum cryptography. The authors claim that all the equipment of the source and of Alice and Bob has proven to operate outside shielded lab environments with a very high reliability. All this shows that entanglement based cryptography can be tomorrows communication technology.

After this small excursion to quantum cryptography, we come back to solid state physics. As follows from the previous paragraphs, the quantum correlations and, to be more specific, entangled photons pairs are a prerequisite for the realization of many quantum communication protocols. We will focus in the following only on possible solid state sources of entangled photon pairs based on single quantum dots as emitters.

4.2 Quantum dots as EPR-photon emitters

In the context of solid state physics, QDs as quantum emitters have drawn a strong attention when it has been proposed to realize entangled photon pair sources based on the biexciton decay[183]. The ideal decay paths are illustrated in Fig.4.4. The biexciton decays emitting either first a σ_+ and second a σ_- polarized photon or vice versa, and the photons are fully polarization-entangled. In principle this idea is ingeniously simple, as it allows to implement such sources on a very small length scale and rises hope for the on-chip sources of entangled photon pairs, which could be easily implemented on nano

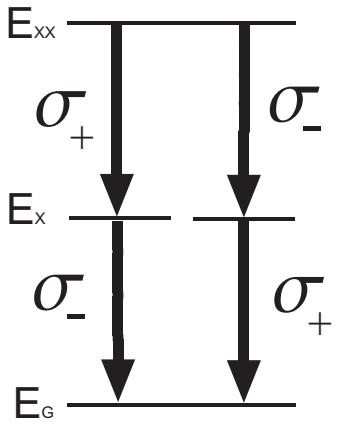

Figure 4.4 | Biexciton decay of an ideal quantum dot: The decay takes place from the biexciton state E_{XX} via two degenerate exciton states, which couple to different polarization of light. The final state is the ground state of the quantum dot.

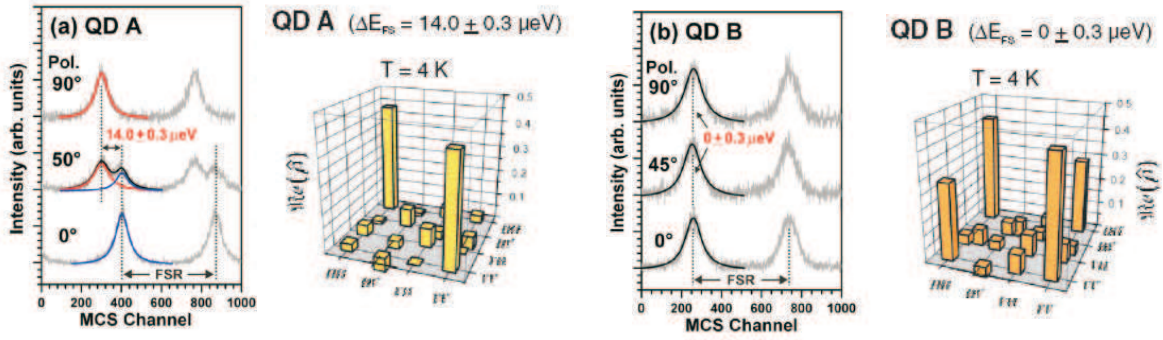

Figure 4.5 | Quantum correlations for selected quantum dots [16]: Selected quantum dots with (a) non-zero finestructure splitting and (b) zero splitting. The corresponding reconstructed density matrices for the selected quantum dots are also shown.

chips for computing purposes.

Unfortunately, this proposal turned out to be hard to implement mainly because the intermediate exciton states of a typical QD are not degenerate due to the anisotropic electron-hole interaction [184, 185]. Also the environment (i.e. the strain induced by the substrate) of the quantum dot can effect the transitions.

This interaction couples degenerate exciton states which split into two resonances coupled to two orthogonal linear polarizations called horizontal (H) and vertical (V), respectively. The resulting photons for the two decay channels are therefore distinguishable and the degree of entanglement becomes zero. The quantum correlations become hidden in time integrated measurements because a QD with split intermediate exciton levels emits photons into a time-evolving entangled state.[186]

Several proposals have been made to overcome this splitting of the exciton lines. The

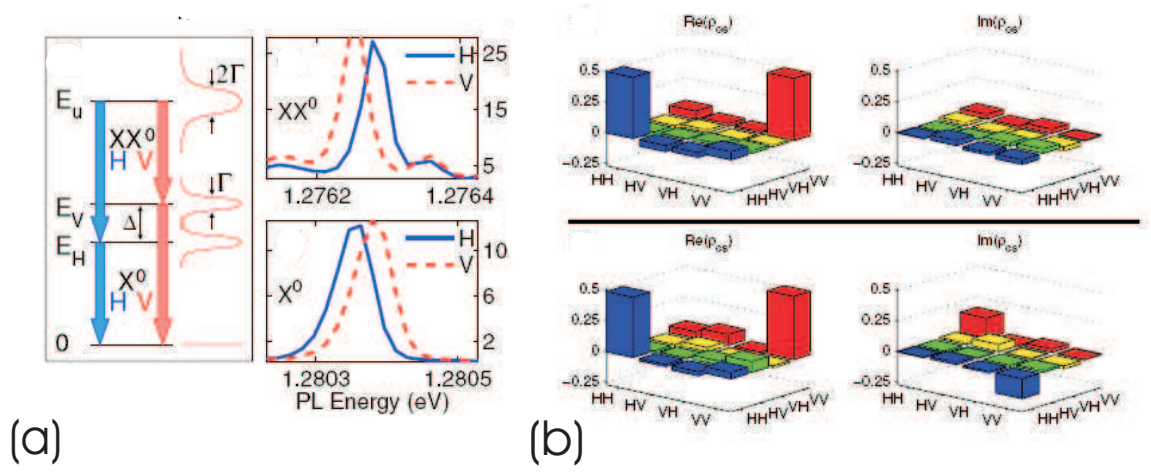

Figure 4.6 | Entanglement and spectral filtering [190]: (a) Shows the photoluminescence spectra, together with a schematic picture of the decay. (b) shows the reconstructed density matrix with a non-zero off-diagonal element for a large width of the spectral windows (upper panel) and for narrow spectral windows (lower panel).

simplest one is of course to grow arrays of quantum dots and select only those, which show no fine structure splitting. This has been published in several reports [187, 16, 188]. Fig 4.5 shows the photoluminescence spectra of two quantum dots with either non-zero or zero splitting. The corresponding reconstructed density matrices show clearly an non-zero off-diagonal element for the zero splitting case, which corresponds directly to a non-zero degree of entanglement [189] (see Appendix C). The disadvantage of this method is that the fabrication process of the quantum dot takes place almost without possibilities of controlling. Thus, it is always necessary to discover among a huge number of QDs those, which show no splitting. This makes future industrial implementation much more complicated because a huge effort is needed to fabricate one entangled photon source.

To avoid this, one needs other techniques to overcome the splitting. One, developed by Akopian et al. [190], is to introduce spectral filters in the experimental setup which select only the overlapping part of the transition. This procedure is illustrated in Fig.4.6 together with the results for the reconstructed density matrix.

Depending on the splitting, the overlap of the transitions may be very small. This requires very narrow spectral windows to obtain entangled photon pairs. The disadvantage here is that the quantum efficiency (the number of detected photons), is very low, which restricts the possible applications of this technique in communication protocols. The third possibility we want to discuss here, is the use of external fields to shift the intermediate states to degeneracy. This has been shown for electrical fields [191, 192] and for magnetic fields [187, 188]. The latter work is illustrated in Fig.4.7. The dependence of the fine

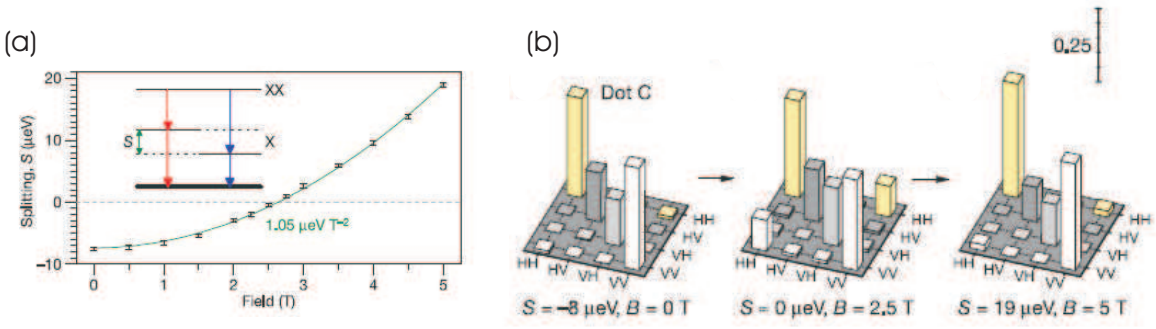

Figure 4.7 | Reduction of the finestructure splitting using external magnetic field [186]: (a) shows the fine structure splitting versus magnetic field. (b) shows the density matrices for different fields, where the matrix in the middle corresponds to a zero finestructure splitting.

structure splitting on the magnetic field is shown on the left hand side, showing the degeneracy of the exciton states for a given magnetic field. Three density matrices for different magnetic fields are shown on the right hand side, where the middle figure of the lower panel corresponds to degeneracy. Both techniques together allows one to use almost arbitrary quantum dots and engineer them to work as EPR-sources.

Nevertheless, the degree of entanglement remains relatively low, due to the imperfections, dephasing [193] and other effects. This implies the need of new ideas and proposals to transform the simple idea of Benson et al. [183] to a real working device, which will be discussed in the next sections.

4.3 Strongly coupled dot-cavity system

The biexciton decay scheme for an ideal quantum dot is shown in Fig.4.4. The intermediate exciton states are degenerate and they couple to circularly polarized light. In a real QD Fig.4.8(a, left part) the exciton resonances coupled to H and V polarized light modes are typically split by an energy δ_X. We consider that such a QD is embedded within a photonic crystal, slightly anisotropic, which shows two confined optical modes polarized along H and V directions and split by a quantity δ_C (see the middle of Fig.4.8(a)). Each of the two non-degenerate exciton states strongly couples to one resonance of the photonic crystal with either vertical (red) or horizontal (blue) polarization, respectively. This coupling gives rise to two polariton doublets polarized H and V. The resulting decay paths of the strongly coupled dot-cavity system can be seen on the Fig.4.8(a, right part).

There are now two possible decay channels for each polarization using either lower or upper polariton state. In Ref.[194] we have shown that for any constant values of δ_X and δ_C, the adjustment of the energy detuning between the group of exciton resonances

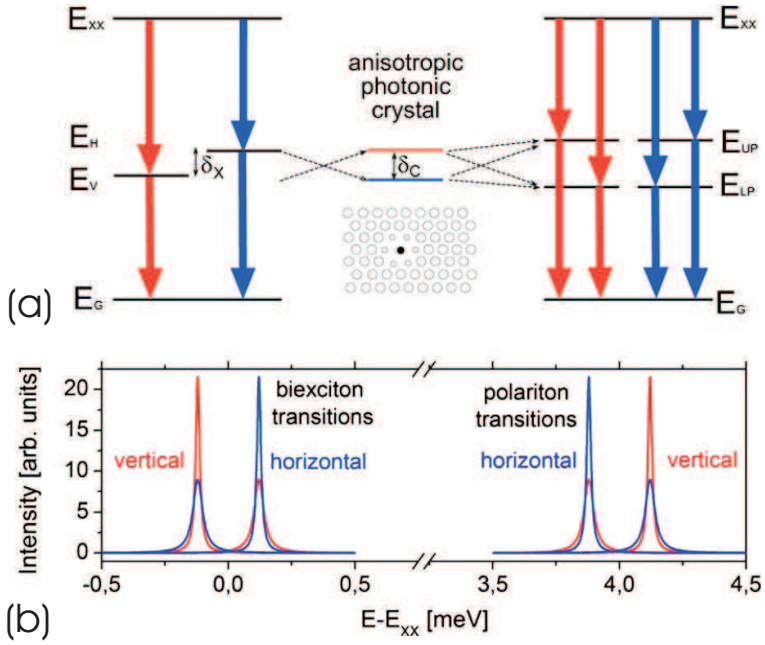

Figure 4.8 | Working scheme 1: (a) biexciton decay of a real quantum dot (left), photonic crystal resonances (middle) and resulting decay scheme for the quantum dot embedded in the photonic crystal in the strong coupling regime (right). The blue arrows correspond to horizontal (H) polarization and the red arrows correspond to vertical (V) polarization. (b) shows the calculated photoluminescence spectra.

and the group of photon resonances allows to make one polariton state with horizontal polarization degenerate with one polariton state with vertical polarization. This alignment makes the two possible decay paths of the biexciton using these two intermediate states distinguishable only by their polarization which results in the generation of entangled photon pairs showing a maximum degree of entanglement.

The energy of the polariton states $E_{\pm}^{H,V}$ can be calculated using [6]

$$E_{\pm}^{H,V} = \frac{E_C^{H,V} + E_X^{H,V}}{2} \pm \frac{1}{2}\sqrt{(E_C^{H,V} - E_X^{H,V})^2 + 4\hbar^2\Omega_{H,V}^2}, \tag{4.2}$$

where H and V indicate the different polarizations, $E_C^{H,V}$ are the cavity resonances, $E_X^{H,V}$ are the exciton energies, and $\Omega_{H,V}$ are the values of Rabi splitting, proportional to the exciton oscillator strength which we assume to be equal for H and V polarized modes. In an isotropic QD, the oscillator strength of the polarized exciton modes can differ by a few percent and can provoke shifts of the polariton energy by a few μeV, which will be discussed later. It follows directly from Eq.(4.2) that the energies of the intermediate polariton states can be tuned by changing the energy of the photonic resonances.

The pairs of polariton states are degenerate($E_{\pm}^{H} = E_{\pm}^{V}$) if $E_H = E_C^V$ and $E_V = E_C^H$, which means that each resonance for V and H polarized light is adjusted to the energy of the exciton state coupled to the perpendicular polarization. In the same time, the biexciton transition is not strongly interacting with the cavity modes because the binding energy of the biexciton is at least one order of magnitude larger than $\hbar\Omega$. This resonance can of course interact with another photonic mode, but we do not want to address this

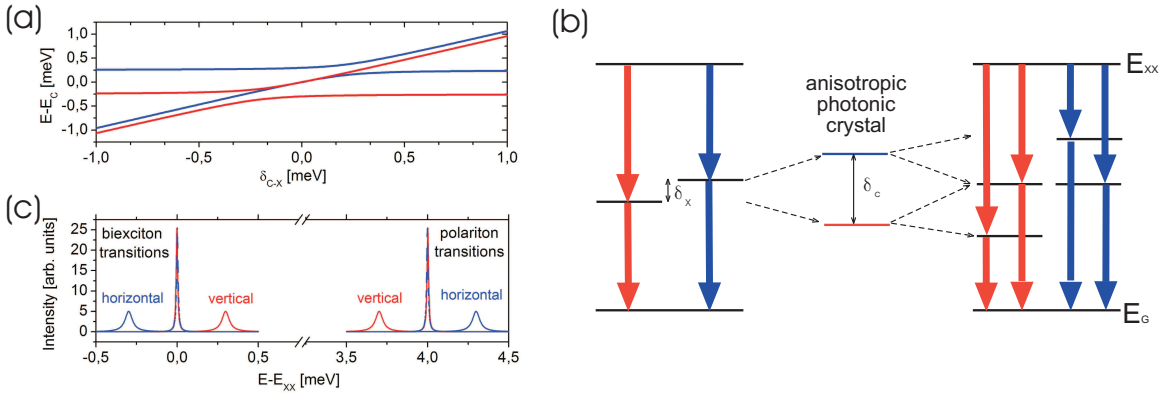

Figure 4.9 | Working scheme 2: (a) Calculated energies of the polariton states for different detuning δ_{C-X} with , δ_x =0.1 meV, δ_C = - 0.5 meV, and $2\Omega_R$ =0.22 meV. Different polarizations are indicated with red (vertical) and blue (horizontal). (b) Distribution of the energy levels for δ_{C-X} =0. (c) Photoluminescence spectra for both polarizations.

case here and we therefore assume that the biexciton emission energy is not perturbed by the presence of the optical cavity. The right hand side of Fig.4.8(a) shows the resulting distribution of the energy levels. There are four possible decay channels for the biexciton. The two decay paths using the UP as an intermediate state produce polarization entangled photon pairs, which is also the case for the decay paths using the LP. This configuration is particularly original and probably useful, since it allows producing two independent EPR pairs. The calculated photoluminescence spectra are shown in Fig.4.8 (b). The technological requirements for this scheme are however quite strong. The first condition is that the Rabi splitting should be larger than the splitting between the H and V exciton states $2\hbar\Omega_R > \delta_x$. The second condition is that the splitting between the optical modes is exactly equal to the splitting between the QD modes with an opposite sign $\delta_x = -\delta_c$. The first condition is usually well fulfilled. In InAS based structures δ_x is of the order of 0.05-0.1 meV, whereas $2\Omega_R \approx$ 0.15-0.25 meV. The second condition, because it is an equality, and because of the small value of δ_x , seems quite demanding, and would, in practice, require the growth and study of many structures.

We therefore propose another configuration, conceptually less ideal, but which should allow an easier experimental implementation. We propose to use an anisotropic photonic crystal showing a splitting δ_C substantially larger than δ_x. Neither the exact value, nor even the sign of δ_C play a crucial role in this scheme. This splitting should not be a problem, since it is difficult rather to fabricate photonic crystals without it. In Ref. [195], for instance, the splitting measured is about 0.5 meV for a cavity with quality factor $Q > 10000$. Figure 4.9 (a) shows the eigenenergies versus the exciton-photon detuning

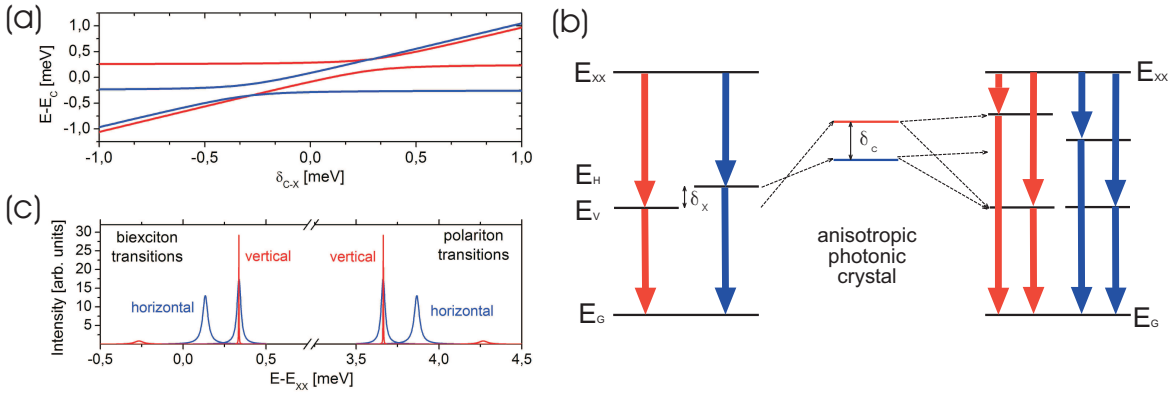

Figure 4.10 | Working scheme 3: (a) Calculated energies of the polariton states for different detuning δ_{C-X} with , δ_x =-0.1 meV, δ_C = - 0.5 meV, and $2\Omega_R$ =0.22 meV. Different polarizations are indicated with red (vertical) and blue (horizontal). (b) Distribution of the energy levels for positive δ_C and negative δ_X. (c) Photoluminescence spectra for both polarizations at δ_{C-X}=-0.275 meV.

$\delta_{C-X} = \frac{E_C^H - E_C^V}{2} - \frac{E_H - E_V}{2}$, keeping δ_x and δ_C constant. This kind of tuning of the exciton resonance energy can be performed experimentally, for example by changing the temperature of the sample [13, 14]. We consider here the case where δ_x and δ_C have the same sign. For a wide range of detuning, the H-polarized LP and the V-polarized UP are almost degenerate. The decay channels of the biexciton are shown on the figure 4.9 (b). The luminescence spectra in two polarizations for positive detuning are shown on the figure 4.9 (c). The spectrum for each polarization consists of two groups of two peaks. The group with the lower energy corresponds to the biexciton decay to the polariton states. The group with the higher energy corresponds to the decay of the polariton states toward the ground state. For each polarization, the peak with the higher energy and the lower energy belong to the same decay cascade. The two central peaks belong to the same decay cascade as well. One can clearly see that the decay channel involving the H-polarized UP and the decay channel involving the V-polarized LP cannot be distinguished by energy measurements, but only by their polarization.

As said before, this degeneracy can also be found if δ_x and δ_C have opposite signs. Fig.4.10 (a) shows the eigenenergies versus δ_{C-X} in that case. The energy degeneracy now occurs at negative detuning between the LP states (H and V), and at positive detuning between the UP states (H and V). The decay channels of the biexciton for the negative detuning case are shown on the Fig.4.10 (b). The luminescence spectra for negative detunings are shown on the Fig.4.10 (c). Note the difference in the degeneracy of the peaks in Fig.4.9 (c) and Fig.4.10 (c): in first case LP is degenerate with UP of different polarization, and in the second case LP is degenerate with LP.

4.4 Degree of Entanglement

To describe the full decay scheme analytically we write the two-photon wavefunction in the following way neglecting cross polarization terms and using the notation UP for the upper and LP for the lower polariton state of the doublet:

$$\begin{aligned} |\Psi\rangle = &\left(\alpha_{LP}\left|p_H^{LP}\right\rangle + \alpha_{UP}\left|p_H^{UP}\right\rangle\right)|HH\rangle + \\ &+ \left(\beta_{LP}\left|p_V^{LP}\right\rangle + \beta_{UP}\left|p_V^{UP}\right\rangle\right)|VV\rangle\,, \end{aligned} \tag{4.3}$$

where we extract the coordinate part $\left|p_{H(V)}^{LP(UP)}\right\rangle$ from the polarization part of the wavefunction $|HH\rangle\,(|VV\rangle)$. The amplitudes α and β are the weights for the possible decay paths satisfying

$$|\alpha_{LP}|^2 + |\alpha_{UP}|^2 + |\beta_{LP}|^2 + |\beta_{UP}|^2 = 1. \tag{4.4}$$

After tracing out over all possible degrees of $|p\rangle$, the corresponding 2 photon density matrix in the basis of HH,HV,VH and VV for scheme 1 of the previous section reads

$$\rho = |\Psi\rangle\langle\Psi| = \begin{pmatrix} |\alpha_{LP}|^2 + |\alpha_{UP}|^2 & 0 & 0 & \gamma \\ 0 & 0 & 0 & 0 \\ 0 & 0 & 0 & 0 \\ \gamma^* & 0 & 0 & |\beta_{LP}|^2 + |\beta_{UP}|^2 \end{pmatrix}, \tag{4.5}$$

where

$$\gamma = \alpha_{LP}\beta_{LP}^*\left\langle p_H^{LP}|p_V^{LP}\right\rangle + \alpha_{UP}\beta_{UP}^*\left\langle p_H^{UP}|p_V^{UP}\right\rangle. \tag{4.6}$$

The detailed derivation of the density matrix is given in the appendix. In case of scheme 2, the off-diagonal element transforms to

$$\gamma = \alpha_{LP}\beta_{UP}^*\left\langle p_H^{LP}|p_V^{UP}\right\rangle \tag{4.7}$$

We select only the degenerate intermediate states using spectral windows, represented by a projection P, around the biexciton emission energy E_{XX} and the polariton energy E_P. One can neglect those scalar products $\langle p_H|p_V\rangle$ which show no overlap assuming that the separation (in the case where two are degenerate) by at least the Rabi splitting Ω is much larger than the width of the wavefunction. This width is mostly governed by the lifetime of the polaritons. It can be more justified by the use of spectral windows where the parts outside of them are not collected and thus do not contribute to the off-diagonal element.

The use of spectral widows, which select only the degenerate LP-polariton states in scheme 1, can be performed by the application of a projection P. The wavefunction has to be retyped by $P\,||\Psi\rangle\,/|P\,||\Psi\rangle\,|^2$ which yield

$$\gamma = \frac{\alpha_{LP}\beta^*_{LP}\left\langle p_H^{LP}|P|p_V^{LP}\right\rangle + \alpha_{UP}\beta^*_{UP}\left\langle p_H^{UP}|P|p_V^{UP}\right\rangle .}{|P\,|\Psi\rangle\,|^2}. \tag{4.8}$$

. Once again, the scalar product $\alpha_{UP}\beta^*_{UP}\left\langle p_H^{UP}|P|p_V^{UP}\right\rangle$ can be neglected, because the spectral windows are centered to detect only the transitions via the lower polariton state.

The final equation for the off-diagonal element of scheme 2 reads

$$\gamma = \frac{\alpha_{LP}\beta^*_{UP}\left\langle p_H^{LP}|P|p_V^{UP}\right\rangle}{|P\,|\Psi\rangle\,|^2}. \tag{4.9}$$

Within the dipole and rotating wave approximations, the perturbation theory [190, 196] gives for the two photon function

$$A_H^{LP} \equiv \alpha_{LP}\left\langle k_1, k_2|p_H^{LP}\right\rangle = \frac{x_{ex}^{H,LP}\sqrt{\Gamma_{XX}}x_{ph}^{H,LP}\sqrt{\Gamma_H^{LP}}/2\pi}{(|k_1|+|k_2|-\epsilon_H^{XX})(|k_2|-\epsilon_H^{LP})}, \tag{4.10}$$

where k_1 and k_2 are the momenta of the photons and $\Gamma_{XX(LP)}$ is the line width of the biexciton (lower polariton). Furthermore, $\epsilon_{XX(LP)} = E_{XX(LP)} + i\Gamma_{XX(LP)}/2$ is the complex energy of the biexciton (lower polariton). The exciton (photon) Hopfield coefficients of the polariton state are denoted by $x_{ex(ph)}^{H,LP}$ and the polariton lifetime is given by the ratio of the square of the photon Hopfield coefficient and the cavity lifetime $\Gamma_{LP} = |x_{ph}^{H,LP}|^2/\tau_C$. A similar expression of Eq.(4.10) can be obtained for the upper polariton state and the perpendicular polarization. The final equation for the off-diagonal element of the density matrix reads for scheme 1 (scheme 2)

$$\gamma' = \frac{\int\int dk_1 dk_2 A_H^{LP*} W A_V^{LP(UP)}}{\int\int dk_1 dk_2 A_H^{LP*} W A_H^{LP} + \int\int dk_1 dk_2 A_V^{LP(UP)*} W A_V^{LP(UP)}}. \tag{4.11}$$

The function W corresponds to the spectral windows at the energies E_{XX} and E_{LP}^H.

Finally, to estimate the quantum correlations of the emitted photons we use the Peres criterion for entanglement [189], which states that the emitted photons are entangled for $\gamma = 1/2$ and not entangled for $\gamma = 0$ (see appendix).

The density matrix of the system is in the so-called "x-form", containing only diagonal and anti-diagonal elements and thus another measure of entanglement – the concurrence C [197] – is simply two times the absolute value of the off-diagonal element of the density matrix [198, 199].

The degree of entanglement is strongly correlated with the line shape of the transitions as it follows from Eq.(4.10)and Eq.(4.11): the better the overlap of the detected emission lines, the higher the off-diagonal element. The photoluminescence spectra for each transition can be calculated by integration of Eq.(4.10) either over k_2 to obtain the biexciton-polariton emission line or over k_1 to obtain the polariton-ground state emission line [196].

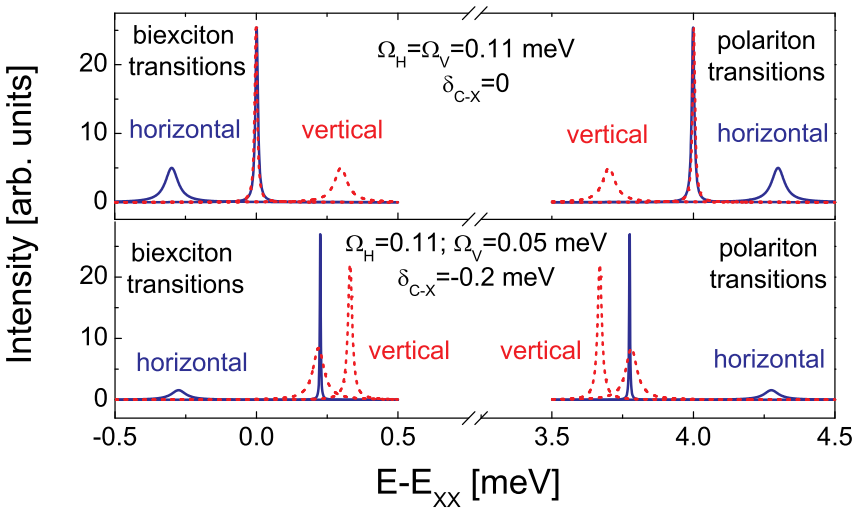

Figure 4.11 | Calculated photoluminescence spectra of the biexciton decay: Photoluminescence spectra for equal splittings (upper panel) at $\delta_{C-X} = 0$ and for splittings $\Omega_H = 0.11$ meV, $\Omega_V = 0.05$ meV at $\delta_{C-X} = -0.2$ meV (lower panel). The blue (red and dashed) line corresponds to horizontal (vertical) polarization.

Fig.4.11 shows the complete spectra of emission resulting from the biexciton decay. The upper panel is calculated for $\Omega_H = \Omega_V$=0.11 meV which corresponds to the experimentally measured value of [8] and the lower one for Ω_H=0.11 meV and Ω_V=0.05 meV. The relative position of the cavity resonance $\delta_{C-X} = (E_C^H + E_C^V)/2 - (E_X^H + E_X^V)/2$ is chosen to degenerate the intermediate polariton states for both cases. The complicated complete spectra shows 4 Lorentzian lines for the biexciton-polariton transitions with a line width $(\Gamma_{XX} + \Gamma_P)$ and 4 Lorentzian lines with Γ_P for the polariton-ground state transitions. The line width depends strongly on the photonic fraction of the polariton because the cavity photon lifetime is typically 100 times shorter that the QD exciton lifetime. One should note that this type of spectra resulting from the biexciton decay in a strongly coupled microcavity has been recently measured but only for one polarization [200]. One can see on the upper panel, that the resonance condition between the two polariton states H and V also corresponds to equal line width of the states and therefore to a high degree of entanglement $\gamma' = 0.49$. On the other hand one can see on the lower panel of the figure that the nice symmetry of the scheme is broken when the oscillator strengths of the two resonances are different. The degree of entanglement is much lower $\gamma' = 0.09$ in this last case, which we are going to analyze in details in the next section.

In [201] the authors have refined our initial proposal improving the calculation of the emission spectra of the transitions by the use of the Weisskopf-Wigner approach. In

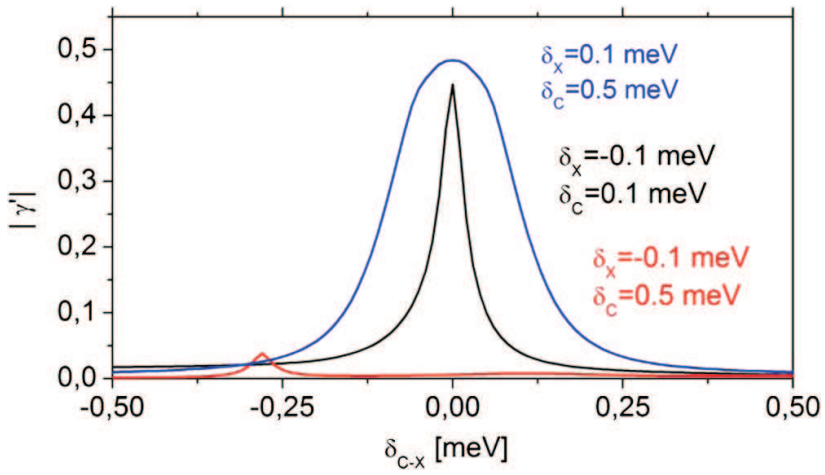

Figure 4.12 | Degree of entanglement: Dependence of the off-diagonal element γ' on the relative position of the cavity resonances δ_{C-X} for the schemes presented in Fig. 4.8 4.9 and Fig. 4.10.

the large coupling constant (g) case, the improvement with respect to the simple picture using Lorenzian lines is not significant. Some changes arise in the small g case, where even without filtering a higher degree of entanglement is predicted with respect to our approach.

Furthermore, more complex approaches for the spectra of strongly coupled quantum dots have been published [202].

To finish this section we compare the degrees of entanglement, which can be obtained for the different schemes. We keep the Rabi-splitting constant for both polarizations. Figure 4.12 shows the numerically obtained off-diagonal element $|\gamma|$ versus $\delta C - X$. The maximum value of $|\gamma|$ for scheme 3 is not optimal, due to the difference between the exciton and photon fractions of the degenerate polariton states. The asymmetry of the curves comes from the small lifetimes for negative detuning δ_{C-X}. Consequently, the line width is larger than the energy difference between the two polariton states, which yields $\left\langle P_H^{LP}|P|P_V^{LP}\right\rangle > 0$. On the other hand, the degree of entanglement achieved within the schemes proposed in Figs. 4.8 and 4.9 reaches almost the maximum value 1/2, which makes these configurations quite favorable.

4.5 Rabi splitting

In the following we analyze the influence of different Rabi splittings of the H and V polariton states on the degree of entanglement γ' of the two photon wave function resulting from the biexciton decay. This polarization anisotropy comes from the asymmetry of the QD or its environment and results in different oscillator strength for excitons which couple to different polarizations [203, 204, 205, 206]. Also misalignment of the quantum dot and the antinode of the cavity mode field in one direction can change the coupling constant [207]. Consequently, the final polariton states of each polarization H and V have different

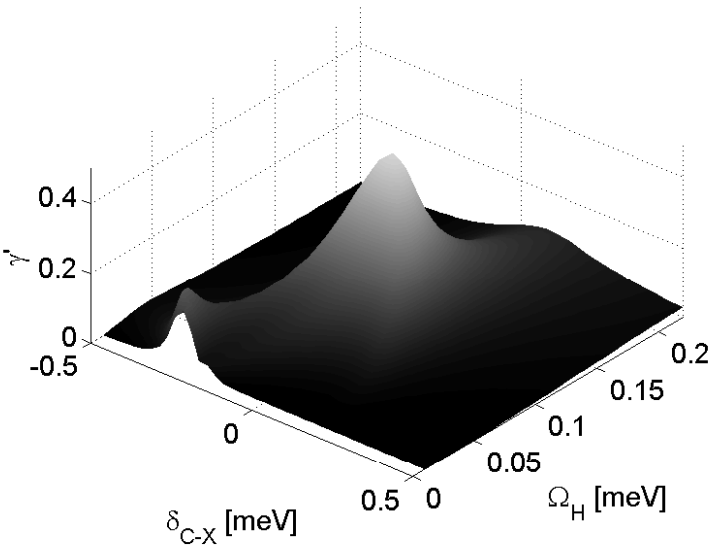

Figure 4.13 | Impact of different Rabi splittings: Dependence of the off-diagonal element γ' on the relative position of the cavity resonances and on the Rabi splitting for one polarization Ω_H. The second splitting is kept constant at $\Omega_V = 0.11$ meV.

values of Rabi splitting Ω_V and Ω_H. We will use only the second scheme, presented in Fig. 4.9 to discuss the effect.

Fig.4.13 shows the degree of entanglement depending on the relative position of the cavity resonances δ_{C-X} and on Ω_H, whereas Ω_V is kept constant, equal to 0.11 meV.

As one can see, the maximum degree of entanglement close to theoretical limit is achieved if both splittings are equal. If one changes the Rabi splitting of one polarization, the degree of entanglement decreases. In the case of $\Omega_H = \Omega_V$, the optimal detuning δ_{C-X} is zero. This optimal value of δ_{C-X} becomes positive when $\Omega_H - \Omega_V$ is positive and negative when $\Omega_H - \Omega_V$ is negative. In addition to the main maximum, the degree of entanglement shows a three-peak structure for small Ω_H and a second small maximum. These effects arise from the interplay between the evolution of the lineshapes and overlaps of the transitions in the region where the polariton states are close to each other, depending on δ_{C-X}.

The difference of the Rabi splittings makes necessary a readjustment of the cavity resonances. In the following we are going to tune independently the energies of the H and V polarized modes. It means that now we tune not only δ_{C-X}, but also δ_C. This can be achieved experimentally by atomic force microscope nano-oxidation of the cavity surface [15]. The results of the calculations are shown on Fig. 4.14. We use Ω_H=0.11 meV, Ω_V=0.05 meV, and δ_X=0.25 meV (as for the lower panel of figure 4.11), which represent a highly asymmetric case. Fig. 4.14 (a) shows γ' versus δ_{C-X} (x-axis) and δ_C (y-axis). One can see that the independent tuning of the position of the two photon modes allows to recover quite a high value $\gamma' = 0.41$. The photoluminescence spectra corresponding to this optimal configuration are shown on the Fig.4.14 (b). Once again,

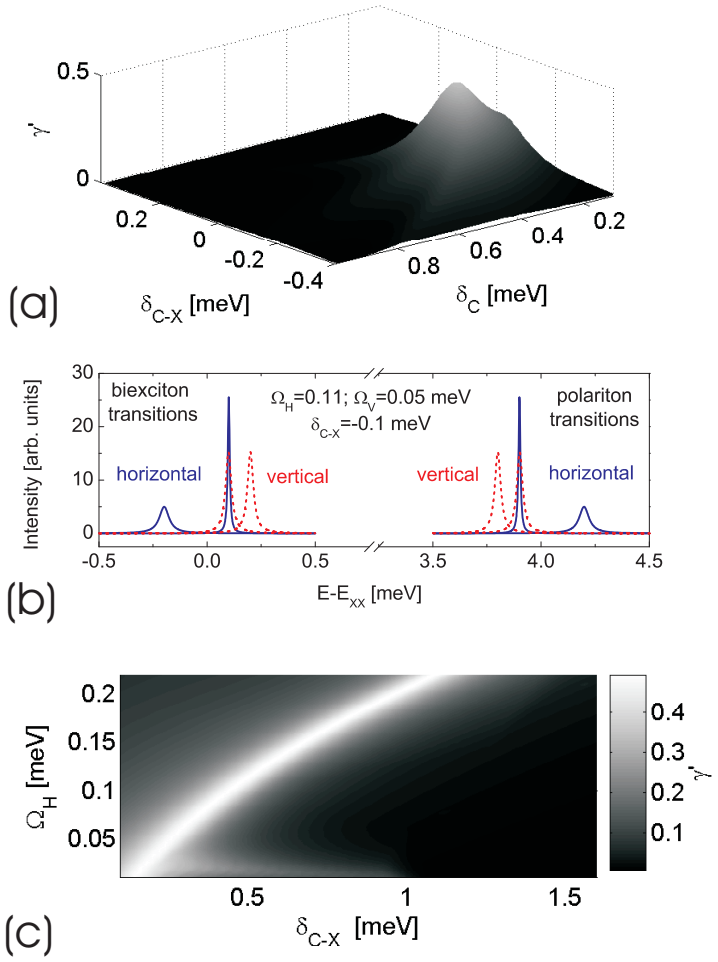

Figure 4.14 | Readjustment of the cavity resonances: (a) Dependence of the off-diagonal element γ' on the relative position of the cavity resonances and on the splitting between the photonic modes δ_C. The Rabi splittings are kept constant at $\Omega_H = 0.11$ meV and $\Omega_V = 0.05$ meV. (b) Photoluminescence spectra for a splitting $\delta_C = 0.3$ meV. The blue (red and dashed) lines corresponds to horizontal (vertical) polarization. (c) Degree of entanglement versus cavity resonance splitting and Rabi splitting.

γ' shows a complicated three-peak-structure when the detunings are not optimized (see Fig.4.14 (a)), which finds its origin in the interplay between the evolution of the lineshapes and overlaps of the transitions.

In Fig. 4.14(c), we keep $\Omega_V = 0.11meV$ constant and show the best value of γ' (which can be obtained tuning δ_{C-X}) versus Ω_H and δ_C. From this figure one can conclude that, whatever the value $\Omega_H - \Omega_V$, it is possible to find the values of δ_C and δ_{C-X} for which γ' is larger than 0.4, which confirms the fact that the detrimental effect induced by the difference of Ω_H and Ω_V can be, in all cases, overcome by the independent tuning of the cavity mode energies.

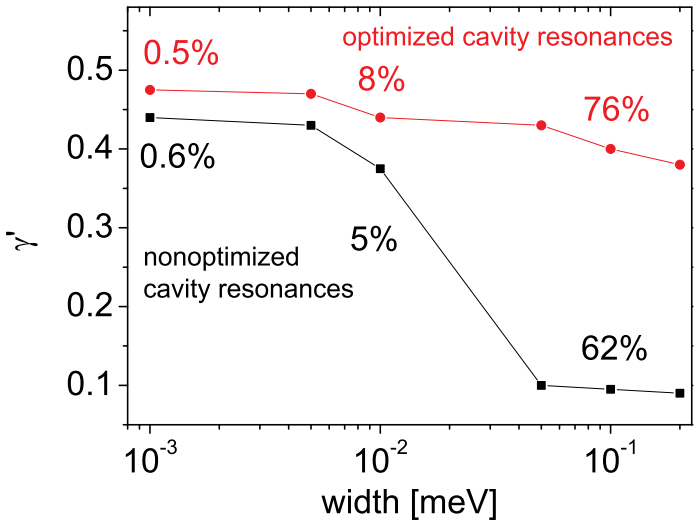

Figure 4.15 | Spectral filtering: Degree of entanglement versus the width of the spectral windows for non-optimized cavity resonances (black squares) and optimized cavity resonances (red points). The percentages are the calculated quantum efficiencies.

4.6 Spectral filtering

Spectral filters have been used by Akopian et al. in 2006 [190] to increase the quantum correlations of detected photons. Therein, the spectral windows were used to select the overlapping part of the non-degenerate exciton emission lines and thus a non-zero off-diagonal element of the density matrix has been observed. This filtering is furthermore robust against fluctuations of the energy levels[208]. We define the quantum efficiency as the ratio between the number of photon pairs emitted and the number of photon pairs detected through the spectral window. This efficiency is expected to become smaller and smaller with the use of a sharper spectral window. The scheme we have proposed above already includes the use of spectral windows to preselect the appropriate transition lines, but there is no filtering in the sense that we always detect the whole emitting line. In the following, we analyze the impact of the width of the spectral windows on the entanglement degree and on the quantum efficiency of the biexciton decay. Fig.4.15 shows the dependence of γ' on the width of the two identical windows around E_p and $E_{XX} - E_p$ together with the evolution of the quantum efficiency.

Two cases are considered, which are: the unfavorable case presented on the lower panel of the figure 2, and the one obtained for the same set of parameters but with the optimization of δ_C maximizing γ'. Both optimized and none optimized configurations show high γ' and low quantum efficiency, below 1% for the smallest width of spectral filters ($< 10\mu eV$). Increasing this spectral width has a dramatic effect on the γ' value for the non-optimized case. In contrast, the optimized setup allows to achieve a high degree of entanglement simultaneously with a large quantum efficiency by using a wide spectral window of 0.1 meV.

4.7 Strongly coupled biexciton

Another possibility which can be taken into account is the existence of additional resonances, e.g. a photonic mode close or at the biexciton-exciton transition energy. The idea is to accelerate the emission of entangled photon pairs by mixing the biexciton with a photon. We add now a V and an H-polarized photon fields at the biexciton-polariton transition energy with energies $E^H_{C_{XX}}$ and $E^V_{C_{XX}}$. One should therefore have a reversible coupling between three possible configurations for each polarization which are: the biexciton, one exciton and one photon, and two photons. Taking into account the polarization degree of freedom and the fact that the bi-exciton is a common state for the two polarization channels, we should describe the reversible coupling between 5 states. The eigenenergies of the resulting dressed states can be found by the diagonalization of the 5X5 matrix M, where $\Omega^{XX}_{H(V)}$ is the coupling to the biexciton state:

$$M = \begin{pmatrix} E_{XX} & \Omega^{XX}_H & \Omega^{XX}_V & 0 & 0 \\ \Omega^{XX}_H & E^H_X + E^H_{C_{XX}} & 0 & \Omega_H & 0 \\ \Omega^{XX}_V & 0 & E^V_X + E^V_{C_{XX}} & 0 & \Omega_V \\ 0 & \Omega_H & 0 & E^H_C + E^H_{CXX} & 0 \\ 0 & 0 & \Omega_V & 0 & E^V_C + E^V_{CXX} \end{pmatrix}. \tag{4.12}$$

The structure of the five eigenvalues and eigenvectors of this matrix is quite complicated in the general case. It is possible to tune $E^H_{C_{XX}}$ and $E^H_{C_{XX}}$ in such a way that the two polarized biexciton-polariton transitions from one initial bipolariton state are symmetric, which means that both polarization paths have the same radiative lifetime and thus the same linewidth. This results in a high degree of entanglement if we assume that the polariton-ground state transitions are optimized and unperturbed. In addition the decay from a "photon-like" bipolariton state is much faster in comparison to the uncoupled biexciton. The full transition to the ground state will take place in a few ps and repetition rates close to THz range become realistic.

The design of a 4-resonance-cavity is the same as for the standard scheme with two modes. It was based on polarization doublet of the 'photonic dot' ground states with close to symmetrical intensity profile. In case of to higher resonances the interplay between the polarization and confinement of the photonic modes results in the formation of the 4 resonances originating from the 'scalar' doublet (0,1)-(1,0), i.e. the states with 1 node line in x or y directions in the intensity profile. The emission pattern of these modes is angular-polarization dependent and this must be accounted for in the analyzing of the outgoing photons, but in principle the design of such a cavity should be possible.

However, the realization and the adjustment of four different photonic resonances at the same time seems to be extremely challenging. Furthermore the resulting fine structure

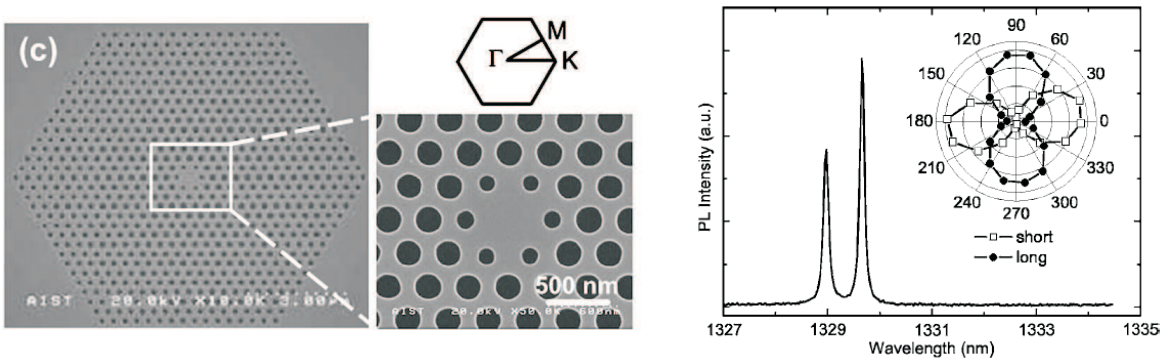

Figure 4.16 | High quality photonic crystal structures with mode splitting [195]: (left) Specifications of fabricated QD-embedded PC nanocavity. SEM image of the PC structure with the corresponding reciprocal lattice space. (right) Typical spectrum of the dipole modes with $Q > 10000$. The small local fabrication error breaks the degeneracy of modes A and B to make a 0.7 nm split. Inset: polar plot of the polarization dependence of short (open squares with line) and long (filled circles with line) wavelength modes.

of the bipolariton is complicated and the selection of the transition lines would be also a difficult problem, which would end up by a huge reduction of the quantum efficiency. Thus, we do not believe at this stage that a biexciton strongly coupled to light modes in addition to the strong coupling of the excitons would be really advantageous for applied purposes.

We do not address the excitation at such frequencies with all arising problems of e.g. multiple photon pair generation. This will be another restriction towards high speed devices. We only discuss fast photon pair emission as a prerequisite to achieve such high repetition rates.

Nevertheless, a photonic resonance weakly coupled to the biexciton-polariton transition may accelerate the first photon emission, either by Purcell effect, or simply by reducing the quenching of the emission which could be provoked by the fact that the resonance is placed within a photonic bandgap. Also dressing the biexciton state modifies the transition properties [209, 210] and stays as a tool for future applications.

4.8 Experimental implementation

As mentioned already in the first chapter, one dimensional polaritons have been observed recently for various cavity designs [13, 14, 15, 18]. In our proposal we focused on photonic crystal cavities. In general, the quantum dot is placed as an defect state into the lattice of holes. The structure of suited cavities with quality factors above 10^4 [207] is shown

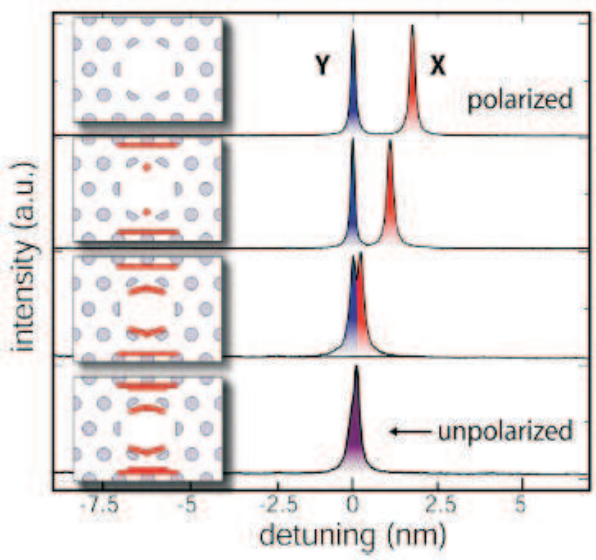

Figure 4.17 | Tuning of photonic crystal resonances [8]: PL spectra showing the detuning of the dipole-mode pair in one cavity resonant at 950 nm. The detuning of a DX mode is reduced from 2 to 0.1 nm as the cavity is sequentially AFM oxidized according to the insets on the left, where the oxide is depicted in red.

in Fig.4.16 on the left hand side. The placement of the dot is now well under control. What we need are split photonic modes for the linear polarizations. In fact, normally one tries to avoid this splitting and the photonic crystal community has made a huge effort to create degenerated photonic modes [195]. The right hand side of Fig. 4.16 shows the photoluminescence of such a structure with non-degenerate cavity dipole modes. We use now this splitting, which comes from any small fabrication imperfection of the holes in the photonic crystal [195].

Once the quantum dot is embedded into the crystal, the resonances have to be adapted carefully if has not been done before, during the fabrication of the crystal. This can be done by AFM nano-oxidation of the cavity surface [8]. Fig. 4.17 shows the application of this technique to shift the photon modes to the desired position. The technique provides nearly continuous tuning of a single mode over several nanometers and is in principle applicable to all photonic crystal based cavity structures. This powerful tool makes our proposal more realistic because the cavity resonances can be modified after the fabrication of the quantum dot. This means the properties of the crystal can be adjusted perfectly to the properties of the embedded dot. Once the cavity modes are precisely tuned to the exciton levels in a QD, efficient nonclassical photon sources can be achieved for quantum information processing.

Finally, a strongly coupled biexciton requires additional resonances in the crystal. this can in principle provided by higher resonances. In the previous picture, we discussed dipole modes of the crystal, with a maximum of the electric field in the center of the quantum dot. Fig. 4.18 shows the electric field distribution of different resonances of the quantum dot together with the energy distribution depending on the crystal parameters.

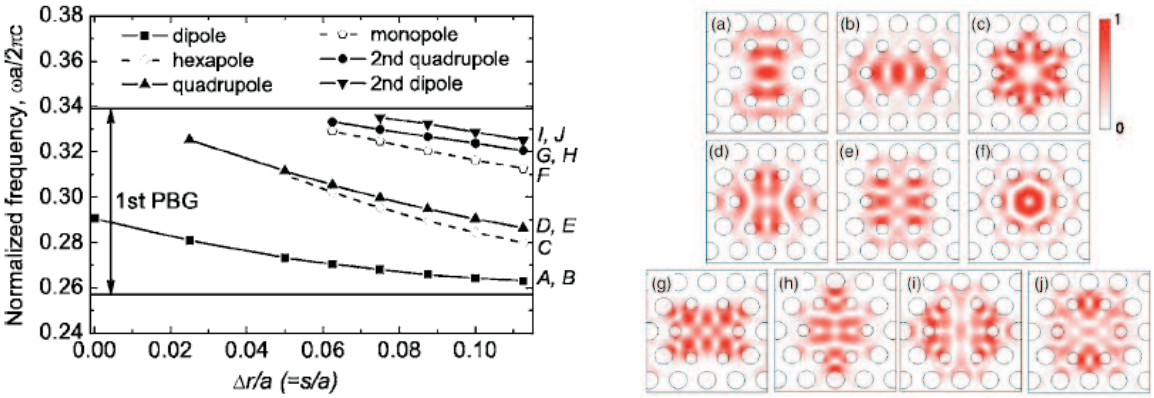

Figure 4.18 | Cavity mode frequencies and electric field inside a photonic crystal [195]: (left) Normalized cavity-mode frequencies as a function of $\Delta r/a$. The solid (dashed) lines correspond to doubly degenerate (nondegenerate) cavity modes. The ten modes are referred to as modes A-J in order of frequency. (right) Calculated electric field distributions in the slab center for ten cavity modes with $\delta r/a = 0.11$. The modes in (a)(j) correspond to modes A-J on the left hand side, respectively.

For example the second dipole modes (i and j in the figure) could be the candidates for strongly coupled biexciton devices.

Of course the coupling between the dot and the cavity depends strongly on the position of the dot in the cavity, and the dot should may be not centered in the defect state because the electric field maxima are not centered.

All these techniques together confirm the possibility to realize the proposal of a entangled photon source, as discussed in this chapter.

Possible other cavity configurations are micropillars. Recently, new fabrication techniques have been developed to place a quantum dot exactly in the center of a micropillar [211]. Extending this techniques, one may fabricate slightly elliptic micropillars to obtain a split of the linear polarized cavity modes. Secondly, the spatial profile of the emission is the same for both polarizations. (By the way, this is not the case for photonic crystals, which make the realization based on crystals a bit more challenging.) Thus, also micropillars with embedded quantum dot can be a promising candidate for the present proposal, beside the exciting results on single photon sources [212, 213]. Nevertheless, this structures are in the process of development and several problems are not solved, i.e. the extraction of the biexciton-exciton photon is still not possible, because it is in the photonic gap. May-be lateral detection can solve this problem.

4.9 Summary and conclusions

We have shown that the difference of exciton oscillator strengths of the exciton states coupled to V and H polarized light strongly affects the entanglement degree of the photon pairs emitted during the biexciton decay, when the excitonic resonance of the QD is strongly coupled to the cavity modes of a photonic crystal. However, we have shown that this detrimental effect can be compensated if it is possible to tune independently the energies of the polarized photonic modes, which has been demonstrated to be possible experimentally [15]. We have also analyzed the impact of a spectral filtering of the different emission lines, showing that an increase of the entanglement degree by this method has to be paid for by a strong reduction of the quantum efficiency. Finally, we have discussed the possible impact of the presence of a cavity mode resonant with the biexciton transition. We found that this coupling can indeed accelerate the biexciton decay and give access to very high repetition rates (close of one THz) for the entangled photon emission. However, the complication brought by the presence of many polariton lines which should be all tuned simultaneously makes this configuration very hard to implement for an experimental point of view. We conclude that the control of the electronic resonances through their strong coupling to confined cavity modes opens new perspectives and is from many points of view extremely advantageous for the fabrication of a solid source of entangled photon pairs emitted on demand.

Appendix A

Polariton scattering amplitudes

In this part we want to describe briefly the main scattering mechanisms in semiconductor microcavities. We restrict ourself to the final equations. The exact scattering matrix elements and the derivation of the scattering amplitudes are given in [5].

A.1 Polariton decay

As a result of the polariton dispersion, the polariton decay varies depending on the wavevector. Three regions can be identified:

1. $k < k_{SC}$: This is the region, where the exciton-photon anticrossing takes place. The decay is mainly dominated by the finite cavity photon livetime:

$$\Gamma_k = \frac{c_k}{\tau_c}, \tag{A.1}$$

where c_k is the photon fraction of the polariton and τ_c is the cavity lifetime.

2. $k_{SC} < k < k_L$,where k_L is the wavevector of light in the medium. In this region excitons are only weakly coupled to the light mode and the polariton decay is $\Gamma_k = \Gamma_0$, which is the radiative decay of quantum well or bulk excitons.

3. $k > k_L$: Beyond the wavevector of the light in the medium, excitons are no longer coupled to the light. The decay is governed by nonradiative processes $\Gamma_k = \Gamma_{nr}$ which we do not want to discuss in detail.

A.2 Polariton-Phonon interaction

The theoretical description of exciton-phonon interaction has received considerably attention throughout the history of semiconductor heterostructures. Scattering events should conserve the wavevector in the plane. The phonon wave-vector is called q with in-plane

component q_{II} and z-component q_z. Using Fermi-Golden Rule the scattering rate between two discrete polariton states of wavevector$k$ and k' reads:

$$W^{phon}_{k\to k'} = \frac{2\pi}{\hbar}\sum_q |M(q)|^2(0, 1 + N^{phon}_{q=k-k'+q_z})\delta(E(k') - E(k) \mp \hbar\omega_q), \tag{A.2}$$

where N^{phon}_q is the phonon distribution function. In equilibrium $N^{phon}_q = 1/e^{-E(q)/k_bT} - 1)$, where $E(q)$ is the phonon dispersion. The 1 and the - holds for absorption of a phonon and 1 and + holds for emission of a phonon. M is the matrix element of interaction between phonons and photons. For polaritons with a finite energy, the delta-function can be replaced by a Lorentzian and this yields

$$W^{phon}_{k\to k'} = \frac{2\pi}{\hbar}\sum_q |M(q)|^2(0, 1 + N^{phon}_{q=k-k'+q_z}) \tag{A.3}$$

$$\times\frac{\hbar\gamma_{k'}/\pi}{(E(k') - E(k) \pm \hbar\omega_q)^2 + (\hbar\gamma_{k'})^2}. \tag{A.4}$$

The energy width of the state can be defined as the imaginary part of its eigenenergy. The energy conservation in the plane limits the sum to the z-direction.

In the framework of the Born approximation the matrix element of interaction can be written as

$$|M(q)| = |\left\langle \Psi^{pol}_k | H^q_{exc-phon} | \Psi^{pol}_{k'} \right\rangle| = \sqrt{x_k x_{k'}}|\left\langle \Psi^{exc}_k | H^q_{exc-phon} | \Psi^{exc}_{k'} \right\rangle|, \tag{A.5}$$

where $\Psi^{pol(exc)}$ is the polariton (exciton) wavefunction:

$$\Psi^{exc}_k(r_e, r_h) = f_e(z_e)f_h(z_h)\frac{1}{\sqrt{S}}e^{ik(\beta_e r_e - \beta_h r_h)}\sqrt{\frac{2}{\pi}}\frac{1}{a^{2D}_b}e^{-|r_e - r_h|/a^{2D}_b}, \tag{A.6}$$

where $z_{e(h)}$ are the coordinates along the growth direction z and $r_{e(h)}$ are the coordinates in the plane, $f_{e(h)}$ are the electron and hole wave-functions in the growth direction. a^{2D}_b is the exciton Borh radius, $\beta_{e(h)} = m_{e(h)}/(m_e + m_h)$ and S is a normalization area.

A.2.1 Interaction with longitudinal optical phonons

The interaction is mainly mediated by the Fröhlich interaction [214]. The Matrix element in two and three dimensions can be approximated as

$$M^{LO}_2 d(q) = \frac{M^{LO}_0}{\pi}\sqrt{\frac{L}{S}}, M^{LO}_3 d(q) = \frac{M^{LO}_0}{\pi\sqrt{SL}}. \tag{A.7}$$

Finally, assuming dispersionless phonons, the scattering rate can be written as:

$$W^{phon-LO}_{k\to k'} = \frac{2L}{\pi^2\hbar S}x_k x_{k'}|M^{LO}_0|\left(0, 1 + \frac{1}{e^{-\hbar\omega_{LO}/k_bT} - 1}\right) \tag{A.8}$$

$$\times\frac{\hbar\gamma_{k'}}{(E(k') - E(k) \mp \hbar\omega_{LO})^2 + (\hbar\gamma_{k'})^2}. \tag{A.9}$$

Optical phonons interact very strongly with carriers. They allow a fast exciton formation. Nevertheless, the energy of optical phonons is in the range from $20-80$ meV and thus an exciton with a kinetic energy below this range can not emit an optical phonon. This is one reason why exciton gases stay at 100-200 K and further cooling via optical phonons is not possible.

A.2.2 Interaction with acoustic phonons

The interaction is mainly mediated by the deformation potential. The exciton-acoustic phonon matrix element reads:

$$M^{ac}(q) = \sqrt{\frac{\hbar q}{2\rho c_s SL}} G(q_{II}, q_z), \tag{A.10}$$

where ρ is the density and c_s is the speed of sound in the medium. Assuming isotropic bands, G reads

$$G(q_{II}, q_z) \quad = D_e I_e^z(q_z) I_e^{II}(q_{II}) + D_h I_h^z(q_z) I_h^{II}(q_{II}) \tag{A.11}$$

$$\approx D_e I_e^{II}(q_{II}) + D_h I_h^{II}(q_{II}). \tag{A.12}$$

D_e and D_h are the deformation coefficients of the conduction and valence band, respectively, and $I_{e(h)}$ are the overlap integrals between the exciton and phonon mode in the growth direction and in plane.

Using this Matrix element and moving to the thermodynamic limit, which means that we let go the system in a given direction to infinity, the scattering rate becomes:

$$W_{k\to k'}^{phon} = \quad \frac{|G(k-k')|^2}{2\pi S\rho c_s} x_k x'_k \int_{q_z} |k-k'+q_z|(0, 1+N_{k-k'+q_z}^{phon}) \tag{A.13}$$

$$\times \frac{\hbar\gamma_{k'}/\pi}{(E(k')-E(k)\mp\hbar\omega_{k-k'+q_z})^2+(\hbar\gamma_{k'})^2} dq_z. \tag{A.14}$$

The scattering with acoustic phonons is the main process for the final down cooling of an exciton gas to the lattice temperature, where optical phonons can not be emitted.

A.3 Polariton-electron interaction

The polariton-electron scattering rate is calculated using Fermi Golden Rule as

$$W_{k\to k'}^{el} = \quad \frac{2\pi}{\hbar} \sum_q |M_{q,k,k'}^{el}|^2 x_k x_{k'} N_q^e (1-N_{q+k'-k}^e) \tag{A.15}$$

$$\times \frac{\hbar\gamma_{k'}/\pi}{(E(k')-E(k)+\frac{\hbar^2}{2m_e}(q^2-|q+k-k'|^2))^2+(\hbar\gamma_{k'})^2}, \tag{A.16}$$

where N_q^e is the electron distribution function and m_e is the electron mass. A detailed calculation of the electron-polariton matrix element can be found in Refs. [32, 215].

The interaction of electrons and polaritons are dipole-charge interaction and take place in a few picoseconds. An equilibrium electron gas can thermalize a polariton gas quite efficiently. However, more complicated effects, such as the formation of trions are also possible.

A.4 Polariton-Polariton interaction

The polariton-polariton scattering rate reads:

$$W_{k\to k'}^{pol} = \frac{2\pi}{\hbar}\sum_q |M_{ex}|^2 x_k x_{k'} x_q x_{q+k'-k} N_q^{pol}(1+N_{q+k'-k}^{pol}) \tag{A.17}$$

$$\times \frac{\hbar\gamma_{k'}/\pi}{(E(k')-E(k)+E(q+k'-k)-E(q))^2+(\hbar\gamma_{k'})^2}, \tag{A.18}$$

The exciton-exciton matrix element of interaction is composed of a direct and an exchange term [41]. Here, we shall use the numerical estimate [34] of this quantity, which we shall assume constant over the whole reciprocal space:

$$M_{ex} \approx 6\frac{(a_b^{2D})^2}{S}E_b, \tag{A.19}$$

where E_b is the exciton binding energy. Passing to the thermodynamic limit in the plane, the scattering rate becomes:

$$W_{k\to k'}^{pol} = \frac{1}{2\pi^2\hbar S}\int d^2q |M_{ex}^0|^2 x_k x_{k'} x_q x_{q+k'-k} N_q^{pol}(1+N_{q+k'-k}^{pol}) \tag{A.20}$$

$$\times \frac{\hbar\gamma_{k'}/\pi}{(E(k')-E(k)+E(q+k'-k)-E(q))^2+(\hbar\gamma_{k'})^2}. \tag{A.21}$$

As one can see, the a priori unknown polariton distribution function is needed to calculate scattering rates. This means that in any simulation these scattering elements should be updated dynamically throughout the simulation time, which can be extremely time consuming. Polariton-polariton scattering has been shown to be extremely efficient, when a cavity is resonantly excited. It also plays a role in the case of non-resonant excitation. Depending on the excitation condition and on the nature of the used semiconductor, the exciton-exciton interaction may be strong enough to self-thermalize the exciton reservoir at a given temperature.

Appendix B

Derivation of Fokker-Planck Equation

B.1 Langevion equation

We follow the description of Ref. [104]. The temporal evolution of the relevant degrees of freedom of dynamical systems that interact with a fluctuating environment is often described by an equation of motion, which is a stochastic equation:

$$\dot{x} = A(x,t) + q(t). \tag{B.1}$$

For different systems the variables in the above equation have different meanings, but to be concrete we will call $x(t)$ $[x(0) = 0]$ a particle coordinate, $A(x,t) = -\partial U(x,t)/\partial x$ a force field, $U(x,t)$ an external deterministic potential, $q(t)$ a random force (noise) resulting from a fluctuating environment.

In order to determine the statistical properties of $x(t)$ we have to specify the properties of $q(t)$. We shall take $q(t)$ to be a Gaussian random process of zero mean

$$\langle q(t) \rangle = 0, \tag{B.2}$$

with extremely rapid fluctuations. We shall therefore approximate the two-time correlation function by a delta-function, and write

$$\langle q_i(t) q_j(t') \rangle = g_{ij}(t) \delta(t - t'). \tag{B.3}$$

Under these conditions Eq.(B.1) is usually known as Langevin equation. As the random process $q(t)$ evolves in its own way so as to drive $x(t)$, it is apparent that $x(t_1)$ will be uncorrelated with $q(t_2)$ at a later time t_2, or

$$\langle x_i(t_1) q_j(t_2) \rangle = 0, t_2 > t_1. \tag{B.4}$$

Moreover, the future evolution of $x(t)$ through Eq.(B.1) is governed only by the present, and the past history of $x(t)$ plays no role, so that $x(t)$ is Markovian of first order. The statistics of $x(t)$ are therefore completely determined by the probability density $p(x,t)$ and by the transition probability density $P(x,t|x_0,t_0)$, which obey Fokker-Planck equations, as we now show.

B.2 Kramers-Moyal differential equation

We use the general integration relation that connects the probability density $p(x_2,t_2)$ with $p(x_1,t_1)$ at an earlier time to obtain the time derivative of $p(x,t)$. We put now $t_1 = t$ and $t_2 = t + \delta t$. The relation can be written as

$$p(x,t+\delta t) = \int P(x,t+\delta t|x_1,t)p(x_1,t)dx_1. \tag{B.5}$$

In the above equation P is the conditional probability density, which connects the probability density $p(x_1,t_1)$ with a later time $p(x_2,t_2)$. Starting from this point the rate of change of $p(x,t)$ can be expressed as follows

$$\frac{\partial p(x,t)}{\partial t} = \lim_{\delta t\to 0}\frac{1}{\delta t}\left[p(x,t+\delta t) - p(x,t)\right] \tag{B.6}$$

$$= \lim_{\delta t\to 0}\frac{1}{\delta t}\left[\int P(x,t+\delta t|x_1,t)p(x_1,t)dx_1 - p(x,t)\right]. \tag{B.7}$$

We make now the change of variable $x - x_1 = \Delta x$, and write

$$\frac{\partial p(x,t)}{\partial t} = \lim_{\delta t\to 0}\frac{1}{\delta t}\left[\int P(x-\Delta x+\Delta x, t+\delta t|x-\Delta x,t)p(x-\Delta x,t)d\Delta x - p(x,t)\right]. \tag{B.8}$$

The integrand can be regarded as a function $f(y,z)$ of the two variables $y = x - \Delta x$ and $z = \Delta x$. With respect to the variable y, let us expand $f(y,z)$ in a Taylor series about $y = x$, keeping z constant,

$$f(x-\Delta x,z) = \sum_{r=0}^{\infty}\frac{(-1)^r}{r!}(\Delta x)^r\frac{\partial^r}{\partial x^r}f(x,z). \tag{B.9}$$

When this expansion is substituted under the integral in Eq.(B.8) we obtain the equation

$$\frac{\partial p(x,t)}{\partial t} = \lim_{\delta t\to 0}\frac{1}{\delta t}\left[\int\sum_{r=0}^{\infty}\frac{(-\Delta x)^r}{r!}\frac{\partial^r}{\partial x^r}P(x+\Delta x,t+\delta t|x,t)p(x,t)d\Delta x - p(x,t)\right]. \tag{B.10}$$

We now interchange the order of summation and integration and integrate term by term. The term $r = 0$ integrates to $p(x,t)$, which cancels the last term. For the remaining terms we define the quantities

$$D_r(x,t) \equiv \lim_{\delta t \to 0} \frac{1}{\delta t} \left[\int (\Delta x)^r \, P(x + \Delta x, t + \delta t | x, t) p(x,t) d\Delta x \right], r = 1, 2, 3..., \quad \text{(B.11)}$$

which are known as the transition moments of the random process $x(t)$. The transition moment $D_r(x,t)$ is proportional to the r'th moment of the change of the process in a short time δt, subject to the initial value x at time t. This is sometimes expressed in the form

$$D_r(x,t) \equiv \lim_{\delta t \to 0} \frac{\langle (\Delta x)^r \rangle_{x,t}}{\delta t}. \quad \text{(B.12)}$$

With the help of this definition Eq.(B.10) can be re-written in the more compact form

$$\frac{\partial p(x,t)}{\partial t} = \sum_{r=1}^{\infty} \frac{(-1)^r}{r!} \frac{\partial^r}{\partial x^r} \left[D_r(x,t) p(x,t) \right], \quad \text{(B.13)}$$

which is known as the Kramers-Moyal differential equation. In general it is a partial differential equation of infinite order, although the order may become finite in certain cases, as we will see. The effect of the first term involving D is called *drift* term, and the second one is called *diffusion* coefficient.

B.3 The Fokker-Planck equation

We can now write the transition moments for the Langevin equation described above. After the integration of equation (B.1) over a very short time interval δt, we have

$$\Delta x_i(t) \equiv x_i(t + \delta t) - x_i(t) = A_i(x,t)\delta t + \int_t^{t+\delta t} q_i(t') dt'. \quad \text{(B.14)}$$

Although δt is very small, the integral in the last equation cannot be replaced by $q_i(t)\delta t$, because $q_i(t')$, being delta-correlated, can fluctuate even in a infinitesimal interval. If we calculate the average of both sides of this equation, subject to the contrained that $x(t)$ has some given value, divide by δt and proceed to the limit $\delta t \to 0$, we obtain the drift vector $D_i(x,t)$ of the random process. Now

$$\begin{aligned} \langle x_i(t + \delta t) - x_i(t) \rangle_{x,t} = & \quad A_i(x,t)\delta t + \int_t^{t+\delta t} \langle q_i(t') \rangle \, dt' \quad \text{(B.15)} \\ = & \quad A_i(x,t)\delta t, \end{aligned}$$

by virtue of $\langle q(t) \rangle = 0$, so that

$$D_i(x,t) = A_i(x,t). \quad \text{(B.16)}$$

We have therefore shown that the average forcing term in the Langevin equation is the Drift vector of the random process. This is also apparent from the fact that $A_i(x,t)$ is the conditional average of the velocity of $x(t)$.

Next we calculate the diffusion tensor. This requires that we average the product $\Delta x_i \Delta x_j$ subject to the constrained that x has a given value at time t. We obtain

$$\begin{aligned} D_{ij}(x,t) &\equiv \lim_{\delta t\to 0}\frac{1}{\delta t}\left\langle \left[A_i(x,t)\delta t + \int_t^{t+\delta t} q_i(t')dt'\right]\left[A_j(x,t)\delta t + \int_t^{t+\delta t} q_j(t')dt'\right]\right\rangle_{x,t} \quad \text{(B.17)}\\ &= \lim_{\delta t\to 0}[A_i(x,t)A_j(x,t)\delta t + \left\langle A_i(x,t)\int_t^{t+\delta t} q_j(t')\right\rangle_{x,t} dt' \\ &+ \left\langle A_j(x,t)\int_t^{t+\delta t} q_i(t')\right\rangle_{x,t} dt' + \frac{1}{\delta t}\int_t^{t+\delta t}\int_t^{t+\delta t}\langle q_i(t')q_j(t'')\rangle\, dt'dt'']. \end{aligned}$$

The first term on the right vanishes in the limit $\delta t \to 0$, and the second term and third terms average to zero by the fact that $x(t)$ is independent of $q(t')$ at later time t'. For the fourth term we make use of approximate that the two-time correlation function is a delta function and obtain finally

$$D_{ij}(x,t) \equiv \lim_{\delta t\to 0}\frac{1}{\delta t}\int_t^{t+\delta t}\int_t^{t+\delta t} g_{ij}(t')\delta(t'-t'')dt'dt'' = g_{ij}(t). \quad \text{(B.18)}$$

It follows that the strength of the Langevin noise yields the diffusion tensor. A similar argument can now be used to calculate any higher-order transition moment and it will be found that all higher moments vanish in the limit $\delta t \to 0$. Plugging these results now in the Kramers-Moyal differential equation yield that p(x,t) obeys the second order Fokker-Planck equation

$$\frac{\partial p(x,t)}{\partial t} = -\frac{\partial}{\partial x_i}\left[A_i(x,t)p(x,t)\right] + \frac{1}{2}\frac{\partial^2}{\partial x_i \partial x_j}\left[g_{ij}(x,t)p(x,t)\right]. \quad \text{(B.19)}$$

The Langevin process obeying the stochastic equation (B.1) is therefore a Fokker-Planck process.

Appendix C

Datta and Das Spin transistor

C.1 Polarization in the spin-Meissner phase

The polarization of the elementary excitations of the condensate in the spin-Meissner phase (region 2) has never been calculated. It can be found by the standard method of linearization with respect to the amplitude of the elementary excitations of the condensate. Let us take the wavefunction

$$\Phi(r,t) = \sqrt{n}\vec{e} + \vec{A}e^{i(kr-\omega t)} + \vec{B}^* e^{-i(kr-\omega t)}, \tag{C.1}$$

where in case $B < B_c$,

$$\vec{e} = \begin{pmatrix} \cos\theta \\ \sin\theta \end{pmatrix}, \theta = \frac{1}{2}\arcsin\sqrt{1-\left(\frac{B}{B_c}\right)^2}, \tag{C.2}$$

and substitute it into the Gross-Pitaevskii equations:

$$\begin{aligned} i\frac{\partial\psi_\uparrow}{\partial t} &= (H_0 - \mu - \Omega/2)\,\psi_\uparrow + \left[\alpha_1 |\psi_\uparrow|^2 + \alpha_2 |\psi_\downarrow|^2\right]\psi_\uparrow \\ i\frac{\partial\psi_\downarrow}{\partial t} &= (H_0 - \mu + \Omega/2)\,\psi_\downarrow + \left[\alpha_1 |\psi_\downarrow|^2 + \alpha_2 |\psi_\uparrow|^2\right]\psi_\downarrow. \end{aligned} \tag{C.3}$$

This gives 6 equations:

$$\begin{gathered} \left(-\mu - \tfrac{\Omega}{2}\right) + \alpha_1 n e_\uparrow^2 + \alpha_2 n e_\downarrow^2 = 0 \\ \left(-\mu + \tfrac{\Omega}{2}\right) + \alpha_1 n e_\downarrow^2 + \alpha_2 n e_\uparrow^2 = 0 \\ A_\uparrow\left(\omega_0 - \omega - \mu - \tfrac{\Omega}{2} + 2\alpha_1 n e_\uparrow^2 + \alpha_2 n e_\downarrow^2\right) + B_\uparrow\left(\alpha_1 n e_\uparrow^2\right) + A_\downarrow\left(\alpha_2 n e_\uparrow e_\downarrow\right) + B_\downarrow\left(\alpha_2 n e_\uparrow e_\downarrow\right) = 0 \\ A_\uparrow\left(\alpha_1 n e_\uparrow^2\right) + B_\uparrow\left(\omega_0 + \omega - \mu - \tfrac{\Omega}{2} + 2\alpha_1 n e_\uparrow^2 + \alpha_2 n e_\downarrow^2\right) + A_\downarrow\left(\alpha_2 n e_\uparrow e_\downarrow\right) + B_\downarrow\left(\alpha_2 n e_\uparrow e_\downarrow\right) = 0 \\ A_\uparrow\left(\alpha_2 n e_\uparrow e_\downarrow\right) + B_\uparrow\left(\alpha_2 n e_\uparrow e_\downarrow\right) + A_\downarrow\left(\omega_0 - \omega - \mu + \tfrac{\Omega}{2} + 2\alpha_1 n e_\downarrow^2 + \alpha_2 n e_\uparrow^2\right) + B_\downarrow\left(\alpha_1 n e_\downarrow^2\right) = 0 \\ A_\uparrow\left(\alpha_2 n e_\uparrow e_\downarrow\right) + B_\uparrow\left(\alpha_2 n e_\uparrow e_\downarrow\right) + A_\downarrow\left(\alpha_1 n e_\downarrow^2\right) + B_\downarrow\left(\omega_0 + \omega - \mu + \tfrac{\Omega}{2} + 2\alpha_1 n e_\downarrow^2 + \alpha_2 n e_\uparrow^2\right) = 0. \end{gathered} \tag{C.4}$$

The first two equations give the expression for the chemical potential:

$$\mu = \frac{\alpha_1 + \alpha_2}{2} n. \tag{C.5}$$

They are also substituted into the next 4 equations, which simplifies to:

$$\begin{aligned}
&A_\uparrow \left(\omega_0 - \omega + \alpha_1 n e_\uparrow^2\right) + B_\uparrow \left(\alpha_1 n e_\uparrow^2\right) + A_\downarrow \left(\alpha_2 n e_\uparrow e_\downarrow\right) + B_\downarrow \left(\alpha_2 n e_\uparrow e_\downarrow\right) = 0 \\
&A_\uparrow \left(\alpha_1 n e_\uparrow^2\right) + B_\uparrow \left(\omega_0 + \omega + \alpha_1 n e_\uparrow^2\right) + A_\downarrow \left(\alpha_2 n e_\uparrow e_\downarrow\right) + B_\downarrow \left(\alpha_2 n e_\uparrow e_\downarrow\right) = 0 \\
&A_\uparrow \left(\alpha_2 n e_\uparrow e_\downarrow\right) + B_\uparrow \left(\alpha_2 n e_\uparrow e_\downarrow\right) + A_\downarrow \left(\omega_0 - \omega + \alpha_1 n e_\downarrow^2\right) + B_\downarrow \left(\alpha_1 n e_\downarrow^2\right) = 0 \\
&A_\uparrow \left(\alpha_2 n e_\uparrow e_\downarrow\right) + B_\uparrow \left(\alpha_2 n e_\uparrow e_\downarrow\right) + A_\downarrow \left(\alpha_1 n e_\downarrow^2\right) + B_\downarrow \left(\omega_0 + \omega + \alpha_1 n e_\downarrow^2\right) = 0
\end{aligned} \tag{C.6}$$

Let us assign $a = \alpha_1 n e_\uparrow^2$, $b = \alpha_1 n e_\downarrow^2$ and $c = \alpha_2 n e_\uparrow e_\downarrow$. Then the first two equations transform to:

$$\begin{aligned}
&\left(\omega_0 - \omega + a\right) A_\uparrow + a B_\uparrow + c A_\downarrow + c B_\downarrow = 0 \\
&a A_\uparrow + \left(\omega_0 + \omega + a\right) B_\uparrow + c A_\downarrow + c B_\downarrow = 0
\end{aligned} \tag{C.7}$$

Taking the difference of the two, one obtains a relation of $A_\uparrow$ and $B_\uparrow$. A similar expression can be obtained for the other spin component:

$$A_{\uparrow(\downarrow)} = \left(\frac{\omega_0 + \omega}{\omega_0 - \omega}\right) B_{\uparrow(\downarrow)}. \tag{C.8}$$

Finally one gets

$$\frac{A_\uparrow}{A_\downarrow} = \frac{B_\uparrow}{B_\downarrow}, \tag{C.9}$$

which means that the two vectors are collinear. Combining the previous equations yields

$$\begin{aligned}
\left(\left(\omega_0 - \omega + a\right)\left(\frac{\omega_0 + \omega}{\omega_0 - \omega}\right) + a\right) B_\uparrow + B_\downarrow c \left(1 + \frac{\omega_0 + \omega}{\omega_0 - \omega}\right) = 0 \\
\left(\omega_0^2 - \omega^2 + 2a\omega_0\right) B_\uparrow + B_\downarrow 2\omega_0 c = 0.
\end{aligned} \tag{C.10}$$

Now, one get the equation for the dispersion relation, which read

$$\left(\omega_0^2 - \omega^2 + 2a\omega_0\right)\left(\omega^2 - \omega_0^2 - 2b\omega_0\right) + 4c^2\omega_0^2 = 0. \tag{C.11}$$

This is expanded to a bi-quadratic equation, which results in the dispersion

$$\omega^2 = \omega_0^2 + \omega_0 \left(a + b\right) \pm \omega_0 \sqrt{\left(a - b\right)^2 + 4c^2} \tag{C.12}$$

and replacing a, b and c yields

$$\omega^2 = \omega_0^2 + \omega_0 n \left[\alpha_1 \pm \sqrt{\alpha_2^2 + \left(\alpha_1^2 - \alpha_2^2\right)\frac{H^2}{H_c^2}}\right]. \tag{C.13}$$

This is the dispersion formula presented in chapter 3. Substituting this into the equation (C.10) one finds the ratio between two components of B:

$$\frac{B_\downarrow}{B_\uparrow} = \frac{-\alpha_1 \cos 2\Theta \pm \sqrt{\alpha_1^2 \cos^2 2\Theta + \alpha_2^2 \sin^2 2\Theta}}{\alpha_2 \sin 2\Theta}, \tag{C.14}$$

which defines two angles

$$\beta_\pm = \arctan \frac{-\alpha_1 \cos 2\Theta \pm \sqrt{\alpha_1^2 \cos^2 2\Theta + \alpha_2^2 \sin^2 2\Theta}}{\alpha_2 \sin 2\Theta}. \tag{C.15}$$

Finally the eigenpolarization vector can be written

$$\begin{pmatrix} \cos\beta_\pm \\ \sin\beta_\pm \end{pmatrix}. \tag{C.16}$$

C.2 Analytical transmission and reflection coefficients

We have three areas 1,2,3 (see chapter 3). In 1 and 3, only the propagation as a σ_+ wave is possible. In the central area of thickness L, the propagation takes place along the eigen states calculated in the previous section. The wave $\begin{pmatrix} 1 \\ 0 \end{pmatrix}$ enters in the area 2 and reads:

$$\begin{pmatrix} 1 \\ 0 \end{pmatrix} = a \begin{pmatrix} \cos\beta_+ \\ \sin\beta_+ \end{pmatrix} + b \begin{pmatrix} -\sin\beta_+ \\ \cos\beta_+ \end{pmatrix}, \tag{C.17}$$

which gives $a = \cos\beta_+, b = -\sin\beta_+$. at the point z, the wave function reads:

$$\psi_1^+(z) = \exp(ik_+ z)\cos\beta_+ \begin{pmatrix} \cos\beta_+ \\ \sin\beta_+ \end{pmatrix} - \exp(ik_- z)\sin\beta_+ \begin{pmatrix} -\sin\beta_+ \\ \cos\beta_+ \end{pmatrix} \tag{C.18}$$

At the point $z = L$ the $\sigma+$ part is fully transmitted, the σ_- part fully reflected which gives:

$$\begin{aligned} t_1^+ &= \exp(ik_+ L)\cos^2\beta_+ + \exp(ik_- L)\sin^2\beta_+ \\ r_1^+ &= \cos\beta_+ \sin\beta_+ \left(\exp(ik_+ L) - \exp(ik_- L)\right) \end{aligned} \tag{C.19}$$

We now consider the wave $r_1^+ \begin{pmatrix} 0 \\ 1 \end{pmatrix}$ propagating in the negative direction:

$$\psi_1^-(z) = r_1^+ \left[\exp(-ik_+(z-L))\sin\beta_+ \begin{pmatrix} \cos\beta_+ \\ \sin\beta_+ \end{pmatrix} + \exp(-ik_-(z-L))\cos\beta_+ \begin{pmatrix} -\sin\beta_+ \\ \cos\beta_+ \end{pmatrix} \right] \tag{C.20}$$

In $z = 0$, the σ_+ part is transmitted, the σ_- part is reflected.

$$\begin{aligned} t_1^- &= r_1^+ \left[\exp(ik_+L) - \exp(ik_-L)\right] \cos\beta_+ \sin\beta_+ \\ r_1^- &= r_1^+ \left[\sin^2\beta_+ \exp(ik_+L) + \cos^2\beta_+ \exp(ik_-L)\right] \end{aligned} \tag{C.21}$$

Once again this procedure in the inverted direction yields

$$\begin{aligned} \psi_2^+(z) &= r_1^- \left[\exp(ik_+z)\sin\beta_+ \begin{pmatrix} \cos\beta_+ \\ \sin\beta_+ \end{pmatrix} + \exp(ik_-z)\cos\beta_+ \begin{pmatrix} -\sin\beta_+ \\ \cos\beta_+ \end{pmatrix}\right] \\ t_2^+ &= r_1^- \left[\left(\exp(ik_+L) - \exp(ik_-L)\right)\cos\beta_+ \sin\beta_+\right] \\ r_2^+ &= r_1^- \left[\sin^2\beta_+ \exp(ik_+L) + \cos^2\beta_+ \exp(ik_-L)\right] \\ &= r_1^+ \left[\sin^2\beta_+ \exp(ik_+L) + \cos^2\beta_+ \exp(ik_-L)\right]^2 . \end{aligned} \tag{C.22}$$

More generally, one can write:

$$\begin{aligned} r_i^- &= r_1^+ \left[\sin^2\beta_+ \exp(ik_+L) + \cos^2\beta_+ \exp(ik_-L)\right]^{2n-1} \\ r_i^+ &= r_1^+ \left[\sin^2\beta_+ \exp(ik_+L) + \cos^2\beta_+ \exp(ik_-L)\right]^{2n-2} \\ t_i^- &= r_i^+ \left[\exp(ik_+L) - \exp(ik_-L)\right]\cos\beta_+ \sin\beta_+ \\ t_i^+ &= r_{i-1}^- \left(\exp(ik_+L) - \exp(ik_-L)\right)\cos\beta_+ \sin\beta_+ \end{aligned} \tag{C.23}$$

(C.24)

Performing this n times and sending n to infinity yields for the total transmitted amplitude

$$t^+ = \sum_n t_n^+ = t_1^+ + \left[\left(\exp(ik_+L) - \exp(ik_-L)\right)\cos\beta_+ \sin\beta_+\right] \sum_{i=2} r_{i-1}^- = \tag{C.25}$$

$$\begin{aligned} t^+ &= \exp(ik_+L)\cos^2\beta_+ + \exp(ik_-L)\sin^2\beta_+ \\ &+ \left[\cos\beta_+ \sin\beta_+ \left(\exp(ik_+L) - \exp(ik_-L)\right)\right]^2 \frac{\left[\sin^2\beta_+ \exp(ik_+L) + \cos^2\beta_+ \exp(ik_-L)\right]}{1 - \left[\sin^2\beta_+ \exp(ik_+L) + \cos^2\beta_+ \exp(ik_-L)\right]^2}. \end{aligned}$$

The same can be done for the total reflected amplitude:

$$t^- = \sum_n t_n^- = \left[\exp(ik_+L) - \exp(ik_-L)\right]\cos\beta_+ \sin\beta_+ \sum_i r_i^+ = \tag{C.26}$$

$$t^- = \frac{\left(\left[\exp(ik_+L) - \exp(ik_-L)\right]\cos\beta_+ \sin\beta_+\right)^2}{1 - \left[\sin^2\beta_+ \exp(ik_+L) + \cos^2\beta_+ \exp(ik_-L)\right]^2}$$

Appendix D

Quantum correlations: Density matrix and Peres criterion

D.1 Derivation of the two-photon density matrix

The two photon wavefunction of the biexciton decay in a semiconductor quantum dot can be written in the following way:

$$\begin{aligned} |\Psi\rangle = &\left(\alpha_{LP}\left|p_H^{LP}\right\rangle + \alpha_{UP}\left|p_H^{UP}\right\rangle\right)|HH\rangle + \\ &+ \left(\beta_{LP}\left|p_V^{LP}\right\rangle + \beta_{UP}\left|p_V^{UP}\right\rangle\right)|VV\rangle\,, \end{aligned} \tag{D.1}$$

Therein we neglect cross-polarization terms. We extract the coordinate part $\left|p_{H(V)}^{LP(UP)}\right\rangle$ from the polarization part of the wavefunction $|HH\rangle\,(|VV\rangle)$. The amplitudes α and β are the weights for the possible decay paths satisfying

$$|\alpha_{LP}|^2 + |\alpha_{UP}|^2 + |\beta_{LP}|^2 + |\beta_{UP}|^2 = 1. \tag{D.2}$$

In general the density matrix of a system can be written as

$$\rho = |\Psi\rangle\langle\Psi|\,. \tag{D.3}$$

Plugging now the wavefunction Eq.(D.1) into Eq.(D.3) yields

$$\begin{aligned} \rho \quad = &\left(\alpha_{LP}\left|p_H^{LP}\right\rangle + \alpha_{UP}\left|p_H^{UP}\right\rangle\right)\left(\alpha_{LP}^*\left\langle p_H^{LP}\right| + \alpha_{UP}^*\left\langle p_H^{UP}\right|\right)|HH\rangle\langle HH| + \\ &+ \left(\beta_{LP}\left|p_V^{LP}\right\rangle + \beta_{UP}\left|p_V^{UP}\right\rangle\right)\left(\beta_{LP}^*\left\langle p_V^{LP}\right| + \beta_{UP}^*\left\langle p_V^{UP}\right|\right)|VV\rangle\langle VV| + \\ &+ \left(\alpha_{LP}\left|p_H^{LP}\right\rangle + \alpha_{UP}\left|p_H^{UP}\right\rangle\right)\left(\beta_{LP}^*\left\langle p_V^{LP}\right| + \beta_{UP}^*\left\langle p_V^{UP}\right|\right)|HH\rangle\langle VV| + \\ &+ \left(\beta_{LP}\left|p_V^{LP}\right\rangle + \beta_{UP}\left|p_V^{UP}\right\rangle\right)\left(\alpha_{LP}^*\left\langle p_H^{LP}\right| + \alpha_{UP}^*\left\langle p_H^{UP}\right|\right)|VV\rangle\langle HH|\,, \end{aligned} \tag{D.4}$$

and finally

$$\begin{aligned}\rho \quad &= (|\alpha_{LP}|^2 \left|p_H^{LP}\right\rangle \left\langle p_H^{LP}\right| + \alpha_{LP}\alpha_{UP}^* \left|p_H^{LP}\right\rangle \left\langle p_H^{UP}\right| \\ &+\alpha_{LP}^*\alpha_{UP} \left|p_H^{UP}\right\rangle \left\langle p_H^{LP}\right| + |\alpha_{UP}|^2 \left|p_H^{UP}\right\rangle \left\langle p_H^{UP}\right|) \left|HH\right\rangle \left\langle HH\right| \\ &+(|\beta_{LP}|^2 \left|p_V^{LP}\right\rangle \left\langle p_V^{LP}\right| + \beta_{LP}\beta_{UP}^* \left|p_V^{LP}\right\rangle \left\langle p_V^{UP}\right| \\ &+\beta_{LP}^*\beta_{UP} \left|p_V^{UP}\right\rangle \left\langle p_V^{LP}\right| + |\beta_{UP}|^2 \left|p_V^{UP}\right\rangle \left\langle p_V^{UP}\right|) \left|VV\right\rangle \left\langle VV\right| \\ &+(\alpha_{LP}\beta_{LP}^* \left|p_H^{LP}\right\rangle \left\langle p_V^{LP}\right| + \alpha_{LP}\beta_{UP}^* \left|p_H^{LP}\right\rangle \left\langle p_V^{UP}\right| \\ &+\alpha_{UP}\beta_{LP}^* \left|p_H^{UP}\right\rangle \left\langle p_V^{LP}\right| + \alpha_{UP}\beta_{UP}^* \left|p_H^{UP}\right\rangle \left\langle p_V^{UP}\right|) \left|HH\right\rangle \left\langle VV\right| \\ &+(\alpha_{LP}^*\beta_{LP} \left|p_V^{LP}\right\rangle \left\langle p_H^{LP}\right| + \alpha_{LP}^*\beta_{UP} \left|p_V^{LP}\right\rangle \left\langle p_H^{UP}\right| \\ &+\alpha_{UP}^*\beta_{LP} \left|p_V^{UP}\right\rangle \left\langle p_H^{LP}\right| + \alpha_{UP}^*\beta_{UP} \left|p_V^{UP}\right\rangle \left\langle p_H^{UP}\right|) \left|VV\right\rangle \left\langle HH\right| . \end{aligned} \tag{D.5}$$

Tracing out all p degrees of freedom with

$$\sum_k \langle p_k|p_j\rangle \langle p_i|p_k\rangle = \sum_k \langle p_j|p_k\rangle \langle p_k|p_i\rangle = \sum_k \langle p_j|p_i\rangle \tag{D.6}$$

and assuming that scalar products between different polariton states are equal to zero (no overlap of the photon wave packages) leads to

$$\begin{aligned}\rho \quad &= (|\alpha_{LP}|^2 + |\alpha_{UP}|^2) \left|HH\right\rangle \left\langle HH\right| + (|\beta_{LP}|^2 + |\beta_{UP}|^2) \left|VV\right\rangle \left\langle VV\right| + \\ &+(\alpha_{LP}\beta_{LP}^* \left|p_H^{LP}\right\rangle \left\langle p_V^{LP}\right| + \alpha_{UP}\beta_{UP}^* \left|p_H^{UP}\right\rangle \left\langle p_V^{UP}\right|) \left|HH\right\rangle \left\langle VV\right| + \\ &+(\alpha_{LP}^*\beta_{LP} \left|p_V^{LP}\right\rangle \left\langle p_H^{LP}\right| + \alpha_{UP}^*\beta_{UP} \left|p_V^{UP}\right\rangle \left\langle p_H^{UP}\right|) \left|VV\right\rangle \left\langle HH\right| . \end{aligned} \tag{D.7}$$

In matrixform ρ looks as follows:

$$\rho = \begin{pmatrix} |\alpha_{LP}|^2 + |\alpha_{UP}|^2 & 0 & 0 & \gamma \\ 0 & 0 & 0 & 0 \\ 0 & 0 & 0 & 0 \\ \gamma^* & 0 & 0 & |\beta_{LP}|^2 + |\beta_{UP}|^2 \end{pmatrix}, \tag{D.8}$$

where

$$\gamma = \alpha_{LP}\beta_{LP}^* \left\langle p_H^{LP}|p_V^{LP}\right\rangle + \alpha_{UP}\beta_{UP}^* \left\langle p_H^{UP}|p_V^{UP}\right\rangle . \tag{D.9}$$

Using the projection P, which corresponds to the spectral windows which select for example only the lower polariton branch, the density matrix reads

$$\rho = \begin{pmatrix} |\alpha_{LP}|^2 & 0 & 0 & \gamma \\ 0 & 0 & 0 & 0 \\ 0 & 0 & 0 & 0 \\ \gamma^* & 0 & 0 & |\beta_{LP}|^2 \end{pmatrix}. \tag{D.10}$$

In this case the off-diagonal element simplifies to

$$\gamma = \frac{\alpha_{LP}\beta_{LP}\left\langle p_H^{LP}|P|p_V^{LP}\right\rangle}{|P\,|\Psi\rangle\,|^2}. \tag{D.11}$$

This derivation is valid for the scheme, where the lower states of both polarization are degenerate. In case of scheme 2 of chapter 4 the indices should be adapted, for example β_{LP} transforms to β_{UP} in the density matrix.

D.2 Peres criterion for entanglement

The used criterion was developed by Peres in 1996 [189]. It is based on the separability of the density matrix. A striking quantum phenomenon is the inseparability of composite quantum systems. Its most famous example is the violation of Bells inequality, which may be detected if two distant observers, who independently measure subsystems of a composite quantum system, report their results to a common site where that information is analyzed. However, even if Bells inequality is satisfied by a given composite quantum system, there is no guarantee that its state can be prepared by two distant observers who receive instructions from a common source. For this to be possible, the density matrix has to be separable into a sum of direct products,

$$\rho = \sum_A w_A \rho'_A \otimes \rho''_A, \tag{D.12}$$

where the positive weights w_A satisfy $\sum_A w_a = 1$, and where ρ'_A and ρ''_A are density matrices for the two subsystems. In the following we derive a simple algebraic test, which is a necessary condition for the existence of the decomposition Eq.(D.12). The derivation of this separability condition is best done by writing the density matrix elements explicitly, with all their indices

$$\rho_{m,\mu,n,\nu} = \sum_A w_A (\rho'_A)_{mn} (\rho''_A)_{\mu\nu}. \tag{D.13}$$

Latin index refer to the first subsystem, Greek index to the second one (the subsystems may have different dimensions).

Let us now define a new matrix,

$$\sigma_{m,\mu,n,\nu} = \rho_{n,\mu,m,\nu}. \tag{D.14}$$

The Latin indices of ρ have been transposed, but not the Greek ones. This is not a unitary transformation but, nevertheless, the matrix σ is Hermitian. When Eq.(D.12) is valid, we have

$$\sigma = \sum_A w_A (\rho'_A)^T \otimes \rho''_A, \tag{D.15}$$

Since the transposed matrices $(\rho'_A)^T \equiv (\rho'_A)^*$ are non-negative matrices with unit trace, they can also be legitimate density matrices. It follows that none of the eigenvalues of σ is negative. This is a necessary condition for Eq. (D.12) to hold.

We perform this test now for the matrix derived in the previous section of the appendix with additional inner diagonal elements

$$\rho = \begin{array}{c} \begin{array}{cccc} HH & HV & VH & VV \end{array} \\ \begin{pmatrix} a_1 & 0 & 0 & \gamma \\ 0 & a_2 & 0 & 0 \\ 0 & 0 & a_3 & 0 \\ \gamma & 0 & 0 & a_4 \end{pmatrix} \end{array} \begin{array}{c} HH \\ HV \\ VH \\ VV \end{array} \tag{D.16}$$

To construct the matrix σ on has to replace all matrix elements where the first letter of the indices are different i.e. $\rho_{VV,HH}$ transforms to $\rho_{HV,VH}$. Application of this transformation yield a matrix σ

$$\sigma = \begin{pmatrix} a_1 & 0 & 0 & 0 \\ 0 & a_2 & \gamma & 0 \\ 0 & \gamma & a_3 & 0 \\ 0 & 0 & 0 & a_4 \end{pmatrix}. \tag{D.17}$$

The eigenvalues can be simply computed:

$$\begin{aligned} \lambda_1 &= \alpha_1 \\ \lambda_2 &= \frac{a_2 + a_3}{2} + \frac{1}{2}\sqrt{(a_2 - a_3)^2 + 4\gamma^2} \\ \lambda_3 &= \frac{a_2 + a_3}{2} - \frac{1}{2}\sqrt{(a_2 - a_3)^2 + 4\gamma^2} \\ \lambda_4 &= \alpha_4. \end{aligned} \tag{D.18}$$

In case of the so-called "x-form" of the density matrix [198], when only the outer diagonal and off-diagonal elements are different from zero, ρ is only separable into the two subsystems for $\gamma = 0$. This means for the two-photon density matrix of the previous section, that the system undergoes quantum correlations only if the off-diagonal element is larger than zero with a maximum possible value of 1/2.

Bibliography

[1] Hopfield, J. Theory of the contribution of excitons to the complex dielectric constants of crystals. *Phys. Rev.* **112**, 1555 (1958).

[2] Agranovich, V. Dispersion of electromagnetic waves in crystals. *JETP Lett.* **37**, 430 (1959).

[3] Weisbuch, C., Nishioka, M., Ishikawa, A. & Arakawa, Y. Observation of the coupled exciton-photon mode splitting in a semiconductor quantum microcavity. *Phys. Rev. Lett.* **69**, 3314 (1992).

[4] Combescot, M. & Betbeder-Matibet, O. Faraday rotation in photoexcited semiconductors: A composite-exciton many-body effect. *Phys. Rev. B* **74**, 125316 (2006).

[5] Kavokin, A. & Malpuech, G. *Cavity polaritons* (Elsevier, 2003).

[6] Kavokin, A. V., Baumberg, J. J., Malpuech, G. & Laussy, F. P. *Microcavities* (Oxford University Press, 2007).

[7] Schmidt-Grund, R., Rheinlander, B., Czekalla, C., Benndorf, G., Hochmuth, H., Lorenz, M. & Grundmann, M. Exciton-polariton formation at room temperature in a planar ZnO resonator structure. *Appl. Phys. B* **93**, 331–337 (2008).

[8] Hennessy, K., Hogerle, C., Hu, E., Badolato, A. & Imamoglu, A. Tuning photonic nanocavities by atomic force microscope nano-oxidation. *Appl. Phys. Lett.* **89**, 041118 (2006).

[9] Savvidis, P. G., Baumberg, J. J., Stevenson, R. M., Skolnick, M. S., Whittaker, D. M. & Roberts, J. S. Angle-resonant stimulated polariton amplifier. *Phys. Rev. Lett.* **84**, 1547 (2000).

[10] Diederichs, C., Tignon, J., Dasbach, G., Ciuti, C., Lemaitre, A., Bloch, J., Roussignol, P. & Delalande, C. Parametric oscillation in vertical triple microcavities. *Nature* **440**, 904–907 (2006).

[11] Solnyshkov, D., Petrolati, E., Carlo, A. D. & Malpuech, G. Theory of an electrically injected bulk polariton laser. *Appl. Phys. Lett.* **94**, 011110 (2009).

[12] Skolnick, M., Astratov, V., Whittaker, D., Armitage, A., Emam-Ismael, M., Stevenson, R., Baumberg, J., Roberts, J., Lidzey, D., Virgili, T. & Bradley, D. Exciton polaritons in single and coupled microcavities. *Journal of Luminescence* **87-89**, 25 – 29 (2000).

[13] Reithmaier, J. P., Sek, G., Loffler, A., Hofmann, C., Kuhn, S., Reitzenstein, S., Keldysh, L. V., Kulakovskii, V. D., Reinecke, T. L. & Forchel1, A. Strong coupling in a single quantum dotsemiconductor microcavity system. *Nature* **432**, 197 (2004).

[14] Peter, E., Senellart, P., Martrou, D., Lemaitre, A., Hours, J., Gerard, J. M. & Bloch, J. Exciton-photon strong-coupling regime for a single quantum dot embedded in a microcavity. *Phys. Rev. Lett.* **95**, 067401 (2005).

[15] Hennessy, K., Badolato, A., Winger, M., Gerace, D., Atature, M., Gulde, S., Falt, S., Hu, E. L. & Imamoglu, A. Quantum nature of a strongly coupled single quantum dot - cavity system. *Nature* **445**, 896 (2007).

[16] Hafenbrak, R., Ulrich, S. M., Michler, P., Wang, L., Rastelli, A. & Schmidt, O. G. Triggered polarization-entangled photon pairs from a single quantum dot up to 30 K. *New Journal of Physics* **9**, 315 (2007).

[17] Young, R. J., Stevenson, R. M., Hudson, A. J., Nicoll, C. A., Ritchie, D. A. & Shields, A. J. Bell-inequality violation with a triggered photon-pair source. *Phys. Rev. Lett.* **102**, 030406 (2009).

[18] Yoshie, T., Scherer, A., Hendrickson, J., Khitrova, G., Gibbs, H. M., Rupper, G., Ell, C., Shchekin, O. B. & Deppe, D. G. Vacuum Rabi splitting with a single quantum dot in a photonic crystal nanocavity. *Nature* **432**, 200 (2004).

[19] Badolato, A., Hennessy, K., Atature, M., Dreiser, J., Hu, E., Petroff, P. M. & Imamoglu, A. Deterministic coupling of single quantum dots to single nanocavity modes. *Science* **308**, 1158 (2005).

[20] Tikhodeev, S. G., Yablonskii, A. L., Muljarov, E. A., Gippius, N. A. & Ishihara, T. Quasiguided modes and optical properties of photonic crystal slabs. *Phys. Rev. B* **66**, 045102 (2002).

[21] Gerace, D. & Andreani, L. C. Quantum theory of exciton-photon coupling in photonic crystal slabs with embedded quantum wells. *Phys. Rev. B* **75**, 235325 (2007).

[22] Kasprzak, J., Richard, M., Kundermann, S., Baas, A., Jeambrun, P., Keeling, J. M., Marchetti, F. M., Szymanska, M. H., André, R., Staehli, J. H., Savona, V., Littlewood, P. B., Deveaud, B. & Dang, L. S. Bose-Einstein condensation of exciton polaritons. *Nature* **443**, 409 (2006).

[23] Einstein, A. Quantentheorie des einatomigen idealen Gases. *Sitzungsberichte der preussischen Akademie der Wissenschaften* **Bd. XXII**, 261–267 (1924).

[24] Balili, R., Hartwell, V., Snoke, D., Pfeiffer, L. & West, K. Bose-Einstein condensation of microcavity polaritons in a trap. *Science* **316**, 1007 (2007).

[25] Lai, C., Kim, N., Utsunomiya, S., Roumpos, G., Deng, H., Fraser, M., Byrnes, T., Recher, P., Kumada, N., Fujisawa, T. & Yamamoto, Y. Coherent zero-state and π-state in an exciton–polariton condensate array. *Nature* **450**, 529–532 (2007).

[26] Baumberg, J. J., Kavokin, A. V., Christopoulos, S., Grundy, A. J. D., Butte, R., Christmann, G., Solnyshkov, D. D., Malpuech, G., von Hogersthal, G. B. H., Feltin, E., Carlin, J. F. & Grandjean, N. Spontaneous polarization buildup in a room-temperature polariton laser. *Phys. Rev. Lett.* **101**, 136409 (2008).

[27] Kasprzak, J., Solnyshkov, D. D., André, R., Dang, L. S. & Malpuech, G. Formation of an exciton polariton condensate: Thermodynamic versus kinetic regimes. *Phys. Rev. Lett.* **101**, 146404 (2008).

[28] Uhlenbeck, G. & Gropper, L. The equation of state of a non-ideal Einstein-Bose or Fermi-Dirac gas. *Phys. Rev.* **41**, 79–90 (1932).

[29] Porras, D., Ciuti, C., Baumberg, J. J. & Tejedor, C. Polariton dynamics and Bose-Einstein condensation in semiconductor microcavities. *Phys. Rev. B* **66**, 085304 (2002).

[30] Shelykh, I., Malpuech, G., Johne, R. & Kavokin, A. The system of interacting polaritons: Classical versus quantum kinetic equation. *Solid State Communications* **144**, 378383 (2007).

[31] Wouters, M. & Savona, V. Stochastic classical field model for polariton condensates. *Phys. Rev. B* **79**, 165302 (2009).

[32] Malpuech, G., Kavokin, A., Di Carlo, A. & Baumberg, J. J. Polariton lasing by exciton-electron scattering in semiconductor microcavities. *Phys. Rev. B* **65**, 153310 (2002).

[33] Tassone, F., Piermarocchia, C., Savona, V., Quattropani, A. & Schwendimann, P. Bottleneck effects in the relaxation and photoluminescence of microcavity polaritons. *Phys. Rev. B* **56**, 7554 (1997).

[34] Tassone, F. & Yamamoto, Y. Exciton-exciton scattering dynamics in a semiconductor microcavity and stimulated scattering into polaritons. *Phys. Rev. B* **59**, 10830–10842 (1999).

[35] Porras, D. & Tejedor, C. Linewidth of a polariton laser: Theoretical analysis of self-interaction effects. *Phys. Rev. B* **67**, 161310 (2003).

[36] Tartakovskii, A. I., Emam-Ismail, M., Stevenson, R. M., Skolnick, M. S., Astratov, V. N., Whittaker, D. M., Baumberg, J. J. & Roberts, J. S. Relaxation bottleneck and its suppression in semiconductor microcavities. *Phys. Rev. B* **62**, R2283–R2286 (2000).

[37] Müller, M., Bleuse, J. & André, R. Dynamics of the cavity polariton in CdTe-based semiconductor microcavities: Evidence for a relaxation edge. *Phys. Rev. B* **62**, 16886–16892 (2000).

[38] Malpuech, G., Rubo, Y. G., Laussy, F. P., Bigenwald, P. & Kavokin, A. V. Polariton laser: Thermodynamics and quantum kinetic theory. *Semicond. Sci. Technol.* **18**, S395–S404 (2003).

[39] Bogoliubov, N. On the theory of superfluidity. *J. Phys.(USSR)* **11**, 23 (1947).

[40] Pitaevskii, L. & Stringari, S. *Bose-Einstein Condensation* (Oxford Science Publications - International Series of Monographs on Physics 116, 2003).

[41] Ciuti, C., Savona, V., Piermarocchi, C., Quattropani, A. & Schwendimann, P. Role of the exchange of carriers in elastic exciton-exciton scattering in quantum wells. *Phys. Rev. B* **58**, 7926–7933 (1998).

[42] Gross, E. Structure of a quantized vortex in boson systems. *Il Nuovo Cimento (1955-1965)* **20**, 454–477 (1961).

[43] Pitaevskii, L. Vortex lines in an imperfect Bose gas. *Sov. Phys. JETP* **13**, 451 (1961).

[44] Kapitza, P. L. Viscosity of liquid helium below the λ-point. *Nature* **141**, 913 (1938).

[45] Allen, J. F. & Misener, A. D. Flow of liquid helium II. *Nature* **141**, 75 (1938).

[46] Keldysh, L. & Kozlov, A. Collective properties of excitons in semiconductors. *JETP Lett.* **27**, 521–528 (1968).

[47] Lozovik, Y. & Yudson, V. Feasibility of superfluidity of paired spatially separated electrons and holes; A new superconductivity mechanism. *JETP Lett.* **22**, 26 (1975).

[48] Lozovik, Y. & Yudson, V. A new mechanism for superconductivity: Pairing between spatially separated electrons and holes. *JETP Lett.* **44**, 389 (1976).

[49] Lozovik, Y. & Yudson, V. Superconductivity at dielectric pairing of spatially separated quasiparticles. *Solid State Communication* **19**, 391–393 (1976).

[50] Butov, L. V., Ivanov, A. L., Imamoglu, A., Littlewood, P. B., Shashkin, A. A., Dolgopolov, V. T., Campman, K. L. & Gossard, A. C. Stimulated scattering of indirect excitons in coupled quantum wells: Signature of a degenerate Bose-gas of excitons. *Phys. Rev. Lett.* **86**, 5608–5611 (2001).

[51] Butov, L., Lai, C., Ivanov, A., Gossard, A. & Chemla, D. Towards Bose–Einstein condensation of excitons in potential traps. *Nature* **417**, 47–52 (2002).

[52] Snoke, D., Denev, S., Liu, Y., Pfeiffer, L. & West, K. Long-range transport in excitonic dark states in coupled quantum wells. *Nature* **418**, 754–757 (2002).

[53] Snoke, D. Spontaneous Bose coherence of excitons and polaritons. *Science* **298**, 1368–1372 (2002).

[54] Lozovik, Y. E., Ovchinnikov, I. V., Volkov, S. Y., Butov, L. V. & Chemla, D. S. Quasi-two-dimensional excitons in finite magnetic fields. *Phys. Rev. B* **65**, 235304 (2002).

[55] Tikhodeev, S. G. Comment on "Critical velocities in exciton superfluidity". *Phys. Rev. Lett.* **84**, 3502 (2000).

[56] Amo, A., Lefrere, J., Pigeon, S., Adrados, C., Ciuti, C., Carusotto, I., Houdre, R., Giacobino, E. & Bramati, A. Observation of superfluidity of polaritons in semiconductor microcavities. *arXiv:0812.2748v1 [cond-mat.mtrl-sci]* .

[57] Malpuech, G., Solnyshkov, D., Ouerdane, H., Glazov, M. & Shelykh, I. Bose glass and superfluid phases of cavity polaritons. *Phys. Rev. Lett.* **98**, 206402 (2007).

[58] Wouters, M. & Carusotto, I. Excitations in a nonequilibrium Bose-Einstein condensate of exciton polaritons. *Phys. Rev. Lett.* **99**, 140402 (2007).

[59] Marchetti, F., Keeling, J., Szymańska, M. & Littlewood, P. Thermodynamics and excitations of condensed polaritons in disordered microcavities. *Phys. Rev. Lett.* **96**, 66405 (2006).

[60] Amo, A., Sanvitto, D., Laussy, F. P., Ballarini, D., del Valle, E., Martin, M. D., Lemaitre, A., Bloch, J., Krizhanovskii, D. N., Skolnick, M. S., Tejedor, C. & Vina, L. Collective fluid dynamics of a polariton condensate in a semiconductor microcavity. *Nature* **457**, 291 (2009).

[61] Utsunomiya, S., Tian, L., Roumpos, G., Lai, C., Kumada, N., Fujisawa, T., Kuwata-Gonokami, M., Forchel, A. & Yamamoto, Y. Observation of Bogoliubov excitations in exciton-polariton condensates. *Nature Physics* **4**, 700 – 705 (2008).

[62] Shelykh, I. A., Rubo, Y. G., Malpuech, G., Solnyshkov, D. D. & Kavokin, A. Polarization and propagation of polariton condensates. *Phys. Rev. Lett.* **97**, 066402 (2006).

[63] Martín, M. D., Aichmayr, G., Viña, L. & André, R. Polarization control of the nonlinear emission of semiconductor microcavities. *Phys. Rev. Lett.* **89**, 077402 (2002).

[64] Maialle, M. Z., de Andrada e Silva, E. A. & Sham, L. J. Exciton spin dynamics in quantum wells. *Phys. Rev. B* **47**, 15776–15788 (1993).

[65] Shelykh, I. A., Pavlovic, G., Solnyshkov, D. D. & Malpuech, G. Proposal for a mesoscopic optical Berry-phase interferometer. *Phys. Rev. Lett.* **102**, 046407 (2009).

[66] Rubo, Y., Kavokin, A. & Shelykh, I. Suppression of superfluidity of exciton-polaritons by magnetic field. *Phys. Lett. A* **358**, 227–230 (2006).

[67] Ciuti, C., Schwendimann, P., Deveaud, B. & Quattropani, A. Theory of the angle-resonant polariton amplifier. *Phys. Rev. B* **62**, R4825–R4828 (2000).

[68] Baas, A., Karr, J. P., Romanelli, M., Bramati, A. & Giacobino, E. Optical bistability in semiconductor microcavities in the nondegenerate parametric oscillation regime: Analogy with the optical parametric oscillator. *Phys. Rev. B* **70**, 161307 (R) (2004).

[69] Tredicucci, A., Chen, Y., Pellegrini, V., Börger, M. & Bassani, F. Optical bistability of semiconductor microcavities in the strong-coupling regime. *Phys. Rev. A* **54**, 3493–3498 (1996).

[70] Gippius, N. A., Tikhodeev, S. G., Kulakovskii, V. D., Krizhanovskii, D. N. & Tartakovskii, A. I. Nonlinear dynamics of polariton scattering in semiconductor microcavity: Bistability vs. stimulated scattering. *Europhys. Lett.* **67**, 997 (2004).

[71] Whittaker, D. M. Effects of polariton-energy renormalization in the microcavity optical parametric oscillator. *Phys. Rev. B* **71**, 115301 (2005).

[72] Gippius, N. A., Shelykh, I. A., Solnyshkov, D. D., Gavrilov, S. S., Rubo, Y. G., Kavokin, A. V., Tikhodeev, S. G. & Malpuech, G. Polarization multistability of cavity polaritons. *Phys. Rev. Lett.* **98**, 236401 (2007).

[73] Renucci, P., Amand, T., Marie, X., Senellart, P., Bloch, J., Sermage, B. & Kavokin, K. V. Microcavity polariton spin quantum beats without a magnetic field: A manifestation of coulomb exchange in dense and polarized polariton systems. *Phys. Rev. B* **72**, 075317 (2005).

[74] Anderson, M., Ensher, J., Matthews, M., Wieman, C. & Cornell, E. Observation of Bose-Einstein condensation in a dilute atomic vapor. *Science* **269**, 198–201 (1995).

[75] Davis, K. B., Mewes, M. O., Andrews, M. R., van Druten, N. J., Durfee, D. S., Kurn, D. M. & Ketterle, W. Bose-Einstein condensation in a gas of sodium atoms. *Phys. Rev. Lett.* **75**, 3969–3973 (1995).

[76] Andrews, M., Townsend, C., Miesner, H., Durfee, D., Kurn, D. & Ketterle, W. Observation of interference between two Bose condensates. *Science* **275**, 637 (1997).

[77] Richard, M., Kasprzak, J., André, R., Romestain, R., Dang, L. S., Malpuech, G. & Kavokin, A. Experimental evidence for nonequilibrium Bose condensation of exciton polaritons. *Phys. Rev. B* **72**, 201301 (2005).

[78] Kasprzak, J., André, R., Dang, L. S., Shelykh, I. A., Kavokin, A. V., Rubo, Y. G., Kavokin, K. V. & Malpuech, G. Build up and pinning of linear polarization in the Bose condensates of exciton polaritons. *Phys. Rev. B* **75**, 045326 (2007).

[79] Zamfirescu, M., Kavokin, A., Gil, B., Malpuech, G. & Kaliteevski, M. ZnO as a material mostly adapted for the realization of room-temperature polariton lasers. *Phys. Rev. B* **65**, 161205(R) (2002).

[80] Malpuech, G., Di Carlo, A., Kavokin, A., Baumberg, J., Zamfirescu, M. & Lugli, P. Room-temperature polariton lasers based on GaN microcavities. *Appl. Phys. Lett.* **81**, 412 (2002).

[81] Keldysh, L. & Kopaev, Y. Possible instability of the semimetal state toward coulomb interaction. *JETP Lett.* **6**, 2219 (1965).

[82] Imamoglu, A. & Ram, J. R. Quantum dynamics of exciton lasers. *Phys. Lett. A* **214**, 193 (1996).

[83] Ciuti, C., Schwendimann, P. & Quattropani, A. Parametric luminescence of microcavity polaritons. *Phys. Rev. B* **63**, 041303 (2001).

[84] Gippius, N. A. & Tikhodeev, S. G. Multiple-polariton scattering in a semiconductor microcavity. *J. Phys.: Condens. Matter* **16**, S3653–S3664 (2004).

[85] Glazov, M. M. & Kavokin, K. V. Cavity polaritons: Classical behavior of a quantum parametric oscillator. *Phys. Rev. B* **73**, 245317 (2006).

[86] Shelykh, I. A., Kavokin, A. V. & Malpuech, G. Spin dynamics of exciton polaritons in microcavities. *phys. stat. sol. (b)* **242**, 2271–2289 (2005).

[87] Carmichael, H. J. *Statistical Methods in Quantum Optics 1: Master Equations and Fokker-Planck Equations* (Springer-Verlag, Berlin, 1999).

[88] Glazov, M., Shelykh, I., Malpuech, G., Kavokin, K., Kavokin, A. & Solnyshkov, D. Anisotropic polariton scattering and spin dynamics of cavity polaritons. *Solid State Communications* **134**, 117–120 (2005).

[89] Laussy, F. P., Shelykh, I. A., Malpuech, G. & Kavokin, A. Effects of Bose-Einstein condensation of exciton polaritons in microcavities on the polarization of emitted light. *Phys. Rev. B* **73**, 035315 (2006).

[90] Verger, A., Carusotto, I. & Ciuti, C. Quantum Monte Carlo study of ring-shaped polariton parametric luminescence in a semiconductor microcavity. *Phys. Rev. B* **76**, 115324 (2007).

[91] Karr, J. P., Baas, A. & Giacobino, E. Twin polaritons in semiconductor microcavities. *Phys. Rev. A* **69**, 063807 (2004).

[92] Romanelli, M., Leyder, C., Karr, J. P., Giacobino, E. & Bramati, A. Four wave mixing oscillation in a semiconductor microcavity: Generation of two correlated polariton populations. *Phys. Rev. Lett.* **98**, 106401 (2007).

[93] Shelykh, I. A., Johne, R., Solnyshkov, D. D., Kavokin, A. V., Gippius, N. A. & Malpuech, G. Quantum kinetic equations for interacting bosons and their application for polariton parametric oscillators. *Phys. Rev. B* **76**, 155308 (2007).

[94] Phillips, K. J., Young, M. R. & Singh, S. Intensity correlation functions of the laser with multiplicative white noise. *Phys. Rev. A* **44**, 3239 (1991).

[95] Hanggi, P., Marchesoni, F. & Grigolini, P. Bistable flow driven by coloured Gaussian noise: A critical study. *Z. Phys. B* **56**, 333–339 (1984).

[96] Luo, X. & Zhu, S. Stochastic resonance driven by two different kinds of colored noise in a bistable system. *Phys. Rev. E* **67**, 021104 (2003).

[97] Jung, P. & Hanggi, P. Bistability and colored noise in nonequilibrium systems. *Phys. Rev. Lett* **61**, 11 (1988).

[98] Jung, P. & Hanggi, P. Invariant measure of a driven nonlinear oscillator with external noise. *Phys. Rev. Lett* **65**, 3365 (1990).

[99] Maslova, N. S., Johne, R. & Gippius, N. A. Role of fluctuations in nonlinear dynamics of driven polariton system in semiconductor microcavities. *JETP Lett.* **2**, 126–131 (2007).

[100] Nyquist, H. Thermal agitation of electric charge in conductors. *Phys. Rev.* **32**, 110–113 (1928).

[101] Callen, H. B. & Welton, T. A. Irreversibility and generalized noise. *Phys. Rev.* **83**, 34–40 (1951).

[102] Dykman, M. I., Luchinsky, D. G., Mannella, R., McClintock, P. V. E., Stein, N. D. & Stocks, N. G. Supernarrow spectral peaks and high-frequency stochastic resonance in systems with coexisting periodic attractors. *Phys. Rev. E* **49**, 1198 (1994).

[103] Risken, H. *The Fokker-Planck equation, Methods of Solution and Applications, 2nd Ed.* (Springer, Berlin, 1989).

[104] Mandel, L. & Wolf, E. *Optical coherence and quantum optics* (Cambridge University Press, 1995).

[105] Makhonin, M. N., Demenev, A. A., Gavrilov, S. S., Kulakovskiia, V. D., Gippius, N. A. & Tikhodeev, S. G. Stimulated parametric scattering of excitonic polaritons in planar GaAs microcavities: Distinctive feature of QW electric field. *Solid State Communications* **144**, 384 (2007).

[106] Maslova, N. S., Johne, R. & Gippius, N. A. Coloured noise controlled dynamics of nonlinear polaritons in semiconductor microcavity. *JETP Lett.* (2009).

[107] Imamoglu, A., Ram, R. J., Pau, S. & Yamamoto, Y. Nonequilibrium condensates and lasers without inversion: Exciton-polariton lasers. *Phys. Rev. A* **53**, 4250–4253 (1996).

[108] Klingshirn, C., Hauschild, R., Priller, H., Decker, M., Zeller, J. & Kalt, H. ZnO rediscoveredonce again!? *Superlattices and Microstructures* **38**, 209–222 (2006).

[109] Look, D. Recent advances in ZnO materials and devices. *Materials Science and Engineering* **B80**, 383387 (2001).

[110] Look, D. C. Electrical and optical properties of p-type ZnO. *Semicond. Sci. Technol.* **20**, S55–S61 (2005).

[111] Solnyshkov, D. & Malpuech, G. A polariton laser based on a bulk GaN microcavity. *Superlattices and Microstructures* **41**, 279–283 (2007).

[112] Stokker-Cheregi, F., Vinattieri, A., Semond, F., Leroux, M., Sellers, I. R., Massies, J., Solnyshkov, D., Malpuech, G., Colocci, M. & Gurioli, M. Polariton relaxation bottleneck and its thermal suppression in bulk GaN microcavities. *Appl. Phys. Lett.* **92**, 042119 (2008).

[113] Alyamani, A., Sanvitto, D., Khalifa, A. A., Skolnick, M. S., Wang, T., Ranalli, F., Parbrook, P., Tahraoui, A. & Airey, R. GaN hybrid microcavities in the strong coupling regime grown by metal-organic chemical vapor deposition on sapphire substrates. *J. Appl. Phys.* **101**, 093110 (2007).

[114] Butte, R., Christmann, G., E.Feltin, Carlin, J.-F., Mosca, M., Ilegems, M. & Grandjean, N. Room-temperature polariton luminescence from a bulk GaN microcavity. *Phys. Rev. B* **73**, 033315 (2006).

[115] Christopoulos, S., von Hogersthal, G. B. H., Grundy, A. J. D., Lagoudakis, P. G., Kavokin, A., Baumberg, J. J., Christmann, G., Butte, R., Feltin, E., Carlin, J.-F. & Grandjean, N. Room-temperature polariton lasing in semiconductor microcavities. *Phys. Rev. Lett.* **98**, 126405 (2007).

[116] Christmann, G., Butte, R., Feltin, E., Mouti, A., Stadelmann, P. A., Castiglia, A., Carlin, J.-F. & Grandjean, N. Large vacuum Rabi splitting in a multiple quantum well GaN-based microcavity in the strong-coupling regime. *Phys. Rev. B* **77**, 085310 (2008).

[117] Shimada, R., Xie, J., Avrutin, V., Özgür, Ü. & Morkoč, H. Cavity polaritons in ZnO-based hybrid microcavities. *Appl. Phys. Lett.* **92**, 011127 (2008).

[118] Schmidt-Grund, R., Rheinlander, B., Czekalla, C., Benndorf, G., Hochmut, H., Rahm, A., Lorenz, M. & Grundmann, M. ZnO based planar and micropillar resonators. *Superlattices and Microstructures* **41**, 360–363 (2007).

[119] Medard, F., Zuniga-Perez, J., Disseix, P., Mihailovic, M., Leymarie, J., A.Vasson, F.Semond, Frayssinet, E., Moreno, J., Leroux, M., Faure, S. & Guillet, T. Experimental observation of strong light-matter coupling in ZnO microcavities: Influence of large excitonic absorption. *arXiv:0812.3383* (2009).

[120] D.G. Lidzey, M. S. T. V. S. D. W., D.D.C. Bradley. Strong exciton-photon coupling in an organic semiconductor microcavity. *Nature* **395**, 53 (1998).

[121] P. Schouwink, L. D. R., H.V. Berlepsch. Observation of strong excitonphoton coupling in an organic microcavity. *Chem. Phys. Lett.* **344**, 352 (2001).

[122] N. Takada, D. B., T. Kamata. Polariton emission from polysilane-based organic microcavities. *Appl. Phys. Lett.* **82**, 1812 (2003).

[123] Sun, L., Chen, Z., Ren, Q., Yu, K., Bai, L., Zhou, W., Xiong, H., Zhu, Z. Q. & Shen, X. Direct observation of whispering gallery mode polaritons and their dispersion in a ZnO tapered microcavity. *Phys. Rev. Lett.* **100**, 156403 (2008).

[124] Mollwo, E. *in Semiconductors: Physics of II-VI and I-VII Compounds, Semimagnetic Semiconductors, Landolt-Börnstein New Series Vol. 17b* (Springer, Berlin, 1982).

[125] Reynolds, D., Look, D., Jogai, B., Hoelscher, J., Sherriff, R., Harris, M. & Callahan, M. Time-resolved photoluminescence lifetime measurements of the γ and γ free excitons in ZnO. *J. Appl. Phys.* **88**, 2152 (2000).

[126] Datta, S. & Das, B. Electronic analog of the electro-optic modulator. *Appl. Phys. Lett.* **56**, 665 (1990).

[127] Žutić, I., Fabian, J. & Das Sarma, S. Spintronics: Fundamentals and applications. *Rev. Mod. Phys.* **76**, 323–410 (2004).

[128] Nitta, J., Akazaki, T., Takayanagi, H. & Enoki, T. Gate control of spin-orbit interaction in an inverted $In_{0.53}Ga_{0.47}As/In_{0.52}Al_{0.48}As$ heterostructure. *Phys. Rev. Lett.* **78**, 1335–1338 (1997).

[129] Heida, J. P., van Wees, B. J., Kuipers, J. J., Klapwijk, T. M. & Borghs, G. Spin-orbit interaction in a two-dimensional electron gas in a $InAs/AlSb$ quantum well with gate-controlled electron density. *Phys. Rev. B* **57**, 11911–11914 (1998).

[130] Engels, G., Lange, J., Schäpers, T. & Lüth, H. Experimental and theoretical approach to spin splitting in modulation-doped $InGaAs/InP$ quantum wells for $B \to 0$. *Phys. Rev. B* **55**, R1958–R1961 (1997).

[131] Shelykh, I. A. & Galkin, N. G. Fano and Breit-Wigner resonances in carrier transport through Datta and Das spin modulators. *Phys. Rev. B* **70**, 205328 (2004).

[132] Shelykh, I., Kavokin, K. V., Kavokin, A. V., Malpuech, G., Bigenwald, P., Deng, H., Weihs, G. & Yamamoto, Y. Semiconductor microcavity as a spin-dependent optoelectronic device. *Phys. Rev. B* **70**, 035320 (2004).

[133] Leyder, C., Liew, T. C. H., Kavokin, A. V., Shelykh, I. A., Romanelli, M., Karr, J. P., Giacobino, E. & Bramati, A. Interference of coherent polariton beams in microcavities: Polarization-controlled optical gates. *Phys. Rev. Lett.* **99**, 196402 (2007).

[134] Liew, T. C. H., Kavokin, A. V. & Shelykh, I. A. Optical circuits based on polariton neurons in semiconductor microcavities. *Phys. Rev. Lett.* **101**, 016402 (2008).

[135] Krizhanovskii, D. N., Sanvitto, D., Shelykh, I. A., Glazov, M. M., Malpuech, G., Solnyshkov, D. D., Kavokin, A., Ceccarelli, S., Skolnick, M. S. & Roberts, J. S. Rotation of the plane of polarization of light in a semiconductor microcavity. *Phys. Rev. B* **73**, 073303 (2006).

[136] Shelykh, I. A., Liew, T. C. H. & Kavokin, A. V. Spin rings in semiconductor microcavities. *Phys. Rev. Lett.* **100**, 116401 (2008).

[137] Kavokin, K. V., Shelykh, I. A., Kavokin, A. V., Malpuech, G. & Bigenwald, P. Quantum theory of spin dynamics of exciton-polaritons in microcavities. *Phys. Rev. Lett.* **92**, 017401 (2004).

[138] Bajoni, D., Miard, A., Lemaître, A., Bouchoule, S., Bloch, J. & Tignon, J. Nonresonant electrical injection of excitons in an InGaAs quantum well. *Applied Physics Letters* **90**, 121114 (2007).

[139] Khalifa, A. A., Love, A. P. D., Krizhanovskii, D. N., Skolnick, M. S. & Roberts, J. S. Electroluminescence emission from polariton states in GaAs-based semiconductor microcavities. *Applied Physics Letters* **92**, 061107 (2008).

[140] Tsintzos, S. I., Pelekanos, N. T., Konstantinidis, G., Hatzopoulos, Z. & Savvidis, P. G. A GaAs polariton light-emitting diode operating near room temperature. *Nature* **453**, 372–375 (2008).

[141] Langbein, W., Shelykh, I., Solnyshkov, D., Malpuech, G., Rubo, Y. & Kavokin, A. Polarization beats in ballistic propagation of exciton-polaritons in microcavities. *Phys. Rev. B* **75**, 075323 (2007).

[142] Malpuech, G., Solnyshkov, D. D., Ouerdane, H., Glazov, M. M. & Shelykh, I. Bose glass and superfluid phases of cavity polaritons. *Phys. Rev. Lett.* **98**, 206402 (2007).

[143] Josephson, B. Possible new effects in superconductive tunneling. *Phys. Lett.* **1**, 251–253 (1962).

[144] Giaever, I. Detection of the ac Josephson effect. *Phys. Rev. Lett.* **14**, 904–906 (1965).

[145] Likharev, K. K. Superconducting weak links. *Rev. Mod. Phys.* **51**, 101–161 (1979).

[146] Pereverzev, S., Loshak, A., Backhaus, S., Davis, J. & Packard, R. Quantum oscillations between two weakly coupled reservoirs of superfluid ^{3}He. *Nature* **388**, 449–451 (1997).

[147] Albiez, M., Gati, R., Fölling, J., Hunsmann, S., Cristiani, M. & Oberthaler, M. K. Direct observation of tunneling and nonlinear self-trapping in a single bosonic Josephson junction. *Phys. Rev. Lett.* **95**, 010402 (2005).

[148] Jack, M. W., Collett, M. J. & Walls, D. F. Coherent quantum tunneling between two Bose-Einstein condensates. *Phys. Rev. A* **54**, R4625–R4628 (1996).

[149] Smerzi, A., Fantoni, S., Giovanazzi, S. & Shenoy, S. R. Quantum coherent atomic tunneling between two trapped Bose-Einstein condensates. *Phys. Rev. Lett.* **79**, 4950–4953 (1997).

[150] Milburn, G., Corney, J., Wright, E. & Walls, D. Quantum dynamics of an atomic Bose-Einstein condensate in a double-well potential. *Phys. Rev. A* **55**, 4318–4324 (1997).

[151] Shelykh, I. A., Solnyshkov, D. D., Pavlovic, G. & Malpuech, G. Josephson effects in condensates of excitons and exciton polaritons. *Phys. Rev. B* **78**, 041302 (2008).

[152] Solnyshkov, D., Shelykh, I., Glazov, M., Malpuech, G., Amand, T., Renucci, P., Marie, X. & Kavokin, A. Nonlinear effects in spin relaxation of cavity polaritons. *Semiconductors* **41**, 1080–1091 (2007).

[153] Poincare, J. H. Sur le probleme des trois corps et les equations de la dynamique. *Acta Mathematica* **13**, 1 (1890).

[154] Lorenz, E. N. Deterministic nonperiodic flow. *Journal of the Atmospheric Sciences* **20**, 130–141 (1963).

[155] Mandelbrot, B. *The Fractal Geometry of Nature* (Macmillan, 1982).

[156] Sarchi, D., Carusotto, I., Wouters, M. & Savona, V. Coherent dynamics and parametric instabilities of microcavity polaritons in double-well systems. *Phys. Rev. B* **77**, 125324 (2008).

[157] Huberman, B., Crutchfield, J. & Packard, N. Noise phenomena in Josephson junctions. *Appl. Phys. Lett.* **37**, 750 (1980).

[158] Kim, K., Kim, M., Chong, Y. & Niemeyer, J. Simulations of collective synchronization in Josephson junction arrays. *Appl. Phys. Lett.* **88**, 062501 (2006).

[159] Snoke, D., Liu, Y., Vrs, Z., Pfeiffer, L. & West, K. Trapping long-lifetime excitons in a two-dimensional harmonic potential. *Solid State Communications* **134**, 37 – 42 (2005). Spontaneous Coherence in Excitonic Systems.

[160] Bajoni, D., Peter, E., Senellart, P., Smirr, J. L., Sagnes, I., Lemaître, A. & Bloch, J. Polariton parametric luminescence in a single micropillar. *Applied Physics Letters* **90**, 051107 (2007).

[161] Pecora, L. M. & Carroll, T. L. Synchronization in chaotic systems. *Phys. Rev. Lett.* **64**, 821–824 (1990).

[162] Boccaletti, S., Kurths, J., Osipov, G., Valladares, D. & Zhou, C. The synchronization of chaotic systems. *Phys. Reports* **366**, 1 (2002).

[163] Cuomo, K. M. & Oppenheim, A. V. Circuit implementation of synchronized chaos with applications to communications. *Phys. Rev. Lett.* **71**, 65–68 (1993).

[164] Einstein, A., Podolsky, B. & Rosen, N. Can quantum-mechanical description of physical reality be considered complete? *Phys. Rev.* **47**, 777 (1935).

[165] Bohr, N. Can quantum-mechanical description of physical reality be considered complete? *Phys. Rev.* **48**, 696–702 (1935).

[166] Bohm, D. A suggested interpretation of the quantum theory in terms of hidden variables. *Phys. Rev* **85**, 166–179 (1952).

[167] Bell, J. On the Einstein Podolsky Rosen paradox. *Physics* **1**, 195–290, [Discontinued with Vol. 4, no. 1, (1968)] (1964).

[168] Bell, J. On the problem of hidden variables in quantum mechanics. *Rev. Mod. Phys.* **38**, 447–452 (1966).

[169] Clauser, J., Horne, M., Shimony, A. & Holt, R. Proposed experiment to test local hidden-variable theories. *Phys. Rev. Lett.* **23**, 880–884 (1969).

[170] Wigner, E. On hidden variables and quantum mechanical probabilities. *American Journal of Physics* **38**, 1005 (1970).

[171] Clauser, J. & Horne, M. Experimental consequences of objective local theories. *Phys. Rev. D* **10**, 526–535 (1974).

[172] Clauser, J. & Shimony, A. Bell's theorem: Experimental tests and implications. *Reports on Progress in Physics* **41**, 1881–1927 (1978).

[173] d'Espagnat, B. The quantum theory and reality. *Scientific American* **241**, 158–181 (1979).

[174] Mermin, N. Bringing home the atomic world: Quantum mysteries for anybody. *Am. J. Phys* **49**, 940–943 (1981).

[175] Mermin, N. Is the moon there when nobody looks? Reality and the quantum theory. *Physics Today* **38**, 38–47 (1985).

[176] Bohm, D. & Aharonov, Y. Discussion of experimental proof for the paradox of Einstein, Rosen, and Podolsky. *Phys. Rev.* **108**, 1070–1076 (1957).

[177] Bennet, C. H. & Brassard, G. *in Proceedings of the IEEE International Conference on Computers, Systems and Signal Processing* (IEEE, New York, 1984).

[178] Bennet, C. H., Brassard, G., Crepeau, C., Jozsa, R., Peres, A. & Wootters, W. K. Teleporting an unknown quantum state via dual classical and Einstein-Podolsky-Rosen channels. *Phys. Rev. Lett.* **70**, 1895 (1993).

[179] Ekert, A. K. Quantum cryptography based on Bell's theorem. *Phys. Rev. Lett.* **67**, 661–663 (1991).

[180] Bennett, C. H., Brassard, G. & Mermin, N. D. Quantum cryptography without Bell's theorem. *Phys. Rev. Lett.* **68**, 557–559 (1992).

[181] Jennewein, T., Simon, C., Weihs, G., Weinfurter, H. & Zeilinger, A. Quantum cryptography with entangled photons. *Phys. Rev. Lett.* **84**, 4729–4732 (2000).

[182] Scarani, V., Bechmann-Pasquinucci, H., Cerf, N. J., Dusek, M., Lutkenhaus, N. & Peev, M. The security of practical quantum key distribution. *arXiv:* **0802.4155** (2008).

[183] Benson, O., Santori, C., Pelton, M. & Yamamoto, Y. Regulated and entangled photons from a single quantum dot. *Phys. Rev. Lett.* **84**, 2513 (2000).

[184] Gammon, D., Snow, E. S., Shanabrook, B. V., Katzer, D. S. & Park, D. Fine structure splitting in the optical spectra of single GaAs quantum dots. *Phys. Rev. Lett.* **76**, 3005 (1996).

[185] Kulakovskii, V. D., Bacher, G., Weigand, R., Kummell, T., Forchel, A., Borovitskaya, E., Leonardi, K. & Hommel, D. Fine structure of biexciton emission in symmetric and asymmetric CdSe/ZnSe single quantum dots. *Phys. Rev. Lett.* **82**, 1780 – 1783 (1999).

[186] Stevenson, R. M., Hudson, A. J., Bennett, A. J., Young, R. J., Nicoll, C. A., Ritchie, D. A. & Shields, A. J. Evolution of entanglement between distinguishable light states. *Phys. Rev. Lett.* **101**, 170501 (2008).

[187] Stevenson, R. M., Young, R. J., Atkinson, P., Cooper, K., Ritchie, D. A. & Shields, A. J. A semiconductor source of triggered entangled photon pairs. *Nature* **439**, 179 (2006).

[188] Young, R. J., Stevenson, R. M., Atkinson, P., Cooper, K., Ritchie, D. A., & Shields, A. J. Improved fidelity of triggered entangled photons from single quantum dots. *New Journal of Physics* **8**, 29 (2006).

[189] Peres, A. Separability criterion for density matrices. *Phys. Rev. Lett.* **77**, 1413 (1996).

[190] Akopian, N., Lindner, N. H., Poem, E., Berlatzky, Y., Avron, J. & Gershoni, D. Entangled photon pairs from semiconductor quantum dots. *Phys. Rev. Lett.* **96**, 130501 (2006).

[191] Vogel, M. M., Ulrich, S. M., Hafenbrak, R., Michler, P., Wang, L., Rastelli, A. & Schmidt, O. G. Influence of lateral electric fields on multiexcitonic transitions and fine structure of single quantum dots. *Appl. Phys. Lett* **91**, 051904 (2007).

[192] Gerardot, B., Seidl, S., Dalgarno, P. A., Warburton, R. J., Granados, D., Garcia, J. M., Kowalik, K., Krebs, O., Karrai, K., Badolato, A. & Petroff, P. M. Manipulating exciton fine structure in quantum dots with a lateral electric field. *Appl. Phys. Lett.* **90**, 041101 (2007).

[193] Pfanner, G., Seliger, M. & Hohenester, U. Entangled photon sources based on semiconductor quantum dots: The role of pure dephasing. *Phys. Rev. B* **78**, 195410 (2008).

[194] Johne, R., Gippius, N. A., Pavlovic, G., Solnyshkov, D. D., Shelykh, I. A. & Malpuech, G. Entangled photon pairs produced by a quantum dot strongly coupled to a microcavity. *Phys. Rev. Lett* **100**, 240404 (2008).

[195] Shirane, M., Kono, S., Ushida, J., Ohkouchi, S., Ikeda, N., Sugimoto, Y. & Tomita, A. Mode identification of high-quality-factor single-defect nanocavities in quantum dot-embedded photonic crystals. *J. Appl. Phys.* **101**, 073107 (2007).

[196] Cohen-Tannoudji, C., Dupont-Roc, J. & Grynberg, G. *Atom-Photons Interactions* (John Wiley & Sons, New York, 1992).

[197] Wootters, W. Entanglement of formation of an arbitrary state of two qubits. *Phys. Rev. Lett.* **80**, 2245–2248 (1998).

[198] Yu, T. & Eberly, J. H. Evolution from entanglement to decoherence of bipartite mixed "x" states. *arXiv:quant-ph/0503089* (2005).

[199] Yonac, M., Yu, T. & Eberly, J. H. Pairwise concurrence dynamics: A four-qubit model. *J. Phys. B* **40**, S45 (2007).

[200] Winger, M., Badolato, A., Hennessy, K. J., Hu, E. L. & Imamoglu, A. Quantum dot spectroscopy using cavity QED. *Phys. Rev. Lett.* **101**, 226808 (2008).

[201] Pathak, P. K. & Hughes, S. Generation of entangled photon-pairs from a single quantum dot embedded in a planar photonic-crystal cavity. *arXiv:0812.2474* (2009).

[202] Laussy, F. P., del Valle, E. & Tejedor, C. Strong coupling of quantum dots in microcavities. *Physical Review Letters* **101**, 083601 (2008).

[203] Stier, O., Grundmann, M. & Bimberg, D. Electronic and optical properties of strained quantum dots modeled by 8-band k-p theory. *Phys. Rev. B* **59**, 5688 (1999).

[204] Cantele, G., Piacente, G., Ninno, D. & Iadonisi, G. Optical anisotropy of ellipsoidal quantum dots. *Phys. Rev. B* **66**, 113308 (2002).

[205] Favero, I., Cassabois, G., Jankovic, A., Ferreira, R., Darson, D., Voisin, C., Delalande, C., Roussignol, P., Badolato, A., Petroff, P. M. & Gerard, J. M. Giant optical anisotropy in a single InAs quantum dot in a very dilute quantum-dot ensemble. *Appl. Phys. Lett.* **86**, 041904 (2005).

[206] Santori, C., Fattal, D., Pelton, M., Solomon, G. S. & Yamamoto, Y. Polarization-correlated photon pairs from a single quantum dot. *Phys. Rev. B* **66**, 045308 (2002).

[207] Vuckovic, J. & Yamamoto, Y. Photonic crystal microcavities for cavity quantum electrodynamics with a single quantum dot. *Appl. Phys. Lett.* **82**, 15 (2003).

[208] Meirom, E. A., Lindner, N. H., Berlatzky, Y., Poem, E., Akopian, N., Avron, J. E. & Gershoni, D. Distilling entanglement from random cascades with partial "which path" ambiguity. *Phys. Rev. A.* **77**, 062310 (2008).

[209] Jundt, G., Robledo, L., Hogele, A., Falt, S. & Imamoglu, A. Observation of dressed excitonic states in a single quantum dot. *Phys. Rev. Lett.* **100**, 177401 (2008).

[210] Muller, A., Fang, W., Lawall, J., & Solomon, G. S. Emission spectrum of a dressed exciton-biexciton complex in a semiconductor quantum dot. *Phys. Rev. Lett.* **101**, 027401 (2008).

[211] Dousse, A., Lanco, L., Suffczyński, J., Semenova, E., Miard, A., Lemaître, A., Sagnes, I., Roblin, C., Bloch, J. & Senellart, P. Controlled light-matter coupling for a single quantum dot embedded in a pillar microcavity using far-field optical lithography. *Phys. Rev. Lett.* **101**, 267404 (2008).

[212] Vamivakas, A., Zhao, Y., Lu, C. & Atatüre, M. Spin-resolved quantum-dot resonance fluorescence. *Nature Physics* **5**, 198–202 (2009).

[213] Flagg, E., Muller, A., Robertson, J., Founta, S., Deppe, D., Xiao, M., Ma, W., Salamo, G. & Shih, C. Resonantly driven coherent oscillations in a solid-state quantum emitter. *Nature Physics* **5**, 203–207 (2009).

[214] Frohlich, H. Theory of electrical breakdown in ionic crystals. *Proc. Roy. Soc. A* **160**, 230 (1937).

[215] Ramon, G., Mann, A. & Cohen, E. Theory of neutral and charged exciton scattering with electrons in semiconductor quantum wells. *Phys. Rev. B* **67**, 045323 (2003).

Publications

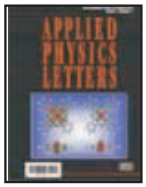

1. M. Lorenz, R. Johne, H. P. D. Schenk, S. I. Borenstain, A. Schon, C. Bekeny,T. Vo, J. Gutowski, T. Nobis, H. Hochmuth, J. Lenzner, M. Grundmann, **Self absorption in the room-temperature cathodoluminescence of ZnO scintillator thin films on sapphire**, Appl. Phys. Lett. **89**, 243510 (2006)

2. R. Johne, M. Lorenz, H. Hochmuth, J. Lenzner, H. von Wenckstern, G. Zimmermann, H. Schmidt, R. Schmidt-Grund, M. Grundmann,**Cathodoluminescence of large-area PLD grown ZnO thin films measured in transmission and reflection**, Appl. Phys. A, **88**, 1 (2007)

3. I. A. Shelykh, G. Malpuech, R. Johne and A.V. Kavokin, **The System of interacting polaritons: classical versus quantum kinetic equation**, Solid State Communications, **144**, Issue 9, Pages 378-383, (2007)

4. I.A. Shelykh, R. Johne, D.D. Solnyshkov, A Kavokin, N. Gippius, and G. Malpuech **Quantum kinetic equations for interacting bosons and their application for polariton parametric oscillators** PHYSICAL REVIEW B **76**, 155308 (2007)

5. N. S. Maslova, R. Johne, N. A. Gippius, **Role of fluctuations in nonlinear dynamics of driven polariton system in semiconductor microcavities**,JETP Letters **86**, 2, 135-140 (2007)

6. R. Johne, N. A Gippius, G. Pavlovic, D. D. Solnyshkov, I. A. Shelykh, and G. Malpuech, **Entangled Photon Pairs Produced by a Quantum Dot Strongly Coupled to a Microcavity**, Physical Review Letters, **100**, 240404 (2008), Selected for: Virtual Journal of Quantum Computation, July (2008)

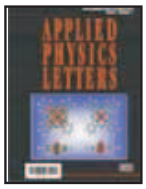

7. R. Johne, D.D. Solnyshkov, G. Malpuech, **Theory of exciton-polariton lasing at room temperature in ZnO microcavities in ZnO microcavities**,Appl. Phys. Lett **93**, 211105 (2008)

8. R.Johne, N. S. Maslova, N. A. Gippius, **Fluctuation-induced transitions of a bistable driven polariton system in the presence of damping**, Solid State Communications **149**, 496-500, (2009)

9. R. Johne, N.A. Gippius, G. Malpuech, **Entangled photons from a strongly coupled quantum dot-cavity system**, Phys. Rev. B **79**, 155317 (2009), Selected for: Virtual Journal of Nanoscale Science & Technology, May (2009), Virtual Journal of Quantum Information, May (2009)

10. N. S. Maslova, R. Johne, N. A. Gippius, **Colored noise controlled dynamics of nonlinear semiconductor Microcavity**, accepted JETP Letters

11. R. Johne, I.A. Shelykh, D.D. Solnyshkov, G. Malpuech, **Polaritonic analogue of Datta and Das spin transistor**, submitted

12. D.D. Solnyshkov, R. Johne, I. A. Shelykh, G Malpuech, **Chaotic Josephson oscillations of exciton-polaritons and their applications**, submitted

Conference contributions

1. R. Johne, Michael Lorenz, Holger Hochmuth, Jrg Lenzner, Holger von Wenckstern, Gabriele Benndorf and Marius Grundmann, Cathodoluminescence of PLD grown ZnO thin films: A comparison of experiment and simulation, German Physical Society Spring Meeting, Dresden, March (2006), (Poster)
2. H. von Wenckstern, M. Brandt, H. Schmidt, G. Zimmermann, R. Johne, J. Lenzner, H. Hochmuth, M. Lorenz, and M. Grundmann, Integral electrical and micro-electrical investigations of ZnO thin films, German Physical Society Spring Meeting, Dresden, March (2006), (Poster)
3. Michael Lorenz, Holger Hochmuth, Robert Johne, Gabriele Benndorf, Jorg Lenzner, Holger von Wenckstern, Matthias Schubert, Marius Grundmann, Advances in high-quality ZnO Thin Films and Heterostructures grown by Pulsed Laser Deposition, The 4th International Workshop on ZnO and Related Materials Giessen, October (2006) (Poster)
4. R. Johne, Ivan Shelykh, Guillaume Malpuech, Dmitry Solnyshkov, Quantum kinetic equations of the optical parametric oscillator, International Conference on Spontaneous Coherence in Excitonic Systems 3 (ICSCE3), Les Houches, January 2007 (Poster)
5. R. Johne, Ivan Shelykh, Guillaume Malpuech, Dmitry Solnyshkov, Modelling of the Quantum kinetic equations of the optical parametric oscillator, L'cole predoctorale "optique quantique", Les Houches, summerschool " optique quantique " September 2007 (Poster)
6. R. Johne, N. A. Gippius, G. Pavlovic, D.D. Solnyshkov , I.A. Shelykh and G. Malpuech, Entangled Photon Pairs Produced by Quantum Dot Strongly Coupled to Microcavity, Fermi-school "quantum coherence in solid state systems" Como, Italy, July (2008) (Poster)
7. R. Johne, N. A. Gippius, G. Pavlovic, D.D. Solnyshkov , I.A. Shelykh and G. Malpuech, A quantum dot strongly coupled to a microcavity - A solid state source of entangled photon pairs, ICPS 29, Rio de Janeiro, Brasil, August (2008) (oral presentation)
8. R. Johne, N. S. Maslova, N. A. Gippius, Fluctuation-induced transitions of a bistable driven polariton system in the presence of damping, ICPS 29, Rio de Janeiro, Brasil, August (2008) (Poster)
9. R. Johne, N. A. Gippius, G. Pavlovic, D.D. Solnyshkov , I.A. Shelykh and G. Malpuech, Entangled Photon Pairs Produced by Quantum Dot Strongly Coupled to Microcavity, PASPS-V , Foz do Iguacu, Brasil, August (2008) (Poster)
10. R. Johne, I.A. Shelykh, D.D. Solnyshkov , N. S. Maslova, N. A. Gippius and G. Malpuech, Polarization Multistability of Cavity Polaritons, PASPS-V , Foz do Iguacu, Brasil, August (2008) (Poster)
11. R. Johne, D.D. Solnyshkov, G. Malpuech, Theory of exciton-polariton lasing in ZnO based microcavities, PLMCN 9, Lecce, Italy, April (2009) (Poster)
12. R. Johne, N.A. Gippius, G. Malpuech, Entangled photons from a strongly coupled quantum dot-cavity structure PLMCN 9, Lecce, Italy, April(2009) (oral presentation)
13. D. D. Solnyshkov, R. Johne, G. Pavlovic, I.A. Shelykh, G. Malpuech, Josephson effect for spinor cavity exciton-polaritons and application to chaotic cryptography, Workshop: Bloch Oscillations and Landau-Zener Tunneling: From Hot Electrons to Ultracold Atoms, Dresden, Germany, April (2009) (invited oral presentation)

ABSTRACT Exciton-polaritons, mixed light-matter particles are on their way to break into the world of optoelectronic devices thanks to unique properties and nonlinear effects in polariton systems. The present thesis is devoted to the investigation of nonlinear effects and applications of exciton-polaritons. The first part of the thesis investigates nonlinear effects such as the polariton parametric oscillator and the polariton bistability: A new mathematical approach in between the semiclassical and the fully coherent picture is developed and the crucial impact of fluctuations on the bistability is in the focus of this work. Applications of exciton-polaritons are the subject of the second part. ZnO based structures are suited candidates for room temperature polariton lasing and we simulate such a structure numerically in dependence of the quality factor and the Rabi splitting. Beside the laser, the unique spin structure opens a lot of possibilities. In analogy to the spintronic Datta and Das spin transistor a new polaritonic spin transistor is developed and presented. Also other analogies, such as the Josephson effect are predicted for polaritons. This effect is complex enough to show chaotic behavior in some parameter range. The chaotic oscillations can be used for secure communication. The last part of the thesis is devoted to 0D polaritons and to an on-chip source of entangled photon pairs. Existing problems blocking the realization of highly correlated two-photon sources based on the biexciton decay in quantum dots can be overcome in the strong coupling regime.

Keywords: exciton-polariton, polarization, ZnO, entanglement, quantum dot, Bose-Einstein condensation

RESUME Les exciton-polaritons sont des particules mixtes de lumière et de matière. Ils peuvent être le futur des applications optoélectroniques, en vertu de leur réponse optique non-linéaire qui est extrêmement forte. Cette thèse est consacrée aux effets non-linéaires et aux applications variées des exciton-polaritons dans les nanostructures à base de semi-conducteurs. Les microcavités planaires et les polaritons 2D sont étudiés dans les premiers chapitres, alors que le dernier chapitre est consacré à l'étude du système de boites quantiques en cavité (polaritons 0D). L'oscillateur paramétrique et la bi stabilité sont le sujet de la première partie de la thèse. Une approche mathématique intermédiaire entre les approches semi-classiques et purement cohérente est présentée. L'impact des fluctuations proches du seuil de bi stabilité est étudié. La deuxième partie est consacrée la présentation de différentes applications basées sur les propriétés des polaritons. Un laser à polaritons basé sur une cavité de ZnO est modélisé et les résultats soulignent les avantages de l'utilisation de ce matériau pour la réalisation de ce type d'application è température ambiante. La structure de spin particulire des polaritons est par la suite utilise pour proposer deux nouvelles applications. La premire est un analogue optique du transistor de spin pour les électrons, appelé transistor Datta et Das. La deuxième propose d'utiliser le comportement chaotique d'une jonction Josephson polaritonique afin d'implémenter un système de cryptage chaotique d'un signal. Le dernier chapitre est consacré aux polaritons 0D. Nous montrons comment la réalisation du régime de couplage fort permet de réaliser une source de photons intriqués basée sur le déclin du bi exciton dans un boite quantique en résolvant un certain nombre de difficultés par rapport au système constitué d'une boite quantique simple.

Mots clef: exciton-polariton, polarisation, ZnO, intriquation, boîte quantique